A STUDY OF HEAT PUMP FIN STAGED EVAPORATORS UNDER FROSTING CONDITIONS

A Dissertation

by

JIANXIN YANG

Submitted to the Office of Graduate Studies of
Texas A&M University
in partial fulfillment of the requirements for the degree of

DOCTOR OF PHILOSOPHY

May 2003

Major Subject: Mechanical Engineering

A STUDY OF HEAT PUMP FIN STAGED EVAPORATORS UNDER FROSTING CONDITIONS

A Dissertation

by

JIANXIN YANG

Submitted to Texas A&M University
in partial fulfillment of the requirements
for the degree of

DOCTOR OF PHILOSOPHY

Approved as to style and content by:

Dennis L. O'Neal (Chair of Committee)	
Nagamangala K. Anand (Member)	Kalyan Annamalai (Member)
Mark T. Holtzapple (Member)	John A. Weese (Head of Department)

May 2003

Major Subject: Mechanical Engineering

ABSTRACT

A Study of Heat Pump Fin Staged Evaporators
Under Frosting Conditions. (May 2003)
Jianxin Yang, B.S., Jiaotong University, Xi'an, China
M.S., Jiaotong University, Xi'an, China
Chair of Advisory Committee: Dr. Dennis L. O'Neal

This dissertation provides a detailed description of the research work completed on fin staged heat exchangers. The effects of staging fin on the frosting performance of heat pump evaporators and the whole heat pump system have been studied experimentally and theoretically.

Frost degrades the performance of fin-and-tube outdoor coils as well as the whole heat pump system. The objective of the experimental part of this study was to investigate the effects of the staging fin on the frost/defrost performance of heat pump outdoor coils under different operating conditions. To accomplish this objective, a series of frosting tests was conducted on an off-the-shelf heat pump system with five (three two-row and two three-row) evaporators over a range of outdoor temperatures and humidities and a range of airflow rates typical of those found in residential sized heat pumps.

Performances of the heat pump unit with baseline or fin staged outdoor coils at either frosting or steady-state test conditions are compared and analyzed. Experimental data showed that for a given two-row heat pump outdoor coil operating at the standard ANSI/ASHRAE 35 ^{o}F (1.7 ^{o}C) frosting conditions, fin staging increased cycle time and COP. There was a small decrease in peak capacity at lower initial airflow rates. At a lower temperature of 28 ^{o}F (2.2 ^{o}C), cycle time continued to be enhanced with fin staging, and cyclic COP was within 5% of the base case when fin staging was used.

In the second step of this work, an analytical model to simulate the performance of both the baseline and fin staged heat pump coils under frosting conditions was developed based on fundamental heat and mass transfer principles. The transient performance of the frosted evaporator was analyzed with the quasi-steady state approach. The section-by-section evaluation scheme was combined with the tube-by-tube approach to model the mass transfer process in the frost formation module. The two-dimensional fin surface was divided into a number of parallel non-overlapping sections. Each of the sections was the calculation unit for the mass transfer. Methods for calculating the airside heat transfer coefficient and friction factor were developed and applied to the simulation model of the fin staged coil.

To verify the validity of the frosted evaporator model, the frosting performance of three two-row coils at the same test conditions was simulated and compared with experimental data. The frosted evaporator model appeared to provide satisfactory simulation of the fin-and-tube heat exchanger during the frost buildup process. Comparisons with the test data indicated that the model could capture the trends

of the coil capacity, pressure drop, airflow and frost growth. The model also provided a variety of other simulation results including frost mass accumulation, air velocity inside coil, air and refrigerant outlet state, and so on. Overall, the numerical results were in reasonable agreement with the test data under different frosting operation conditions.

To My Parents

To My Wife

ACKNOWLEDGEMENTS

The research reported in this dissertation was funded by ASHRAE project 1002-TRP and an ASHRAE grant-in-aid for graduate students. The heat pump system and fin staged coils were donated by the Career Corporation. I am grateful to ASHRAE and Career for their support and help throughout the research study.

I appreciate the guidance from my adviser and committee chair, Dr. Dennis L. O'Neal. My thanks are also extended to Dr. N. K. Anand, Dr. Kalyan Annamalai and Dr. Mark T. Holtzapple for serving on my committee.

I would like to thank Dr. William Dan Turner, the director of Energy Systems Lab, for his financial assistance during the last period of this research work. His kindness is deeply appreciated. Special thanks are also owed to Dr. Charles H. Culp for his encouragement and advice on writing this dissertation.

TABLE OF CONTENTS

CHAPTER Page

LIST OF TABLES

LIST OF FIGURES

Figure Page

Figure Page

Figure Page

Figure Page

Figure Page

Figure Page

Figure Page

NOMENCLATURE

A	=	cross section area of a tube, inch^2
$A_{c.t}$	=	minimum flow area for bare tube bank
A_{fin}	=	surface area of fins
A_{total}	=	airside surface area (fins and tubes)
A_{tube}	=	surface area of bare tubes
Bo	=	boiling number
d_e	=	tube hydraulic diameter, inch
D	=	saturated discharge temperature at compressor discharge pressure, ^oF
D_h	=	tube hydraulic diameter, inch
D_i	=	tube inner diameter, inch
D_o	=	outside diameter of tube, inch
D_{tube}	=	tube outside diameter, inch
E	=	weighting factors to average h_{liq} and h_{pool}
f_{fin}	=	friction factor associated with fin area
f_m	=	mean friction factor
f_{tube}	=	friction factor associated with bare tube area
G	=	refrigerant mass flux
h_{an}	=	heat transfer coefficient at the end of annular flow (X=0.85)
h_{inlet}	=	refrigerant enthalpy at the inlet of heat exchanger, Btu/lb_m
h_{outlet}	=	refrigerant enthalpy at the outlet of heat exchanger, Btu/lb_m
h_{liq}	=	liquid convection heat transfer coefficient, Btu/lb_m
h_{pool}	=	pool boiling heat transfer coefficient, Btu/lb_m
h_{sp}	=	heat transfer coefficient at the saturated vapor point (X=1.0)
j_4	=	j-factor for four or greater number of rows
K_l	=	thermal conductivity of refrigerant liquid
K_{sp}	=	thermal conductivity of single-phase refrigerant
L	=	length of the evaporator tube, inch
M	=	molecular weight of refrigerant
$\dot{m}_{refrigerant}$	=	mass rate of refrigerant flowing through heat exchanger, lb_m/min

n	=	number of return bends
P	=	pressure drop, psia
P_{fin}	=	fin pitch
Pr_l	=	liquid Prandtl number
Pr_{sp}	=	Prandtl number of single-phase refrigerant
P_{red}	=	reduced pressure, psia
$P_{vel.coil}$	=	velocity head of air through coil, psia
$P_{vel.fan}$	=	velocity head of air through fan, psia
ΔP	=	pressure drop of a tube, psia
$\Delta P_{coil.static}$	=	coil static pressure drop, psia
$\Delta P_{fan.static}$	=	fan curve static pressure, psia
ΔP_{static}	=	gauge static pressure at fan exit, psia
q	=	heat flux, Btu/(hr·ft^2)
Re	=	Reynolds number
Re_{Dtube}	=	the Reynolds number based on tube outside diameter
Re_{sp}	=	Reynolds number of single-phase refrigerant
S	=	saturated suction temperature at compressor suction pressure, ^{o}F
S	=	spacing between adjacent fins
S_l	=	tube spacing in air flow direction
S_t	=	tube spacing normal to air flow
S_{tube}	=	tube spacing normal to flow
t_{fin}	=	fin thickness, inch
v	=	refrigerant specific volume, ft^3/lb$_m$
v_m	=	mean specific volume of refrigerant, ft^3/lb$_m$
X	=	flow vapor quality
x_2-x_1	=	quality change from tube inlet to outlet
x_m	=	mean quality value of a tube
ξ_{rm}	=	resistance factor of the return bend
ρ	=	humid air density

CHAPTER I

INTRODUCTION

The heat pump is a popular and reliable means to maintain interior comfort levels in residential building for both heating and cooling. During the cooling season, it transfers heat energy from the indoor space to the outdoor air the same as an air conditioner. The operation is reversed during the heating season. It extracts heat energy from low temperature outdoor air and delivers that heat energy to the indoor conditioned space.

In cold and humid climates, when the surface temperature of the outdoor heat pump evaporator is below 32^{o}F (0^{o}C) and lower than the dew point temperature of outdoor air, moisture will first condense on the coil and then freeze. After freezing, frost grows and accumulates on the outdoor coil surface. The frost blocks the airflow and increases the pressure drop through the coil. Because the fan used with the heat pump outdoor coil is normally a propeller type fan, its capacity drops rapidly as the pressure drop across the coil increases. The capacity of the evaporator decreases due to the airflow drop, which reduces the overall heating capacity and coefficient of performance of the heat pump. The frost layer also adds an additional thermal resistance to the heat transfer between the air and refrigerant. The reduction in airflow and increased thermal resistance reduces the heat energy extracted by the evaporator and decreases the heat pump capacity and efficiency. Eventually, the capacity is reduced so much that the evaporator has to be defrosted. A heat pump is normally defrosted by reversing the cycle. Because the heating cycle has to be interrupted and additional energy is used to melt the frost off the evaporator, the defrosting process increases energy consumption and reduces the seasonal efficiency of the heat pump.

Frost formation and the subsequent defrost process continues to be a source of degradation in the performance of heat pump. Therefore, better understanding of the impact of frost formation and continued refinements of heat pump equipment should be pursued. One option for improving heat pump frosting performance is the use of staged fins (Ogawa 1993). Both experimental and modeling work on the effects of staged fin on the frosting performance of outdoor coil has been conducted at the Energy Systems Laboratory (ESL) at Texas A&M University. The experimental results and analysis is presented in this dissertation. Also, the numerical methods are applied to study the mechanism of the effects of staged fin on the performance of a frosted evaporator.

This dissertation follows the style and format of *ASHRAE Transactions*.

The main objectives of this work were to: (1) develop an evaporation simulation program that could model the transient performance of fin staged coil under frosting conditions; and (2) to compare the simulation results with the experimental data and validate the model. To accomplish these objectives, the modeling work started with a survey of available literature on the fin staged coils and the development of frosted evaporator model. A frosted evaporator model developed at the Energy Systems Laboratory of Texas A&M University (O'Neal and Gong, 1996) was used as a starting point for the simulation work. Significant modifications in the simulation model have been made for this project. These modifications include: implementing a fin staging model, updating airside heat transfer and pressure drop calculations, including R-410A thermodynamics and transportation property calculation for refrigerant-side simulation, incorporating a refrigerant distributor model into the simulation, making numerous corrections and additions on the calculation correlations and algorithms. The frosted evaporator model has been significantly improved and expanded from the earlier version.

The problem involved in modeling the fin staged heat exchanger under frosting conditions is quite complicated because frost growth varies by location and time. In fact, the problem is three dimensional and transient. In this study, a method of computing the heat transfer and frost growth rates as well as the frost thickness and surface temperature as functions of time and position was developed. The method utilized known convection heat transfer correlations for different geometries and the Lewis analogy to determine the convection mass transfer coefficient. An iterative quasi-steady state approach was adopted to compute the air-frost interface temperature, the partial pressure of water vapor at the frost surface, and the frost properties. The technique provided the capability for adjusting the frost density and thermal conductivity properties. The model also considered the performance losses due to added pressure drop and heat transfer resistance that resulted from the growth of the frost layer. Model results were compared with existing experimental data and good agreement was obtained.

This dissertation provides a detailed description of the research work completed on both experiment and simulation. The dissertation is divided into eight chapters. Chapter II presents an introduction to the staged fin and its effects on the frosting performance of heat exchanger. A brief review on the relevant simulation work is also included. Chapter III summaries the experimental work. A complete description of the experimental facility, conditions and procedures for the heat pump unit with different outdoor coils is presented. In chapter IV, test results for both baseline and fin staged coils at either frosting or steady-state test conditions are compared and analyzed. The heat pump system performances with different outdoor coils are also presented. Chapter V describes the development of a mathematical model of the frosting process on a heat exchanger. The chapter includes the details of modeling methodology, program structure and solution logic. Chapter VI focuses on some major modifications and improvements that have been done for refrigerant property calculations, as well as both refrigerant and air side heat transfer and pressure drop. Physical principles and general correlation are

discussed. In Chapter VII, comparisons are made between the experimental data and the sample results from the model for heat transfer capacity, frost layer growth, pressure drop and air flow rate. Necessary discussions on the model validation and experimental results are presented. Conclusions are drawn on the simulation work and presented in Chapter VIII. The limitations of this investigation and recommendations for future work are also presented in this chapter. Major calculation equations of frost layer properties, comparison of R410A property calculations, and fan performance test and air pressure drop calculation are provided in the appendices.

CHAPTER II

LITERATURE SURVEY

In 1970's the National Bureau of Standards conducted tests on residential heat pumps. Their tests revealed two effects that significantly degrade heat pump performance: (1) cycling effects on system performance and (2) frosting effects on outdoor coil (Didion, et al. 1979). Thereafter, extensive experimental and theoretical investigations have been done on heat pump to study evaporator and system performance under frosting condition.

Early frost experimental work concentrated on frost properties, mechanism of frost growth, and heat transfer for simple geometry: such as tubes, annulii, cylinders, flat plates and parallel plates. O'Neal and Tree (1985) gave a comprehensive review of frosting in these geometries. Other researchers focused their attention on the effects of frost formation on the performance of heat exchangers (Stoecker 1957, Bonne 1980, Young 1980, Bittle 1983, Miller 1984, Emery 1990, Senshu 1990, Kondepudi and O'Neal 1990). Most of these investigations discussed the frosting effects on heat exchanger performance. Some empirical correlations were presented to describe how the variations of environmental conditions affected frost growth as well as frost properties such as density and thermal conductivity.

Other researchers worked on developing computer models of the transient behavior of frosted heat exchangers. In the 1970's, simulation work first focused on developing steady-state heat pump models that could be used to improve heat pump system design (Flower 1978, Ellison, et al.1978). Later, more detailed steady-state models were developed to analyze and predict heat pump/heat exchanger performance without considering frost formation (Fisher and Rice 1983, Bechley 1986, Crawford 1987, Welsby 1988, Domanski 1989 and Sami 1992).

A review of the previously published research on heat pump performance was done to examine the performance degradation due to frosting and investigate any outdoor evaporator fin modifications that were done. The literature reviewed showed that the frost/defrost cycling of the heat pump accounts for losses in performance. Progress has been made in understanding the basic parameters that govern frost growth on a cold surface and the interactions of frost with heat exchanger performance. Frosting research was surveyed in an effort to better quantify the effects of the frost layer on finned coil heat exchanger efficiency and particularly upon airflow through the coil. The literature surveyed has been organized into two different parts: experimental study and numerical analysis.

Experimental Study

Most researchers who studied heat pump degradation due to frost formation have viewed the formation of frost as a transient problem that was limited to certain temperature ranges and relative humidity levels. The way frost forms and the effects of frost on heat exchanger performance is one area that has received some attention by researchers.

Research conducted by Bryant (1995) found that when the outdoor temperature was at or near 32°F (0°C), the surface of the outdoor heat exchanger would fall below 32°F (0°C). When this surface was then exposed to a moist air stream, water droplets would condense on the surface and then freeze. Frost crystals would grow from the frozen droplets and begin to block the airflow passage through the heat exchanger fins. The blockage increased the pressure drop through the evaporator, which reduced the airflow. The reduced airflow reduced the capacity and the coefficient of performance of the heat pump.

Additional frosting research was done to find the influence of frost formation on the outdoor heat exchanger. Payne (1992) performed an experiment to investigate the insulating effects of frost by controlling airflow. When the airflow through the outdoor heat exchanger was kept constant, the heating capacity remained within 5% of its peak value and cycle times were increased by as much as 43%. Payne's research showed that the associated drop in airflow due to the presence of frost on the fins was the primary factor in reducing capacity and COP.

Rite and Crawford (1991a) performed an investigation into the effects of frosting on heat exchanger performance. Their experimental investigation commenced with a baseline performance evaluation of a test heat exchanger. The important parameters being measured were overall heat transfer UA-value and airside pressure drop. Once baseline performance had been recorded, the investigators varied inlet RH, airflow rate, air inlet temperature, and inlet refrigerant temperature. These parameters were varied to judge the effects of their variations on the UA-value and on airside pressure drop.

As the relative humidity was increased, the rate of increase in airside pressure drop continued to increase. For the time of the frosting experiments, the pressure drop increased 13 times over the baseline pressure drop (Rite and Crawford, 1991a). Increasing the airflow rate increased the pressure drop, but the rate of increase in pressure drop was found to be the same as seen in the baseline tests. Increasing the inlet air temperature to the test heat exchanger had the same effect as raising the relative humidity. The frosting rate increased and the airside pressure drop followed the same trends seen in the relative humidity variation tests. By increasing the air inlet temperature, Rite and Crawford increased the dew point temperature for the same relative humidity condition. This increase in the dew point temperature had the same effect as raising the relative humidity. Decreasing the refrigerant temperature caused an increase in the rate of frost formation and therefore increased the rate of airside pressure drop. In all experiments, the rate of frost formation was the key element when examining the airside pressure drop.

Rite and Crawford (1991a) looked at the rate of mass transfer to the coil surface to explain the effects of frost formation on the airside pressure drop. They explained the relationship between frosting rate and airflow rate as a function of four parameters: (1) the mass transfer coefficient, (2) the evaporator surface temperature, (3) the air temperature, and (4) the moisture carrying capacity of the air stream. Increasing the air temperature and the relative humidity would increase the mass transfer driving potential. Raising the evaporator surface temperature had the opposite effect by decreasing the mass transfer driving potential. Airflow rate affects the rate of frost accumulation due to its effects on the mass transfer coefficient and the air temperature. Rite and Crawford (1991a) found that increasing the airflow rate decreased the mass transfer driving potential.

As airflow rate increased, the convective heat transfer rate increased, and caused the evaporator surface temperature to increase closer to the air temperature (Rite and Crawford, 1991a). This increase in surface temperature also increased the surface humidity ratio and decreased the driving potential of mass transfer. The ability of the evaporator to remove water from the air was also decreased as the airflow was increased. Research showed that as the mass flow rate of air was increased, the humidity ratio difference decreased for a given water removal rate. Therefore, a higher airflow rate will result in a higher mass transfer driving potential because the humidity ratio of the air is higher during its passage over the evaporator surface. Rite and Crawford also noted that if an increase in air temperature, moisture capacity, and mass transfer coefficient are balanced by an increase in the surface temperature, then the rate of frost formation would be the same for all airflow rates.

The review of the research by Bryant, Payne, and Rite and Crawford was meant to clarify the real effects of frost formation on the airside pressure drop and reduction in airflow across outdoor heat exchangers for heat pumps. Bryant explained the formation of frost, and Rite and Crawford further clarified the processes occurring at the heat exchanger surface as frost forms. Payne showed good proof that the greatest impact of frost is in the airflow degradation and not the insulating effects of the frost layer.

The major cause of heat pump performance degradation can be attributed to the effects of frost/defrost cycling that occurs during heating operation. Frost reduces the heating capacity by partially insulating the heat exchanger surfaces and, more importantly, by blocking airflow passages through the heat exchanger. This problem is more obvious during periods of higher ambient humidity levels or lower temperatures when the fin surfaces are more prone to frost accumulation, resulting in frequent frost/defrost cycling of the heat pump. Operation with this frequent cycling results in a great deal of heat pump capacity being used to overcome lower fin surface temperatures and melt frost. Many researchers have investigated the degree of such losses, but only a few are presented here.

Frosting and defrosting losses were studied on a 3-ton (10.6-kW) residential air-source heat pump, which used a single row spiny fin outdoor heat exchanger, by Miller (1984). He studied the effects

of frosting on COP and heating capacity under the frosting conditions of 47°F (8.3°C) to 17°F (-8.3°C) with relative humidity levels of 50% to 90% (Miller, 1984). The test heat pump incorporated a thermostatic expansion valve (TXV) as the heating mode expansion device and used no suction line accumulator. Defrosting of the outdoor heat exchanger was based upon a 50% reduction in airflow from clean coil values. Data were taken for dry, wet, and frosted coil conditions to quantify the effect of relative humidity on evaporator performance.

Miller (1984) found that once frosting began, higher relative humidity values enhanced the rate of frost accumulation, resulting in greater rates of performance degradation. Additionally, frosting and defrosting energy losses were insignificant for all conditions where the relative humidity was less than 60%. However, these losses rose considerably for ambient temperatures less than 40°F (4.4°C) with a relative humidity of 70% or greater. Based on his seasonal analysis, Miller was able to clearly show that the frosting/defrosting degradation was primarily due to defrosting of the outdoor heat exchanger. The defrosting losses were almost three times larger than those associated with the frost accumulation. Also, the use of auxiliary heat during defrost periods caused significant cumulative reductions in COP. Furthermore, the more susceptible the outdoor coil is to frost accumulation, the larger the penalty in increased power consumption and COP degradation due to defrost.

Young (1980) also evaluated several prototype residential heat pumps to maximize their winter seasonal efficiency. The experimental heat pump was designed to operate in the primarily heating dominated environment of southern Canada. The configuration chosen incorporated the indoor air handling unit that contained the compressor and all the electrical controls. The outdoor section contained only the outdoor heat exchanger, fan, and defrost termination device. This configuration was selected to facilitate servicing a heat pump in severe, cold weather and also to increase the reliability of the heat pump control electronics. An outdoor coil with 8 fpi (3 fins/cm) was chosen for the heavy frosting conditions. The heating mode expansion device for the first experimental heat pump was chosen to be an electric expansion valve (EEV). The EEV used a sensor in the evaporator outlet to sense the presence of liquid and control the valve opening accordingly. The final design incorporated the EEV, an accumulator heat exchanger, and a liquid receiver at the condenser outlet (Young, 1980). Early testing of the prototype heat pump showed that the reversing valve was an area of significant loss. Reversing valve design resulted in a 10% loss in heat pump performance caused by refrigerant leakage and heat transfer between the hot discharge gas and the cooler suction line gas. Test on another prototype heat pump incorporated four solenoid valves in place of the reversing valve to eliminate the inherent losses caused by the close proximity of the hot and cold vapor.

Young (1980) also reoriented the outdoor heat exchanger at a 45° angle. This orientation allowed melted frost to drain more effectively than the conventional vertical orientation of the heat exchanger. With the coil in a horizontal position, only 66% of the melted frost drained as compared to 97% with the

45° oriented evaporator (Young, 1980). Tests of the modified heat pumps at 32°F (0°C) showed a 38% and 45% increase in COP over commercially available models of the same capacity. Use of the EEV and elimination of reversing valve showed a maximum COP improvement of 4% and 10%, respectively (Young, 1980).

During frost accumulation, Ameen (1993) also showed that the heat extracted from the air by the evaporator was reduced as a result of the insulating effect of the frost and the blockage of airflow. This decreased the refrigerant temperature, and decreased refrigerant density at the compressor inlet, leading to a reduction in both refrigerant flow rate and compressor power. The decreased air mass flow rate caused by the increased resistance of the passages due to frosting also directly affected the fan power consumption.

All the investigations of frosting and defrosting performance degradation show the importance of delaying defrost initiation. Frosting and defrosting losses are the major source of performance degradation for heat pumps. Less frequent defrosts, and prolonged operation at a higher capacity would result from delayed frost accumulation on the outdoor heat exchanger, and methods to decrease the effects of frost should focus on the decreasing the airflow blockage in order to realize the greatest benefit.

During heating operation, the heat pump is prone to frost formation. Studies have examined this phenomenon and found that the associated drop in airflow is the primary cause of performance degradation. To maintain prolonged airflow and achieve higher heat pump performance, researchers have investigated different fin configurations. The results of some of these studies are included here.

The effects of different fin configurations on the performance of finned-tube heat exchangers in the presence of frost have been examined (Kondepudi and O'Neal, 1990). The heat exchangers tested varied in fin geometry from flat to wavy to louvered, and fin spacing was varied for testing with 10, 14, and 18 fpi (4, 6, and 7 fins/cm). Test conditions of 32°F (0°C) and 80% RH were used for most tests to determine the amount of frost accumulation, the pressure drop across the coil, the overall sensible heat transfer coefficient, the enthalpy drop across the coils, and the heat exchanger effectiveness.

Louvered fins showed the greatest amount of frost accumulation for the given time periods whereas flat and wavy fins were within 5% in frost accumulation (Kondepudi and O'Neal, 1990). This larger accumulation of frost was attributed to the larger heat transfer area of the louvered fin when compared to the flat and wavy fin geometry. Also, at higher humidity and air velocity, there were higher amounts of frost growth, and thus larger pressure drops across the heat exchanger. Increasing fin spacing led to an increased heat transfer coefficient. This was attributed to the higher heat transfer area available with the higher fin spacing. Overall heat transfer coefficient was also shown to vary with the relative humidity.

For tests of the louvered fin heat exchanger with 18 fpi (7 fins/cm) and 130 ft/min (39.6 m/min) face velocity, the overall heat transfer coefficient was shown to be 40 Btu/h-ft^2°F (227 W/m^2°C) and 52

Btu/h-ft^{2}°F (295 W/m^{2}°C) at 65% and 80% relative humidity, respectively (Kondepudi and O'Neal, 1990). The louvered fin heat exchanger performed better than other 18 fpi (7 fins/cm) heat exchangers based on overall heat transfer coefficient. The variation of heat transfer coefficient with time for the period of the tests (about 50 minutes) showed almost no decrease in heat exchanger performance due to frosting for all fin configurations.

Kondepudi and O'Neal also examined the amount of energy transferred from the air to the refrigerant by examining the enthalpy drop across the heat exchanger. The enthalpy drop of the air increased at higher humidity levels due to the large contribution of latent energy exchange between the moist air and the refrigerant. Kondepudi and O'Neal (1990) concluded that the use of lower fin density coil for longer periods of time could delay the decline of the overall heat transfer coefficient. The louvered fin heat exchanger showed a higher rate of decline in enthalpy drop than the flat and wavy fin configurations with enthalpy drop averaging 3100 Btu/lb$_m$ (7210 kJ/kg), 3900 Btu/lb$_m$ (9070 kJ/kg), and 4800 Btu/lb$_m$ (11160 kJ/kg) for the flat, wavy and louvered fins, respectively (Kondepudi and O'Neal). Kondepudi and O'Neal found that the louvered fin configuration had the highest effectiveness of the fin configurations tested.

Fin staging was discussed by Ogawa et al. (1993). In this investigation, it was proposed that frost should partly decrease at the leading edge of fins to reduce air pressure drop. Therefore, front staging, side staging, and partial cutting of fins were provided at the leading edge of the heat exchanger fins. Staging and partial cutting of fins allowed air to move to the rear of the coil and was found to be very effective in decreasing air pressure drop and increasing the heat transfer rate. The heat transfer coefficients are typically very large at the leading edge of the fins and thick frost accumulation occurs at these edges. A decrease in the frost accumulation at the leading edge and a resulting increase at the rear were proposed to be an effective method to improve the performance of the heat exchanger. This effect depended upon the number of rows. For coils with many rows, the rear fins contributed little to the heat transfer of the coil, and bypassing the airflow to the rear then promoted heat transfer because the temperature difference remained large and the decrease in airflow volume was reduced.

Techniques such as the coupling of both front staging, or wide fin spacing at the entrance, and side staging could be effective for many tube rows. An alternative for a single row coil was fin width extension in the direction of airflow. Ogawa et al. (1993) investigated nine configurations: Front staging, side staging, partial cutting of fins, and combinations of the three. Results showed that the heat transfer rate for a unit with front and side staging was 8% larger than that with side staging only when frost accumulation was 0.006 lb$_m$/ft^3 (0.1 kg/m^3). As the frost accumulation increased, the difference in the heat transfer rate between these units increased (Ogawa et al., 1993). Furthermore, the pressure loss in the coil with front staging and side staging was about 30% smaller than that with only side staging. It was found that side staging was advantageous for improving heat exchanger performance. Front staging succeeded

in reducing airflow blockage at the leading edge of fins of heat exchangers and reduced air pressure loss. A unit with side staging only was more intensely affected by the frost accumulation at the leading edge and had a 30% larger pressure loss coefficient when compared to a unit with front and side staging. The heat transfer rate of the heat pump with side staging was 25% larger than that without side staging when frost accumulation was 0.009 lb_m/ft^3 (0.14 kg/m^3) (Ogawa et al., 1993).

Fin width extension was also analyzed and found to effectively improve the performance under frosting conditions (Ogawa et al., 1993). The fin surface temperature around the leading edge was increased, frost accumulation was reduced at the leading edge, and airflow blockage was decreased. The heat transfer rate was 30% smaller than that of the basic heat exchanger, while the frost accumulation was small. The rate of decrease, though, in the heat transfer was much less when the quantity of frost accumulation was large (Ogawa et al., 1993).

Investigations of different fin configurations emphasized the potential benefit of fin geometry and fin spacing on the overall heat transfer of the outdoor heat exchanger. Different fin geometries were found to maintain prolonged airflow and achieve higher heat pump performance. Research by Ogawa (et al., 1993) found a smaller pressure drop due to front staging. All the investigations included here highlighted the need for increased fin spacing on the leading edge.

Numerical Analysis

To better understand the operating characteristics of heat pumps, researchers have developed models of heat pump components. This work was started early in the history of the heat pump to quantify the effects of individual components and understand how to affect various improvements. The individual components could then be brought together for an overall model of heat pump operation.

EVSIM is a simulation program used to model refrigerant-to-air heat exchangers that are used in residential air conditioner evaporators. It was written in FORTRAN by Domanski (1989) and the source code is in public domain. The model estimates evaporator performance for a given refrigerant quality at the heat exchanger inlet, saturation temperature and superheat at the heat exchanger outlet, and a set of airflow parameters through the coil. EVSIM allows for a variety of fin types. Three different fin geometries (flat, wavy and louvered fins) could be treated in the model.

The tube-by-tube approach is applied to evaluate each tube performance independently based on average refrigerant temperature in the tube, the inlet air temperature, humidity and mass flow rate of the tube in a given row. The assignment of tubes for evaluation is consistent with the refrigerant flow through the heat exchanger. This tube selection scheme assumes that refrigerant parameters are always known at the entrance of each tube and they are equal to the outlet parameters of the proceeding tube. The simulation starts with the refrigerant inlet tube of a given circuit and progresses consecutively to the

following tubes until the outlet is reached. Once calculations for one circuit are completed, the remaining circuits are calculated starting with the corresponding inlet tubes again.

At the outset of the simulation, the temperature and the humidity ratio of the air are known only for tubes in the first row and are estimated for other rows. These estimates are updated with new calculated values as the calculation progresses. EVSIM can handle one-dimensional, non-uniform air distribution between coil tubes. From the input data of air velocity distribution at beginning of the simulation, the model can derive the air mass flow rate associated with each tube in the first depth row. Each tube with uniform air distribution over its length is assumed. Air mass flow rates of tubes past the first row are calculated based on mass flow rates associated with the preceding tubes. A given tube is assumed to be exposed to the air stream that consists of 50% of the air streams associated with the two closest neighbors in the proceeding row. Air temperature and humidity at each tube past the first row are calculated by standard psychrometric mixing equations.

EVSIM estimates the refrigerant flow faction in each tube and determines the portions of specific flow regimes (i.e., subcooling, annular, mist, or superheated flow) for each tube. Also, it calculates refrigerant pressure drop for each tube. The model initially estimates refrigerant distribution based on the refrigerant circuit layout. A uniform resistance to flow in each tube is assumed. Once all the tube pressure drops have been calculated, refrigerant mass flow rates through each circuit are adjusted to get the same pressure drop at each tube outlet.

Because the model uses a tube-by-tube approach, a single tube is the fundamental calculation unit for coil performance evaluation. This provides a more detailed and adjustable model for evaporator studies and makes it possible to predict the frost information for each finned tube during freezing process. Therefore, EVSIM was selected to serve as the basis to develop the transient model for freezing coil.

EVSIM is a steady-state heat exchanger simulation model and does not consider frosting effects. To simulate the transient behavior of frost growth on a coil, it had to be transformed into a quasi-steady state model. Significant modifications and rearrangements of both the main program and subroutines were necessary. EVSIM did not provide any subroutines to calculate the airside pressure drop across the evaporator coil. Without a pressure drop and fan model, the simulation model could not account for the effect of the decrease of airflow rate as frost grows. Thus, subroutines to estimate airside pressure drop and reduction of airflow rate needed to be developed and inserted into EVSIM.

EVSIM also does not include any provisions for estimating the refrigerant-side pressure drop across the coil distributor. Most residential heat pump systems incorporate a distributor to feed refrigerant into the heat exchanger. A program must be developed to account for the refrigerant pressure drop and mass flow distribution through distributor nozzles and tubes.

Evaporator models have been established and analyzed for operation with dry, wet, and frosted surface conditions using equations for both airside and refrigerant side heat transfer coefficients and

pressure loss factors (Oskarsson et al., 1990). It has been reiterated that evaporators operating under wet and frosted surface conditions not only cool the air but also dehumidify it, and at temperatures below the freezing point, frost will form on the evaporator surface. As frost accumulates on the outdoor heat exchanger, the coil performance is now a transient phenomenon. This transient condition of increased thermal resistance and decreased area for free airflow can be represented by quasi-static conditions after assuming a small time interval (Oskarsson et al., 1990). This corroborates the use of a quasi-steady-state computer model for analysis and prediction of heat pump performance during frosting conditions.

Tao et al. (1994) stated a need for more work to be done in order to quantify heat and mass transfer characteristics of frost formation on heat exchanger surfaces. Numerical modeling of frost growth, however, provided an efficient way to examine the physical interaction among these complex transport phenomena. It demonstrates that as the ambient temperature increased, the reduction of frost growth due to frost formation on the heat exchanger surface was more significant. Frost density and frost thickness both increased with ambient temperature (Tao et al., 1994).

A method of predicting the performance of cross-finned tube heat exchangers under frosting conditions has also been presented by Senshu et al. (1990). The performances of the test heat exchangers were experimentally investigated, and based on the results, an analytical method to predict frost formation speed was developed. The method exhibited good agreement with the experimental data. This was expounded upon and a computer simulation of the test heat pump was created (Yasuda et al., 1990). The model consisted of a refrigeration simulator, a frost formation simulator, and a fan characteristic simulator. The results were compared with experimental data from the prototype heat pump operating under frosting conditions, and they were in good agreement. For a heat pump under frosting conditions, it was assumed that the fin conditions and the air conditions around the fin surface were represented by averaged values (Yasuda et al., 1990). This was used in a discussion to find the fin efficiency as a function of fin configurations, fin surface heat transfer, and temperature and relative humidity of the moist air.

Frost formation speed on the heat exchanger was found to be constant when the airside and refrigerant-side conditions were held constant. Even under frosting conditions, though, the airside heat transfer coefficient was not significantly different from that found under dry coil conditions (Senshu et al., 1990, Yasuda et al., 1990). The previous study was on one fin configuration.

O'Neill and Crawford (1989) developed a modeling technique for a finned tube heat exchanger of the type commonly used in domestic refrigerators. It was also shown that the overall heat transfer increased as the airflow rate increased and also as the fin density increased.

The general trend of heat pump simulation programs has been toward special case modeling of a given system and location to the more general approach of component module programs. Once the model was verified against experimental data, the computer simulation was given weather conditions for an entire heating or cooling season to calculate the overall seasonal efficiency. Later programs attempted to

solve the differential equations of mass, momentum, and energy conservation for the given heat pump components. Work is still continuing with emphasis on modeling the dynamic and transient behavior of heat pump on/off cycling. The ability to accurately model frosting coil heat transfer rates is still subject to a better understanding of the basic frosting process.

Heat pump performance also depends on transient operations such as cycling, frosting and defrosting of the outdoor coil. Frost modeling efforts have focused on developing models that can realistically predict the growth of frost on heat exchangers and its effect on heat pump system performance. Oskarsson (1990) presented a frost evaporator model based on a set of empirical equations and correlations. Yasuda and Senshu (1990) developed a simulation for estimating heat pump heating characteristics under frosting conditions. The simulation consisted of a refrigeration cycle model, a frost formation model, and a fan performance model. Their simulation results compared favorably with experimental data. Detailed work on frost modeling was performed by O'Neal and his group (1993 and 1996). A brief description is given below.

LGAMHX is a simulation model for frosted evaporator described in O'Neal and Gu (1995), and O'Neal and Gong (1996). It is a quasi-steady state heat exchanger model developed to model the transient behavior of a specific company's (LG Electronics) heat pump evaporator under frosting conditions. It estimates the growth of frost layer on a coil and the subsequent degradation in cooling capacity and airflow over time.

LGAMHX is a program established with the combination of three subprograms: EVSIM, PCFROST and PRCFM. Kondepudi, in his dissertation research (1988), developed a frost growth model (PCFROST) for fin-and-tube heat exchanger based on previous research work of Sanders (1974) and O'Neal (1982). Based upon fundamental heat and mass transfer principles, the model described the general phenomena of frost growth and gave a reasonable prediction of the performance of frosting coil. When the surface temperature of evaporator was below the freezing point, PCFROST estimated mass transfer and frost growth on the coil surface. The varying properties of frost layer, such as density, conductivity and thickness, also were estimated in the model.

After validation by comparison with experimental results (Kondepudi and O'Neal, 1987), Kondepudi's model reasonably predicted the resulting average thickness of the frost layer which consisted of two layers: a low-density frost layer and an high-density frost layer (or the ice layer). This model considered mass diffusion inside of the frost layer by assigning different thermo-physical properties (density and thermal conductivity) to both frost and ice layers. The average frost thickness for the given time and environmental condition can be more accurately predicted than in the case of assuming uniform frost density or thermal conductivity.

One limitation of Kondepudi's frost grow model was the lack of heat transfer correlations for airside heat transfer coefficient for frosting conditions. In addition, the original model was designed only

for a flat plate fin. Modifications for other geometries, such as louvered, corrugated, or spine fins, would be desirable.

Another subprogram, PRCFM, was designed to calculate airside pressure drop through the frosted coil and the decreased air volume flow rate with frost buildup, which mainly came from the ORNL pressure drop model. The airside pressure drop was first calculated by one subroutine and a new flow rate was then determined from the fan characteristic curve.

Because EVSIM is a steady state simulation model for heat exchangers operating under dry or wet conditions, a time iteration loop had to be established in the main program of original EVSIM to allow the previously steady-state program to give time-dependent results. The main program of EVSIM also needed to be modified before incorporating with the other two subprograms (PCFROST and PRCFM) to build the frosted evaporator model (LGAMHX). The frost growth model, PCFROST, was inserted into the tube-by-tube iteration loop of EVSIM to calculate the mean frost thickness of individual tubes for the given time interval and both air and refrigerant conditions at the inlet and outlet. The subprogram, PRCFM, was incorporated into the main iteration loop of EVSIM. Thus, it could be called in the main program at the end of each time step to update the air volume flow rate and pressure drop with frost growth.

Summary of Literature Survey

Some of the factors that determine heat pump performance degradation have been examined in the literature reviewed. This examination was done to better understand those factors that influence heat pump performance and to better understand the methods used to quantify these degradations. The importance of computer models of heat pump performance was examined. These computer simulations allow for comparisons with actual performance data and for optimization studies. A review of literature shows that limited work is available on modeling heat exchanger performance under frosting conditions. So more efforts need to be devoted to this direction.

Frosting losses were seen to reduce heat pump performance by decreasing the steady-state capacity. The losses due to reduced airflow can be managed to maximize heating efficiency. Reduction in outdoor heat exchanger airflow was the main cause of heat pump performance degradation. An explanation of the processes leading to this reduction in airflow was examined in the literature. Several investigators showed how relative humidity, air temperature, and other parameters affected airflow and pressure drop. The mass transfer driving potential was shown to be the factor that controls the deposition of frost on the outdoor coil. Increases in airflow led to higher pressure drops and higher overall heat transfer coefficients. The rate of frost formation also seemed to increase with increasing airflow. Wider fin spacing in the front led to a lower pressure drop at the outdoor heat exchanger and different fin configurations were found to increase the heat transfer coefficient. This research will examine fin staging to decrease the pressure drop, delay frost accumulation, and increase heat pump performance.

CHAPTER III

EXPERIMENTAL APPARATUS

The experimental study was conducted in the Energy Systems Laboratory (ESL) of Texas A&M University. The objectives of the experimental work were i) to investigate the effects of staging fin on the frost performance of heat pump outdoor coils under different operation conditions, and ii) to provided test data to verify the frosted evaporator model that will be discussed in Chapters V, VI and VII.

This chapter summaries the experimental work that was completed. Fin staged coils are first discussed, then a complete description of the experimental facility and setup for the heat pump system with different outdoor coils under test is presented. Experimental conditions and procedures are discussed along with the fan performance test for the outdoor coil blowers.

Fin Staged Heat Exchanger

Fin staged coils in this study were multi-row heat exchangers based upon the front staging idea. Each row of the coil was made individually as a single row heat exchanger and then joined together at the ends with U-tubes to form the multi-row heat exchanger. This type of coil is commonly called a "sandwich" coil. Fin spacing of each row decreased with row depth. The fins of the front row were not connected to those of the following row. Figure 3.1 illustrates an arrangement sketch of two-row staging flat fins.

When the fin surface temperature is lower than the freezing point 32 ^{o}F (0 ^{o}C) of water, frost may form on the surface. As the frost layer grows, the local heat transfer coefficient starts to fall and the airflow drops due to the frost blocking the passages between the fins. These factors cause the fin surface heat transfer rates to decrease rapidly with the growth of the frost layer. For multi-row heat exchangers, the heat transfer coefficient of the leading edge of fin is larger than that of the following fin surface (Soboya and Sparrow, 1974). From experimental observations, the frost distribution across the depth of coil is uneven, and more frost builds up at the leading edges of the heat exchanger fins (Chen et al., 2000).

Figure 3.2 shows a representation of the side view of the frost layer distribution on the two-row staging flat fins. The double dot line indicates the discontinuity of the fins of the first and second rows. To diminish the negative effect of the larger frost growth at the coil leading edges, the idea of multi-row fin staged coil was proposed to slow the reduction of airflow and heat transfer rate as frost grew on the coil (Ogawa et al. 1993).

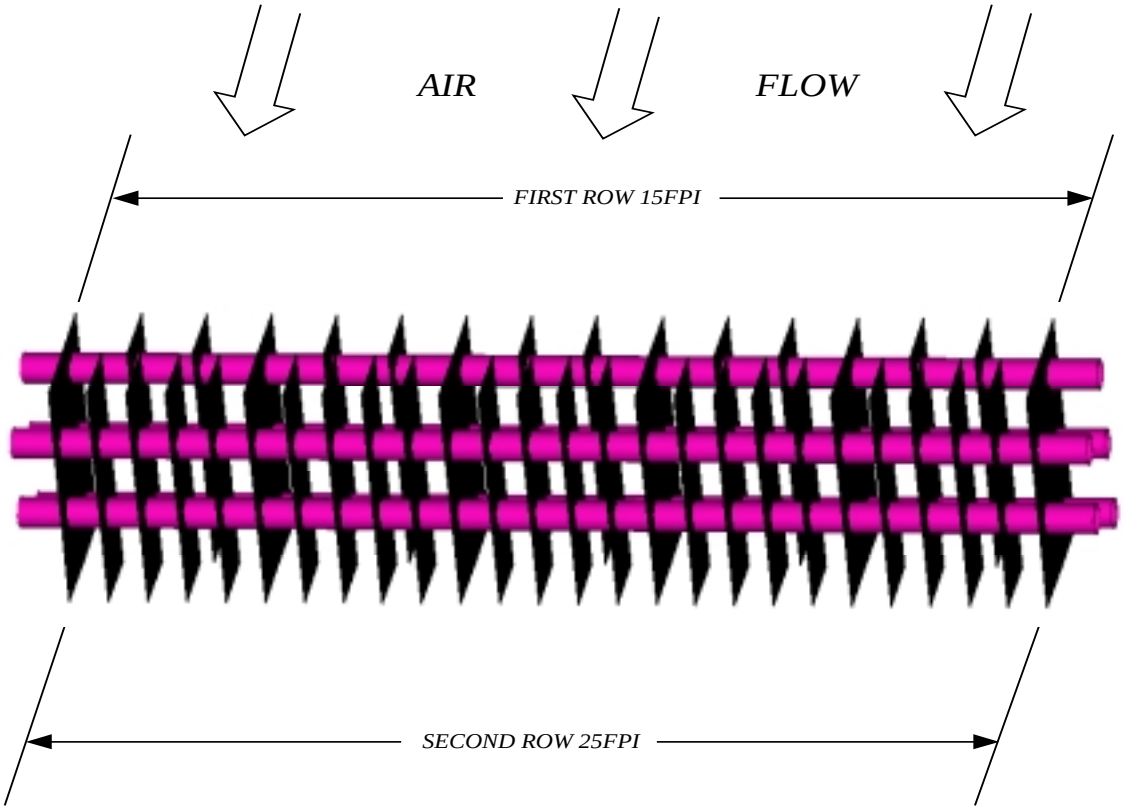

Figure 3.1 Sketch of two-row front staging flat fins

With fin staging, frost is expected to block a smaller proportion of the front row, allowing more airflow to the rear rows. This would promote increased heat transfer and frost deposition on the rear rows of the heat exchanger. The increased fin spacing also postpones the eventual blockage of the frost layer at the leading edges of the coil and lengthens the "on" cycle between two defrosting cycles. Therefore, the heat exchanger with greater fin spacing on the front row is expected to increase the time before the outdoor coil is fully frosted. It should also reduce the required number of defrosting cycles, and thereby improve the performance of heat pump systems under frosting conditions.

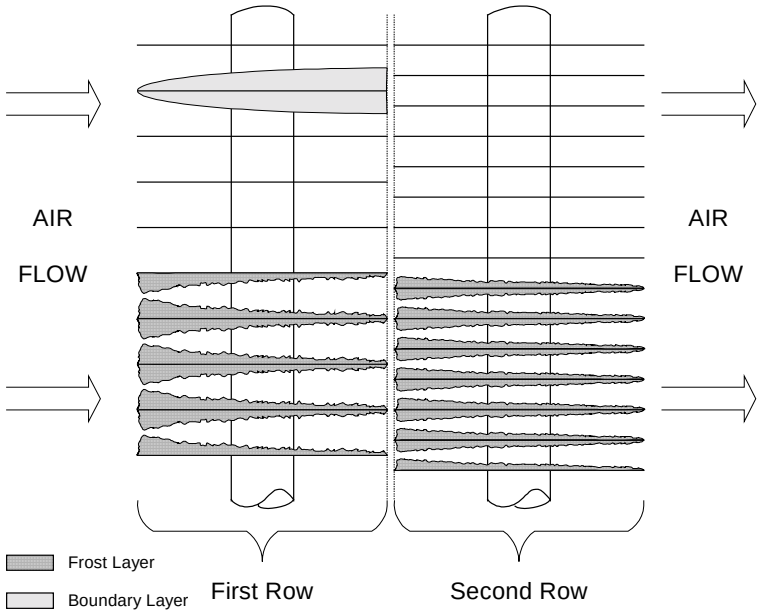

Figure 3.2 Illustration of frost deposition on staging flat fin surface

Another inherent advantage of a fin staged coil is that the local heat transfer at the front part of fin surfaces of the rear rows should be enhanced by redeveloping the thermal boundary layer. Normally, the second-row fins of a two-row coil are less effective as heat transfer surfaces than the first-row fins. This is because the first row has a boundary layer developing region, whereas the following second row has no such boundary-layer initial development. However, for a fin staged coil, due to the discontinuity of fin surface of each row, the leading edge of second row fin breaks the boundary layer developing along the first-row fin surface. This leads to the boundary layer redeveloping at the upstream area of the second and subsequent rows. Therefore, the contribution of boundary layer developing at the front part of the fin surface effectively increases the heat transfer capability of the second row. The above analysis is only applicable to flat fin geometry. For many types of enhanced fins, because of the repeated growth and destruction of the thermal and momentum boundary layers due to each strip, the effect of the leading edge of the second row is less important.

In an effort to investigate the effect of staging fins on the frosting performance of a heat exchanger, three 2-row and two 3-row outdoor coils with different fin-spacing configurations were tested in this study. All the five test coils, together with the associated heat pump unit, were donated by Carrier Corporation and had the same fin pattern: 7-element lanced sine-wave fin. Figure 3.3 provides a front view of the coil fins. For the two-row coils, there was one baseline coil (20/20 fpi) and two fin staged coils (15/20 fpi and 15/25 fpi). The two bare 2-row fin staged coils are shown in Figure 3.4. For the

three-row coils, there was one baseline coil (20/20/20 fpi) and one fin staged coil (15/20/25 fpi). Both the 2-row fin staged coils decreased the fin density of the front row to 15 fpi (5.9 fin/cm) while one coil increased the fin density of the back row to 25 fpi (9.8 fin/cm) and another remained unchanged at 20 fpi (7.9 fin/cm). For the 3-row coils, one fin staged coil with 15/20/25 fpi (5.9/7.9/9.8 fin/cm) fin pitch combination was tested as well. The fin staged coil results were compared against that of the corresponding baseline coil. The detailed geometrical dimensions are tabulated in Table 3.1.

Each row of tubes was subdivided into three or four circuits to help maintain an approximately isothermal surface in each row. The circuitry and pertinent geometric parameters are shown in Figures 3.5 and 3.6 for two-row and three-row test coils, respectively. The small numbers next to each tube are the index numbers of the coil tubes, which were used in the frosted evaporator model to track refrigerant flow through the heat exchanger. The arrows on both figures indicate the direction of refrigerant flow.

The coils had the common “horseshoe” profile of outdoor coil of residential heat pump. One propeller fan was installed at the top of the coil to pull air out. The temperature difference at the first row of parallel-flow heat exchanger is typically smaller than that of counter-flow heat exchanger. The application of parallel-flow structure is favorable for lengthening the frost formation at the first row and allowing more frost to build up on the fin surfaces of rear rows. Therefore, all the test coils were parallel-flow heat exchangers.

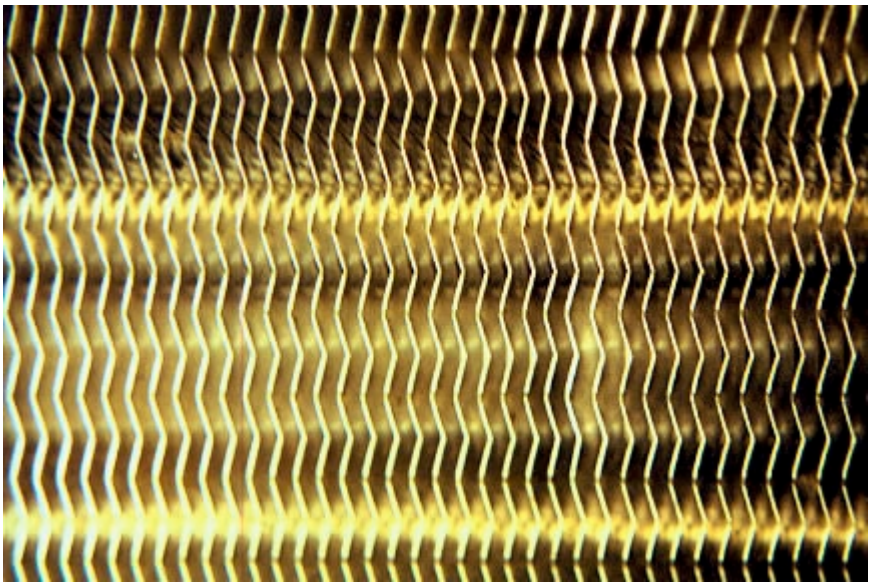

Figure 3.3 A photograph of the leading edges of fins in the test coil

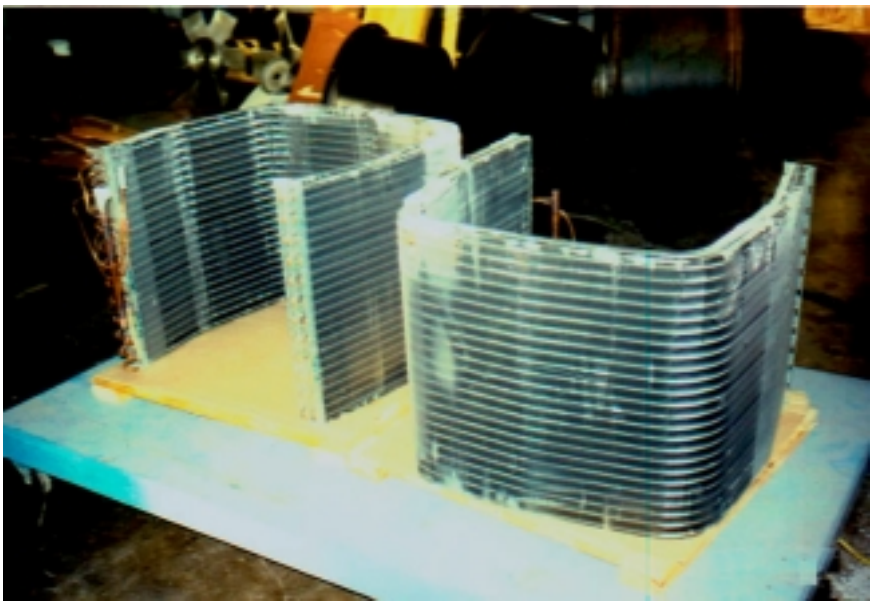

Figure 3.4 Two 2-row fin staged coils used in the tests

A distributor was installed at the inlet of each test coil as a flow control device to distribute the refrigerant mass flow and equalize the pressure drop of refrigerant flowing through each circuit. The size of distributor nozzle varied from 0.120 to 0.130 inch (3.05 to 3.30 mm). The inner diameter of the connection tube was 0.131 inch (3.34 mm) and the length was 0.150 inch (3.81 mm).

Table 3.1. Geometry parameters for the outdoor coils under test

Parameter	Value
Number of Rows	2 or 3
Height	24 inch (61 cm)
Width	74 inch (188cm)
Face Area	12.12 ft^2 (1.13 m^2)
Fin Density	15, 20 or 25 fpi (5.9, 7.9 or 9.8 fin/cm)
Fin Thickness	0.0042 inch (0.11 mm)
Fin Type	7 element lanced sine-wave
Tube Outer Diameter	0.391 inch (9.93 mm)
Tube Inner Diameter	0.367 inch (9.32 mm)
Tube & Row Spacing	1 inch x 1 inch (2.54 cm x 2.54 cm)
Refrigerant Circuit	3 or 4

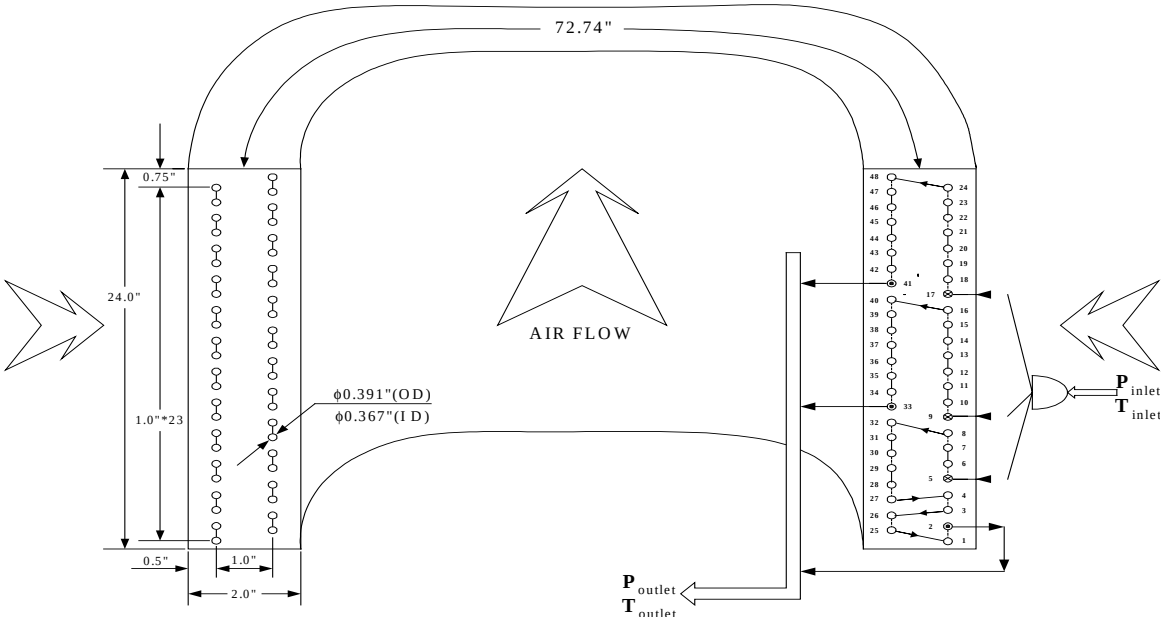

Figure 3.5 Schematic of the two-row outdoor coils used in the tests

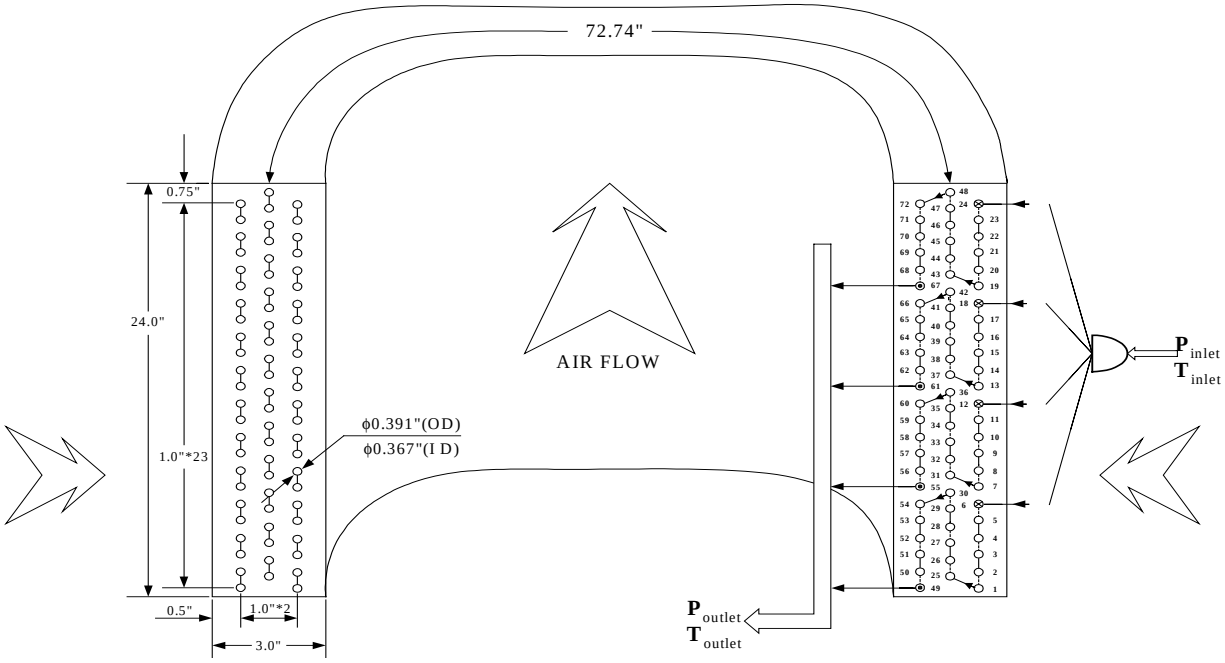

Figure 3.6 Schematic of the three-row outdoor coils used in the tests

Heat Pump Test Facilities

The focus of the experimental study was on the effect of staged fins on the heat transfer performance of a heat pump evaporator (outdoor coil) under frosting conditions. All the tests of the evaporators were conducted in the psychrometric rooms at the Energy Systems Laboratory. The rooms could provide a constant temperature and humidity environment to conduct full heat pump system tests or component tests. These test facilities offered advantages over a conventional heat exchanger calorimeter.

An advantage of the psychrometric rooms over a conventional heat exchanger calorimeter was that unusual heat exchanger shapes could easily be tested. Many heat pump evaporators use a propeller fan to draw air through a "horseshoe" shaped coil. The airflow distribution through the coil is typically not uniform. In a typical calorimeter, only a flat, rectangular section of the coil would be used and the airflow would be kept as uniform across the coil. This could yield different frosting results than on the actual coil.

Another advantage of testing in the psychrometric rooms was the opportunity to run the complete heat pump system versus just the coil by itself. The performance of the outdoor coil could be measured as well as how the changes in the coil affected system performance. Thus, testing in the psychrometric facility allowed for the isolation of the evaporator as well as getting some system performance data "free".

This section describes the psychrometric experimental facilities for the heat pump system with fin staged outdoor coils under test.

There were five major components of the test facilities:

1) Psychrometric rooms
2) Heat pump test system
3) Indoor air-side test facility
4) Outdoor air-side test facility
5) Data and images acquisition system

Each is discussed below.

Psychrometric Rooms

All the heat pump tests of this experimental study were conducted in the psychrometric rooms of the Energy Systems Laboratory. The performances of the fin staged coils, as well as their impact on the heat pump system operation, could be measured simultaneously in the psychrometric rooms. The psychrometric rooms are designed to provide various constant temperature and humidity environments for experimental studies of air conditioner and heat pump systems. The psychrometric rooms were able to control air temperatures from 10 ^{o}F (-12.2 ^{o}C) to 130 ^{o}F (54.4 ^{o}C) and relative humidities from 10% up to 95%. The test facility of the psychrometric rooms consisted of the cooling system, the coolant circulation system, the test rooms associated with the reconditioning apparatus, and the control system of the psychrometric rooms. A schematic diagram of the psychrometric rooms is provided in Figure 3.7.

The cooling system of the psychrometric rooms contained a 70-ton (246-kW), water-cooled chiller system manufactured by Trane (Figure 3.8), which was used to cool the ethylene-glycol and water solution. A cooling tower (Figure 3.9) worked as an open water evaporator unit to remove heat from the chiller refrigeration system to the ambient. The water, circulated by the centrifugal pump, was used to transfer heat generated by the chiller to the cooling tower through the water-cooled tube-in-shell condenser of the chiller system.

An ethylene-glycol and water solution was used as the coolant to transfer heat energy from the psychrometric rooms to the chiller system through the coolant circulation loops. A 500-gallon (1.89 m^3) well-insulated tank, as seen in Figure 3.10, was used in the coolant circulation lines to provide thermal inertia and prevent frequent running of the chiller refrigeration system. The ethylene glycol-water solution stored in the coolant tank was maintained at an approximately constant temperature by the chiller system. The coolant temperature required needed to be set before running the test via a thermostat type controller provided with the chiller system. For different tests, the appropriate coolant temperature needed to be chosen to allow the air temperatures and humidities of the psychrometric rooms to reach the desired set points.

The chilled coolant from the storage tank was circulated through separate pumping circuits to the room conditioning coils to cool and dehumidify the psychrometric room air. The piping layout with individual circuits allowed for better control on the coolant flow through either the cooling or dehumidifying coils of each room with the use of electronic valves in the corresponding coolant circulation lines. These 3-way electronic valves, adjusted through the actuators of Barber-Colman Company, permitted the desired amount of chilled coolant to flow into the reconditioning coils and bypass the other circulated coolant back to the storage tank. The circuit was completed when the coolant through the reconditioning coils flowed back into the coolant tank.

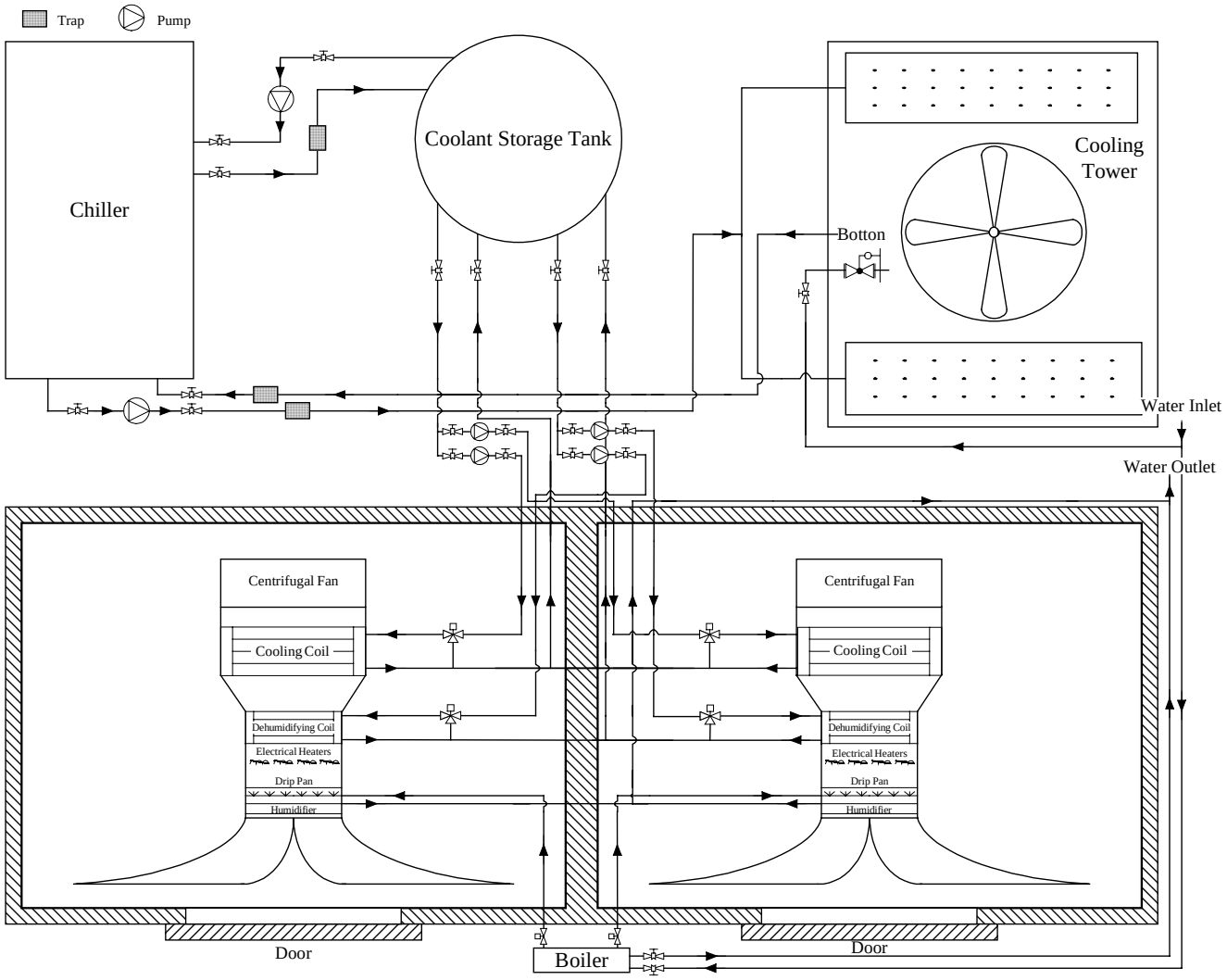

Figure 3.7 Schematic diagram of the conditioning system for the psychrometric rooms

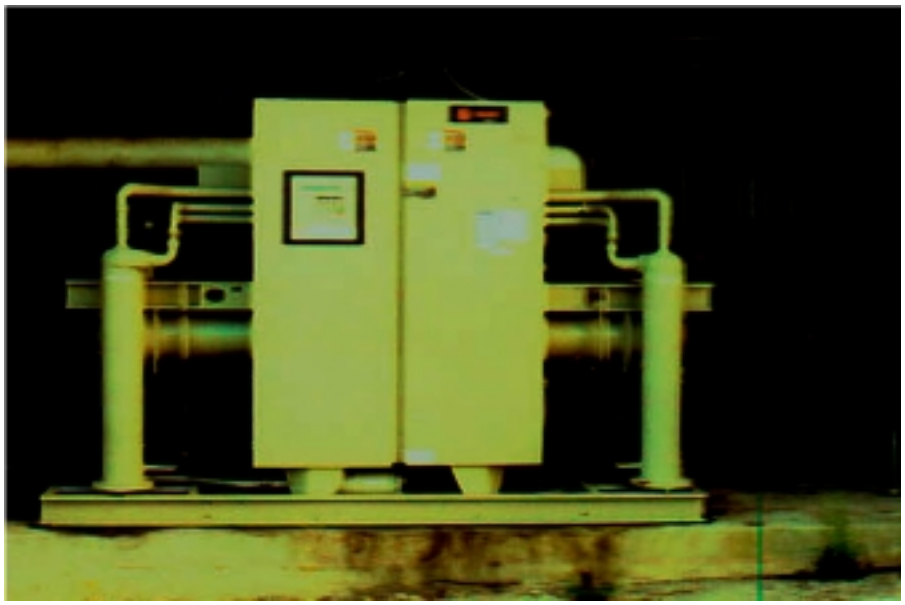

Figure 3.8 The chiller system at the Energy Systems Laboratory

Figure 3.9 The cooling tower at the Energy Systems Laboratory

Figure 3.10 The coolant tank at the Energy Systems Laboratory

The psychrometric rooms, as seen in Figure 3.11, contained the indoor and outdoor two test rooms with the same geometric size, in which the desired test conditions could be maintained within the required tolerance. Both rooms had been well insulated and sealed from the surrounding atmosphere. Each room contained separate airflow test chambers. The heat pump system tested was setup in the two test rooms.

The air temperature and humidity of each room, coolant temperature, and the airflow rate through the conditioning coils of each room was held constant throughout each test. During the steady state tests, the coolant flow rates of the cooling and dehumidifying coils did not vary with time. Ranges for the air dry-bulb and wet-bulb temperatures of each psychrometric room could be kept within ±1 ^{o}F (0.56 ^{o}C) during the steady state and frost tests and ±2 ^{o}F (1.1 ^{o}C) during the defrost of the heat pump.

Constant speed centrifugal fans were used to circulate air into each psychrometric room. A plexiglass window allowed for visual monitoring of the performance of the conditioning coils to see how much frost blocked the coils. Both thermocouple (Copper-Contantan) grids and humidity sensors were in place at the exit of the conditioning duct system to monitor the changes of the rooms air temperatures and humidities. Turning vanes and flow straighteners were also installed at the exit of the conditioning ducts to reduce the swirl of the airflow and ensure uniform distribution of the air in the psychrometric rooms.

Figure 3.11 The psychrometric rooms at the Energy Systems Laboratory

The air temperatures of the psychrometric rooms were normally controlled by the air cooling coils and electric heaters inside the room conditioning ducts. Sometimes, the dehumidifying coil also needed to work as an auxiliary cooling heat exchanger while the required room temperatures were so low that the cooling coil alone was not able to provide enough cooling capacity to lower the air temperature. The capacities of the room reconditioning coils and electric heaters are specified in Table 3.2.

Table 3.2 Facility reconditioning capacities of the psychrometric rooms

Facility	Indoor Room		Outdoor Room	
	MBtu/h	kW	MBtu/h	kW
Cooling Coil	180	52.8	216	63.3
Dehumidifying Coil	40	11.7	40	11.7
Electric Heater	35×4	10.3×4	35×4	10.3×4

The cooling and dehumidifying coils were two fin-and-tube air-to-liquid heat exchangers fed with the ethylene-glycol and water solution supplied by the coolant circulation system. They were used in the

room reconditioning apparatus as the major cooling and dehumidifying equipment. The cooling coil was installed in front of the dehumidifying coil inside the room reconditioning duct. The air flowing through the reconditioning duct was cooled by the cooling coil first, and then further removed moisture by the dehumidifying coil.

There were four sets of electric resistance heaters for each room reconditioning apparatus. Two heaters were wired together as a bank, which was controlled by a relay module on the controller of each psychrometric room. These heaters were installed downstream of the dehumidifying coil. The cooled air through the cooling and dehumidifying coils could be reheated again by the electric heaters. Such an arrangement enabled more accurate control of the air temperature. By switching on and off each bank of heaters, the desired values of the air temperatures could be achieved in a relatively short time and maintained approximately constant within ± 1 ^{o}F (0.56 ^{o}C). In some situations, such as dehumidification, the temperatures of air stream after the cooling and dehumidifying coils were below the test required temperatures. The duct heaters were desired at this moment to bring the temperature of over-cooled air stream up to the test set points.

Humidity was controlled by employing either a dehumidifying coil or steam injector when the air humidity ratio was higher or lower than the test required values, respectively. The dehumidification normally happens when there was a moisture source in the psychrometric rooms (such as a water evaporative cooling system) which continuously input moisture into the air. In addition, initial start-up of the psychrometric rooms often required some dehumidification when the humidity ratio of the ambient air was greater than the desired set point for a test. In this situation, a certain amount of moisture needed to be removed through the dehumidifying process.

The dehumidifying coil operated with the similar coolant supply circuit as the cooling coil. In the dehumidifying process, the cooling coil could help to cool the air stream before the dehumidifying coil. Therefore, the dehumidifying coil and the cooling coil were used together to cool and dehumidify the air stream flowing through the room reconditioning duct.

While the coil coolant temperature was higher than the freezing point of water, 32 ^{o}F (0 ^{o}C), moisture would condensate on the dehumidifying coil and/or the cooling coil. The water would then drain out of the room. While the coil coolant temperature was lower than the freezing point of water (such as the frost tests), frost could buildup on the coil surface. Dehumidification needed to be continued by successively frosting and defrosting coils until the desired humidity level was reached. Although the melted frost was removed from the room by means of a drain, the defrosting process added additional heat and moisture to the room air, which caused a temporary increase in room air temperature and humidity.

A steam injector was employed to increase the air humidity by spraying steam into the air stream while flowing through the room reconditioning duct. The steam injector consisted of stainless steel pipes with small perforation, which allowed steam to spray into the air steam directly. Excess steam would be

condensed on the duct plates. Then the water dripped to the bottom pan and drained out of the psychrometric rooms.

The steam was supplied by a small electric boiler with working pressures from 20 to 25 psig. The steam injectors were controlled through a Honeywell integrated valve actuators. The amount of steam was adjusted continuously so that the desired values of humidity at room conditioning duct exit were achieved in a relatively short time and maintained approximately constant. This process of spraying steam also added heat energy into the air stream, which caused a small increase in the air temperature.

Because the insulated psychrometric rooms were closed and sealed during the tests, air circulated in each room with cyclic psychrometric equilibrium. A simplified description of the psychrometric variations of the outdoor room air during the frost test as follow:

At first, the air approached the outdoor evaporator coil at the required temperature and humidity. When the air left the frosted coil, it had a lower temperature and humidity. After the air was discharged from the outdoor test chamber and on the way to the room conditioning duct, it absorbed the heat conducted into the room through the wall of the psychrometric rooms. The air flow friction and the heat generated by the fan motor and compressor were also considered to be released to the flowing air. Once the air entered the conditioning duct, it was cooled and dehumidified again by the conditioning coils to balance the heat energy absorbed. The electric duct heaters and the steam injectors provided sensible heat and moisture to adjust the air flow back to the desired temperature and humidity levels.

It was a continuously dynamic equilibrium process. Under ideal conditions, no heat conduction would occur through the insulated walls, the discharge air from the room reconditioning duct would be drawn into the front of the test coil at the same temperature.

The present control system of the psychrometric rooms was not flexible enough to collect all the data points needed for each individual research projects. Also it was not necessary to be adding or deleting points on the control system on a continuing basis. Therefore, the control system was separated from the data acquisition system in the design of the psychrometric rooms.

The major control system of the psychrometric rooms was the Siemens programmable logic controller (PLC): SIMATIC TI-505 with three I/O modules (8CH INPUT ANALOG 505-6108A, 8CH OUTPUT ANALOG 505-6208A, and 32CH RELAY OUTPUT 505-4916). The points of each module are shown in Table 3.3.

Each heater was assigned a channel on the relay module though they were switched on/off in four groups. In Figure 3.12, the PLC and the desktop PC running the PLC ladder program is at the right side of the main control panel of the psychrometric rooms, which consisted of the switches of blowers, heaters, and coil pumps of both indoor and outdoor psychrometric rooms.

Figure 3.12 The control facility of the psychrometric rooms

Table 3.3 Connection point table of the control system of the psychrometric rooms

Module	Channel Point	Signal
ANALOG INPUT 505-6108A	Indoor Air Dry-Bulb Temperature Indoor Air Relative Humidity Outdoor Air Dry-Bulb Temperature Outdoor Air Relative Humidity	4 ~ 20 mA 4 ~ 20 mA 4 ~ 20 mA 4 ~ 20 mA
ANALOG OUTPUT 505-6208A	Indoor Cooling Coil Valve Indoor Dehumidifying Coil Valve Outdoor Cooling Coil Valve Outdoor Dehumidifying Coil Valve Indoor Stream Valve Outdoor Stream Valve	6 ~ 9 VDC 6 ~ 9 VDC 6 ~ 9 VDC 6 ~ 9 VDC 0 ~ 10 VDC 0 ~ 10 VDC
RELAY OUTPUT 505-4916	Indoor Heater #1 Indoor Heater #2 Indoor Heater #3 Indoor Heater #4 Outdoor Heater #1 Outdoor Heater #2 Outdoor Heater #3 Outdoor Heater #4	24 VAC 24 VAC 24 VAC 24 VAC 24 VAC 24 VAC 24 VAC 24 VAC

Heat Pump Test System

A 3-ton (10.6-kW) air source heat pump, *Carrier 38YXA036/FX4*, was used in this experimental study. The heat pump system consisted of an indoor unit, an outdoor unit, and the connection tubes. An overall schematic diagram of both the test loop of the heat pump system and the primary instrumentation is shown in Figure 3.13. The specifications of the components of the heat pump system are listed in Table 3.4 as well. The arrows in solid or dashed lines nearby the circuit lines indicate the direction of refrigerant flow during cooling or heating operation, respectively.

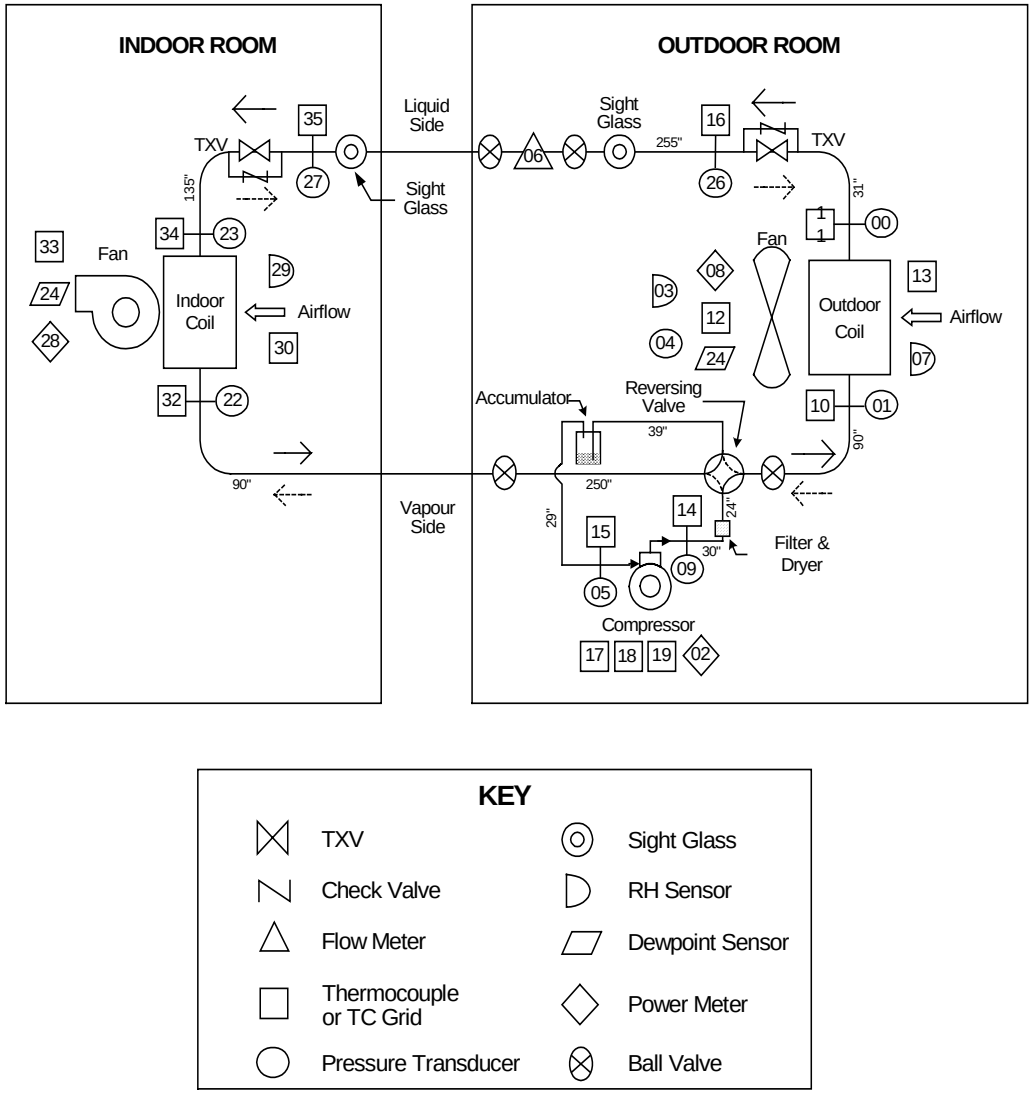

Figure 3.13 Schematic diagram of the heat pump test system

Table 3.4 Specifications of the heat pump system components

Indoor Coil	3-row, 3-circuit, V-shape face area 4.45 ft^2 (0.41 m^2) fin pitch 14.5 fpi (5.7 fin/cm) fin type: 7-element lanced sine wave tube & row spacing 1 inch × 0.75 inch (2.54 cm x 1.91 cm) tube expanded outside diameter 0.391 inch (9.93 mm)
Indoor Fan	nominal air flow rate 1600 cfm (45.3 m^3/min) nominal blower motor size ¾ hp (559W) 208/230 VAC single phase motor
Heat Pack	heating capacity 0~18 kW
Indoor TXV	rated capacity 3 ton static, rating and maximum operating superheat 5±2 ^oF
Outdoor Coil	2 or3 row, 3 or 4 circuit, horseshoe-shape face area 12.12 ft^2 (1.13 m^2) fin pitch 15, 20 or 25 fpi (5.9, 7.9 or 9.8 fin/cm) fin type: 7-element lanced sine wave tube & row spacing 1 inch × 1 inch (2.54 cm x 2.54 cm) tube expanded outside diameter 0.391 inch (9.93 mm)
Outdoor fan	nominal air flow rate 2800/3600 cfm (79/102 m^3/min) nominal blower motor size 1/5 or 1/4 hp (149/186 W) GE motor with single phase 208/230 VAC
Compressor (Copeland ZP32K3E-PFV)	nominal capacity 3 ton (10.6 kW) base compressor displacement 1.873 $inch^3$/rev (30.7 cm^3/rev) nominal compressor speed 3500 rpm internal void space volume 160 $inch^3$ (2622 cm^3)
Accumulator	operating storage capacity 128 $inch^3$ (2.097 dm^3) outside diameter 5 inch (559W) height 8.27 inch (21.0 cm)

The outdoor unit included an outdoor coil, propeller fan, combination of TXV and check valve, compressor, accumulator and reversing valve. Appropriately sized copper tubing was used to connect these components. The unit was instrumented and placed in the psychrometric outdoor room.

The outdoor coil associated with the heat pump unit was a two-row “horseshoe” shape fin-and-tube heat exchanger with a fin density of 20 fpi (7.9 fin/cm). This evaporator coil served as the two-row baseline coil with standard fin spacing. After the tests of this coil were done, it was removed and replaced

with other test coils having various configurations with different fin spacing and tube rows. Section 3.1 specified the details of these test evaporator coils. In addition, a drain pan was installed under the outdoor coil to collect the condensate as it was defrosted.

Two four-blade propeller fans with either 1/5- or 1/4-hp GE motors were used to pull air through the two-row or three-row evaporator coils, respectively. The initial clean coil flow rate could be adjusted through the input voltage by a transformer inside the control room.

In the original design of the heat pump system, an outdoor orifice was used as the expansion device for the outdoor coil during heating operation. In the tested unit, as seen in Figure 3.14, the outdoor orifice was replaced with a thermostatic expansion valve (TXV) rated for refrigerant R-410A and a 500 psia (3.45 MPa), one-way check valve. During heating operation, the outdoor TXV continuously adjusted the refrigerant flow to maintain a specific leaving superheat (5±2 ^{o}F) for the outdoor coil which work as an evaporator in heating mode. During cooling operation, the check valve bypassed the outdoor TXV, and instead the refrigerant condensation from the outdoor coil was throttled by the indoor TXV.

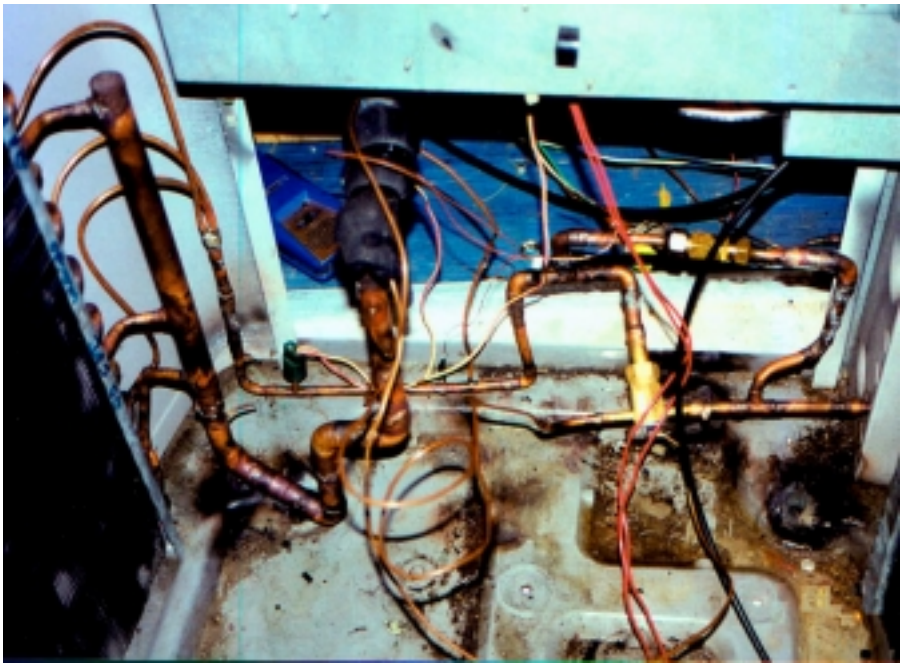

Figure 3.14 The combination of TXV and check valve inside the outdoor coil cabinet

The compressor was the Copeland compliant scroll compressor, model number ZP32K36-PFV. Before the tests, the compressor, accumulator, and reversing valve were moved out of the evaporator cabinet and placed on a pad directly in front of the unit (Figure 3.15). Additional copper tubes with an outside diameter of 3/8 inch (9.53 mm) were used to connect the reversing valve to the indoor and outdoor coils, respectively. This modification removed the compressor heat source from the inside of the outdoor coil and provided plenty of room inside the coil cabinet to setup the video camera. In an effort to minimize heat loss, the outdoor test loop, excluding the coil, was properly insulated.

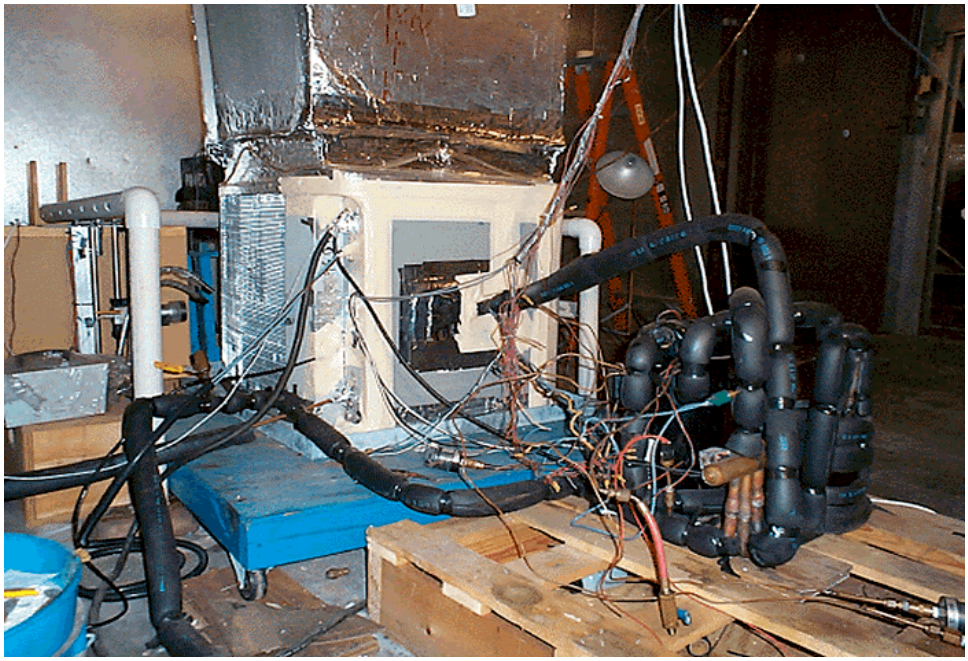

Figure 3.15 The outdoor coil with the compressor, accumulator, and reversing valve moved out

In addition, the manufacturer's control system was replaced with 24-VAC relays and manual switches. Thus, the indoor and outdoor fans, the compressor, and the reversing valve could be energized or de-energized independently by the tester. This allowed manual control of the initiation and termination of the frost/defrost operation according to the different test requirements.

The insulated indoor unit, *Carrier FA4ANF048*, contained the heat exchanger, TXV, centrifugal blower and heat pack. A V-shape fin-and-tube heat exchanger was mounted at the inlet of the indoor unit, which had three-row fins with 14.5 fpi (5.7 fin/cm) fin pitch. The instrumented indoor unit is shown in Figure 3.16.

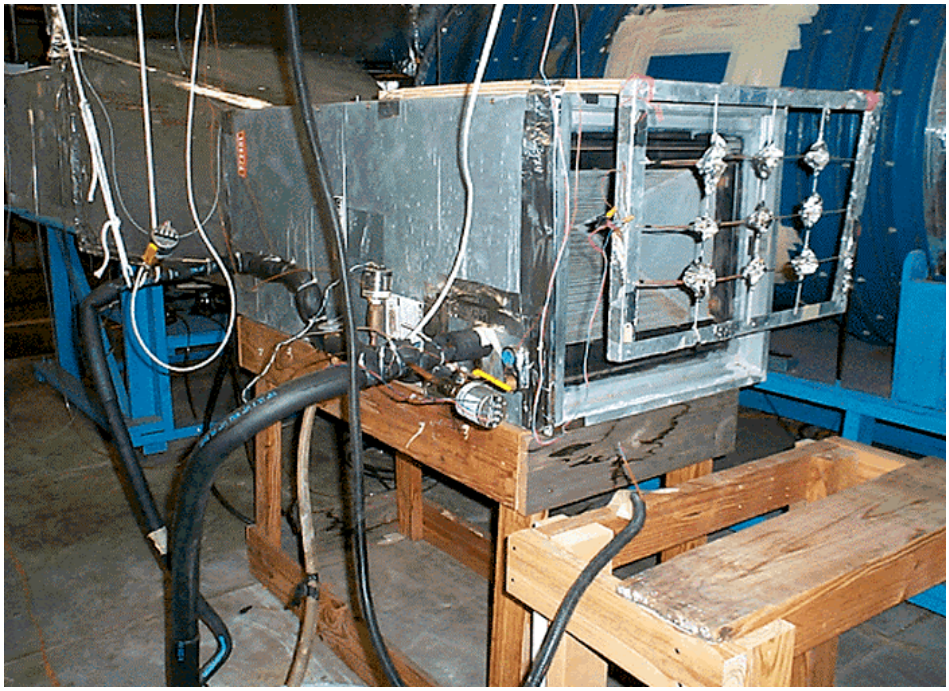

Figure 3.16 The indoor unit of the test heat pump system

The centrifugal blower, driven by a 208/230 VAC single-phase motor, was used to pull the air through the indoor coil. Air flow was maintained by a blower/damper combination at the exit of the indoor test chamber, which was partially blocked off by the chamber to ensure a constant flow rate of 1100 cfm (31 m^3/min) during all the cooling /heating tests.

The test heat pump used two thermal expansion valve (TXV) and check valve combinations as the expansion device in the cooling and heating mode, respectively. The indoor TXV and check valve combination was installed right upstream of the indoor coil in the liquid line and functioned similarly as the outdoor combination of TXV and check valve.

The indoor and outdoor units of the test heat pump were connected by copper tubes through the insulated wall of the psychrometric rooms. The liquid line, with a nominal outside diameter of 3/8 inch (9.53 mm), connected the two coil expansion devices (TXV and check valve combination) with the indoor and outdoor coils. For the vapor line, the copper tubes with a larger nominal outside diameter of 5/8 inch (15.9 mm) were used to connect the compressor, accumulator and reversing valve. The length of each piece of the connection tube is indicated in Figure 3.17. Ball valves were installed on both lines to isolate

the refrigerant circuit apart for component installation and leak detection of either side of the indoor or outdoor unit.

The designed R410A charge was 8.00 lb_m (3.63 kg) for the unit with 25 ft (7.62 m) line set. Because 81 ft (24.69 m) of copper tube was used to connect the indoor and outdoor units of the test heat pump system, an additional charge had to added to the system. For the test unit with two-row outdoor coils, the actual charge amount of R410A was 8 lb_m 9 oz (3.88 kg).

While the focus of the experimental study was on the outdoor evaporators, the heat pump system was instrumented with temperature and pressure sensors throughout the refrigerant circuit to monitor the operation of the whole system. Figure 3.13 shows the locations of the sensors on the heat pump test loop as well. Each sensor was assigned a number that corresponded to the data channel in the data acquisition system. The specifications of the instrument can be found in Table 3.5.

The refrigerant temperatures were measured with T-type copper-contantan thermocouples, which were mounted in the thermocouple wells centered in the tube lines of the refrigerant circuit. The tips of the thermocouples were inserted into the bottom of the thermocouple wells through the small holes. And the holes were filled with high thermal conductivity paste.

Pressure transducers with range of 0 to 500 psia (0 to 3.4 MPa) were also installed near the thermocouple wells to measure the refrigerant pressure. All the pressure transducers used in this project were calibrated with a dead weight for a range from 0 to 500 psia (0 to 3.4 MPa).

Because the liquid flow meter of refrigerant failed to work, the refrigerant mass flow rate $\dot{m}_{refrigerant}$, instead, was calculated with the ARI ten-coefficient formula provided by the compressor manufacturer. The equation and coefficients were:

$$\dot{m}_{refrigerant} = M_0 + (M_1 \times S) + (M_2 \times D) + (M_3 \times S^2) + (M_4 \times S \times D) + (M_5 \times D^2)$$
$$+ (M_6 \times S^3) + (M_7 \times S^2 \times D) + (M_8 \times S \times D^2) + (M_9 \times D^3) \quad (3.1)$$

M_0 = 138.2089996 M_1 = 5.8349967 M_2 = 1.728189588
M_3 = 0.035797261 M_4 = -0.028784713 M_5 = -0.014490423
M_6 = 0.000162653 M_7 = -2.32154E-06 M_8 = 0.000141083
M_9 = 2.2729E-05
S = Saturated Suction Temperature at Compressor Suction Pressure
D = Saturated Discharge Temperature at Compressor Discharge Pressure
($\dot{m}_{refrigerant}$ in lb_m/min, S & D in ^oF)

With the temperature, pressure and mass flow measurements available on the refrigerant side of the heat pump system, the refrigerant-side capacities of both the indoor and outdoor coils could be determined by:

$$\dot{q}_{refrigerant-side} = \dot{m}_{refrigerant} \times (h_{inlet} - h_{outlet}) \quad (3.2)$$

where

$\dot{m}_{refrigerant}$: mass rate of refrigerant flowing through heat exchanger
h_{inlet} : refrigerant enthalpy at the inlet of heat exchanger
h_{outlet} : refrigerant enthalpy at the outlet of heat exchanger

Indoor Air Side Test Facility

The primary indoor air-side test facility, as shown in Figure 3.17, consisted of indoor unit of the heat pump system, connection duct, indoor nozzle apparatus, and attached measuring device. In Figure3.17, each measuring instrument was assigned a number that corresponded to the data channel of the data acquisition system.

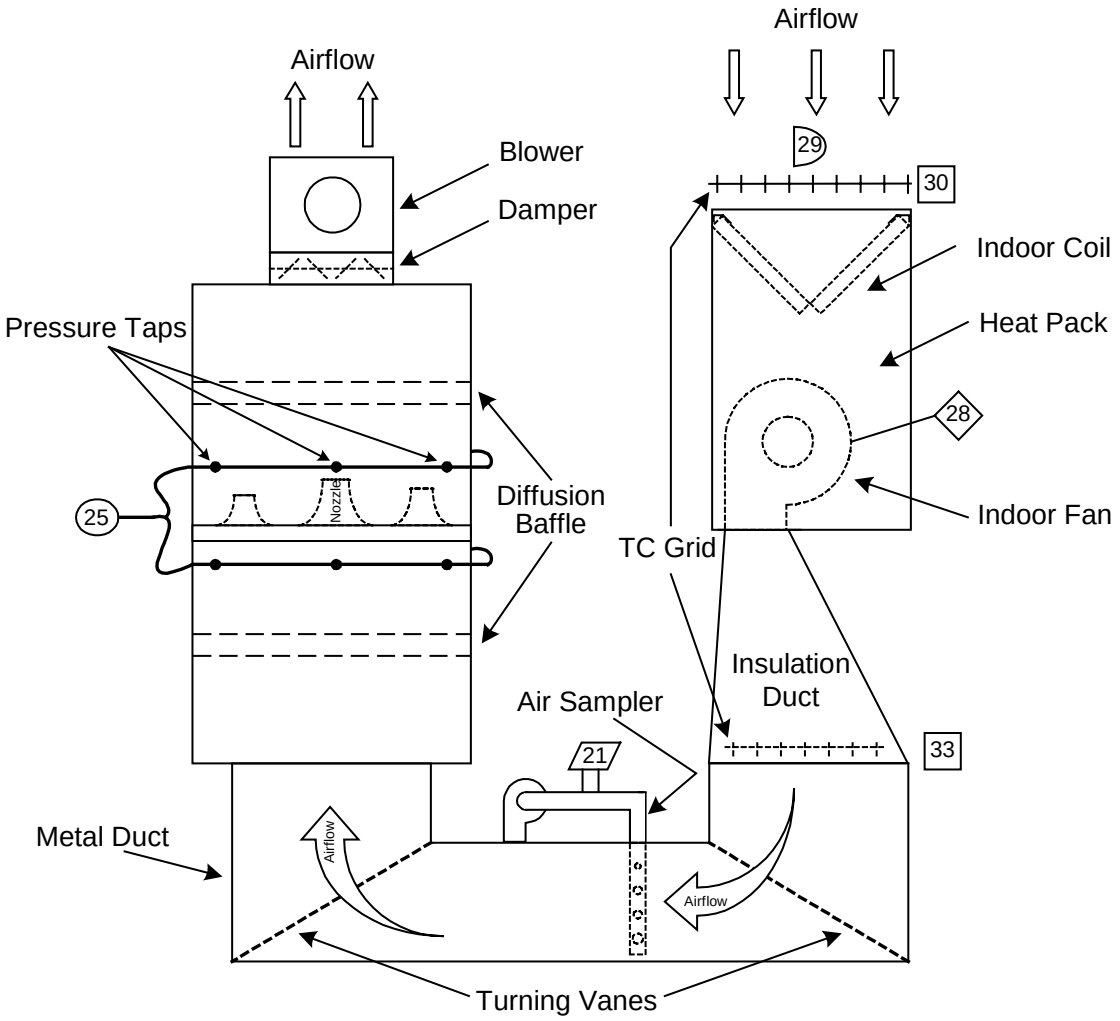

Figure 3.17 Schematic diagram of the indoor air-side test facility

A V-type fin-and-tube heat exchanger, an electric heat pack and a centrifugal fan were encased in an insulated metal sheet box as the indoor unit of the heat pump system under test. At the inlet of the indoor unit, a 9-node T-type thermocouple grid and an electronic VAISALA relative humidity (RH) sensor, which are shown in Figure 3.18, were used to measure the inlet air temperature and humidity. An aluminum shield was placed at the back of each thermocouple to reduce any radiant effect from the bare indoor coil. All the VAISALA RH sensor employed in the tests were calibrated to ±2% RH. There was zero temperature dependence for the RH sensor from 50 ^{o}F to 104 ^{o}F (10 ^{o}C to 40 ^{o}C), and this increased to ±0.5% RH at 32 ^{o}F (0 ^{o}C).

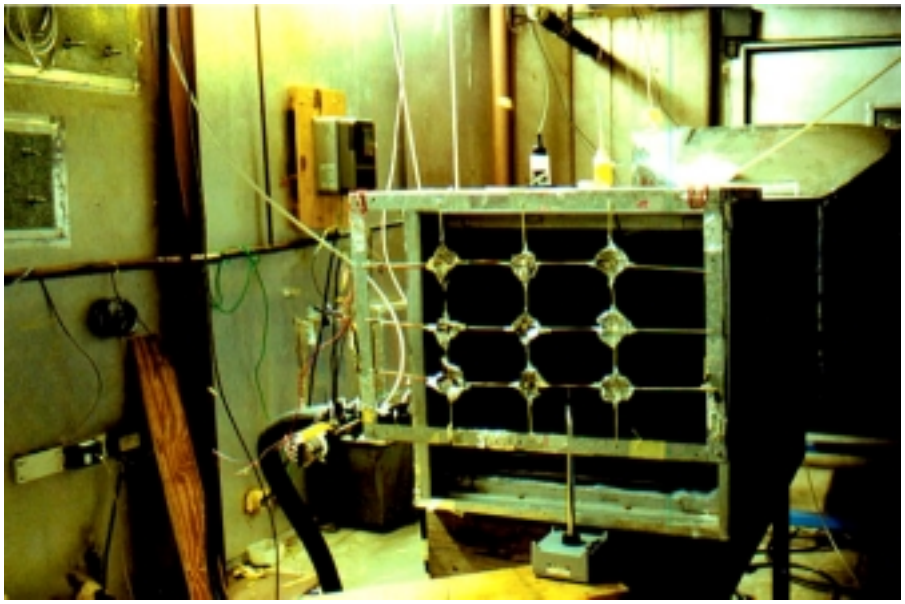

Figure 3.18 The shielded TC grid and the RH sensor in front of the indoor unit

A U-shape connection duct was located downstream the indoor unit to connect it to the nozzle apparatus, in which the thermocouple grid, the dew point sensor facility, and the turning vanes were installed. The exhausted air through the indoor unit was pulled out by the unit centrifugal fan, and then directed to the U-shape connection duct. The average air temperature was measured by a thermocouple grid with 16 thermocouple nodes at the inlet of the U-shape connection duct. The portion of duct between the indoor unit and the thermocouple grid was properly insulated.

A dew point sensor was used to measure the exhaust air humidity through the air-sampling device. A small blower pulled the exhausted air over the sensor through a sampling PVC tube grid which was placed in the connection duct, and then dumped the air back into the connection duck. During the heating tests, the indoor coil served as the condenser of the heat pump system. The humidity of the air stream through the indoor unit did not change. Therefore, the measurement of the inlet RH sensor and the exhaust dew point sensor should be same. During the cooling or defrosting tests, the indoor coil served as the evaporator. Because there could be some condensation of moisture over the indoor coil, it was necessary to us both the RH sensor and the dew point sensor to measure the humidity variance of the air stream.

Air flow through the indoor unit was measured by a nozzle apparatus attached to the connection duct outlet. The indoor nozzle apparatus consisted of a receiving chamber and a discharge chamber

separated by a nozzle plate, on which one 3-inch (76.2-mm), two 5-inch (127-mm), and one 8-inch (203-mm) nozzles were installed. The throat velocity of any nozzle in use should be more than 3000 fpm (15.24 m/s) and lower than 7000 fpm (35.56 m/s) in accordance with the applicable range of the Reynolds number in the calculation equation for the nozzle discharge coefficient. The measurement range of the airflow rate through this nozzle plate was from 150 to 4100 cfm (4.26 to 116.1 m^3/min) with the different arrangement of open nozzles.

The static pressure drop across the open nozzles was measured by a differential pressure transducer with a range of 0 to 5 inches H_2O (0 to 1244 Pa). One end of the pressure transducer was connected to six externally manifolded pressure taps located flush with the inner wall of the receiving chamber upstream the nozzle plate, and the other end was connected to the same amount of static pressure taps mounted on the discharge chamber downstream of the nozzle plate.

A blower and damper combination, located at the exit of the discharge chamber, was used to maintain the airflow rates through the nozzle plate. The capacity of the pulling blower could be changed by adjusting the opening of the butterfly damper installed right before the blower. The blower and the unit centrifugal fan worked together to overcome the flow resistance of the indoor coil and the nozzle plate to pull the air through the indoor air-side test facility. The fresh air from the indoor psychrometric room was first pulled through the indoor unit by the unit centrifugal fan. Then the air stream was ducted to the receiving chamber through the connection duct. After it passed through the open nozzles, the air stream was exhausted back to the indoor psychrometric room by the blower.

In this study, the outlet damper was set at the beginning of the tests to maintain a constant airflow rate through the nozzle chambers. During all the tests, two 5 inch (127 mm) nozzles were opened with a measured pressure drop of 0.98 inch H_2O (244 Pa), which corresponded to air flow rate of 1100 cfm (31.1 m^3/min).

Air side capacity of the indoor coil could be determined from the measurements of air flow rate and of entering and leaving wet- and dry-bulb temperatures for air being cooled and dry-bulb temperature for air being heated. The air-side capacity, $\dot{q}_{air-side}$, of the indoor coil was calculated by:

$$\dot{q}_{air-side} = \dot{m}_{air} \times (h_{inlet} - h_{outlet}) \tag{3.3}$$

where

$\dot{m}_{air}$: mass rate of air flowing across heat exchanger

h_{inlet} : air enthalpy at the inlet of heat exchanger

h_{outlet} : air enthalpy at the outlet of heat exchanger

With the air-side capacity of the indoor coil available, it could be compared with the measured refrigerant-side capacity of the indoor coil to check the accuracy of test facility of both air-side and refrigerant-side.

Outdoor Air Side Test Facility

The outdoor air-side test facility consisted of outdoor unit of the heat pump system, connection duct, outdoor nozzle apparatus, booster fan and variable frequency device (VFD), and various measuring device. Figure 3.19 shows the primary air-side test facility and measurement instrumentation for the outdoor unit. The test facility allowed for the measurement of temperature and humidity of the air entering and leaving the outdoor coil, static pressure downstream of the coil fan, airflow rate through the outdoor coil, and frost mass accumulated on the test coil. Also, a simulated free discharge condition at the exit of the outdoor unit was provided by the air-side test facility.

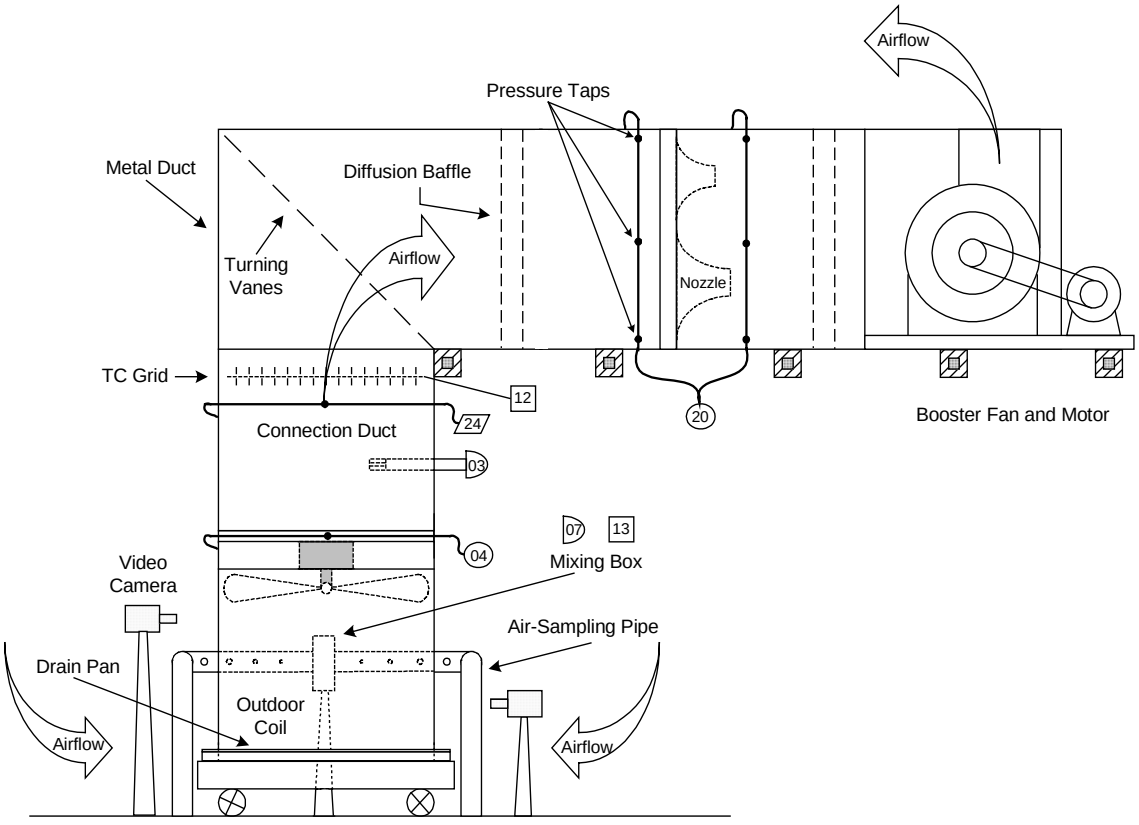

Figure 3.19 Schematic diagram of the outdoor air-side test facility

To accurately measure the entering air temperature and humidity of the outdoor coil under test, an air-sampling PVC piping, as shown in Figure 3.20, was constructed to wrap around the bare outdoor coil. The air-sampling pipes were connected to a mixing box in which a T-type thermocouple and a VAISALA RH sensor were installed to measure the temperature and humidity of the mixing sample air, which was pulled by a small centrifugal blower mounted at the outlet of the mixing box. The PVC piping had holes ranging from 3/8 inch (9.5 mm) at points farthest from the mixing box to 1/8 inch (3.2 mm) at points nearest to the mixing box. Centrally located holes were ¼ inch (6.3 mm) in diameter. This configuration allowed for uniform sampling of the entering air because the suction pressure of the sampling blower was lowest at the farthest pipe points. The measured temperature and humidity through this air-sampling equipment could best represent the ambient air conditions surrounding the outdoor test coil.

Figure 3.20 Air-sampling pipes and mixing box setup around the outdoor coil

Downstream the outdoor coil, as shown in Figure 3.19, the exhausted air stream was directed to the outdoor airflow test apparatus through the connection duct. A 16-node thermocouple grid, shown in Figure 3.21, was made in the middle of duct to measure the average dry-bulb temperature of the air stream flowing over. In an effort to minimize heat leaks, the duct between the exit of the outdoor coil unit and the thermocouple grid was constructed with 1.5 inch (3.81 cm) thick fiberglass board.

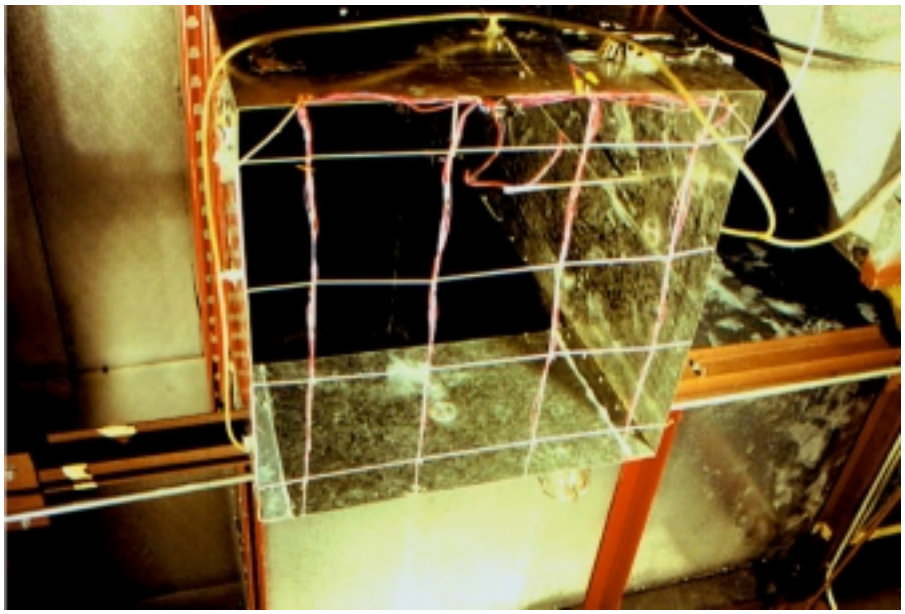

Figure 3.21 The thermocouple grid and externally manifolded wall taps installed downstream of the outdoor unit

To determine the humidity change of the air stream through the outdoor coil, a chilled mirror hygrometer dew points sensor was used to measure air humidity. The dew point sensor was placed in the indoor psychrometric room to prevent its exposure to the frost test conditions with extreme low temperature and high humidity. A small blower was used to pull samples of the outdoor air to the dew point sensor located in the indoor psychrometric room through the externally manifolded wall taps mounted on each side of the rectangular duct shown in Figure 3.21.

In addition, a RH sensor was used as an auxiliary humidity measurement to check against the primary measurement of the dew point sensor. The advantage of RH sensors is their responsiveness to changes of humidity. In the past, we had difficulties with dew point sensors for measuring the leaving humidity because of the "fog" that occurred in the air stream after a defrost. It has been seen that the dew point sensor took as long as 10 minutes to stabilize after defrost process of the coil.

After leaving the connection duct, the air stream was ducted into the airflow test apparatus. In this section, the airflow rate was measured by a nozzle plate, as seen in Figure 3.22, with two 3-inch (76.2-mm), three 5-inch (127-mm), and one 7-inch (168-mm) nozzles. The designed measurement range of this nozzle plate was approximately from 150 cfm (4.25 m^3/min) to 5400 cfm (152.9 m^3/min). In this study, the effect of airflow rate on the frosting performance of outdoor coil was investigated. So different open nozzle combination was chosen to measure various air flow rates. Pressure taps were located upstream

and downstream the nozzle plate as shown in Figure 3.22. A differential pressure transducer with an operating range of 0 to 10 inch w.g. (0 to 2490 Pa) was used to measure the air pressure drop across the nozzle plate.

A centrifugal fan with forward-curved blades was used at the exit of the airflow test chamber to draw the air through the whole test facility and exhaust the air back into the outdoor psychrometric room. The fan had a 7.5-hp (5.65-kW) electric motor rated at 230 VAC. The rotation speed of this motor was controlled by a variable frequency device (VFD): Toshiba Q-FLOWSAVER II. This allowed the adjustment of the capacity of the booster fan during frost tests to keep approximately zero static pressure inside duct at the exit of the outdoor unit.

Figure 3.22 The nozzle plate of the outdoor airflow test chamber

The static pressure inside the duct at the exit of the outdoor unit was measured by a 0 to 1 inch w.g. (0 to 249 Pa) differential pressure transducer. One end of the pressure transducer was connected to four externally manifolded pressure taps (Figure 3.23) centered on each side of the rectangular connection duct right above the coil top cover. The other end of the pressure transducer was open to the surrounding atmosphere of the outdoor room. The analog signal of the pressure transducer was sent to the data

acquisition system so that the variation of the static pressures at the exit of the outdoor unit could be monitored.

Figure 3.23 The externally manifolded pressure taps used to measure the static pressure at the exit of the outdoor unit

During frosting tests, the air pressure drop through the outdoor coil increased continuously as the test coil was blocked with the growing frost. As a result, the airflow rate decreased gradually. To model the real operating condition of the outdoor unit with free discharge condition, the static pressure inside duct at the unit exit should be zero through the frost test operation. In most frost tests, the increase in pressure drop through the frost coil occurred slowly. So the zero static pressure downstream the unit was able to be maintained manually through adjusting the VFD which controlled the rotation speed of the booster fan. Manual adjustment of the VFD was accomplished with a 0 to 10 VDC voltage signal sent from a regulated power source in the control room, which would operate the VFD from 0% to 100% of the maximum programmed output. As the static pressure increased and the airflow rate decreased, a smaller voltage signal went to the VFD to decrease the speed of the booster fan so that the desired zero static gauge pressure right downstream of the outdoor unit was achieved.

A Variac was setup for the motor of the outdoor coil fan so that the fan speed could be adjusted externally. That allowed the operator to modulate the initial air flow rate for the outdoor coil during frost

tests so the effects of different air flow rates on the frosting performance of fin staged coils could be tested.

The moisture removed from the air flowing through the outdoor coil at any time was estimated as:

$$\dot{m}_{moisture} = \dot{m}_{air} \times (w_{\text{entering}} - w_{\text{leaving}}) \tag{3.4}$$

where,

$\dot{m}_{moisture}$: mass rate of moisture removed from the air flowing through the heat exchanger

$\dot{m}_{air}$: mass rate of the air flowing through the heat exchanger

$w_{entering}$: entering air humidity ratio of the heat exchanger

$w_{leaving}$: leaving air humidity ratio of the heat exchanger

The total frost mass accumulated on the coil over the whole test time could be calculated by integrating the instantaneous moisture removal amount at each scan time interval:

$$M_{frost} = \int_0^T \dot{m}_{moisture} dt = \sum (\dot{m}_{moisture} \times \Delta t) \tag{3.5}$$

where,

M_{frost} : frost mass accumulated on the heat exchanger

$\dot{m}_{moisture}$:mass rate of moisture removed from the air flowing through the heat exchanger

Δt : scan time interval of the data acquisition system

The collection of water drained out from the pan under the test coil was used as another method to measure the total weight of frost formed on the he During the last part of test, the curves decreased more rapidly. This phenomenon can be explained by the accelerated degradation of the air-side heat transfer and airflow. With frost accumulation, the frost layer blocked the airflow passages between fins and gradually insulated the fin and tube surface from the surrounding air. All these deteriorated the coil air-side heat transfer significantly. Model predictions reveal that the temperature and the pressure of refrigerant at coil outlet show trends similar to the test data.

The air temperature and humidity ratio showed similar trends to the coil refrigerant pressure and temperature. Both gradually decreased during the first 30 minutes of the test, then they began to fall rapidly during the last 15 minutes. The decreasing evaporation temperature, together with the lower airflow rate, caused this rapid drop of airflow temperature and humidity ratio at coil exit.

During the last part of test, the curves decreased more rapidly. This phenomenon can be explained by the accelerated degradation of the air-side heat transfer and airflow. With frost accumulation, the frost layer blocked the airflow passages between fins and gradually insulated the fin and tube surface from the surrounding air. All these deteriorated the coil air-side heat transfer significantly.

Model predictions reveal that the temperature and the pressure of refrigerant at coil outlet show trends similar to the test data.

The air temperature and humidity ratio showed similar trends to the coil refrigerant pressure and temperature. Both gradually decreased during the first 30 minutes of the test, then they began to fall rapidly during the last 15 minutes. The decreasing evaporation temperature, together with the lower airflow rate, caused this rapid drop of airflow temperature and humidity ratio at coil exit.

at exchanger. After defrosting, the water from the melted frost dripped into the collection pan at the bottom of the outdoor coil, and drained into a volumetric flask. Because some of the water evaporated during the defrost process and some of it stayed on the coil, it was not possible to collect all of the water from melted frost. It had been verified in the tests that repeatable amounts of water were collected after two frost/defrost cycles. However, the water was still smaller than the frost mass calculated by Equation 3.4 and 3.5.

A method that has been used by other researchers to measure the frost buildup on a heat exchanger is to place the heat exchanger on a load cell. The load cell would register the change in weight of the heat exchanger. However, this technique cannot be used effectively with a heat exchanger that uses a refrigerant to cool the heat exchanger. The load cell measurement assumes that the amount of refrigerant inside the heat exchanger is constant during the frost buildup period. With a refrigeration system, the amount of refrigerant in the heat exchanger changes as frost forms on the heat exchanger. The result is that the load cell would register the change in refrigerant mass and frost together. Using a load cell would require using an ethylene-glycol/chilled water solution for the coolant in the heat exchanger rather than a refrigerant. Also, flexible tubing would have to be used to connect the cooling system to heat exchanger. Therefore, the method with a load cell was not attempted to measure the frost buildup in this experimental study.

Data and Images Acquisition System

During the tests of the heat pump system, data were continuously collected by the data acquisition (DAQ) system from the instruments and stored for the later data processing and analysis.

All the voltage signals transmitted from thermocouples, pressure transducers, RH sensors, power meters, etc., were directed to a signal conditioning and acquisition system located in the indoor psychrometric room (Figure 3.24) where better operating conditions were provided compared to the outdoor room. This DAQ system, made by Kaye Instruments, communicated with a PC in the control room via an RS-2323 serial port. Data acquisition software, NETCOM, was used to record the real-time data.

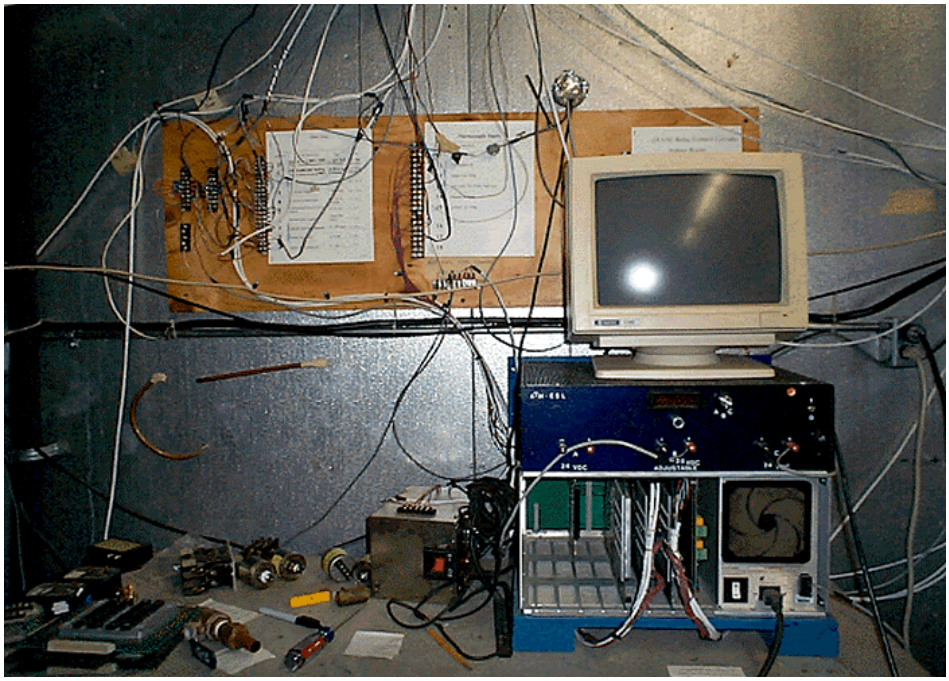

Figure 3.24 The DAQ equipment located in the indoor psychrometric room

A complete description of the measurement channels is provided in Table 3.5. All the current input signals with 4-20 mA had been converted into the 1-5 voltage signals by the 250-Ohm precision resistors. The locations of the sensors could be found in Figures 3.13, 3.17 and 3.19 referring to the channel numbers in Table 3.5.

Table 3.5 The channel chart of the DAQ system

Channel	Description	Signal (V)	Range	Unit
00	Outdoor R410A Liquid Line Pressure	0.1 - 5.1	0 - 500	psig
01	Outdoor R410A Vapor Line Pressure	0.1 - 5.1	0 - 500	psig
02	Compressor Electric Power	1 - 5	0 - 4	kW
03	Outdoor Exhaust Air RH	1 - 5	0 - 100	%
04	Static Pressure Downstream Outdoor Fan	0 - 5	0 - 5	in. w.g.
05	Compressor Suction Pressure	0.1 - 5.1	0 - 500	psig
06	R410A Mass Flow Rate	1 - 5	0 - 40	lb_m/min
07	Outdoor Room Air RH	1 - 5	0 - 100	%
08	Outdoor Unit Electric Power	1 - 5	0 - 8	kW
09	Compressor Discharge Pressure	0.1 - 5.1	0 - 500	psig
10	Outdoor R410A Vapor Line Temperature			^oF
11	Outdoor R410A Liquid line Temperature			^oF
12	Outdoor Exhaust Air Dry-Bulb Temperature			^oF
13	Outdoor Room Air Dry-Bulb Temperature			^oF
14	Compressor Discharge Temperature			^oF
15	Compressor Suction Temperature			^oF
16	R410A Temperature Upstream Outdoor TXV			^oF
17	Compressor Shell Temperature - Top			^oF
18	Compressor Shell Temperature - Mid			^oF
19	Compressor Shell Temperature - Btm			^oF
20	Outdoor Nozzle Differential Pressure	0 - 5	0 - 5	in. w.g.
21	Indoor Exhaust Air Dewpoint Temperature	0 - 2.5	0 - 100	^oF
22	Indoor R410A Vapor Line Pressure	0.1 - 5.1	0 - 500	psig
23	Indoor R410A Liquid Line Pressure	0.1 - 5.1	0 - 500	psig
24	Outdoor Exhaust Air Dewpoint Temperature	0 - 5	-40 - 140	^oF
25	Indoor Nozzle Differential Pressure	1 - 5	0 - 5	in. w.g.
26	R410A Pressure Upstream Outdoor TXV	0.1 - 5.1	0 - 500	psig
27	R410A Pressure Upstream Indoor TXV	0.1 - 5.1	0 - 500	psig
28	Indoor Unit Electric Power	0 - 10	0 - 1	kW
29	Indoor Room Air RH	1 - 5	0 - 100	%
30	Air Dry-Bulb Temperature Before Indoor Unit			^oF
31				
32	Indoor R410A Vapor Line Temperature			^oF
33	Air Dry-Bulb Temperature After Indoor Fan			^oF
34	Indoor R410A Liquid Line Temperature			^oF
35	R410A Temperature Upstream Indoor TXV			^oF

Data are normally scanned approximately every 10 to 60 seconds, depending on the required test accuracy and the duration of the test. In this project, data was collected in the fixed 10-second interval during all the tests. The scanned data were stored on the hard drive of the PC. Backups of the data files were made on a floppy disk.

Once an experimental run was completed, the stored data was processed by a QuickBasic program on another PC to analyze the performance of the heat pump system and evaluate the progress of the test. The processed data were used to generate reports and plots of the performance curves of various parameters. Trends of the data were smoothed by a method of 3-points moving average.

A PC-based image acquisition (IMAQ) system was setup in the project to continuously acquire and capture images and to monitor and measure the frost growing on the fin surface. This IMAQ system was composed of capture system, image acquisition card, personal computer and suitable image processing software, and real-time video monitor equipment.

The capture system consisted of video cameras, close-up lenses, lighting and accessory equipment. The video cameras, equipped with Tiffen +7 close-up lens set, were the monochrome charged coupled device (CCD) with the resolution of 512 by 480 pixels, which used a field composed of light-sensitive semiconductor sensors to capture images. Two video cameras were placed around the test coil for inspecting the leading edges of different circuit fins, while another video camera was placed inside “horseshoe” shape coil to monitor the frost growth at the rear edges of the coil fins. The video camera that focused on the lower circuit fins is shown in Figure 3.25. Frost growth could be observed simultaneously at up to three locations corresponding to different refrigerant circuits in the evaporator.

One of the front cameras was mounted on a moveable platform with a DC stepper motor that could be controlled remotely in the control room of the psychrometric rooms. Three position switches were located on the platform to stop the moving camera so that the camera could shoot the same set of fins at three different vertical or horizontal positions. This facility is shown in Figure 3.26. Lighting was an important consideration in the capturing system. Different lighting equipment and arrangement were attempted to provide sufficient illustration on the fin surfaces for the video cameras.

An image acquisition card, Snappy, connected the video cameras to the PC through a parallel port. An associated interface software was used to capture and adjust the video images. The simple images snapshot by the Snappy were saved as individual graphics files in the PC waiting for the further processing and measurement after the frost test. Measurement of the frost thickness on the images was done with Mocha software, which was developed by Jandel Scientific. Also, TVs and VCR, as seen in Figure 3.27, were used to monitor and record the live video of the continuous frost growing process.

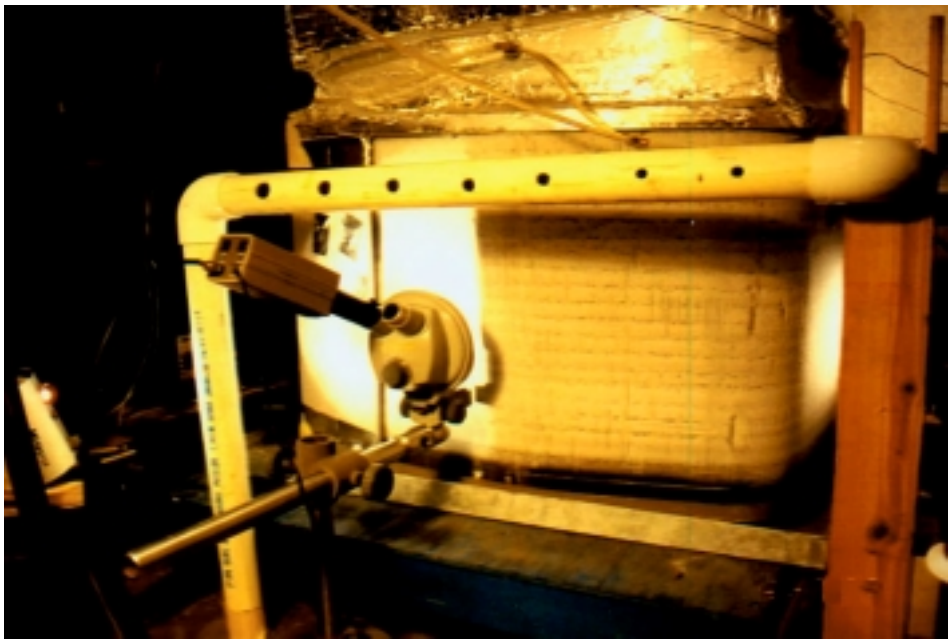

Figure 3.25 The video camera that focused on the lower circuit fins

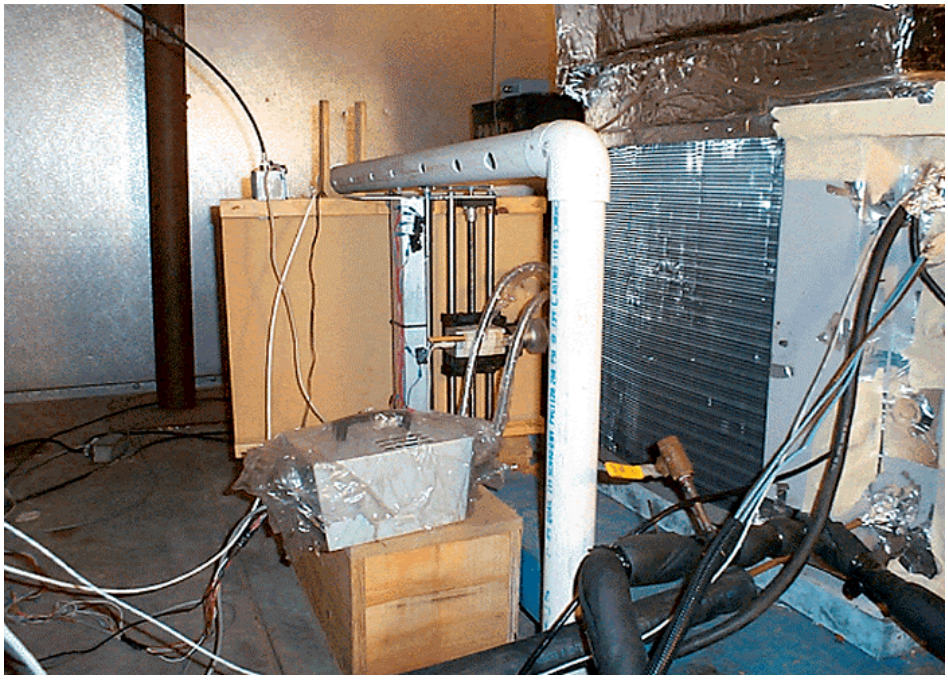

Figure 3.26 The video camera moving facility

Figure 3.27 The IMAQ facility located in the control room

The IMAQ system was used to measure the frost thickness on the fins during the frost growing process. Images were taken at regular time intervals (typically 3 to 5 minutes) depending upon the time of the frost test. Measurement of frost thickness was made on multiple fins as well as multiple locations. The measured frost heights at different locations were averaged to develop an estimate of the average frost thickness. A sample of images obtained from the IMAQ system is shown in Figures 3.28 through 3.30.

Figure 3.28 shows the leading edges of coil fins right before any frost had formed. Figure 3.29 was 20 minutes after the start of the frost test, and Figure 3.30 was 30 minutes after the start of the test. The data taken from these images were used to plot the growth of frost layer in Figure 3.31.

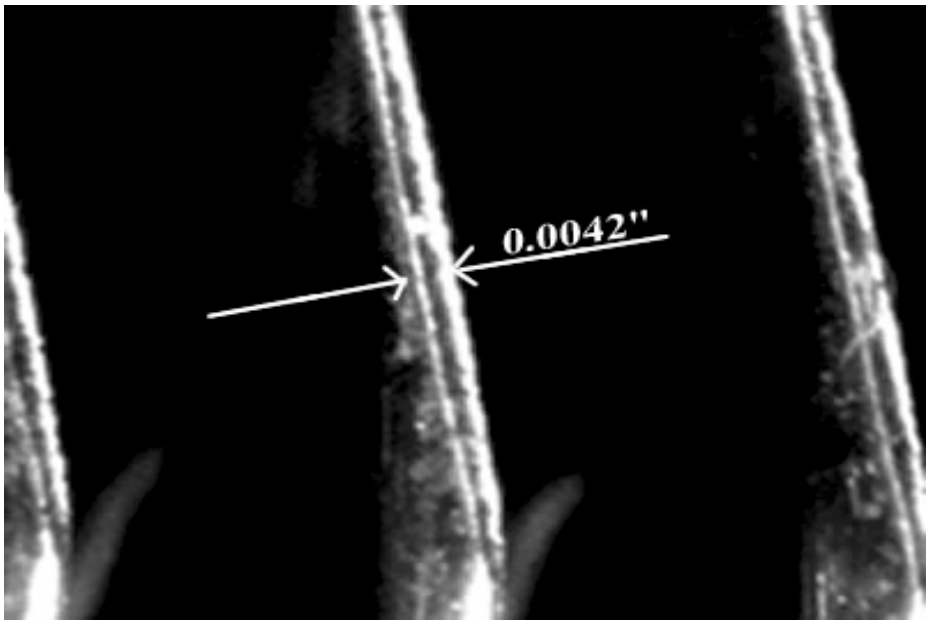

Figure 3.28 Sample image of the fin leading edges at the start of the frost test for two-row fin staged coil (15/20 fpi) with medium airflow (2100 cfm) at 28°F DB and 90% RH

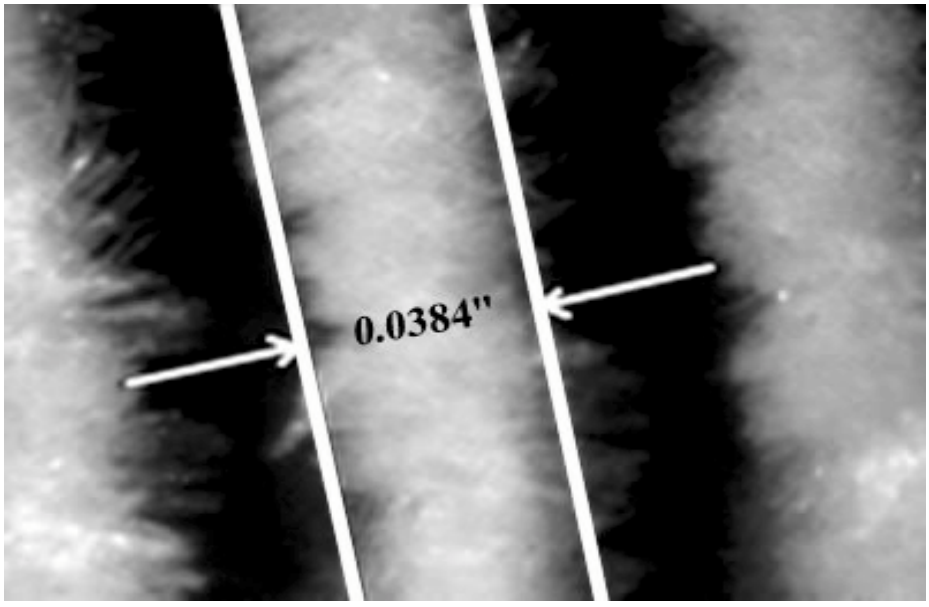

Figure 3.29 Sample image of the frost growth at the fin leading edges 20 minutes after the start of the frost test for two-row fin staged coil (15/20 fpi) with medium airflow (2100 cfm) at 28°F DB and 90% RH

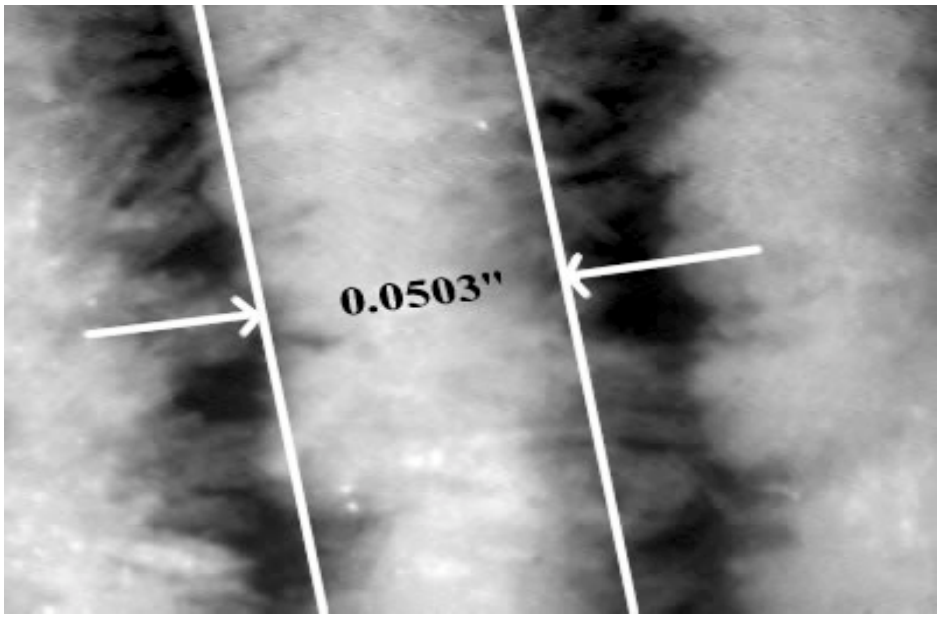

Figure 3.30 Sample image of the frost growth at the fin leading edges 30 minutes after the start of the frost test for two-row fin staged coil (15/20 fpi) with medium airflow (2100 cfm) at 28°F DB and 90% RH

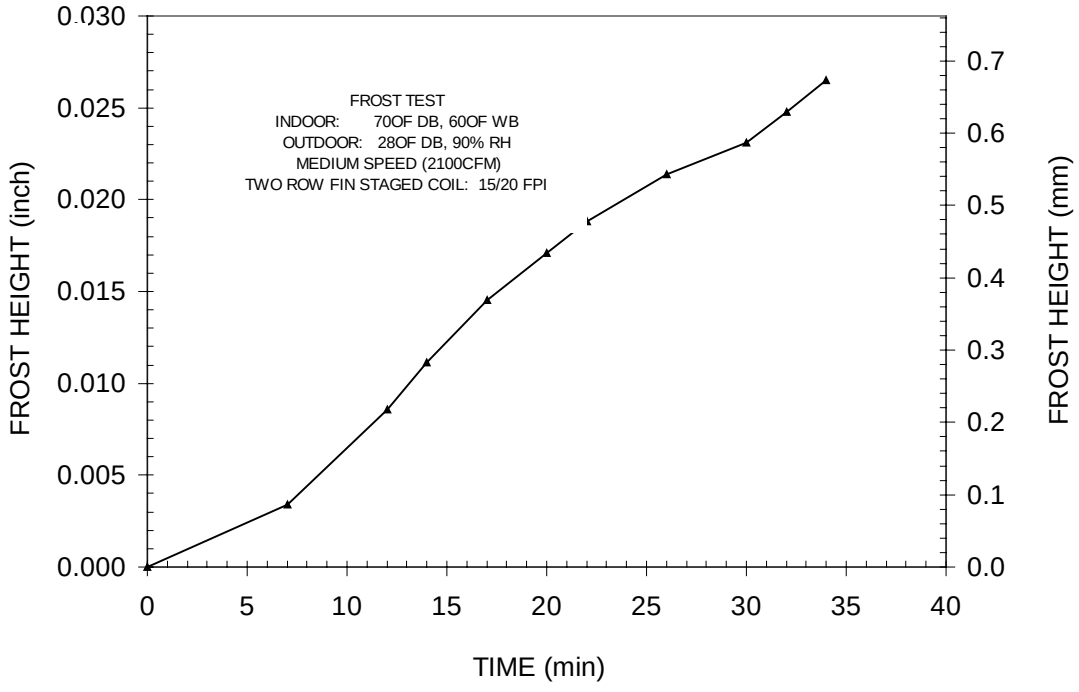

Figure 3.31 Sample plot of frost thickness versus time for two-row fin staged coil (15/20 fpi) with medium airflow (2100 cfm) at 28°F DB and 90% RH frost test

Heat Pump Test Conditions and Procedure

Performances of the heat pump system, equipped with different outdoor coils, were tested at steady-state, frost, and defrost operation conditions. The specifications of these test conditions are shown in Table 3.6. The focus of the tests was on the effects of different staging fins on the performance of the heat pump outdoor coil under frosting conditions.

Heat Pump Test Conditions

Five outdoor coils with varying fin-spacing rows were examined to quantify and compare the impact of fin staging on the frosting performance of the outdoor coil itself as well as the whole heat pump system.

Both the two-row and three-row baseline coils had the same fin pitch of 20 fpi (7.9 fin/cm) at each row. The two two-row fin staged coils had the fin pitch as 15/20 fpi (5.9/7.9 fin/cm) and 15/25 fpi (5.9/9.8 fin/cm), respectively. Also, a three-row fin staged coil with 15/20/25 fpi (5.9/7.9/9.8 fin/cm) fin pitch was tested. The baseline coils provided the comparison to the fin staging technique. The details of the test coils have been described in Section 3.1. The same compressor and indoor unit were used through the tests with either two-row or three-row outdoor coils.

In the steady-state test part, two cooling tests (DOE A ad DOE B) and one heating test (DOE E) were run sequentially to measure the heat pump system performance. These test results allowed quantitative comparisons of the cooling and heating performance of heat pump system with different fin staged coils.

To examine the effects of airflow, test of the units under high, medium, and/or low airflow rates across the outdoor coils were also conducted. The starting volumes of these three setting airflow rates were 2800 cfm (79.3 m^3/min), 2200 cfm (62.3 m^3/min), and 1400 cfm (39.6 m^3/min), respectively. The fan-speed was adjusted by changing the input voltage to the fan motor by a transformer.

Frosting performance of the heat pump system with baseline or fin staged outdoor coils were tested with up to five outdoor frosting conditions and three airflow rates of outdoor fan, which simulated the standard, heavy humidity and worst-case conditions of the heat pump frosting operation. Four variables were examined: coil type, air temperature and humidity, and airflow rate (Table 3.6). The outdoor air temperature ranges from 28 ^oF (-2.2 ^oC) to 35 ^oF (1.7 ^oC) and the relative humidity ranges from 82% to 95%.

Table 3.6 The matrix of test conditions

Test Coil		Steady State Test			Frost Test			Defrost Test	
		OD Fan Speed	Indoor Condition	Outdoor Condition	OD Fan Speed	Indoor Condition	Outdoor Condition	Indoor Condition	Outdoor Condition
Two Row	Baseline (20/20 fpi)	2800 cfm (1.322 m^3/s)	80°F(26.7°C) DB 67°F(19.4°C) WB	95°F(35.0°C) DB 75°F(23.9°C) WB	1400 cfm (0.661 m^3/s)	70°F(21.1°C) DB <60°F(15.6°C) WB	35°F(1.7°C) DB 33°F(0.6°C) WB	70°F(21.1°C) DB <60°F(15.6°C) WB	35°F(1.7°C) DB 33°F(0.6°C) WB
				82°F(27.8°C) DB 65°F(18.3°C) WB	2200 cfm (1.038 m^3/s)		35°F(1.7°C) DB, 90% RH*		35°F(1.7°C) DB, 90% RH*
							35°F(1.7°C) DB, 95% RH*		35°F(1.7°C) DB, 95% RH*
			70°F(21.1°C) DB <60°F(15.6°C) WB	47°F(8.3°C) DB 43°F(6.1°C) WB	2800 cfm (1.322 m^3/s)		28°F(-2.2°C) DB, 90% RH		28°F(-2.2°C) DB, 90% RH
							28°F(-2.2°C) DB, 95% RH**		28°F(-2.2°C) DB, 95% RH**
	Staging Fin (15/20 fpi)		80°F(26.7°C) DB 67°F(19.4°C) WB	95°F(35.0°C) DB 75°F(23.9°C) WB	1400 cfm (0.661 m^3/s)	70°F(21.1°C) DB <60°F(15.6°C) WB	35°F(1.7°C) DB 33°F(0.6°C) WB	70°F(21.1°C) DB <60°F(15.6°C) WB	35°F(1.7°C) DB 33°F(0.6°C) WB
				82°F(27.8°C) DB 65°F(18.3°C) WB	2200 cfm (1.038 m^3/s)		35°F(1.7°C) DB, 90% RH*		35°F(1.7°C) DB, 90% RH*
							35°F(1.7°C) DB, 95% RH*		35°F(1.7°C) DB, 95% RH*
			70°F(21.1°C) DB <60°F(15.6°C) WB	47°F(8.3°C) DB 43°F(6.1°C) WB	2800 cfm (1.322 m^3/s)		28°F(-2.2°C) DB, 90% RH		28°F(-2.2°C) DB, 90% RH
							28°F(-2.2°C) DB, 95% RH**		28°F(-2.2°C) DB, 95% RH**
	Staging Fin (15/25 fpi)		80°F(26.7°C) DB 67°F(19.4°C) WB	95°F(35.0°C) DB 75°F(23.9°C) WB	1400 cfm (0.661 m^3/s)	70°F(21.1°C) DB <60°F(15.6°C) WB	35°F(1.7°C) DB 33°F(0.6°C) WB	70°F(21.1°C) DB <60°F(15.6°C) WB	35°F(1.7°C) DB 33°F(0.6°C) WB
				82°F(27.8°C) DB 65°F(18.3°C) WB	2200 cfm (1.038 m^3/s)		35°F(1.7°C) DB, 90% RH*		35°F(1.7°C) DB, 90% RH*
							35°F(1.7°C) DB, 95% RH*		35°F(1.7°C) DB, 95% RH*
			70°F(21.1°C) DB <60°F(15.6°C) WB	47°F(8.3°C) DB 43°F(6.1°C) WB	2800 cfm (1.322 m^3/s)		28°F(-2.2°C) DB, 90% RH		28°F(-2.2°C) DB, 90% RH
							28°F(-2.2°C) DB, 95% RH**		28°F(-2.2°C) DB, 95% RH**
Three Row	Baseline (20/20/20 fpi)	2800 cfm (1.322 m^3/s)	80°F(26.7°C) DB 67°F(19.4°C) WB	95°F(35.0°C) DB 75°F(23.9°C) WB	2200 cfm (1.038 m^3/s)	70°F(21.1°C) DB <60°F(15.6°C) WB	35°F(1.7°C) DB 33°F(0.6°C) WB	70°F(21.1°C) DB <60°F(15.6°C) WB	35°F(1.7°C) DB 33°F(0.6°C) WB
				82°F(27.8°C) DB 65°F(18.3°C) WB			35°F(1.7°C) DB, 90% RH*		35°F(1.7°C) DB, 90% RH
			70°F(21.1°C) DB <60°F(15.6°C) WB	47°F(8.3°C) DB 43°F(6.1°C) WB	2800 cfm (1.322 m^3/s)		28°F(-2.2°C) DB, 90% RH		28°F(-2.2°C) DB, 90% RH
	Staging Fin (15/20/25 fpi)		80°F(26.7°C) DB 67°F(19.4°C) WB	95°F(35.0°C) DB 75°F(23.9°C) WB	2200 cfm (1.038 m^3/s)	70°F(21.1°C) DB <60°F(15.6°C) WB	35°F(1.7°C) DB 33°F(0.6°C) WB	70°F(21.1°C) DB <60°F(15.6°C) WB	35°F(1.7°C) DB 33°F(0.6°C) WB
				82°F(27.8°C) DB 65°F(18.3°C) WB			35°F(1.7°C) DB, 90% RH*		35°F(1.7°C) DB, 90% RH
			70°F(21.1°C) DB <60°F(15.6°C) WB	47°F(8.3°C) DB 43°F(6.1°C) WB	2800 cfm (1.322 m^3/s)		28°F(-2.2°C) DB, 90% RH		28°F(-2.2°C) DB, 90% RH

*The test was done only at medium fan speed (2200 cfm); **The tests were done at high and medium fan speeds (2800 cfm and 2200 cfm).

The frost/defrost test was started under the standard frosting test condition. Based on the ANSI/ASHRAE Standard (1995), the standard condition for frosting test of a heat pump unit is that the outdoor room is maintained at 35 ^{o}F (1.7 ^{o}C) dry bulb and 33 ^{o}F (0.56 ^{o}C) wet bulb temperature with an indoor dry bulb temperature of 60 ^{o}F (21.1 ^{o}C) and maximum wet bulb temperature of 60 ^{o}F (15.6 ^{o}C). In this standard test condition, the corresponding relative humidity of the outdoor air is 83%. For the other two test conditions with 35 ^{o}F dry-bulb temperature, the air relative humidity was raised from the 82% RH of the standard test to 90 % RH and 95% RH, respectively, whereas all the other test conditions remained unchanged. The higher humidity conditions allowed frost to grow faster.

In the two worst-case frosting test conditions, the outdoor dry-bulb temperature was further reduced to 28 ^{o}F (-2.2 ^{o}C) with two high relative humidity of 90% and 95A%, respectively.

For all the frost/defrost tests, the indoor room was maintained at a dry bulb temperature of 70 ^{o}F (21.1 ^{o}C) and maximum wet bulb temperature of 60 ^{o}F (15.6 ^{o}C). And the indoor airflow rate was 1100 cfm (31.1 m^3/min) constantly. Through all the tests, the compressor speed was constant as well.

Heat Pump Test Procedure

Five outdoor coils were studied in the order from two-row coils to three-row coils. Among either set of the two-row or three-row coils, the complete set of tests for the heat pump system with the baseline outdoor coil was run first. The test results could be used as the reference to those of the fin staged coils. Therefore, the testing procedure began with installing the two-row baseline coil in the heat pump system. A flow chart of the whole test procedure is shown in Figure 3.32.

After the test coil was setup and instrumented, a leak check had to be done on the heat pump system before a series of tests were started. The heat pump unit was charged with the nitrogen gas at 250 to 300 psig. The leakage points were located by a leak detector, and melded with solder after the N_2 was discharged. The leakage detection was then repeated by changing the system with N_2 again.

If no detectable leakage was found, the unit with high pressure N_2 was then monitored by the DAQ system for two to three days to make sure there was no small leaks. The pressure difference due to the change of ambient temperature was considered by the DAQ system.

After all leaks were found and repaired, the N_2 was removed and the system was vacuumed and prepared to charge with refrigerant R410A. Based on the manufacturer's specification, the heat pump unit was charged under DOE B test conditions (Outdoor: 82 ^{o}F (27.8 ^{o}C) DB and 65 ^{o}F (18.3 ^{o}C) WB; Indoor: 80 ^{o}F (26.7 ^{o}C) DB and 67 ^{o}F (19.4 ^{o}C) WB).

The psychrometric facility was started through the control panel located in the control room. To achieve the required test conditions, the temperature of the glycol-water solution had to be set properly through the control box of the chiller. It took time to achieve the desired test states because the air inside

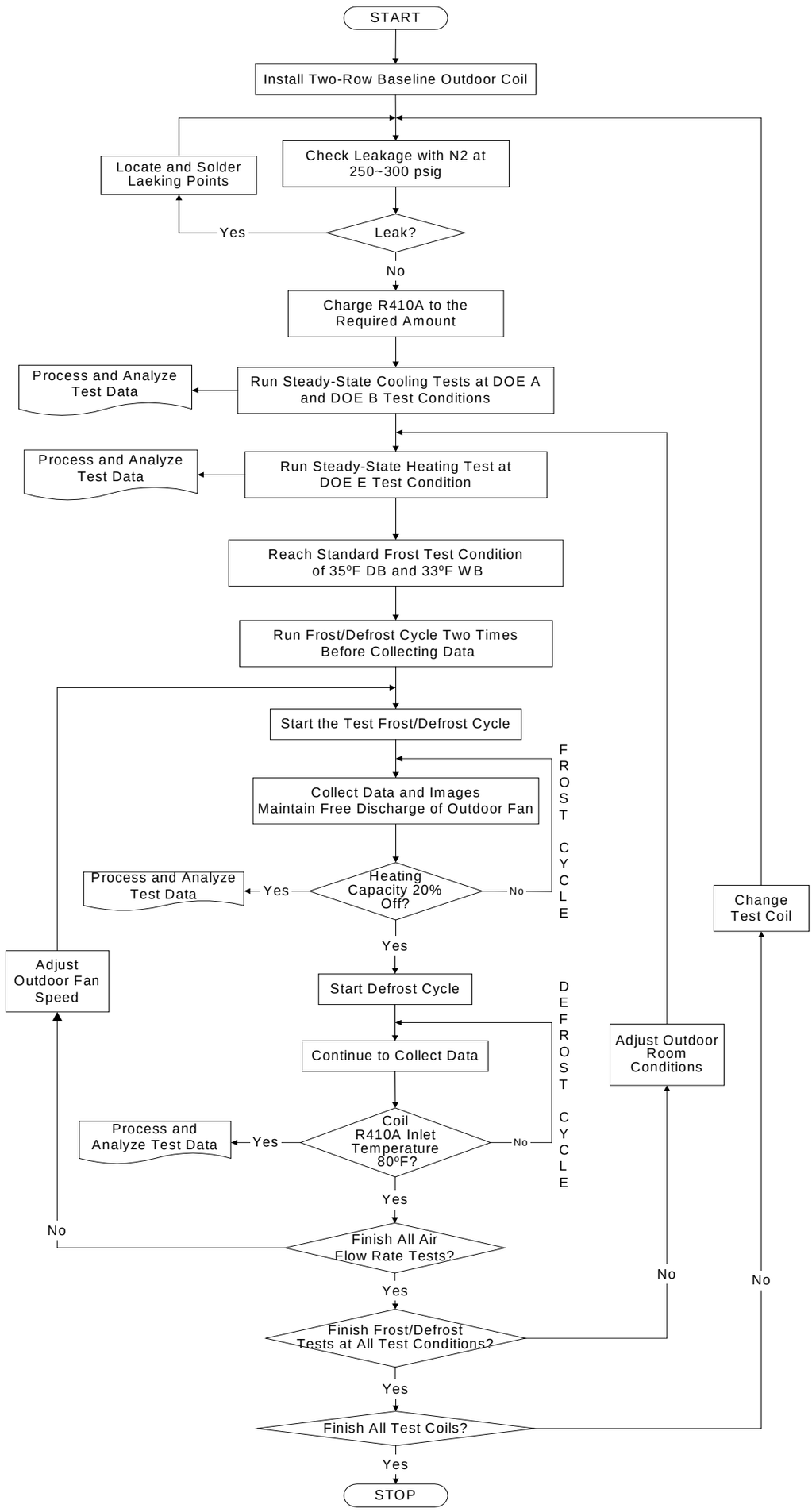

Figure 3.32 Test procedure chart

the psychrometric rooms was initially at the ambient conditions. Once the psychrometric rooms reached the DOE B test conditions, the refrigerant was added through the service valve on the liquid line. After the initial charge was completed, the unit was cycled on in the cooling mode, and charging continued slowly until the pressure at the liquid service valve reached 385 psig (2.65 MPa), which provided 9 ^{o}F (±2 ^{o}F) (-12.8 ^{o}C (±1.1 ^{o}C)) subcooling at the liquid service valve. At this moment, the unit was considered properly charged. The electronic scale showed the total charged amount was 8 lb_m 9 oz (3.88 kg) or 9 lb_m 8 oz (4.31 kg) for the heat pump system with two-row or three-row coils, respectively. The system was then ready to be tested.

Two steady state cooling tests were conducted first to measure the heat pump system performance under DOE A and DOE B test conditions. The temperatures and humidities of both psychrometric rooms, the coolant temperature and flow rate through each coil, and the air flow rates of room conditioning systems and air test chambers needed to be constants throughout the running of each steady-state test. Also, the heat pump system needed to be operating constantly during the steady-state tests. To couple the heat pump system and the psychrometric rooms and to avoid the variation of any parameters during the test run, it was necessary to establish the equilibrium between the heat pump system and the psychrometric rooms prior to taking data.

After the temperature and humidity of the psychrometric rooms stabilized at the set test points and the thermodynamic equilibrium was established between the heat pump system and the psychrometric rooms, the DAQ system began to record the data. Each steady-state test was continued about 60 minutes. The final test report could be printed out right after the test. To verify the accuracy and stability of the system and test facility, the indoor and outdoor capacities at both refrigerant side and air side were constantly monitored during the test procedure. Each difference of the refrigerant-side and air-side capacities should be within ±5%.

After the cooling tests were complete, the reversing valve of the heat pump unit was switched to heating mode and the psychrometric rooms were adjusted to the DOE E heating test conditions.

Upon completing the steady-state heating test, the temperature of the chiller water-glycol solution needed to be reset to lower the outdoor room temperature to the required value of the following frost tests. The test procedure for the frost/defrost tests started with letting the unit to proceed through at least two frost/defrost cycles before any data were collected for the frosting tests. After the first frost/defrost cycle, small amounts of condensate were trapped or remained on the coil surface, which acted as the new sites for water to condense and freeze on the outdoor coil in the following frost cycle. The condensate collected after the second defrost cycle should be close to the actual amount of frost building up on the outdoor coil. This made it possible to collect a repeatable amount of condensate from the drain pan under the outdoor coil. Also, the frosting test under this test procedure was better for simulating the conditions in the field where the unit cycles on and off and coil never really cleans completely of condensate. Because all the

frosting tests corresponding to one outdoor coil could not be finished one time, this two-time frost/defrost cycle had to be repeated at the beginning of each frosting test time.

The first frost test on the two-row baseline coil started on the third frost/defrost cycle. Data and images were continuously collected by the DAQ and IMAQ system. During the frosting process, the speed of the booster fan at the exit of the outdoor flow chamber was continuously modified to maintain the ductwork free discharged condition at the exit of the outdoor unit.

The frost test continued until 20% degradation of the airside heating capacity was observed. At this moment, the defrost cycle began by switching the reversing valve to divert the refrigerant flow and turning off the outdoor pulling fan to stop blowing cold air over the frosted coil.

DAQ system continued the data collection during the defrost cycle. As defrosting progressed, the water was drained out of the coil and collected by a pan under the coil. When the refrigerant inlet temperature at the outdoor coil climbed up to 80 ^{o}F (26.7 ^{o}C), the coil was regarded as free of frost, and then the defrost cycle was terminated. Meanwhile, the DAQ system stopped to store the data, which would be processed and analyzed later to report the frost/defrost test results. After several minutes, the water stored in the bottom pan was used to determine the frost weight by a volumetric flask. During the frost/defrost test cycle, the test conditions of both indoor and outdoor rooms were maintained by the psychrometric facility. The capacities of the refrigerant and air sides agreed within ±10% during the frost tests, which was a slow transient process.

To achieve the frost test condition of either 35 ^{o}F (1.7 ^{o}C) or 28 ^{o}F (-2.2 ^{o}C) air dry bulb temperature, the coolant temperature was set lower than 32 ^{o}F (0 ^{o}C) during the frost test period. The frost could buildup on both the cooling and dehumidifying coils. So they needed to be defrosted at the running interval of the frost tests. This happened every 2 to 3 hours depending upon the coolant temperature and the air conditions of the outdoor room. Defrosting was accomplished by switching on all the electric heaters located in the air reconditioning duct of the outdoor room, and, at the meantime, bypassing the coolant flow back to the tank through the 3-way electronic valve. The defrosting process disturbed the original psychrometric equilibrium and added some heat and moisture into the outdoor air, which caused a temporary increase in the air temperature and humidity. It took 20 to 30 minutes for the outdoor air conditions to return completely to the desired frost test levels.

Each outdoor coil needed to be tested under high, medium, and/or low initial airflow rate at a specified frost test condition. Therefore, the outdoor airflow rate was changed first without adjusting the temperature and humidity of the outdoor psychrometric room. Among the other variables (coil type, temperature and humidity) to be examined, the relative humidity was changed while maintaining the air temperature of outdoor room at 35 ^{o}F (1.7 ^{o}C).

All the frost/defrost tests in this project were conducted at an air dry-bulb temperature of either 35 ^{o}F (1.7 ^{o}C) or 28 ^{o}F (0.6 ^{o}C). After all the tests were completed at 35 ^{o}F (1.7 ^{o}C) dry-bulb temperature,

the outdoor conditions of the psychrometric rooms were adjusted to 28 ^{o}F (0.6 ^{o}C) dry-bulb temperature and the new test conditions with either 90% RH or 95% RH. A new set of frost/defrost tests with different initial airflow rates would be complete at these test conditions with 28 ^{o}F (0.6 ^{o}C) dry-bulb temperature.

After the required tests for one coil were complete, it was replaced by the next test coil. Before removing the outdoor coil, it was necessary to retrieve the refrigerant from the system. All the tests specified in Table 3.6 for the different coils, airflow rates, air temperatures and humidities were completed. For each two-row coils, five 35 ^{o}F (1.7 ^{o}C) and five 28 ^{o}F (0.6 ^{o}C) frost/defrost test corresponding to different humidities and airflow rates were completed, while three 35 ^{o}F (1.7 ^{o}C) and two 28 ^{o}F (0.6 ^{o}C) frost/defrost tests were completed for each three-row coil.

Fan Performance Test

For this study, two different propeller fans were used for the two- or three-row fin staged coils. The fan models were REVCOR LA01EA025B and LA01EA024B, which were equipped with GE motor 5KCP39JG (1100 rpm, 1/4 hp) or 5KCP39EG (825 rpm, 1/5 hp), respectively.

During frosting tests, each of the fan/motor combinations was operated with three initial airflow points: high, medium and low. These were implemented by adjusting the input voltage of fan motor (Table 3.7).

Table 3.7 Input voltages of fan motor for different airflow rates (VAC)

	High	Medium	Low
Two-Row	208	178	137
Three-Row	208	140	108

To provide the simulation equations to PRCFM for the estimation of air-side pressure drop through the coil during frosting tests, it was necessary to get accurate fan performance curves. Fan tests were conducted with an Air Movement and Control Association (AMCA 1992) multi-nozzle inlet test chamber, as seen in Figures 3.33 and 3.34, at the Energy Systems Laboratory. The entire testing facility and measurement followed ANSI/AMCA Standard 210-85 (1985). To simulate the installation of a fan exhausting air from heat pump outdoor coil, the fan, together with the outdoor coil top cover, was mounted at the outlet of the test chamber without any outlet ducts (Figure 3.35). The testing fans exhausted air from the chamber outlet. The static pressure at the fan outlet was equal to the barometric pressure. The settling screens inside the chamber help to produce the uniform airflow and eliminate the swirls generated in the air stream.

For each of the test points, the pressure drop through the bank of nozzles, total pressure head before the fan, static pressure increment across the fan, power input for the fan motor, air dry-bulb temperature and relative humidity, and the barometric pressure were measured. The multi-nozzle facility allowed the flexibility of selecting nozzle combinations that matched the fan capabilities. To avoid the inaccuracy caused by the pressure drop measurement through the multi-nozzles, different multi-nozzle combinations were chosen to fit a variety of tested airflow rates. Table 3.8 below shows the proper measurement ranges of air volume flow rate corresponding to the nozzles with three diameters.

Figure 3.33 Multi-nozzle inlet fan test chamber at Energy Systems Laboratory

To chart fan air performance, tests at selected increments of volume flow rate were conducted. Both total and static fan pressures were measured. The input power of fan was not the same as the motor input power read by the watt meter. The motor calibration curve or motor efficiency should be used to get motor output power, which is equal to the fan input power, from watt input. The air dry-bulb temperatures and humidities were measured by T-type thermocouple grids and RH sensors, respectively, at the chamber entrance and exit (Figure 3.34). The data signals of each thermocouple were individually detected and then averaged by the data acquisition system. During all the fan tests, the differences between thermocouple mesh and glass thermometer were within $\pm 0.2^{o}C$. The pressure difference was measured by the inclined manometer with a readability of 0.01 inches of water. All the test instruments were calibrated before being used.

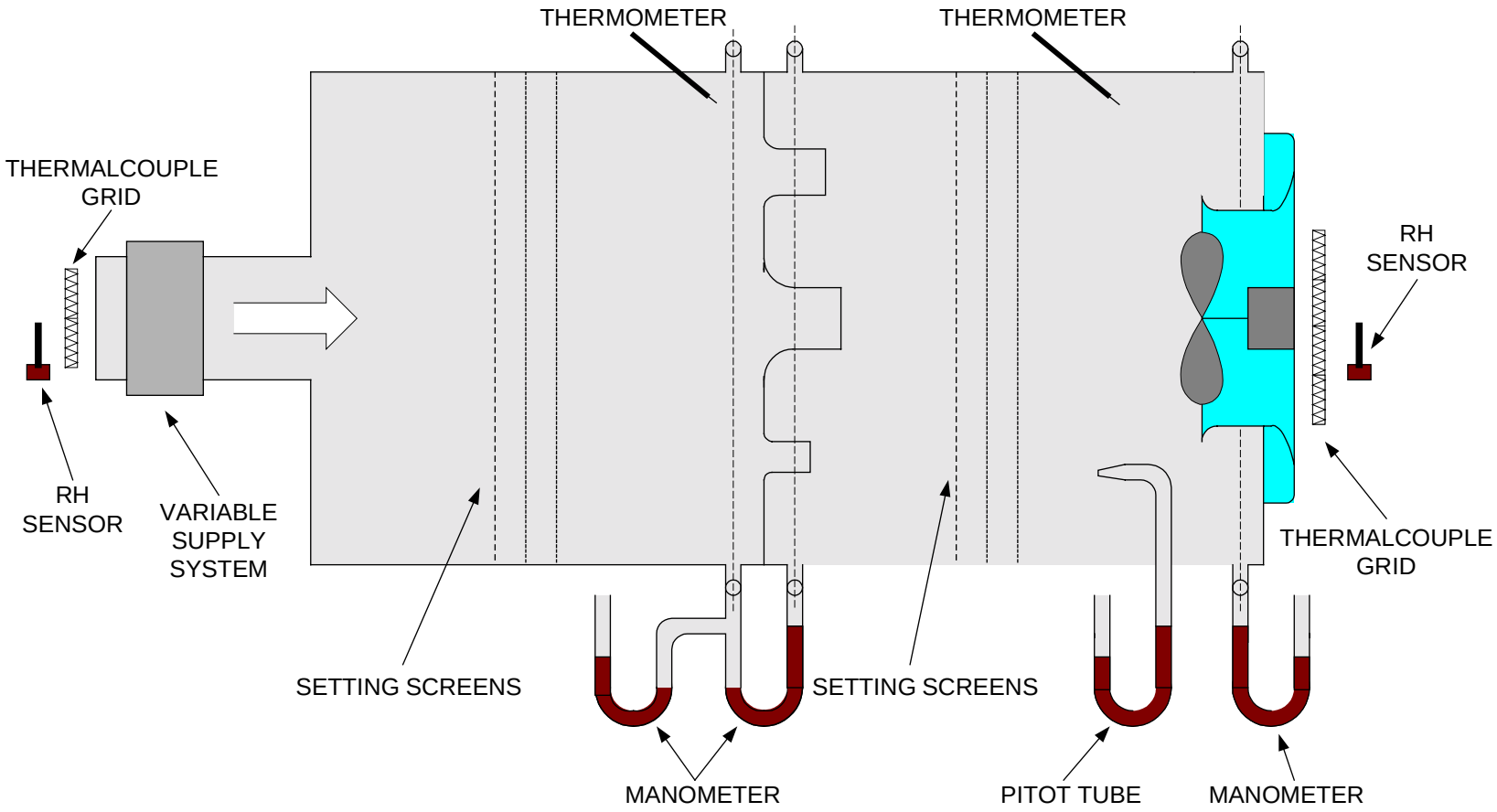

Figure 3.34 Schematic diagram of the multi-nozzle inlet fan test chamber

Table 3.8 Measurement ranges of the nozzles with different diameters

Nozzle (inch)	Throat Area (ft^2)	Measurable Flow Rate (cfm)
3.0314	0.049087	147-344
4.9663	0.136354	409-954
7.0080	0.267253	802-1871

The airflow for each test point was calculated by using the nozzle pressure drop and air density. The air pressure drop through the multiple-nozzle plate was read through the wall pressure taps by the manometer. The air density was determined by the dry-bulb temperature, relative humidity and barometric pressure. The sum of each nozzle flow rate was the volume flow rate of the test fan.

The static pressure and power consumption curves corresponding to three fan speeds for the two tested fans are shown in Figures 3.36 and 3.37. The fan power consumption increases as the flow rate reduces, which is similar to that of fan pressure. Because the air velocity head inside chamber was small (less than 0.0015 in. w.g.), the difference between the total and static pressures was neglected.

Figure 3.35 The fan and outdoor coil top cover mounted at the outlet of the test chamber

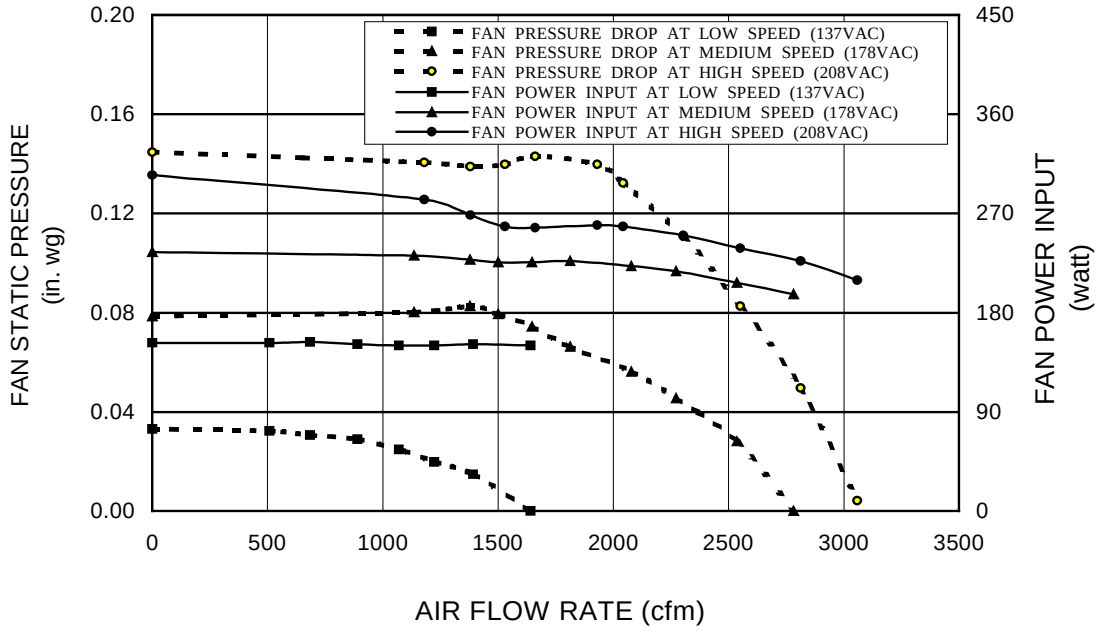

Figure 3.36 Static pressure and power consumption at three speeds for the two-row coil fan

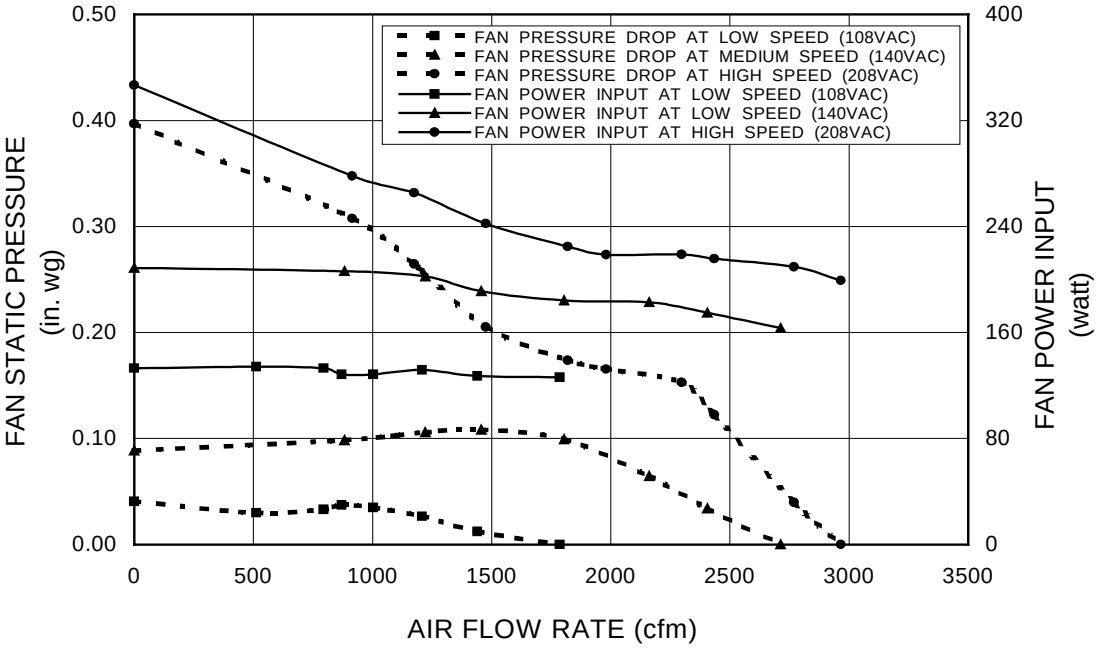

Figure 3.37 Static pressure and power consumption at three speeds for the three-row coil fan

CHAPTER IV

EXPERIMENTAL RESULTS

The objective of the experimental study was to quantify how the front staging fins would affect the frost/defrost performance of a heat pump evaporator under frosting conditions. In this chapter, some experimental data are summarized and discussed.

Frost Test Results

During the frosting tests, the heat pump unit with both baseline and fin staged outdoor coils under a variety of environmental conditions were tested. Frost was allowed to grow on the coils until the heating capacity of the condenser (indoor coil) degraded by 20%. Then, the evaporator was defrosted by reversing the cycle on the heat pump system.

Major variables measured for the outdoor coils included frost growth on the leading edges of front row, evaporating temperature, frost mass accumulation, airflow drop, energy transfer capacity, latent and sensible heat transfer, and airflow pressure drop across the frosting coil. Each of the data sets is presented in a variety of plots versus time.

In addition, with the data available, the effects of fin staging on the outdoor coil on the heat pump system performance are discussed as well. The major variables measured were total heat pump heating capacity (indoor coil capacity), coefficient of performance of heat pump unit, refrigerant flow rate, frost and defrost cycle times, and some other performance parameters of the heat pump system.

Frost Growth at the Leading Edges of the Coil Front Row

Frost formation on a fin surface is a complicated heat and mass transfer process. It is affected by a number of variables including the fin surface temperature, the ambient air temperature and humidity, the air flowing velocity through the passages between fin plates, fin geometry (fin spacing, fin type…), frost properties (density, thermal conductivity, tortuosity…), and time. In this experiment, the effects of fin staging on the frost growth at the leading edges of the test coils was studied with different fin spacing, air conditions, and airflow rates.

During the frost tests, the growth of the frost layer was monitored through video cameras from three locations on the outdoor coils under tests. Two video cameras were placed around the coil to inspect the leading edges of the front row fins, which belong to different circuits. Images were taken at regular intervals to record the frost growing with time. The frost growth on each image was measured, and the two frost heights from the images captured at the same time on two different positions were averaged to be the mean frost height on the fin leading edges at that moment. Another camera was placed inside the

"horse-shoe" shape coil to observe the frost formation at the trailing edges of the rear row fins of the outdoor coil. The frost growth on both the front leading and the back trailing edges of the test coils could be observed and measured.

The test started with the two-row baseline coil, which had a uniform fin density of 20 fins/inch (7.87 fins/cm) on both rows. Two 2-row fin staged coils were also examined. The first coil had a decreased fin density of 15 fins/inch (5.91 fins/cm) on the front row, while the second coil had the same fin density of 15 fins/inch (5.91 fins/cm) on the front row and a fin density of 25 fins/inch (9.84 fins/cm) on the second row.

The transfer of heat and mass at the leading edges of the coil front row fins are typically large and more frost accumulates at this part of the coil (Chen et al, 1999). The wider fin spacing on the front row of fin staged coils was expected to decrease the frost growth at the leading edge of the front row and increase frost formation on the rear part of the coil; and thus slow the airflow reduction due to the blockage of frost layer and allow the heat pump system to operate longer before having to start defrost cycle.

Figures 4.1 through 4.3 illustrated the behavior of frost growth on the leading edges of the three 2-row coils at different initial airflow. These airflow rates are marked in the figures as high 2800 cfm (79.3 m^3/min), medium 2200 cfm (62.3 m^3/min), and low 1400 cfm (39.6 m^3/min), which correspond to face velocities of 2312 fpm (70.4 m/min), 181fpm (55.3 m/min), and 116 fpm (35.2 m/min), respectively. The tests presented here with varying airflow rates were all conducted at the same outdoor air conditions of 35^{o}F (1.7^{o}C) dry bulb and 33^{o}F (0.6^{o}C) wet bulb temperatures.

For each outdoor coil tested, the trends of frost growth on the leading edges at different initial airflow rates were similar to each other. Reducing the initial airflow across the outdoor coil resulted in an increased frost growth on the leading edges of the coil frost row. The frost grew fastest for the low airflow and slowest for the high airflow. Reducing the airflow across the test coils also decreased the frost cycle time. For the two fin staged coils, both the frost cycles at the low airflow were less than half of those at the high airflow (Figures 4.2 and 4.3). During the frost/defrost tests, the frost cycles were terminated when the heating capacities of the heat pump indoor coil dropped by 20%. This provided a consistent termination of all the frost tests and made it possible to compare the frost cycle times.

During the frost tests of two fin staged coil at 35^{o}F (1.07^{o}C) dry bulb temperature, there occurred a "zero" frost growth process at the beginning of the tests, which was followed by a rapid growth thereafter until the termination of the frost cycle (Figures 4.2 and 4.3). This phenomenon became much more evident for the 15/25 fpi coil. The time periods of the "zero" frost growth process before frost started to grow rapidly were different for each airflow rate. The significant different between the baseline and fin staged coils could improve the frost performance of fin staged coils and prolonged the frost cycle time.

Due to the lack of information on the fin surface temperatures at the leading edges of the test coils, the exact reason for this "zero" frost growth process is not clear. It might be related to the relatively high fin temperatures at the leading edges and the nearly constant evaporating temperature at the early portion of the test. Clearly, if the fin surface temperatures at the leading edges was so high that it is at or above the dew (or frost) point of the incoming air stream, then there would be little or no condensation of moisture out of the air. No moisture would freeze above the freezing point. The local heat transfer coefficient for the front row should have decreased due to wider fin spacing.

These results indicated that the frost growth at the leading edges strongly depended upon the initial airflow rates. With the "zero" frost growth period at the early portion of the frost test, the fin staged coils, especially the 15/25 fpi coil, have evident advantages over the baseline 20/20 fpi coils.

The frost formation and growth was highly dependent on the ambient air conditions and initial airflow rates. Figures 4.4 through 4.9 show the effect of air temperature, humidity and airflow rate on the mean frost growth at the leading edges of both baseline and fin staged coils at two different test conditions and three airflow rates, respectively.

As the outdoor air conditions were lowered from the ANSI/ASHRAE (1995) test conditions of 35^{o}F (1.7^{o}C) dry bulb and 33^{o}F wet bulb temperatures (the corresponding relatively humidity is 82%) to 28^{o}F (-2.2^{o}C) dry bulb temperature and 90 % RH, the frost growth of both the baseline and fin staged coils increased and the improvement in frost cycle time due to staging fin was reduced. With decreasing air temperature and increasing humidity, the mass transfer between the fin surface and the air stream must be increased. These test results also indicated a moderate effect of airflow on the frost growth. As the airflow reduced, the growth rate of frost layer at the leading edges increased.

For the 20/20 fpi baseline coil, the rate of frost growth was approximately linear during both the 35^{o}F and 28^{o}F frost tests. This can be verified from Figures 4.4 through 4.9 by examining the slope of the frost height curves of the baseline coil.

The speed of frost growth for both fin staged coils varied with time during the whole frost test periods. Frost grew at a much slower rate than that on the baseline coil. At the 35^{o}F frost tests (Figures 4.4, 4.6 and 4.8), the frost growth rates at the leading edges of the two fin staged coils were slower at the early of the tests, and started to grow faster at the later part. Frost grew more rapidly at the end of the frost cycle. At the 28^{o}F frost tests (Figures 4.5 and 4.7), the frost growth progressed at a much faster rate, and the phenomenon with different length delays of frost growth at the early portion of the frost tests disappeared.

Fin staged coils with wider fin spacing at the front row provided longer operating time before defrost was needed. Comparing the fin staged coils and the baseline coil in Figures 4.4 and 4.5, which had the same initial airflow, temperature and relative humidity, the frost cycles of 15/20 fpi and 20/20 fpi coils stopped in 87 and 102 minutes compared to 50 minutes for 20/20 fpi baseline coil. Similarly, at 28^{o}F and

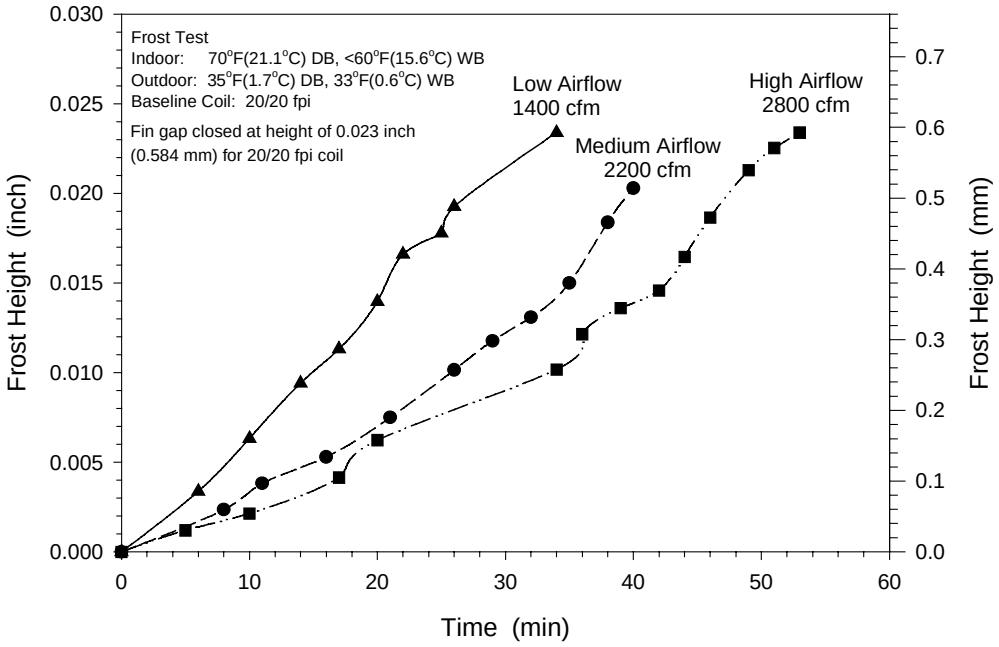

Figure 4.1 Leading edge frost growth of baseline coil (20/20 fpi) at different airflow during frost test at 35°F (1.7°C) dry bulb and 33°F (0.6°C) wet bulb temperatures

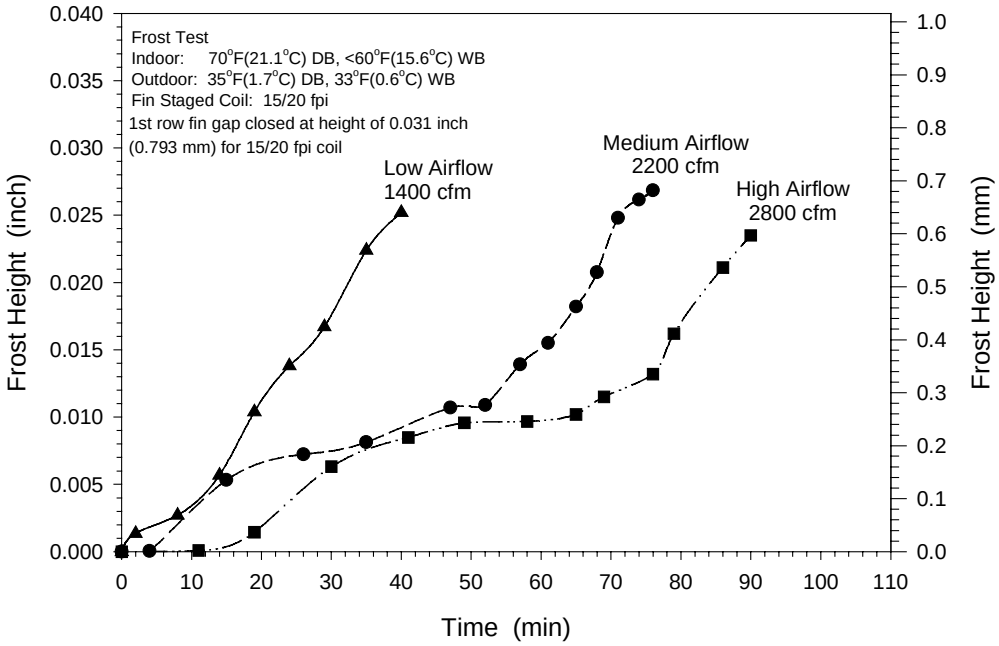

Figure 4.2 Leading edge frost growth of fin staged coil (15/20 fpi) at different airflow during frost test at 35°F (1.7°C) dry bulb and 33°F (0.6°C) wet bulb temperatures

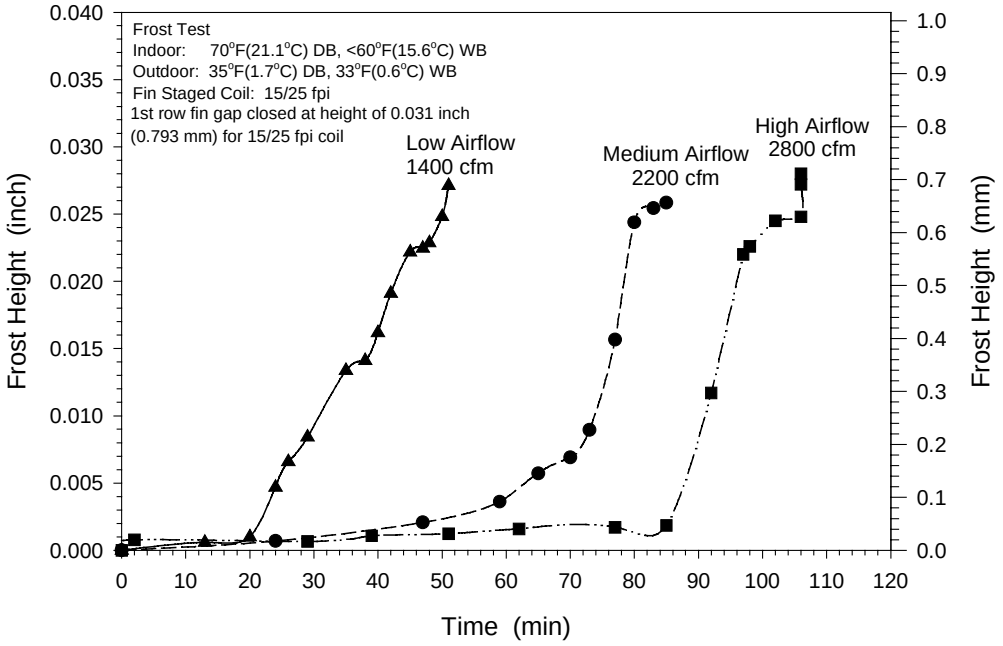

Figure 4.3 Leading edge frost growth of fin staged coil (15/25 fpi) at different airflow during frost test at 35°F (1.7°C) dry bulb and 33°F (0.6°C) wet bulb temperatures

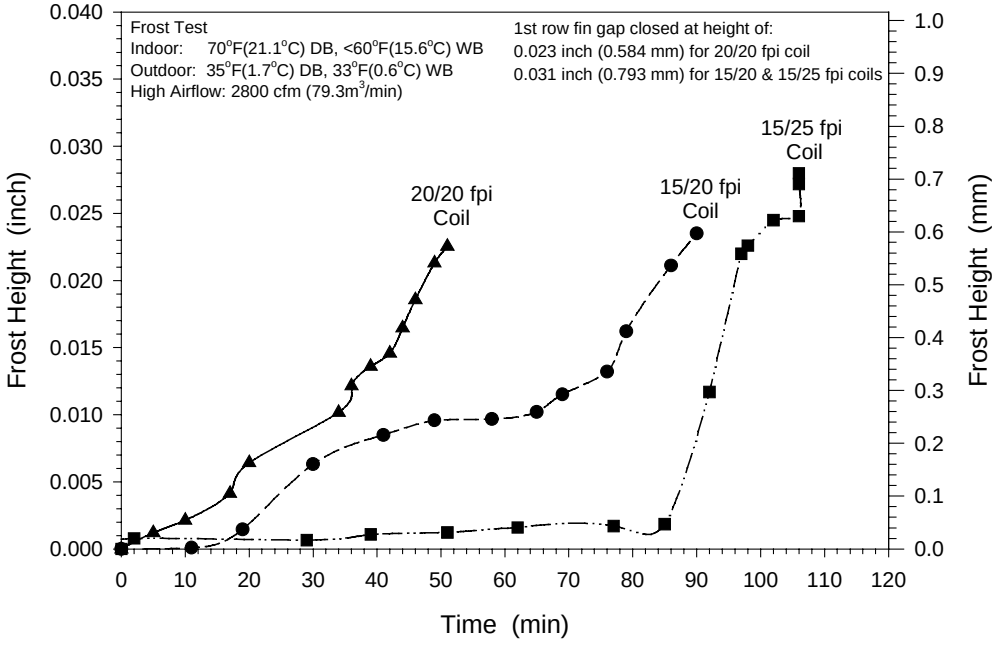

Figure 4.4 Leading edge frost height on the front row of three 2-row coils operating at 35°F (1.7°C) dry bulb and 33°F (0.56°C) wet bulb temperatures and high airflow 2800 cfm (79.3 m^3/min)

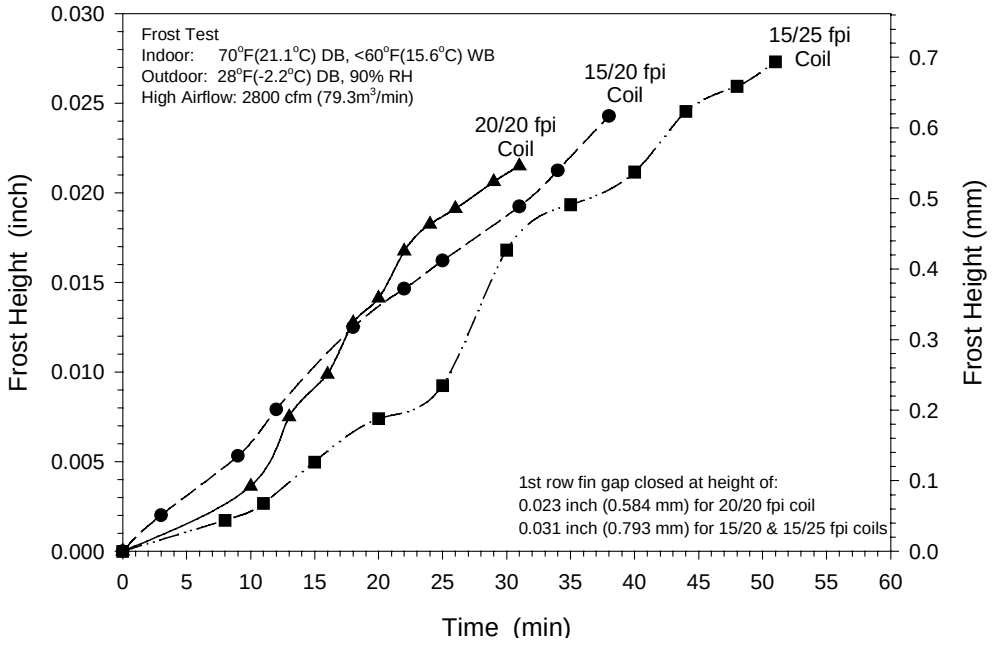

Figure 4.5 Leading edge frost height on the front row of three 2-row coils operating at 28°F (-2.2°C) dry bulb temperature and 90% relative humidity and high airflow 2800 cfm (79.3 m^3/min)

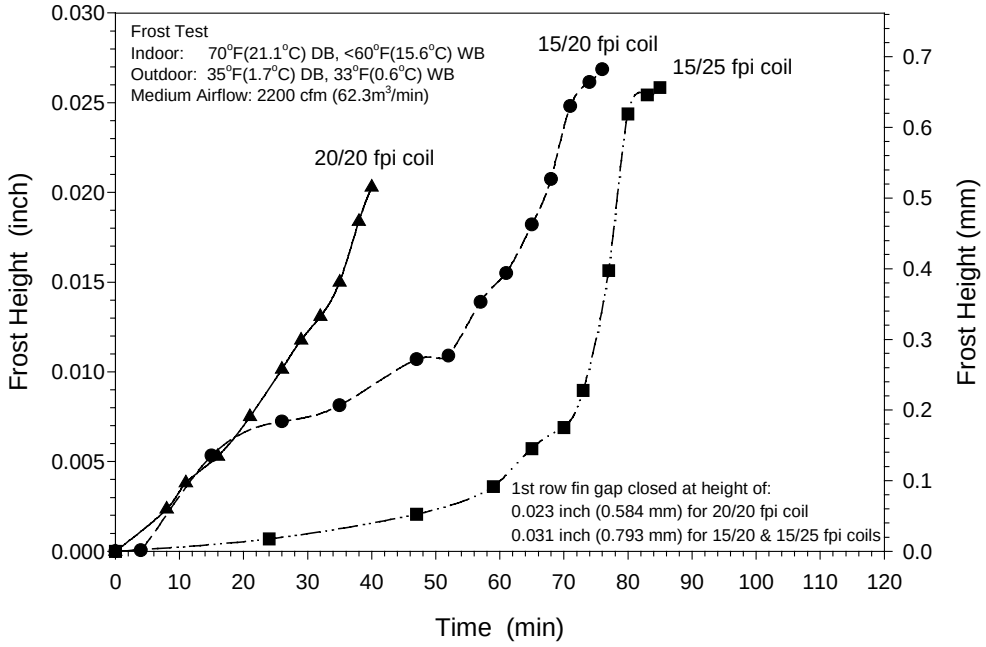

Figure 4.6 Leading edge frost height on the front row of three 2-row coils operating at 35°F (1.7°C) dry bulb and 33°F (0.56°C) wet bulb temperatures and medium airflow 2200 cfm (62.3 m^3/min)

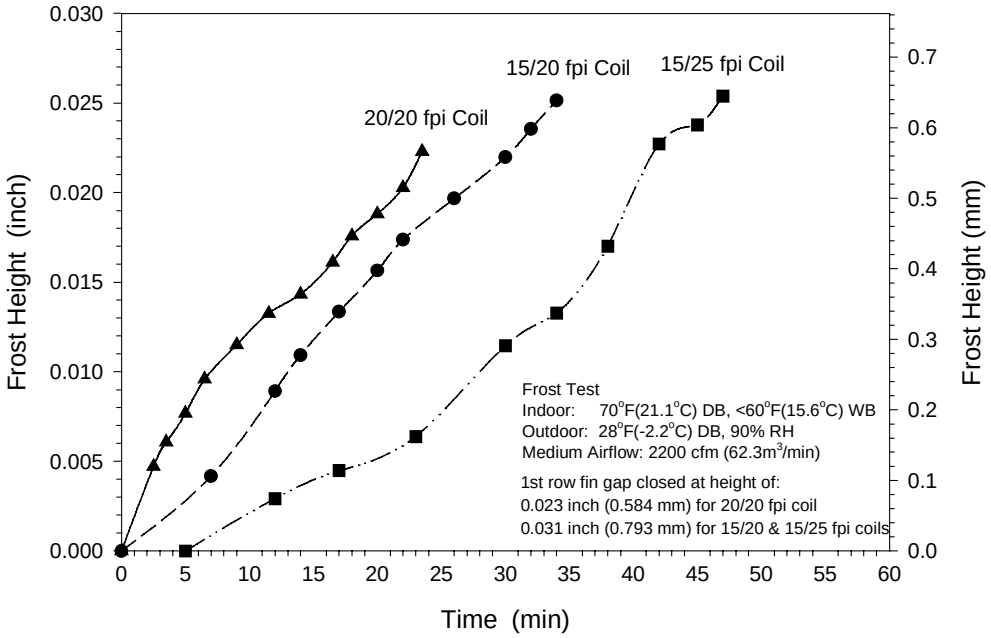

Figure 4.7 Leading edge frost height on the front row of three 2-row coils operating at 28°F (-2.2°C) dry bulb temperature and 90% relative humidity and medium airflow 2200 cfm (62.3 m^3/min)

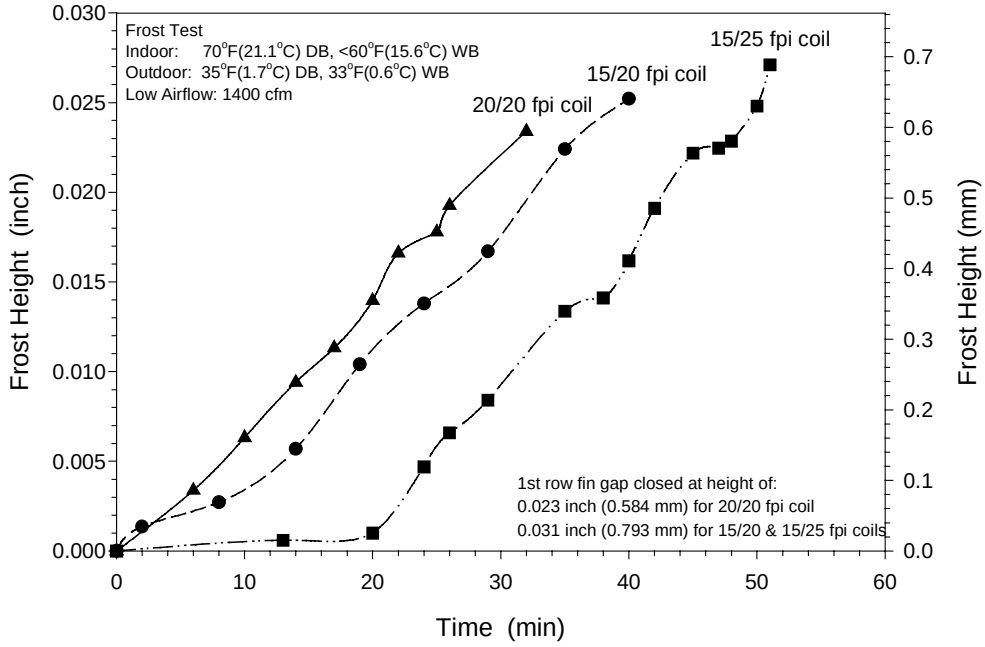

Figure 4.8 Leading edge frost height on the front row of three 2-row coils operating at 35°F (1.7°C) dry bulb and 33°F (0.56°C) wet bulb temperatures and low airflow 1400 cfm (39.6 m^3/min)

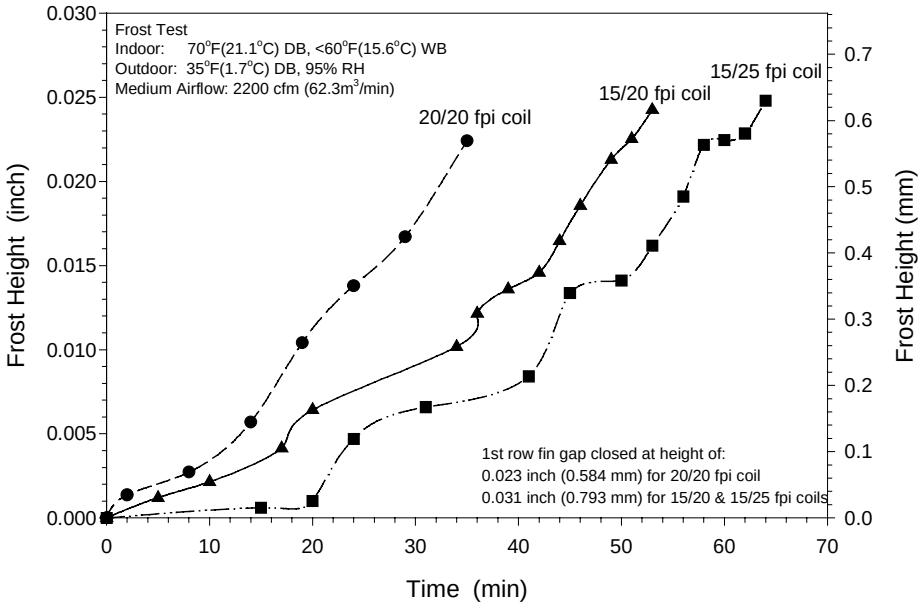

Figure 4.9 Leading edge frost height on the front row of three 2-row coils operating at 35°F (1.7°C) dry bulb temperature and 95% relative humidity and medium airflow 2200 cfm (62.3 m^3/min)

90% RH, the operating time for two fin staged coils were 38 and 50 minutes compared to 30 minutes for the baseline coil.

Frost growth on the leading edges of the two fin staged coils proceeded similarly. The frost always grew slightly slower for the 15/25 fpi coil than the 15/20 fpi coil. So, the 15/25 fpi coil had longest frosting time compared to the other fin staged coil and the baseline coil.

In addition, due to the wider fin spacing at the front row of the fin staged coils, the maximum heights that frost reached at the end of frost cycles for the fin staged coils were higher than those the baseline coil could reach. Based on the test results, during most of frost tests for the baseline coil with 20/20 fpi, the leading edges were visually completely blocked when the tests stopped while there still existed some gaps between two neighboring frost layers for the fin staged coils at the end of the frost tests.

Figure 4.9 shows the frost growth on the coils with different fin spacing at the same conditions of the tests presented in Figure 4.6 excepted increasing the air relative humidity (RH) from 82% (35°F DB & 33°F WB) to 95%. The baseline coil and two fin staged coils were tested with the same initial airflow rate of 2200 cfm (62.3 m^3/min), which corresponded to a face velocity of 181 ft/min (55.3 m/min). This allowed to examine the individual effect of air humidity on the frost growth.

As the relative humidity of air flowing through the test coil increased from 82% RH to 95% RH, there was a corresponding increase in the frost growth rate at the leading edges. For instance, in Figure 4.6 at 82% RH, the frost layer of 15/25 fpi coil grew from 0 to 0.025 inch in almost 80 minutes, while it took 65 minutes for the same fin staged coil to reach the 0.0225 inch frost height at 95% RH. Higher air humidity increased the difference of water vapor concentration between the surface of the frost layer and the air stream. So, a higher air humidity yielded an increase in frost growth rate.

For the 82% RH tests, as shown in Figure 4.6, the frost growth of the two fin staged coils were slower during the first 50 to 60 minutes, respectively, and rapidly increased after that. For the 95% RH tests, as shown in Figure 4.9, the frost growth of the fin staged coils was more rapidly. The frost height at the leading edges of the baseline coil grew steadily with time for both the 82% and 95% RH tests. There was no delay of frost growth at the early part of the test period. At a given dry-bulb temperature of 35^{o}F (1.7^{o}C) and medium airflow, when the relative humidity was increased from 82% to 95%, the improvement of frost performance of the fin staged coils decreased because of the increased frost growth rate at the extremely high 95% RH.

Based on these experimental results, the fin staged coils slowed the frost growth on the leading edges of the front row and prolong the frost cycle time. Lower airflow, a lower air temperature, higher air humidity and smaller fin spacing lead to more frost accumulated on the leading edges of both baseline and fin staged coils.

It was difficult to measure the variation of frost growth inside the test coils with the traditional vision cameras. No information on frost growth along the length of the fin surface was provided on this experimental study. The video camera setup inside the coil revealed that there was no frost formation on the trailing edges of the coil rear rows through all the frost tests. The trends of the measured frost growth at the leading edges of the coils may not be able to represent the frost layer grew over the whole coil surface. Any analysis of the overall frost accumulation on the test coils has to be made based on the measurement of frost mass accumulation with time.

Evaporating Temperature

Due to the transient characteristics of the freezing process, most of dynamic variables of the outdoor coil change with time during the frost tests. The evaporating temperature is one of these variables. It is an important factor that affects the frost growth on the surface of the evaporator. Knowing the variations of the evaporating temperature would help in understanding the frost growth process and trends observed in the tests. The evaporating temperature in this study was the saturated temperature corresponding to the outlet pressure of the evaporator and would represent the lowest refrigerant temperature in the evaporator.

In Figures 4.10 to 4.12, the variations of the evaporating temperature at different initial airflow during frosting are shown. After the startup of the heat pump system, the evaporating temperature climbed to a peak value due to the increased heat/mass convection and surface roughness at the initial period of frost formation. Later, the evaporating temperature tended to stabilize round a temperature for a period of time. In the last part, the evaporating temperature had a substantial drop before the end of frost cycle.

The oscillations of the evaporating temperature curves toward the later parts of the frost tests were caused by “hunting” of the thermal expansion valve (TXV). System operation was stable with the outdoor TXV under normal operation. However, as the airflow through the evaporator dropped, system

performance became unstable and the evaporating temperature and pressure started to vary. Due to this "hunting" phenomenon of the TXV, the plots of other variables discussed later also showed similar trends in the last portion of the frost buildup period.

When frost formed on the outdoor coil of heat pump system, the operating temperature of evaporator tended to decline continuously. The evaporator heat transfer rate increased with decreasing evaporating temperature and the rate of frost accumulation also increased with the declining evaporating temperature of other variables kept constantly. Frost accumulation decreased the evaporator heat transfer rate, which caused the superheat at the outlet of evaporator to decrease. To hold a constant superheat, the TXV reduced the refrigerant flow rate. Meanwhile, the enhanced throttling caused more pressure drop of refrigerant through the TXV. Therefore, both the temperature and pressure of the two-phase refrigerant inside the evaporator declined.

The high airflow increased the average evaporating temperature and delayed the drop of evaporating temperature while the low airflow accelerated this process. For example, in Figure 4.12, the average evaporating temperatures of the fin staged coil with 15/25 fpi were 13.7 ^{o}F (-10.1 ^{o}C), 13.6 ^{o}F (-10.2 ^{o}C), and 9.8 ^{o}F (-12.3 ^{o}C) for the high, medium and low airflow at the 35 ^{o}F (1.7 ^{o}C) dry-bulb and 33 ^{o}F (0.6 ^{o}C) wet-bulb test temperatures. The evaporating temperature at low airflow decreased from 13.5 ^{o}F (-10.3 ^{o}C) to 2.5 ^{o}F (-16.4 ^{o}C) in 50-minute frost formation process while at high airflow it took 99 minutes to reduce the evaporating temperature from 17.5 ^{o}F (-8.1 ^{o}C) to 2.0 ^{o}F (-16.7 ^{o}C).

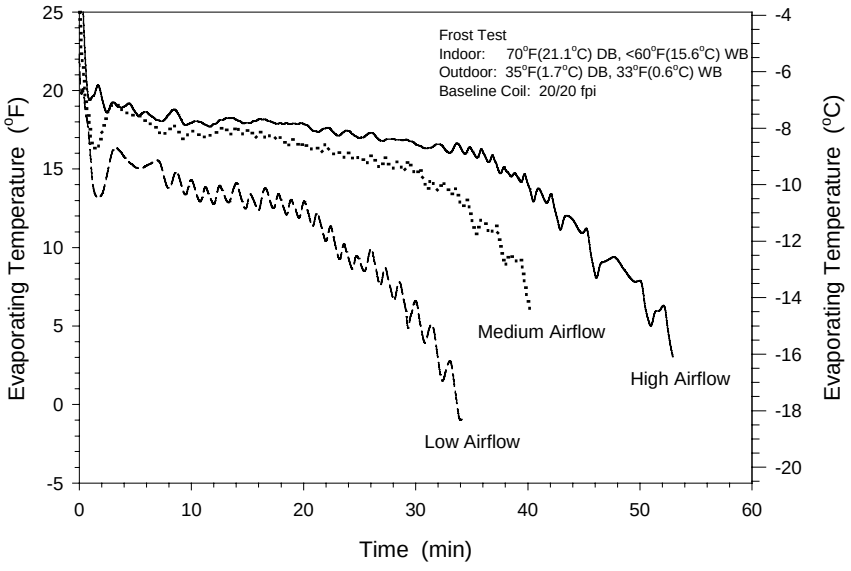

Figure 4.10 Variations of evaporating temperature of baseline coil (20/20 fpi) during different airflow frost tests at 35^{o}F (1.7^{o}C) dry bulb and 33^{o}F (0.6^{o}C) wet bulb temperatures

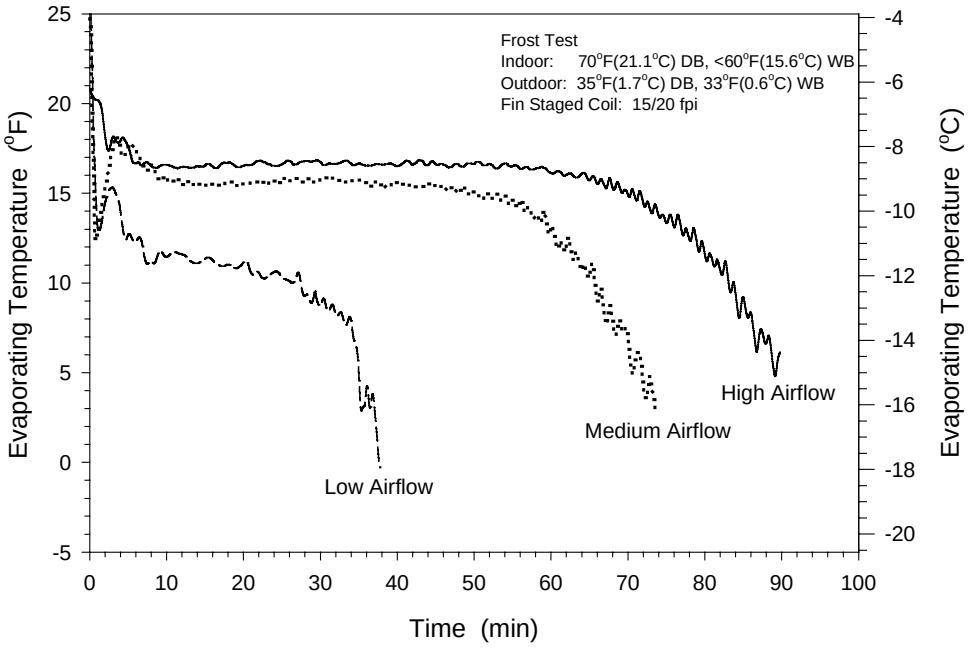

Figure 4.11 Variations of evaporating temperature of fin staged coil (15/20 fpi) during different airflow frost tests at 35°F (1.7°C) dry bulb and 33°F (0.6°C) wet bulb temperatures

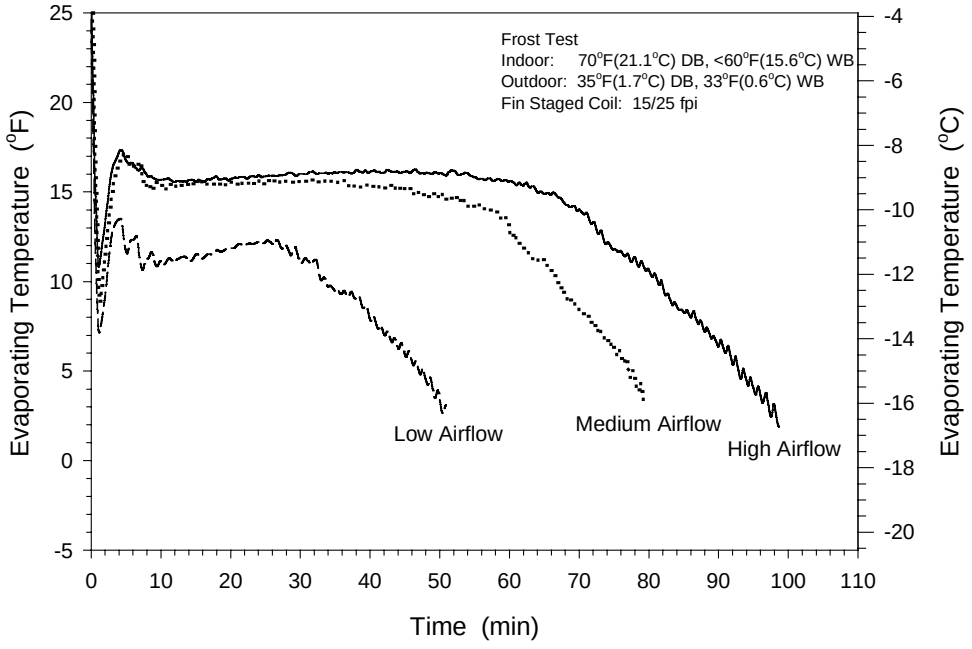

Figure 4.12 Variations of evaporating temperature of fin staged coil (15/25 fpi) during different airflow frost tests at 35°F (1.7°C) dry bulb and 33°F (0.6°C) wet bulb temperatures

In addition, with the decrease of airflow, the stable period for the evaporating temperature also decreased. For the fin staged coil with 15/25 fpi, the evaporating temperature at the high airflow could stabilized around 16 ^{o}F (-8.9 ^{o}C) for almost 55 minutes while at low airflow it could hold at 11 ^{o}F (-11.7 ^{o}C) for only 25 minutes before the abrupt falling down. There existed a 5 ^{o}F (2.8 ^{o}C) temperature gap between low and high airflow.

The surface temperature of the heat exchanger was partially determined by the refrigerant temperature inside the heat exchanger tubes. During the frost tests, as the evaporating temperature decreased, so did the coil surface temperature, which was expected to have the same trends as the evaporating temperature. The driving potential for moisture transport during the frost buildup process is the difference between the humidity ratio of the air and the saturated humidity ratio corresponding to the temperature at the surface of frost covered coil. A reduction in the coil surface temperature should decrease the humidity ratio corresponding to that surface temperature, which causes an increase in the air to surface humidity ratio difference. This could increase the frost deposition on the coil surface.

Low airflow, shown in Figures 4.10 to 4.12, lowered the evaporating temperature and accelerated the decline in the evaporating temperature. Thus, the lower evaporating temperature caused a lower coil surface temperature, which promoted the early formation of frost and accelerated the frost buildup process. On the other hand, by increasing the evaporating temperature, high airflow decreased the rate of frost formation and promoted longer frost cycle times. These could be used to explain the frost growth trends at the coil leading edges shown in Figures 4.1, 4.2 and 4.3.

Figures 4.13 through 4.18 compare the variations of evaporating temperature for the three 2-row coils at different test conditions. Typically, the evaporating temperature of the baseline coil had larger initial peak values and faster declination during the frost tests when compared to the fin staged coils. The variations of evaporating temperature of the two fin staged coils were similar and much slower. At 35^{o}F (1.7^{o}C) dry-bulb and 33^{o}F (0.6^{o}C) wet-bulb temperatures, as shown in Figure 4.13, the baseline coil had a maximum peak temperature of 20^{o}F (-6.7^{o}C) among the three test coils. After about 35-minute, the evaporating temperature of the baseline coil fell sharply below those of the fin staged coils. Apparently, the two fin staged coils had much longer periods with relatively constant evaporating temperatures compared to the baseline coil.

The test results at different air temperatures, shown in Figures 4.13 through 4.16, also demonstrate the faster drop in evaporating temperature as frost formed on the evaporator at the colder air dry-bulb temperature of 28^{o}F (-2.2^{o}C). The evaporating temperature of the baseline coil dropped from 16^{o}F to -3^{o}F (-8.9^{o}C to -19.4^{o}C) at 28^{o}F (-2.2^{o}C) frost test in 31 minutes (Figure 4.14). However, it took nearly 52 minutes during 35^{o}F (1.7^{o}C) frost test for the evaporating temperature of the baseline coil to drop from 20^{o}F to 3^{o}F (-6.7^{o}C to -16.1^{o}C) in Figure 4.13.

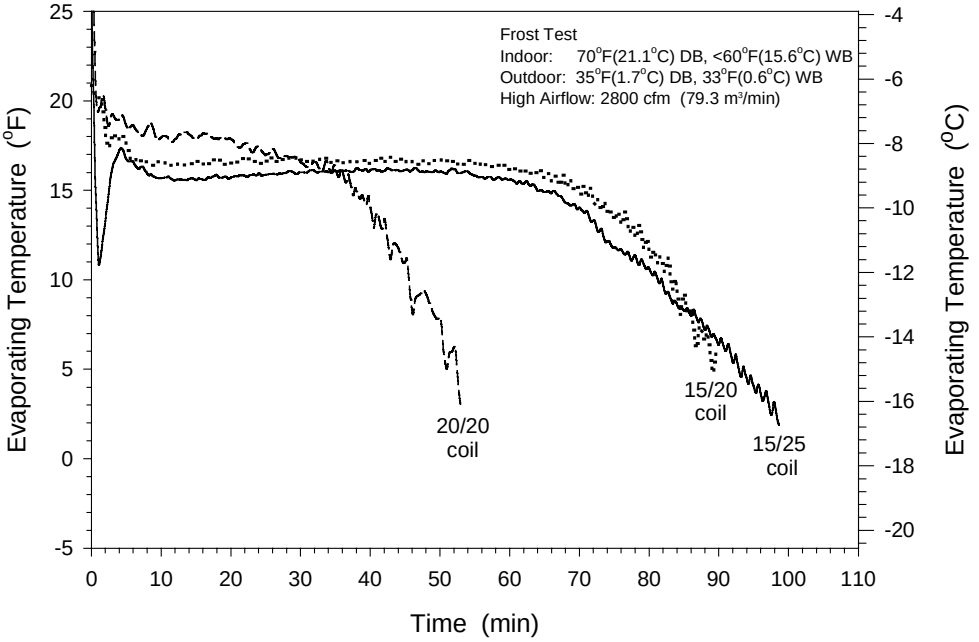

Figure 4.13 Variations of evaporating temperature of three 2-row coils during high airflow frost test at 35°F (1.7°C) dry bulb and 33°F (0.6°C) wet bulb temperatures

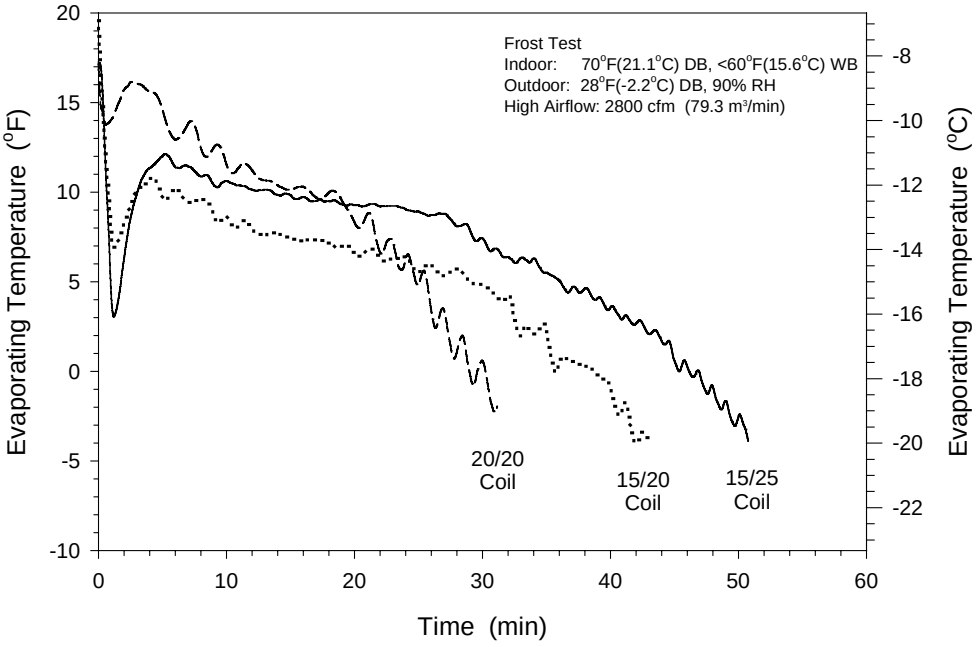

Figure 4.14 Variations of evaporating temperatures of three 2-row coils during high airflow frost test at 28°F (-2.2°C) dry bulb temperature and 90% relative humidity

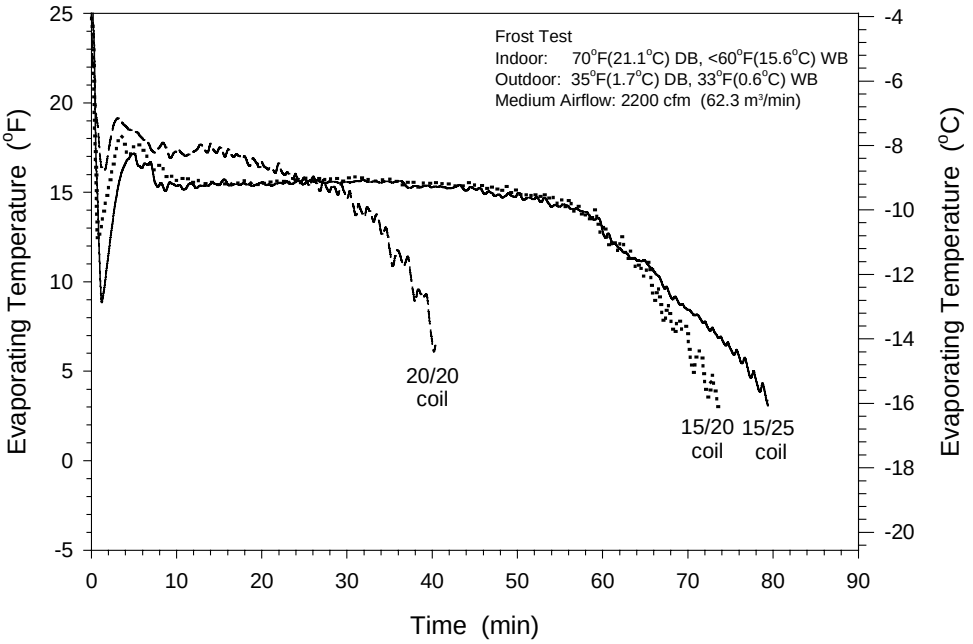

Figure 4.15 Variations of evaporating temperature of three 2-row coils during medium airflow frost test at 35°F (1.7°C) dry bulb and 33°F (0.6°C) wet bulb temperatures

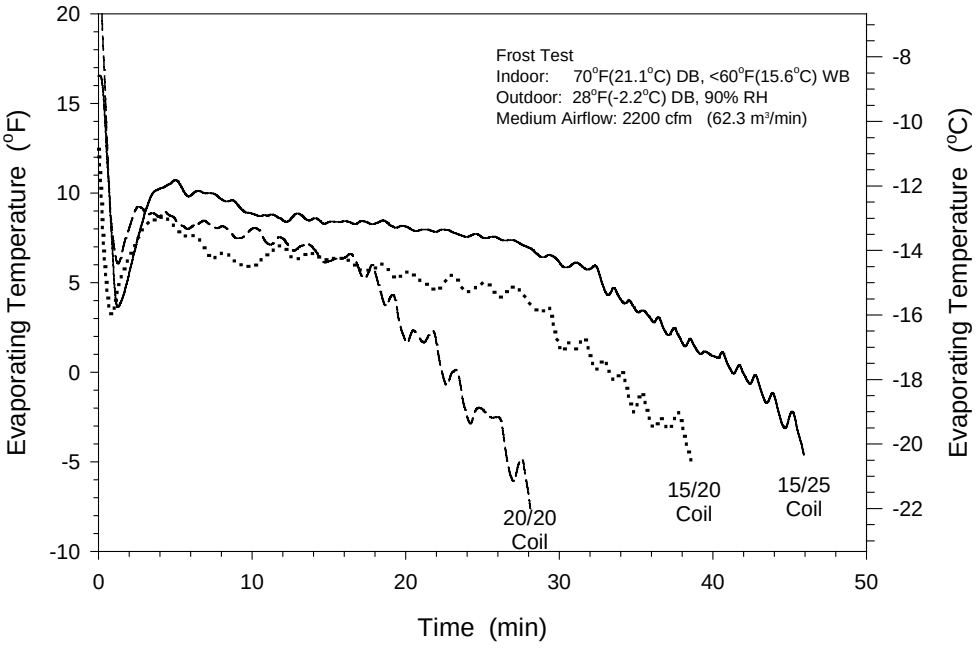

Figure 4.16 Variations of evaporating temperature of three 2-row coils during medium airflow frost test at 28°F (-2.2°C) dry bulb temperature and 90% relative humidity

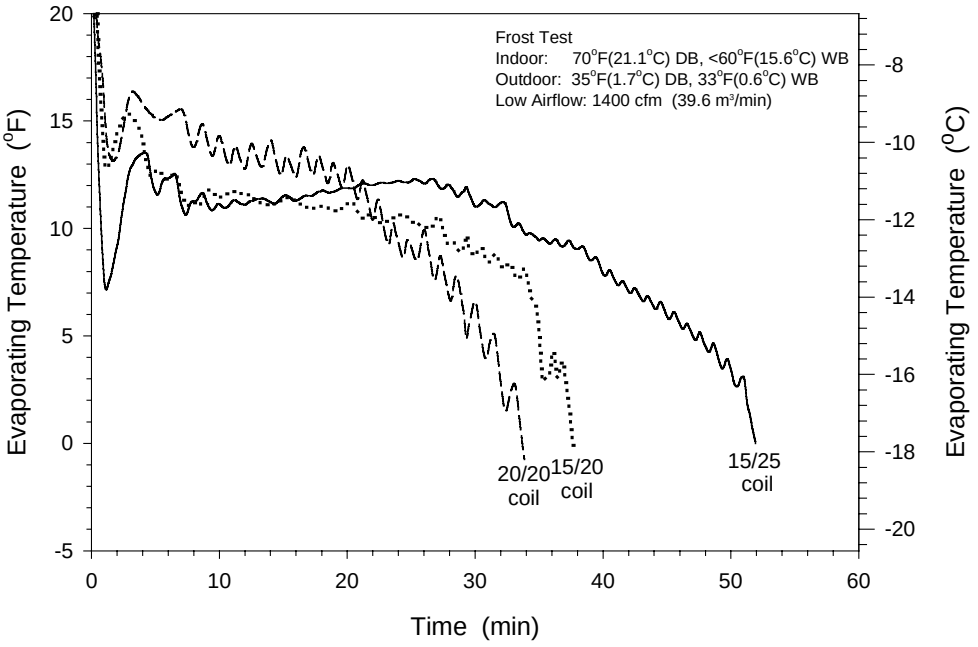

Figure 4.17 Variations of evaporating temperature of three 2-row coils during low airflow frost test at 35°F (1.7°C) dry bulb and 33°F (0.6°C) wet bulb temperatures

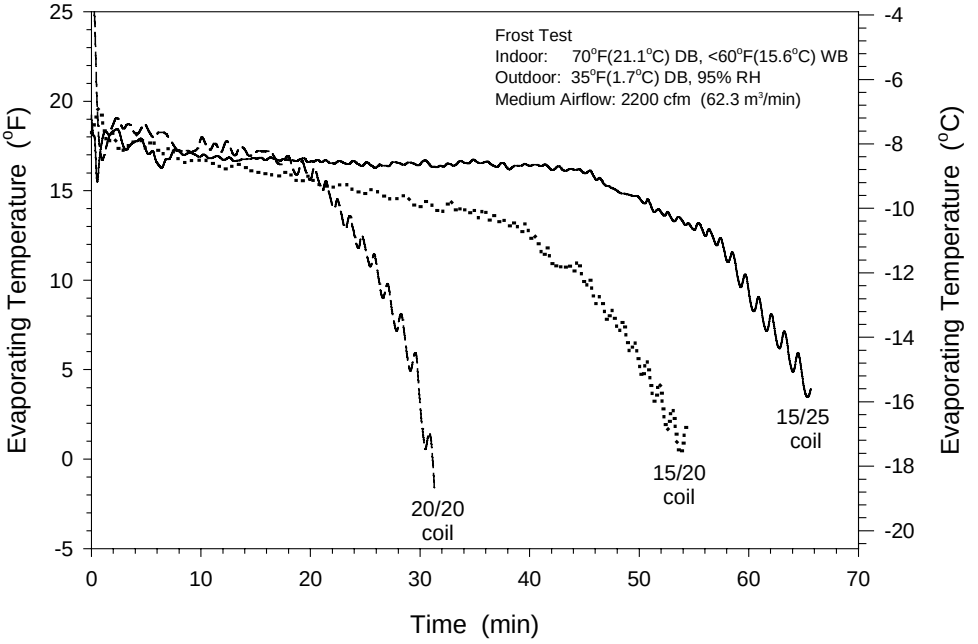

Figure 4.18 Variations of evaporating temperature of three 2-row coils during medium airflow frost test at 35°F (1.7°C) dry bulb temperature and 95% relative humidity

The faster drop in evaporating temperature of the baseline coil accelerated the frost growth whereas the longer periods with relatively constant evaporating temperature of the two fin staged coil delayed the frost growth and prolonged the frost cycle time. The accelerated growth trends of frost height on the coil leading edges at the later portion of the frost tests were related to the substantial drop of evaporating temperature during the same period of time.

Frost Mass Accumulation and Airflow Rate

During the frost tests, the static pressure existing the outdoor coil was maintained at approximately zero to simulate the free discharge condition during the real application of heat pump outdoor unit. This allowed the airflow across the outdoor coil to decrease normally as the coil was being covered with frost. The decrease in airflow was caused directly by the blockage of frost formed on the fin surface. Meanwhile, the decreasing airflow accelerated the frost growth. The frost mass accumulation could be estimated using the air mass flow and the change in moisture content of the air stream as it passed through the outdoor coil at each scan time interval of the DAQ system. Because the frost mass accumulation and the airflow were related to each other, the variations of both variables during the same frost test are shown in one plot.

Detailed data on the variations of airflow and frost mass accumulation with different initial airflow for three 2-row coils are presented in Figures 4.19, 4.20 and 4.21, respectively. The increase of frost mass accumulation on the coil surface was approximately linear with time. For the same entering air conditions and elapsed time, frost mass grew fastest at the low airflow and slowest at the high airflow. The longer the frost test continued, the more frost built up. For instance, as shown in Figure 4.21, the total frost mass accumulation of the fin staged coil with 15/25 fpi was 7.9 lb_m (3.58 kg) at the end of 98-minute high airflow test. The amount of frost mass accumulation were 6.9 lb_m (3.13 kg) and 5.5 lb_m (2.49 kg) at the 79-minute medium and 51-minute low airflow tests, respectively. The overall trends of the data in Figures 4.19 through 4.21 show that increasing the initial airflow through the evaporator decreased the rate of frost mass accumulation and prolonged the frost cycle time. This indicated that increasing airflow could benefit the frosting operation of heat pump evaporator. However, the trade-off was that more frost needed to be melted during the defrost cycle.

The increased airflow improved the heat and mass transfer between the air stream and coil surface, which tended to increase the rate of frost mass accumulation. However, as the initial airflow was increased, there was a corresponding rise in the evaporating temperature in Figures 4.10 through 4.12, which in turn produced higher coil surface temperature and tended to reduce the potential of frost growth. Thus, the two counteracting factors affected the frost growth of the evaporator. From the test results shown in Figures 4.19 through 4.21, it could be observed that at the lower airflow rate, the frost growth was faster. So, the evaporating temperature was the more dominant one of the two factors during the frost tests.

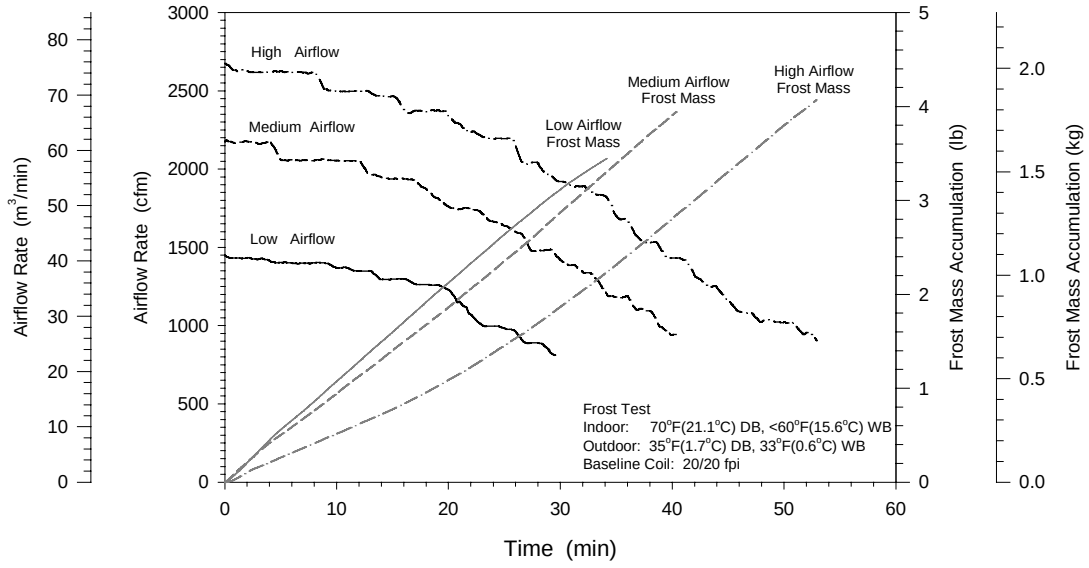

Figure 4.19 Variations of airflow and frost mass accumulation for baseline coil (20/20 fpi) during different initial airflow frost tests at 35°F (1.7°C) dry bulb and 33°F (0.6°C) wet bulb temperatures

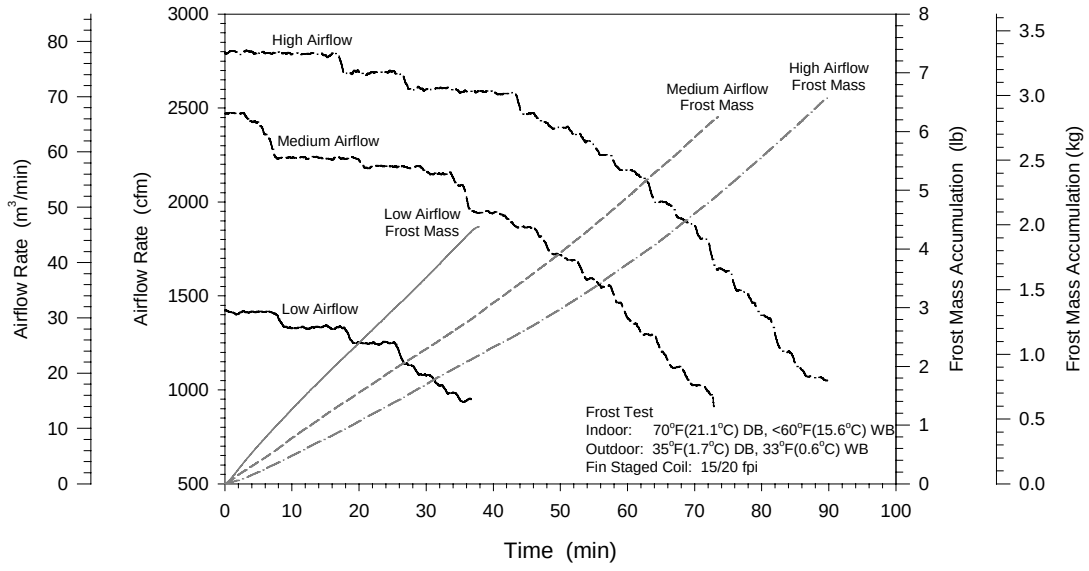

Figure 4.20 Variations of airflow and frost mass accumulation for fin staged coil (15/20 fpi) during different initial airflow frost tests at 35°F (1.7°C) dry bulb and 33°F (0.6°C) wet bulb temperatures

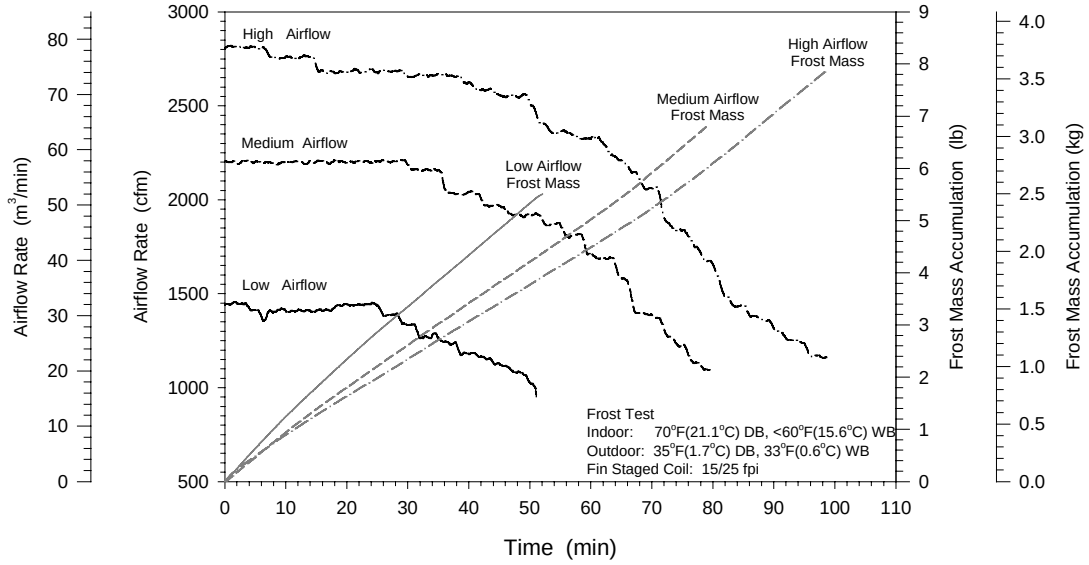

Figure 4.21 Variations of airflow and frost mass accumulation for fin staged coil (15/25 fpi) during different initial airflow frost tests at 35°F (1.7°C) dry bulb and 33°F (0.6°C) wet bulb temperatures

For both fin staged coils, from the beginning of frost test, the frost mass accumulation started to increase in a relatively constant rate like the baseline coil even though the test results in Figures 4.2 and 4.3 indicated that the fin staged coils delayed the frost growth on the coil leading edges. This implied that staged fins successfully shifted frost growth to locations away from the leading edges of the front row.

If the frost density is assumed to be unchanged, the trends of total frost mass accumulation would be the same as that of the average frost height overall the coil surfaces. Apparently, the direct impact of the frost growth on the coil was to block the air passages between the adjacent fins and reduce the airflow across the evaporator covered with frost. Figures 4.19, 4.20 and 4.21 also show how the airflow at different initial flow rates decreased with frost growth.

The outdoor airflow fell as frost grew on the coil surface. The airflow showed an accelerated drop at all three initial airflow rates. The airflow drop across the outdoor coil was a variable that directly correlated to the frost growth and its blockage to the airflow. The falling airflow produced a lower refrigerant temperature in the evaporator. The more rapid frost growth caused by the lower evaporator temperature would accelerate the rate of blockage and the reduction of airflow. In addition, at the early

time of frost growth, the airflow decreased slowly with time. This made it possible for the evaporating temperature shown in Figures 4.10 to 4.12 to remain approximately constant for a relatively long period of time.

The three 2-row coils were examined at 35 ^{o}F (1.7 ^{o}C) dry-bulb and 33 ^{o}F (0.6 ^{o}C) wet-bulb temperatures with the initial airflow rates of 2800 cfm (79.3 m^3/min), 2200 cfm (62.3 m^3/min), and 1400 cfm (39.6 m^3/min), respectively. The drop in airflow was dramatic as the coil frosted up. For the baseline coil during high airflow test at 35 ^{o}F dry-bulb and 33 ^{o}F wet-bulb temperatures, airflow dropped 66% from a peak value of 2675 cfm (75.7 m^3/min) to 903 cfm (25.6 m^3/min). At medium and low airflow rates, the drop was 57% and 60%, respectively. The average airflow rates were 1252 cfm (35.4 m^3/min), 1709 cfm (48.4 m^3/min), and 1957 cfm (55.4 m^3/min) corresponding to high, medium and low initial airflow. The defrost cycle was initiated when the heating capacity of indoor coil dropped by 20% from the peak heating capacity. The test results discussed above reveal that a 20% reduction in heating capacity corresponded to almost 60% drop in outdoor coil airflow at three different initial airflow rates.

Reducing the evaporator airflow always decreased the frost cycle time. For example, for the 20/20 fpi baseline coil, reducing the airflow by 50% from 2800 cfm (79.3 m^3/min) to 1400 cfm (39.6 m^3/min) shortened the frost cycle time from 53 to 34 minutes, which is shown in Figure 4.19. This trend of reduction in the frost cycle time was even more evident for both fin staged coils in Figures 4.20 and 4.21. The lower airflow produced a faster frost growth, especially, at the leading edges of the coil front row, and thus increased the blockage of the frost layer on the airflow and reduced frost cycle time. Therefore, the lower airflow had a faster drop in airflow and shorter frost cycle time. The faster drop of airflow and the resulting decrease in frost cycle time are the main reasons that low airflow across the outdoor coil under frosting conditions should be avoided.

Figures 4.22 through 4.27 provide the variations of frost mass accumulation on the three 2-row coils with respect to time. The rates of frost mass accumulation were always stable for both baseline and fin staged coils at different test conditions and airflow rates. The growing trends of frost mass accumulation for the baseline coil were less linear compared to the two fin staged coils. Although with the declination of airflow, the mass transfer between the air stream and coil surface tended to decrease, the fast drop of the evaporating temperature counteracted this decreasing trend of frost mass accumulation and kept the frost accumulation increasing consistently.

For each coil, the longer the frost cycle continued, the more frost built up. Frost accumulations of the two fin staged coils were significant more than that of the baseline coil due to longer frosting times. The final frost accumulation of the fin staged coil with 15/25 fpi was always maximum. It needed more time and energy to melt during the defrost cycle. For the high airflow tests at 35 ^{o}F (1.7 ^{o}C) dry-bulb and 33 ^{o}F (0.6 ^{o}C) wet-bulb temperatures, the total frost accumulation for the fin staged coil with 15/20 fpi was 6.6 lbm (2.99 kg), 43.5% higher than the 20/20 fpi baseline coil's 4.1 lbm (1.86 kg), while the total frost

mass was 7.8 lbm (3.54 kg), which was 90% more than that of the baseline coil (Figure 4.22). Apparently, the fin staged coils allowed more amounts of frost accumulated on the coil surface before the heating capacity of indoor coil dropped 20%.

The 20/20 fpi baseline coil and the 15/25 fpi fin staged coil had the same amount of total fin surface and the 15/20 fpi fin staged coil had 12.5% less fin surface. However, no trend could be found from the test results that the coil with more fin surface had a higher rate of frost mass accumulation. When correlating the variations of evaporating temperature with frost mass accumulation, it could be seen that the evaporating temperature directly affected the rate of frost formation. For example, in Figure 4.13, the evaporating temperature of the 15/20 fpi coil was slightly higher than that of the 15/25 fpi coil whereas, in Figure 4.25, the corresponding rate of frost mass accumulation and airflow rate for the 15/20 fpi coil was always less than those of the 15/25 fpi coil. This implied that the lower evaporating temperature, instead of the larger fin surface on the second row, was the major reason that caused the faster frost mass accumulation in these tests. This also indirectly demonstrates the assumption that more frost accumulated on the front row. Evaporating temperature could be used to explain the difference of frost accumulation rate between 15/20 fpi and 15/25 fpi coils in other tests. Although the 20/20 fpi coil had 33% more fin surface on the front row than the 15/20 fpi coil, the higher evaporating temperature and lower airflow rate of the 20/20 fpi coil at the first 23 minutes, as shown in Figure 4.13, made it impossible for the 20/20 fpi coil to frost faster than 15/20 fpi coil. The accelerated growth of frost on the 20/20 fpi coil after 23 minutes was caused by the substantial drop of evaporating temperature shown in Figure 4.13. It should be noted here that the thermal insulation of the frost layer and the temperature difference between the refrigerant and frost surface temperature reduced the potential for frost formation due to the substantial drop of evaporating temperature at the later period of the test.

Figures 4.23 and 4.25 show the effects of decreasing air temperature and increasing relative humidity from 35 ^{o}F dry-bulb temperature and 82% RH to 28 ^{o}C dry-bulb temperature and 90% RH. The lower evaporating temperature and higher relative humidity of the supply airflow at 28 ^{o}F frost tests encouraged faster frost accumulation and blockage of airflow. Additionally, because the air temperature was below the freezing point during the 28 ^{o}F (-2.2 ^{o}C) test, moisture condensing out of the air should more readily freeze when contacted on the coil surface. At 28 ^{o}F dry-bulb temperature and 90% relative humidity (Figure 4.23), the frost growth rate of frost mass for the baseline coil was slowest among the three test coils. After only 31 minutes the frost cycle stop with 2.2 lb_m (1.00 kg) frost accumulation. The 15/20 fpi fin staged coil had the fastest rate of frost mass accumulation and resulted in a total, frost mass accumulation of 4.2 lb_m (1.91 kg) at the ends of the 43 minutes frost test cycle. The 15/25 fpi coil had the second high speed of frost mass accumulation. The total amount of frost collected was 4.6 lb_m (2.09 kg) during the 50 minutes frost test, which was 109% more than that for the baseline coil and 10 % more than the 15/20 fpi coil.

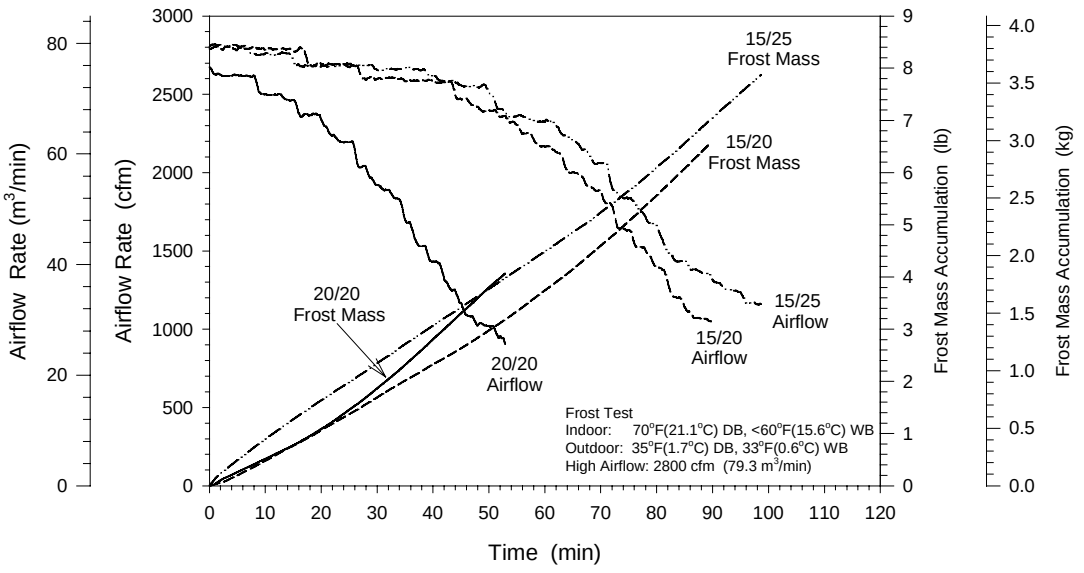

Figure 4.22 Variations of airflow and frost mass accumulation for three 2-row coils during frost test with high initial airflow 2800 cfm (79.3 m^3/min) at 35°F (1.7°C) dry bulb and 33°F (0.6°C) wet bulb temperatures

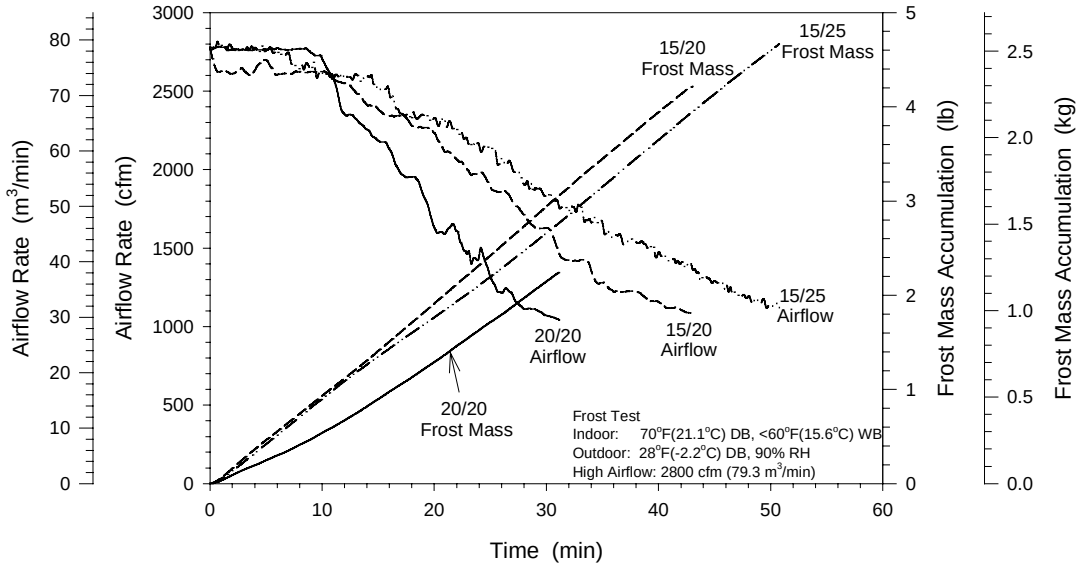

Figure 4.23 Variations of airflow and frost mass accumulation for three 2-row coils during frost test with high initial airflow 2800 cfm (79.3 m^3/min) at 28°F (-2.2°C) dry bulb temperature and 90% relative humidity

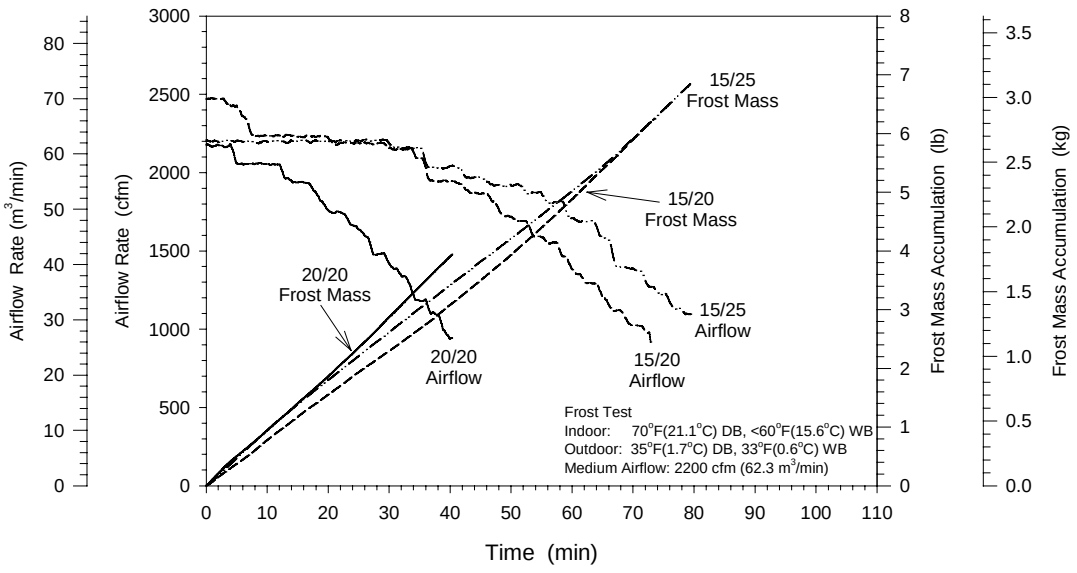

Figure 4.24 Variations of airflow and frost mass accumulation for three 2-row coils during frost test with medium initial airflow 2200 cfm (62.3 m^3/min) at 35°F (1.7°C) dry bulb and 33°F (0.6°C) wet bulb temperatures

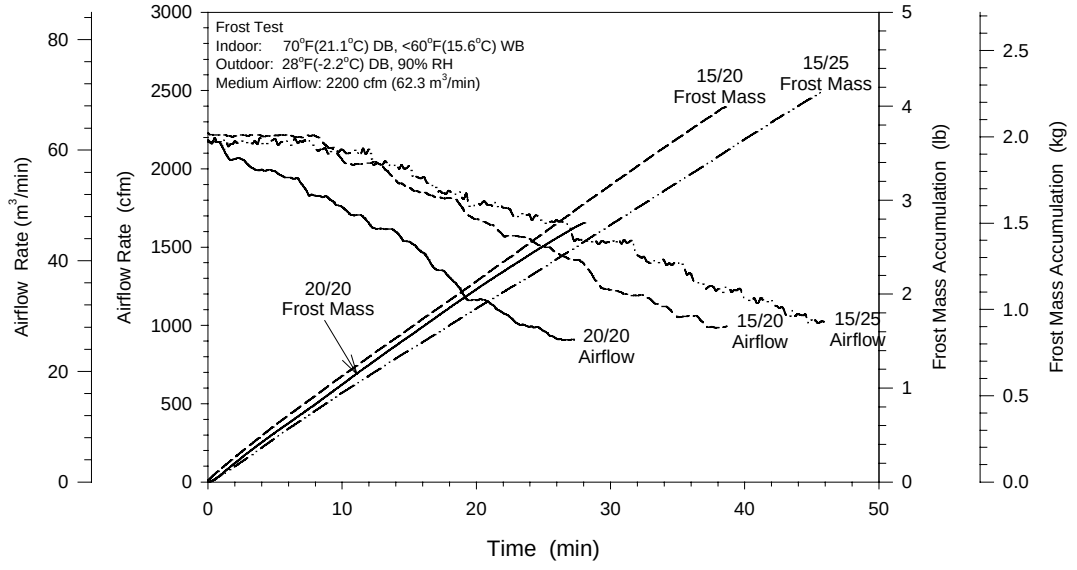

Figure 4.25 Variations of airflow and frost mass accumulation for three 2-row coils during frost test with medium initial airflow 2200 cfm (62.3 m^3/min) at 28°F (-2.2°C) dry bulb temperature and 90% relative humidity

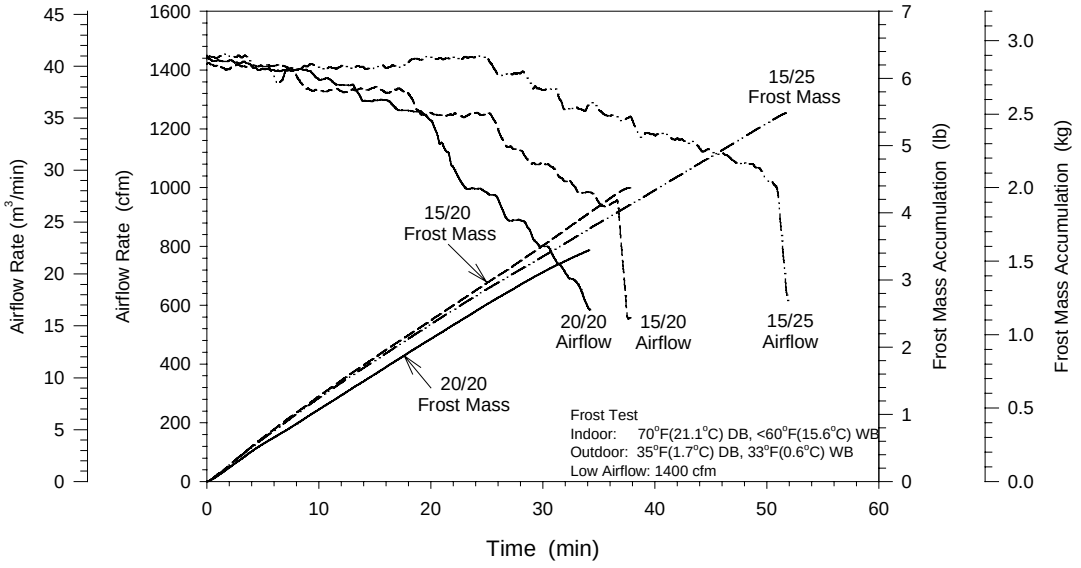

Figure 4.26 Variations of airflow and frost mass accumulation for three 2-row coils during frost test with low initial airflow 1400 cfm (39.6 m^3/min) at 35°F (1.7°C) dry bulb and 33°F (0.6°C) wet bulb temperatures

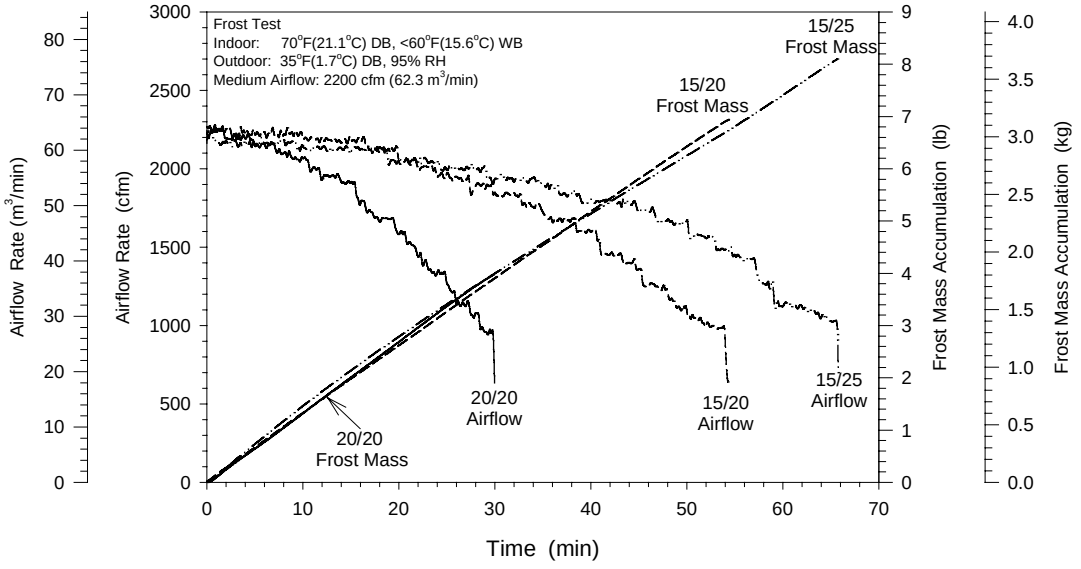

Figure 4.27 Variations of airflow and frost mass accumulation for three 2-row coils during frost test with medium initial airflow 2200 cfm (62.3 m^3/min) at 35°F (1.7°C) dry bulb temperature and 95% relative humidity

The frost mass accumulation of each coil in Figures 4.22 through 4.27 was not consistent with the corresponding frost growth at the leading edges shown earlier in Figures 4.4 through 4.9. The 20/20 fpi baseline coil and the 15/25 fpi fin staged coils always provided the fastest and the slowest frost growth at the leading edges, respectively. The inconsistency between leading edge frost growth and total frost mass accumulation, together with no frost formation observed on the trailing edges of coil, indirectly demonstrated that the frost depositions on the fin and tube surfaces were not uniform. As discussed in the section of frost growth on the leading edges, both fin staged coils slowed frost growth on the leading edges of the front row even though the frost mass accumulation data indicated similar growth rates and a larger total frost mass when compared to the baseline coil. These trends implied that staging fins could move frost accumulation away from the leading edges of the front row to the rear portion of the coil.

The absence of frost formation on the trailing edges of the rear row of the test coil was observed during all the frost tests of this experimental study. This would occur when the air humidity ratio approached the saturated humidity ration at the fin surface temperature or the fin surface temperatures at trailing edges were above the 32 ^{o}F (0 ^{o}C) freezing point. With the moisture condensed and froze along the fin length, the air stream humidity ratio would decrease. This would reduce the potential for mass transfer because the difference between the air stream humidity ratio and the saturated humidity ratio at the fin surface temperature approached zero for the coil trailing edges. Additionally, the distribution of temperature along the fin surface was not uniform and was affected by both convection heat transfer and latent heat transfer due to frost formation. Normally, the fin surface temperature at the trailing edges was higher compared to the region of the fin surface close to the coil tubes. In some test conditions, the fin surface temperature at the trailing edges might be higher than the freezing point.

Figures 4.22 through 4.27 show the variations of airflow at different air conditions and flow rates. As frost formed on the outdoor coil, the airflow dropped primarily due to the frost blocking the airflow passages between the adjacent fins. The airflow drops for both fin staged coils progressed much slower when compared to the baseline coil. Reduced airflow decreased the evaporating temperature, which caused faster frost formation and accelerated the airflow drop. The baseline coil showed the fastest airflow drop and minimum frost mass accumulation while the fin staged coil with fin density of 15/25 fpi had the slowest airflow drop and maximum frost mass accumulation. Though there was much more frost formed on the fin staged coils, the larger airflow drops at the end of frost tests were not observed. Actually, the final minimum airflow rates for both baseline and fin staged coils were close because all the frost tests were terminated at the same condition when the heating capacity of heat pump unit was 20% off. Frost blockage on the airflow drop was affected by the geometric of frost coil, the special distribution of frost deposition, the thickness of frost layer, and the growth history of frost. So, the airflow drop of frost coil was not directly correlated to the frost mass accumulation.

Airflow drops of both fin staged coils had similar trends and could be attributed to the same fin spacing of 1/15 inch (1.69 mm) at the front row and the similar growths of frost mass accumulation of the two fin staged coils. The slowness of airflow drops could be attributed to slower frost growth at the leading edges and wider fin spacing of the coil frost row. Although the frost mass accumulations increased in the similar speeds, the growths of frost at the leading edges of both fin staged coils were much slower than that of the baseline coil. So, for the fin staged coils, frost did not block the airflow passages at the leading edges as fast as it did for the baseline coil. This postponed the major blockage of frost to the airflow. In addition, the fin staged coils had the wider fin spacing of 1/25 inch (1.69 mm) at the front row than the baseline coil's 1/20 inch (1.27 mm). The reduction of the flow area by the frost growth on the front row fins would be as pronounced as that of the baseline coil, and this reduce the dropping speed of airflow for both fin staged coils as well.

Figures 4.23 and 4.25 show faster reductions in airflow as frost formed on the coils at 28 ^{o}F (-2.2 ^{o}C) dry-bulb temperature and 90% relative humidity. With the decreased air temperature and increased relative humidity, the rate of frost formation became more rapid, which accelerated the blockage of airflow passages. So the airflow at 28 ^{o}F frost test had a faster and sharper decline than that at 35 ^{o}F frost test. The difference of airflow drops between the baseline and fin staged coils decreased with the faster airflow drop trends. The fin staged coils always performed much better than the baseline coil. In addition, it should be noted that in Figure 4.23, airflow drop for two fin staged coils progressed slower than the baseline coil despite both of them having larger rates of frost mass accumulation. Between two fin staged coils, although the fin staged coil with 15/25 fpi had more fins on the second row than the fin staged coil with 15/20 fpi, the test results showed a less blockage on the airflow for the 15/25 fpi coil than that for the 15/20 fpi coil even sometime the 15/20 fpi coil had larger rate of frost mass accumulation (Figures 4.23 and 4.25).

To show the air humidity effect on the frost formation and airflow drop, as shown in Figure 4.27, a series of 35^{o}F frost tests with higher relative humidity of 95% were conducted at medium airflow. Compared to the inlet air relative humidity 82% at 35^{o}F dry-bulb temperature, the absolute humidity at 95% RH increased from 0.00349 to 0.00405 lbm_w/lbm_a (1.583 to 1.837 g_w/g_a). At extremely high humidity, the frost mass accumulation was approximately independent of fin spacing and progressed at about the same rate for both fin staged and baseline coils. Compared the test results shown in Figure 4.24 at the same air dry-bulb temperature of 35^{o}F (1.7^{o}C) and initial medium airflow, the frost accumulated on the evaporator at a given time increased with the air humidity. This is expected because higher air humidity at constant entering air temperature and flow rate increased mass transfer potential between air stream and coil surface.

The higher rate of frost accumulation produced increased blockage, faster airflow drop and shorter frost cycle time. Comparing the test results shown in Figures 4.24 and 4.27, for the 20/20 fpi coil

the drop in airflow took about 30 minutes at 95% RH, which was 10 minutes less than the 40 minutes at 82% RH. And the operation times of 15/20 fpi and 15/25 fpi coils decreases, respectively, from 72 to 54 minutes and 79 to 65 minutes when the relative humidity dropped from 95% to 82%. All three coils showed accelerated airflow drops until each coil reached the termination airflow at about 1000 cfm (28.3 m^3/min) in both Figures 4.24 and 4.27. Although the frost cycle times became shorter at higher humidity, the final frost accumulation of each test coil at 95% RH was larger than that at 82% RH due to the faster frost rate.

The test results at different air conditions and airflow rates revealed that the slower drop of airflow and the resulting extension in frost cycle time were the main advantage of the fin staged coils compared to the baseline coil. The major effects of decreasing airflow on the outdoor coil were the accelerated decreases in the coil capacity and t evaporating temperature. With the use of wider fin spacing on the coil front row, the slower airflow drop of fin staged coil allowed the coil capacity to undergo longer time to start fast drop.

Outdoor Coil Capacity

The refrigerant-side capacity of the outdoor coil was determined from estimation of the refrigerant mass flow and the enthalpy change of refrigerant flowing through the heat exchanger. The pressure and temperature measurements upstream and downstream of the outdoor coil were combined to determine the entering and leaving enthalpies of the refrigerant. Coil heat transfer varied with the growth of frost, which generally reduced the cooling capacity of frosting heat exchanger. The total cooling capacity of the outdoor coil was the combination of sensible and latent heat transfer occurring together during the frosting tests. In this experimental study, the energy transfer capacities of the outdoor coils with different staging fin configuration were examined under frosting conditions at various airflow rates, temperatures and humidities.

Figures 4.28 through 4.30 compare the variations of refrigerant-side capacities of the three 2-row outdoor coils at high, medium, and low initial airflow rates under the frosting test conditions of 35 ^oF (1.7 ^oC) dry-bulb and 35 ^oF (0.6 ^oC) wet-bulb temperatures. The capacity of the outdoor coil initially increased after startup of the frost test. After reaching a peak, it remained high for a short time, then began to decrease as the frost grew and airflow dropped.

The energy transfer of outdoor coil under the frosting process included both sensible and latent heat transfer, which corresponded to the heat and mass transfer, respectively. The Chilton-Colburn analogy relating heat and mass transfer should be valid for the frost formation process. If the heat transfer coefficient can be determined, then the mass transfer coefficient can be estimated and rise-versa. Therefore, only the heat transfer process during frosting test is discussed below.

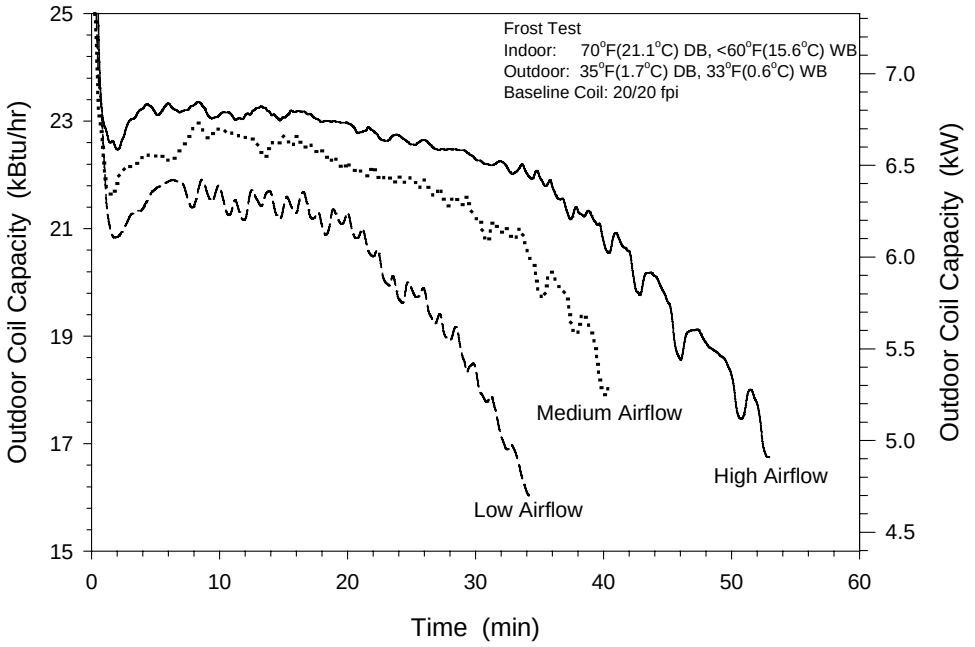

Figure 4.28 Refrigerant side capacities of baseline coil (20/20 fpi) under different airflow during frost tests at 35°F (1.7°C) dry bulb and 33°F (0.6°C) wet bulb temperatures

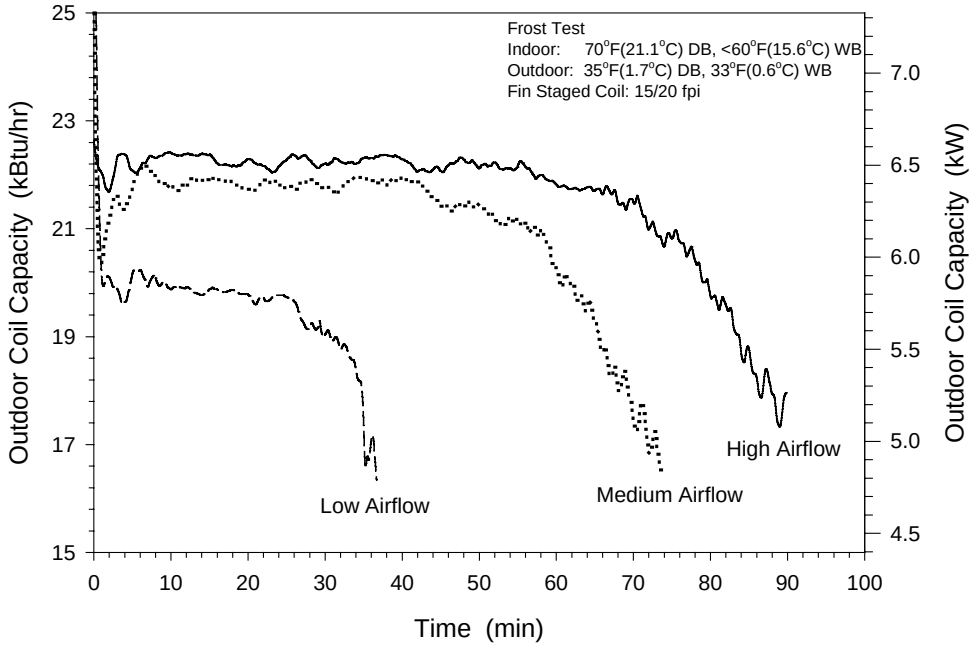

Figure 4.29 Refrigerant side capacities of fin staged coil (15/20 fpi) under different airflow during frost tests at 35°F (1.7°C) dry bulb and 33°F (0.6°C) wet bulb temperatures

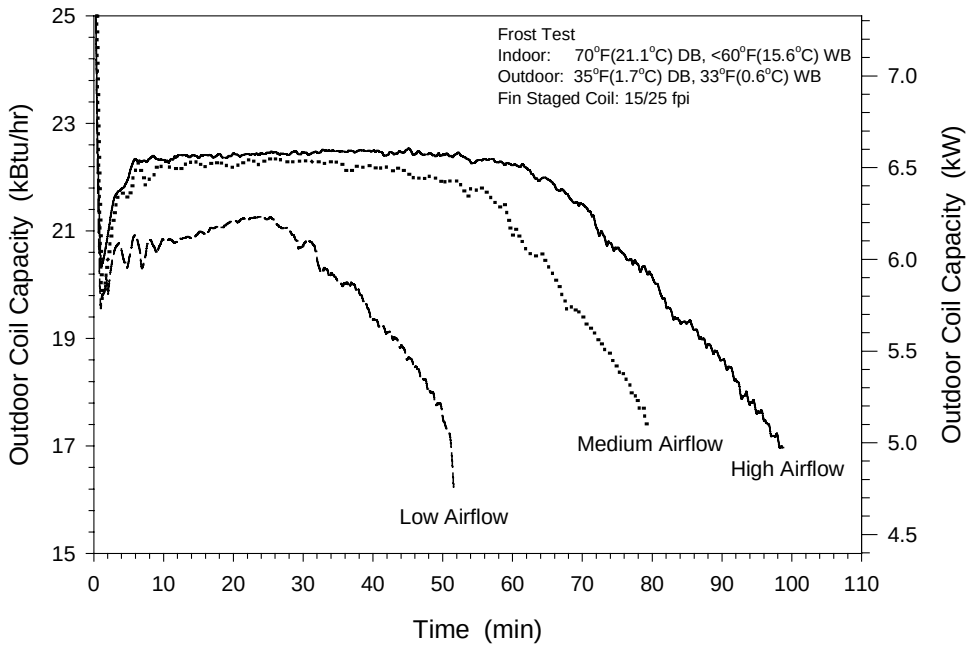

Figure 4.30 Refrigerant side capacities of fin staged coil (15/25 fpi) under different airflow during frost tests at 35°F (1.7°C) dry bulb and 33°F (0.6°C) wet bulb temperatures

The sensible cooling capacity of the outdoor coil is normally determined by the total heat transfer coefficient, the temperature difference between air stream and coil surface, and the airflow rate. During frosting tests, the heat transfer coefficient was not only a function of the fin geometry and the velocity of the air flowing through the coil but also a function of the frost thickness, properties, and the distribution of frost accumulation on the coil surface.

The heat transfer coefficient keeps varying with the frost formation. Many researchers, including Chung and Algren (1958), Beatty (1951), and Yonko and Sepsy (1967), have reported that the overall heat transfer coefficient went through three distinct phases as the frost growth. First, there is an increase in overall heat transfer coefficient, which is attributed to the increase in roughness and surface area due to initial frost formation. The crystalline structure of the frost results in the frost surface being rough and uneven. This increases the localized turbulence and heat exchange area on the coil surface. Normally, the increased surface roughness due to frost formation has a greater impact on the flat fin than the enhanced fins such as the 7-element lanced sine-wave fin used in this study. The slits and perforations on the lanced fins already increased the local turbulence, and thus the additional turbulence produced by the frost might not have much of an impact on the lanced fin as that on the flat fin. With more frost growth, the frost layer gradually covers the uneven fin surface and may reduce the turbulence of the enhanced fin surface.

In the second phase, the heat transfer coefficient remains approximately constant. This is attributed to a compensating effect of increasing thermal conductivity of the frost layer for an increased frost thickness. The surface roughness enhances the heat transfer only in the early stage of frost formation. As frost grows, the insulating effect of the frost layer gradually increases. Especially when the fin surface temperature becomes lower, the thermal conductivity and density of the frost accumulated tends to decrease. This produces a frost layer that is thicker and higher in thermal resistance. So, the insulating effect of the frost layer on the decline of coil capacity increases not only as the frost grows but also with the reduction of evaporating temperature. In the final phase, the heat transfer coefficient decreases with time. The increase in thermal resistance of the frost layer eventually becomes dominant and decrease the value of total heat transfer coefficient. Both the airflow across the outdoor coil and the evaporating temperature decreased with the frost growth, which have been discussed in the front sections.

The initial increase in capacity when frost first started to form could be explained by the increased heat transfer coefficient and surface area produced by the frost. Although the driving potential of heat transfer: the temperature difference between air stream and coil surface, increased with the decline of the evaporating temperature, the overall heat transfer decreased. When comparing Figures 4.10 through 4.12 with Figures 4.28 through 4.30, it could be seen that the outdoor coil capacities dropped along with the decreases of the evaporating temperature. As frosting continued, the heat extracted from the air stream by the evaporator decreased along with both the total heat transfer coefficient and airflow rate.

The high airflow case had the highest energy transfer during the frosting while the low airflow had the poorest performance compared to the other two airflow rates. For the higher airflow rate, the amount of energy transferred across the outdoor coil was more than that with a lower airflow rate. Also, the higher airflow increased the peak capacity and delayed the capacity degradation. For example, in Figure 4.28, high airflow capacity for the 20/20 fpi baseline coil peaked at 23.4 kBtu/hr (6.86 kW) and reduced to 16.8 kBtu/hr (4.92 kW) in 52.5 minutes at defrost initiation compared to the drop from 21.9 kBtu/hr (6.42 kW) to 15.8 kBtu/hr (4.63 kW) in 34 minutes at the low airflow for entering air conditions of 35 ^{o}F (1.7^{o}) dry-bulb and 33 ^{o}F (0.6 ^{o}C) wet-bulb temperatures.

Decreasing the airflow rate by 50% from 2800 cfm (79.3 m^3/min) to 1400 cfm (39.6 m^3/min) had a large effect on coil capacity. Although the temperature difference between the air stream and refrigerant inside tube became larger due to the lower evaporating temperature at the smaller initial airflow rate (Figures 4.10, 4.11 and 4.12), the energy transfer capacity of the outdoor coil was less at the lower airflow (Figures 4.28, 4.29 and 4.30). The lower airflow rate (face velocity) led to a lower Reynolds number and hence a decreased heat/mass transfer coefficient. As shown earlier in the frost accumulation plots (Figures 4.1,4.2 and 4.3), the frost layer blocked the heat exchanger quicker at the lower initial airflow rate. This slowed the increase of temperature difference between air stream and frost surface, which was caused by

the accelerated decline of evaporating temperature. Between airflow and evaporating temperature, airflow appeared to be the dominant factor in energy transfer performance during the frosting test.

Comparisons of the energy transfer capacities for different testing coils at various conditions are shown in Figures 4.31 through 4.36. In all the frost tests, there was a general trend of the capacity going through a slight rise and then a drop. The coil capacity included the sensible and latent energy transfer under frosting conditions. From the section of frost mass accumulation and airflow, it can be seen that the growths of frost mass accumulation were approximately the same for all three outdoor coils at the consistent test conditions. So the dominant factor affecting the variation of coil capacity was the sensible component of the total energy transfer which was dependent upon the airflow rate, overall heat transfer coefficient and the temperature difference between the air stream and frost covered coil surface. The airflow across the outdoor coil was the most dominant among the three variables in determining the effect of frost on the coil heat transfer. As the airflow dropped and the frost layer increased, the amount of sensible heat transfer declined rapidly, which led to a decrease in the total energy transfer, even if there was a corresponding decrease in the evaporating temperature as the airflow decreased.

For the baseline coil, especially at the high initial airflow, clearly there existed a capacity peak at the early portion of the test. This phenomenon was also present though not quite apparent for the fin staged coils. Figure 4.37 shows the refrigerant side capacities for three 2-row coils during the high airflow tests at 35^{o}F (1.7^{o}C) dry-bulb and 33^{o}F (0.6^{o}C) wet-bulb temperatures. After termination of the defrost, it took less than five minutes for the baseline coil to reach its maximum capacity of 23.4 MBtu/h (6.86 kW). Most of the drop in capacity occurred during the last 20 minutes of the frost buildup period. For the 20/20 fpi baseline coil, a higher fin density of the first row resulted in a higher energy transfer. This was a direct consequence of the increased energy transfer area and coefficient as the number of fins per inch increased. The increased capacity of energy transfer was desirable. However, for the baseline coil, as more frost accumulated, there was a more rapid performance degradation due to the blockage of airflow and the insulating effect of frost layer.

Figures 4.31 and 4.32 show the effect of a lower approaching air temperature on the cooling capacity of the outdoor coil. As the air dry-bulb temperature decreased, there was also a decrease in temperature difference between the air stream and coil surface, which could be used to explain the slightly lower energy transfer capacity at 28 ^{o}F frosting test. Air at 35 ^{o}F, 82% RH had a humidity ratio of 0.003489 lbm_w/lbm_a (1.583 g_w/g_a). That was more than the air humidity ratio of 0.00282 lbm_w/lbm_a (1.279 g_w/g_a) at 28 ^{o}F, 90% RH. However, due to the corresponding drop of evaporating temperature at 28 ^{o}F test, the latent heat transfer at 28 ^{o}F test (related to the rate of frost mass accumulation shown in Figures 4.23 and 4.25), almost same as those at 35 ^{o}F test could be attributed to the drop insensible energy transfer due to the decrease of temperature difference between air stream and refrigerant inside tubes. The more rapid decline of energy transfer capacity at 28 ^{o}F, when compare to the test results at 35 ^{o}F, could be attributed to the faster frost growth and blockage of airflow at the lower 28 ^{o}F.

The 20/20 fpi baseline coil showed the poorest overall performance in all the frosting tests. It had the fastest decrease in capacity and resulting shortest performance time. The 15/25 fpi coil performed the best with respect to the other two coils and had the longest stable energy transfer process during the frost test. The 15/20 fpi had similar trends in capacity as the 15/25 fpi coil. The capacity value was slightly smaller than the 15/25 fpi coil but much more than the 20/20 fpi baseline coil. The 20/20 fpi baseline coil didn't show the constant capacity in the middle of frosting tests. After it reached the peak capacity, the baseline coil began to drop. When the airflow was reduced from 2800 cfm (79.3 m^3/min) to 2200 cfm (62.3 m^3/min) (Figures 4.31 through 4.34), the 20/20 fpi baseline coil showed larger degradation in capacity than both the fin staged coils. The decrease in heat exchanger performance as a result of frosting was mainly due to a drop in airflow. The baseline coil produced the fastest frost growth and airflow drop.

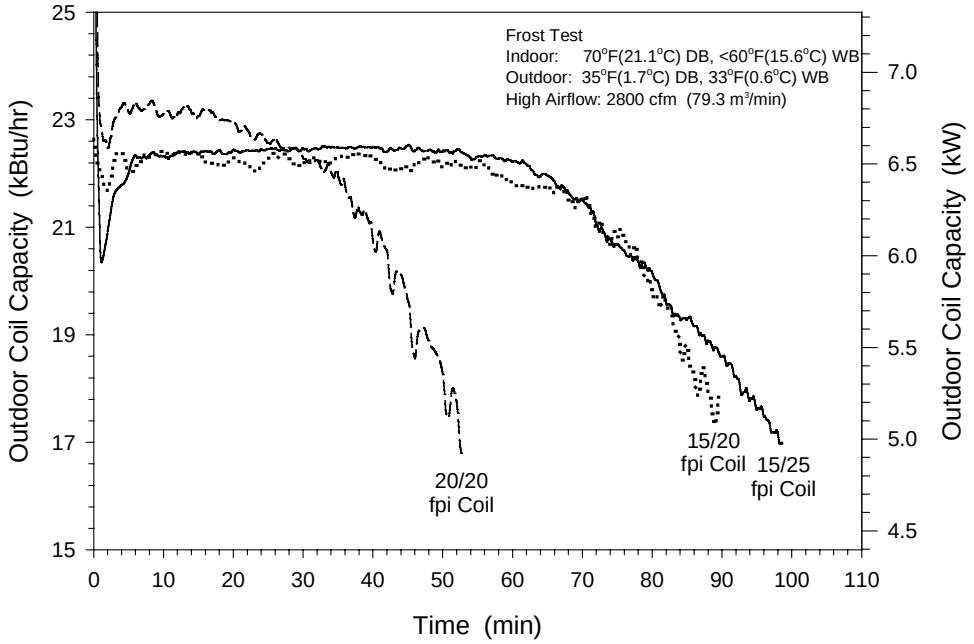

Figure 4.31 Refrigerant side capacities of three 2-row outdoor coils during high airflow frost tests at 35°F (1.7°C) dry bulb and 33°F (0.6°C) wet bulb temperatures

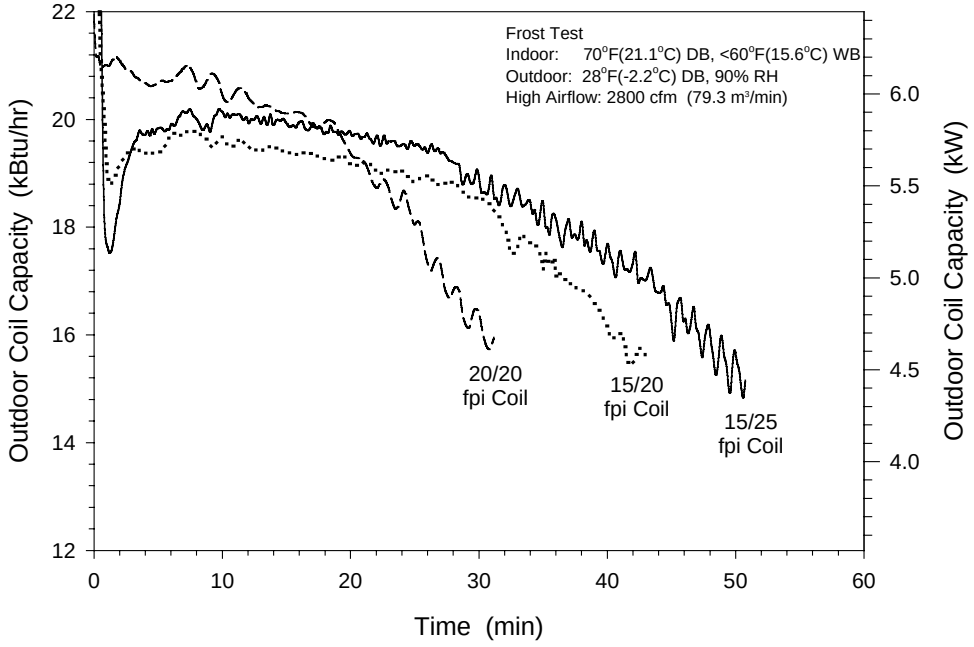

Figure 4.32 Refrigerant side capacities of three 2-row outdoor coils during high airflow frost tests at 28°F (-2.2°C) dry bulb temperature and 90% relative humidity

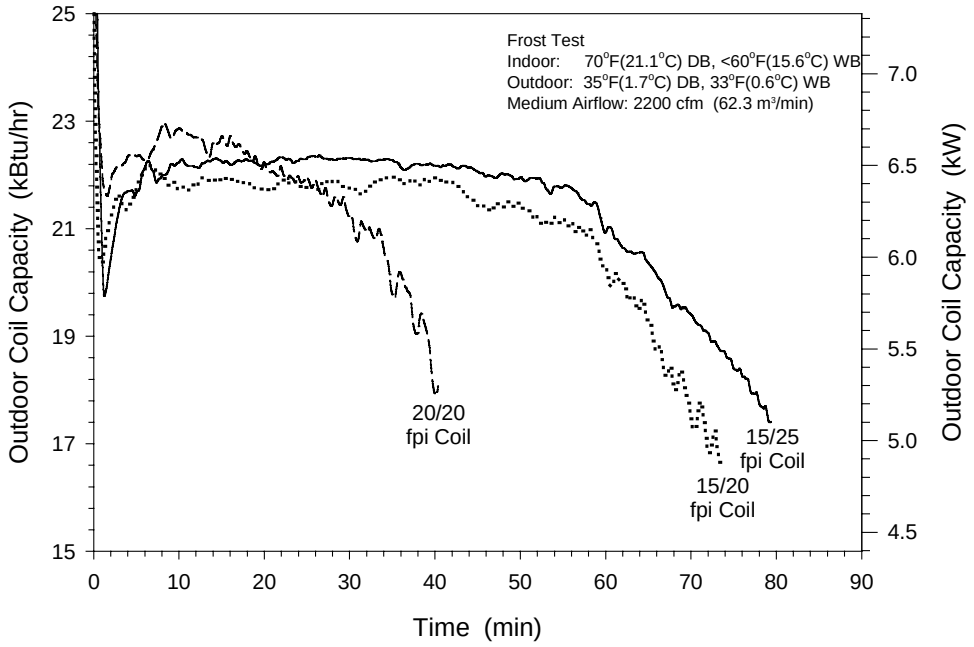

Figure 4.33 Refrigerant side capacities of three 2-row outdoor coils during medium airflow frost tests at 35°F (1.7°C) dry bulb and 33°F (0.6°C) wet bulb temperatures

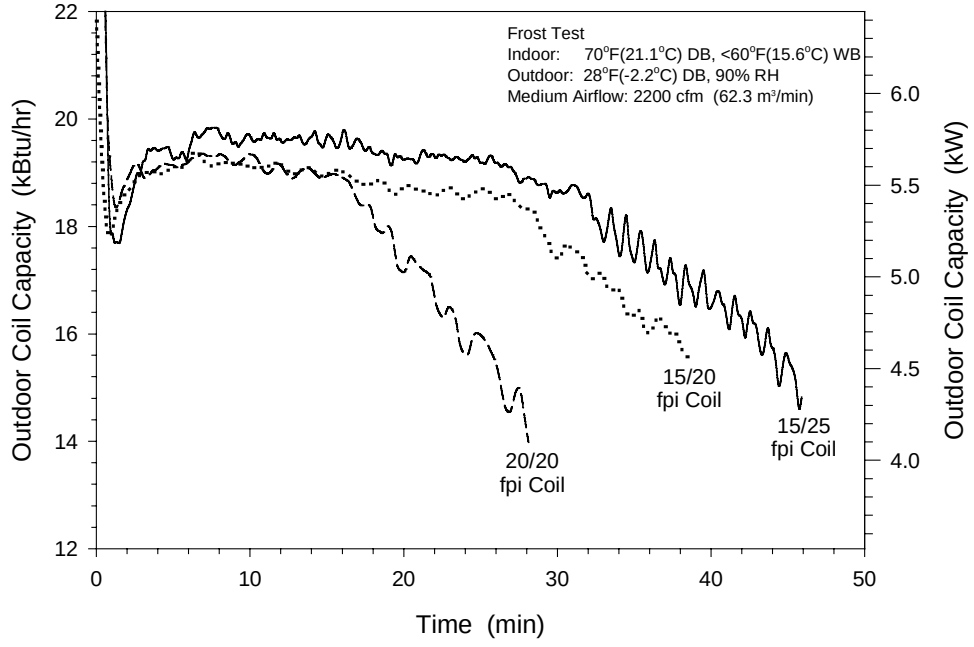

Figure 4.34 Refrigerant side capacities of three 2-row outdoor coils during medium airflow frost tests at 28°F (-2.2°C) dry bulb temperature and 90% relative humidity

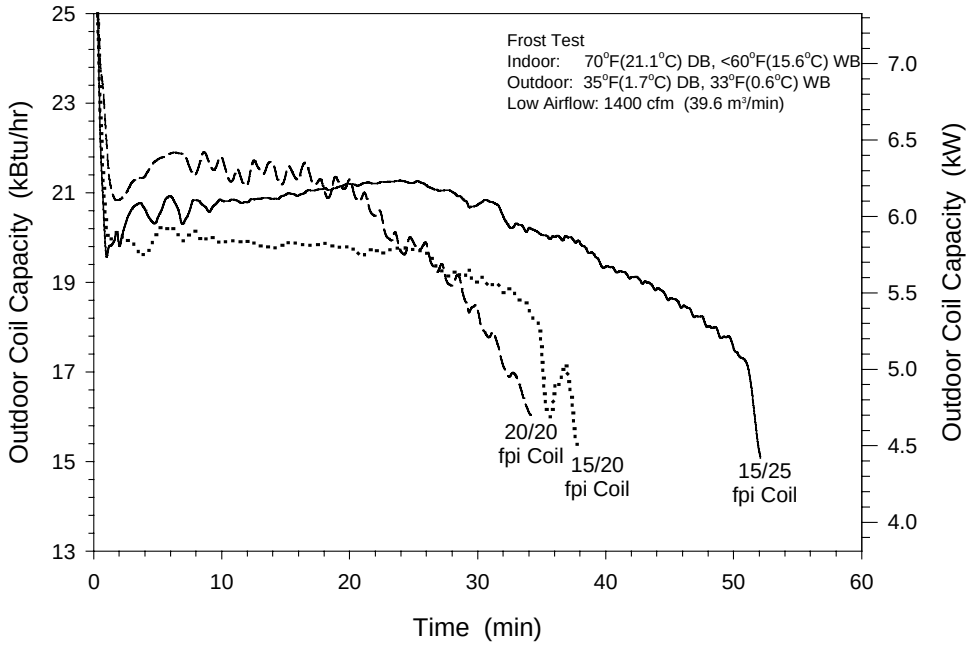

Figure 4.35 Refrigerant side capacities of three 2-row outdoor coils during low airflow frost tests at 35°F (1.7°C) dry bulb and 33°F (0.6°C) wet bulb temperatures

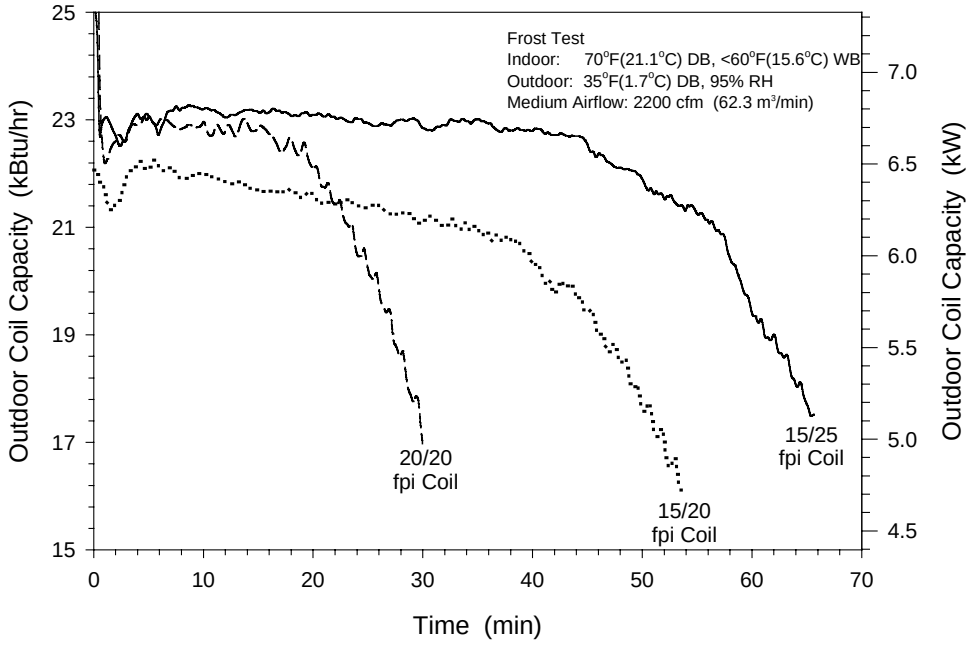

Figure 4.36 Refrigerant side capacities of three 2-row outdoor coils during medium airflow frost tests at 35°F (1.7°C) dry bulb temperature and 95% relative humidity

These results show that the fin staged coils with a wider fin spacing in the first row appeared to have better energy transfer performance than the baseline coil with a narrow fin spacing under frosting conditions. For the second rows of the fin staged coils, due to the higher fin density compared to their first rows, both the fin surface area and heat transfer coefficient of ten second row were increased. The second row of fin staged coil appeared to have a larger sensible and latent heat transfer contribution to the total coil energy transfer.

Between the two fin staged coils, it appears that the 15/25 fpi coil had a better performance than the 15/20 fpi coil. The 15/20 fpi coil for some tests had lower evaporating temperatures than the 15/25 fpi coil (Figures 4.14 through 4.18). However, the heat transfer capacity of the 15/20 fpi coil was always less than that of the15/25 fpi coil due to lower airflow rate and less fin surface on the second row. The 15/25 fpi coil also had the longest time for stable energy transfer. Considering that the 15/25 fpi fin staged coil had the slowest frost growth, airflow drop and the maximum surface area, this was to be expected.

The variations of coil capacities at the higher humidity are shown in Figure 4.36. When comparing the test results shown in Figure 4.39 at 35 ^{o}F dry-bulb temperature and 82% RH, it appears that the capacity of the outdoor coil increased with humidity. Fore the 20/20 fpi baseline coil, the capacity at 95% RH stayed approximately constant in the first 15 minutes (Figure 4.36) while at 82% RH, the capacity started to drop down immediately after reaching a peak (Figure 4.33). For the fin staged coil with 15/25 fpi, the coil capacity was apparently influenced by the relative humidity of the air. With the RH raised from 82% to 95%, there was an approximately 5% increase in the coil capacity, but it resulted on an earlier and more rapid drop in coil capacity. For both the 20/20 and 15/20 fpi coils, the final capacities of the 95% RH test were actually lower than the corresponding coil capacities at defrost initiation for the 82% RH test, respectively.

At a constant refrigerant temperature, a higher humidity normally increases the driving force potential of the mass transfer and more frost forms on the coil. So, the total energy transfer of the outdoor coil is higher with the increase of latent heat transfer. However, as time progress, the higher humidity produces more frost and thus the insulating effect of frost layer occurs earlier than that at a lower humidity. Because of the earlier and faster frost formation and coil capacity drop, the frost cycle time because shorter at the higher humidity.

Steady State Test Results

Although this experimental study concentrated on the effects of fin staging on the transient performance of the heat pump outdoor coil under frosting conditions, two steady-state cooling and one steady-state heating test were also conducted on the heat pump system with the baseline and fin staged outdoor coil. The outdoor coil was operated in the dry working conditions either as condenser or evaporator of heat pump unit in cooling or heating mode, respectively. Even if the fin staged coil could improve the frosting performance of the heat pump system, if it showed a negative effect on the heat pump cooling or heating performance under non-frosting conditions, the fin staged coil would not be used. A heat pump system operates much more time under the non-frosting conditions. These steady-state cooling and heating tests provide more information on the performance of fin staged coils for the heart pump manufacturers who may be interested in the application of fin staged coils on their heat pump units.

Two steady-sate cooling tests (DOE A&B) of the heat pump unit were conducted at the outdoor dry-bulb temperatures of 95 ^{o}F (35.0 ^{o}C) and 82 ^{o}F (27.8 ^{o}C) with the cooling standard indoor condition of 80 ^{o}F (26.7 ^{o}C) dry-bulb and 67 ^{o}F (19.4 ^{o}C) wet-bulb temperatures (ANSI/ASHRAE, 1995). Steady-state heating test (DOE E) of heat pump system was conducted at outdoor conditions of 47 ^{o}F (8.33 ^{o}C) dry-bulb and 43 ^{o}F (6.1 ^{o}C) wet-bulb temperatures with the indoor dry-bulb temperature of 70 ^{o}F (21.1 ^{o}C) (ANSI/ASHRAE, 1995). All the steady-state tests were operated at the nominal outdoor airflow rate of 2800 cfm (1.322 m^3/s). A sample steady state test result outputted by the DAQ system is shown in Figure 4.37. All the details of the heat pump system and component performance for the baseline coil cooling test at 95 ^{o}F dry-bulb temperature are provided.

ASHRAE PROJECT 1002-TRP HEAT PUMP TEST REPORT

ENERGY SYSTEMS LAB, TEXAS A&M UNIVERSITY

TEST DESCRIPTION			
Input File Name	:		2020-95.pra
Start of Test	:	15;47;44	04-12-1999
End of Test	:	16;50;23	04-12-1999
Length of Test (min)	:		62.82
Number of Data Scan	:		375
SYSTEM PERFORMANCE	:	AVERAGE	STD DEV
System EER	:	10.30	0.33
System COP	:	3.02	0.10
Cooling Capacity (MBtu/h)	:	33.54	1.04
Unit Power (MBtu/h)	:	11.11	0.10
OUTDOOR COIL CONDITIONS			
AIR PROPERTIES			
Air Side Capacity (MBtu/h)	:	41.93	1.01
Entering Dry Bulb (^oF)	:	95.02	0.42
Entering Dew Point (^oF)	:	62.39	0.22
Exiting Dry Bulb (^oF)	:	111.24	0.71
Exiting Dew Point (^oF)	:	62.39	0.22
Flow Rate (cfm)	:	2592.1	15.70
Fan Power (MBtu/h)	:	0.86	0.01
REFRIGERANT PROPERTIES			
Rfrg Side Capacity (MBtu/h)	:	42.74	0.25
Liquid Line Pressure (psia)	:	390.43	4.09
Liquid Line Temperature (^oF)	:	103.85	0.94
Liquid Line -SubC/+SupH (^oF)	:	-8.27	0.27
Vapor Line Pressure (psia)	:	397.87	3.99
Vapor Line Temperature (^oF)	:	158.36	1.06
Vapor Line -SubC/+SupH (^oF)	:	44.80	0.90
Coil Energy Balance (%)	:	1.90	
INDOOR COIL CONDITIONS			
AIR PROPERTIES			
Air Side Capacity (MBtu/h)	:	33.54	1.04
Entering Dry Bulb (^oF)	:	80.43	0.12
Entering Dew Point (^oF)	:	60.11	0.22
Exiting Dry Bulb (^oF)	:	58.37	0.21
Exiting Dew Point (^oF)	:	55.56	0.50
Flow Rate (cfm)	:	1067.6	5.59
Fan Power (MBtu/h)	:	1.50	0.03
Avrg Dehumidify Rate (lb_m/h)	:	7.700	0.96
Intgr Dehumidify Value (lb_m)	:	8.060	
REFRIGERANT PROPERTIES			
Rfrg Side Capacity (MBtu/h)	:	34.59	0.27
Liquid Line Pressure (psia	:	194.52	1.14
Liquid Line Temperature (^oF)	:	64.07	0.34

Figure 4.37 Test report of heat pump unit with 2-row standard outdoor coil during high airflow at DOE A steady state cooling test condition

Liquid Line -SubC/+SupH (°F) :	0.64	0.22
Vapor Line Pressure (psia) :	156.07	0.79
Vapor Line Temperature (°F) :	53.04	1.42
Vapor Line -SubC/+SupH (°F) :	3.36	1.64
Coil Energy Balance (%) :	3.03	
COMPRESSOR PROPERTIES		
Compressor Power (MBtu/h) :	8.74	0.09
Suction Pressure (psia) :	152.49	0.67
Suction Temperature (°F) :	56.59	2.09
Suction Line -SubC/+SupH (°F):	8.32	2.15
Discharge Pressure (psia) :	04.71	4.00
Discharge Temperature (°F) :	61.63	1.38
Discharge Line -SubC/+SupH(°F):	46.75	1.24
Refrigerant Flow Rate(lb_m/min):	8.22	0.04
Shell Top Temperature (°F) :	160.34	0.85
Shell Middle Temperature (°F):	100.24	0.37
Shell Bottom Temperature (°F):	100.24	0.37
EXPANSION VALVE PROPERTIES		
INDOOR TXV PROPERTIES		
Upstream Pressure (psia) :	378.31	4.07
Upstream Temperature (°F) :	101.43	0.85
Downstream Pressure (psia) :	194.52	1.14
Downstream Temperature (°F) :	64.07	0.34
OUTDOOR TXV PROPERTIES		
Upstream Pressure (psia) :	384.04	4.04
Upstream Temperature (°F) :	103.74	0.89
Downstream Pressure (psia) :	390.43	4.09
Downstream Temperature (°F) :	103.85	0.94

Figure 4.37 continued

During the steady-state tests, the performance of the whole heat pump, not just the outdoor coil itself, was measured. The test results allowed for comparison of the performance of the heat pump with different outdoor coils, and thus quantify the impact of fin staged outdoor coil on the heat pump system performance under non-frosting conditions. Table 4.1 shows the performance of the heat pump with different outdoor coils at two cooling (DOE A&B) and one heating (DOE E) steady-state test conditions.

For the 20/20 fpi baseline coil and 15/25 fpi fin staged coil, the total areas of fin surface were the same. Because the front row of the fin-and-tube heat exchanger normally has the higher local heat transfer coefficient, at the same operating conditions, the 20/20 fpi baseline coil should have higher heat transfer than the 15/25 fpi fin staged coil. For the 15/20 fpi fin staged coil, the heat transfer should be smallest among the three 2-row outdoor coils tested. The test results showed that the 20/20 fpi baseline coil could provide more heat transfer capacity than the fin staged coils with less fin surface on the front row.

The impact of fin staging on the heat pump unit capacity (indoor coil capacity) was not large. The difference of cooling/heating capacities of the heat pump unit with different two-row outdoor coils was less than ±6%, which was close to the test uncertainty of the unit capacity measurements. Among the three two-row coils, the fin staged coil with 15/20 fpi always had the maximum unit power due to larger compressor power consumption. This caused the lower heating cycle EER and cooling cycle COP for the 15/20 fpi coil when compared to the other two-row testing coils. For the entering refrigerant state of compressor, both compressor suction temperature and superheat of the 15/25 fpi coil were higher. And both of the fin staged coils showed less compressor discharge pressures than the baseline coil. Other variables, such as compressor suction pressure, discharge temperature and refrigerant flow rate were relatively consistent for the heat pump unit with different two-row outdoor coils. With respect to the baseline coil, the two-row fin staged coils generally didn't show obvious disadvantage except the 15/02 fpi coil had higher compressor power consumption and resulting lower unit EER and COP.

The addition of one more row of fin surface should have increased the heat and mass transfer capacities of the three-row outdoor coil. Based on the test results shown in Table 4.1, both heating and cooling capacities of the baseline three-row coil were larger than any of the two-row coil were larger than any of the two-row coil at the same test condition. However, the cooling or heating capacity of heat pump unit didn't show observable difference compared to the heat pump units with the two-row outdoor coils. Furthermore, due to the increase of compressor and outdoor fan power consumption, the EER/COP of the heat pump units with three-row outdoor coils seemed to be less than the corresponding values of the heat pump unit with two-row outdoor coils.

Between two three-row baseline and fin staged coils, apparently the heart transfer capacity of the fin staged coil with 15/20/25 fpi was not as large as the 20/20/20 fpi baseline coil although both of them had the same amount of total fin surfaces. This caused the larger capacity of heat pump unit with the 20/20/20 fpi baseline coil. So both cooling cycle EER and heating cycle COP of the heat pump unit with the 15/20/25 fpi coil tended to be less with the almost same unit powers.

Steady-state test results showed only a light degradation in performance of the heat pump unit with three-row fin staged outdoor coil. This degradation due to the use of fin staged outdoor coil might be reduced through optimizing the circuit design of three-row coil and the airflow rate across the coil.

Table 4.1 Comparisons of steady-state test results

Steady State Unit Property	Cooling Test DOE A					Cooling Test DOE B					Heating Test DOE E				
	Two-Row Coil			Three-Row Coil		Two-Row Coil			Three-Row Coil		Two-Row Coil			Three-Row Coil	
	20/20	15/20	15/25	20/20/20	15/20/25	20/20	15/20	15/25	20/20/20	15/20/25	20/20	15/20	15/25	20/20/20	15/20/25
Unit Capacity (MBtu/h)	33.5	33.6	32.3	33.5	32.6	35.3	37.5	35.7	35.9	35.0	32.3	31.9	30.7	33.0	32.8
Unit Power (MBtu/h)	11.1	11.8	10.9	11.7	11.6	9.75	10.4	9.55	10.2	10.2	10.3	10.8	10.0	11.4	11.4
EER (COP)	10.3	9.71	10.1	9.82	9.63	12.4	12.3	12.8	12.1	11.7	(3.12)	(2.97)	(3.08)	(2.90)	(2.89)
Indoor Coil Airflow (cfm)	1068	1089	1058	1086	1092	1061	1085	1060	1084	1090	1093	1109	1082	1105	1114
Outdoor Coil Airflow (cfm)	2592	2860	2830	2770	2825	2868	2888	2789	2759	2810	2815	2841	2808	2806	2806
Outdoor Coil Capacity (MBtu/h)	41.9	39.8	40.1	44.8	42.6	44.7	42.3	41.1	46.1	43.2	27.3	27.3	26.8	28.5	26.8
Compressor Power (MBtu/h)	8.70	9.38	8.46	9.10	9.00	7.33	7.89	7.10	7.61	7.64	7.93	8.21	7.47	8.81	8.78
Compressor Suction Temperature (^{o}F)	56.6	56.7	57.4	56.6	57.5	54.4	55.6	56.2	55.6	56.0	44.3	43.7	43.7	42.5	42.8
Compressor Suction Pressure (psia)	152	152	152	153	154	149	152	150	151	151	111	110	109	109	108
Compressor Sunction Line Superheat (^{o}F)	8.32	8.78	9.20	7.94	8.76	7.32	7.47	8.88	7.88	8.48	14.8	14.6	15.3	13.9	14.4
Compressor Discharge Temperature (^{o}F)	162	166	160	163	163	142	146	142	145	145	170	171	163	179	182
Compressor Discharge Pressure (psia)	405	395	396	389	385	344	344	338	333	329	362	344	344	366	362
Compressor Discharge Line Superheat (^{o}F)	46.8	52.5	46.8	51.6	52.3	39.1	43.7	40.2	44.2	45.7	63.9	68.2	60.8	71.6	75.3
Refrigerant Flow Rate (lb_m/min)	8.22	8.18	8.22	8.30	8.32	8.14	8.31	8.19	8.26	8.25	5.82	5.81	5.74	5.71	5.70

CHAPTER V

MODEL DESCRIPTION

Quasi-Steady State Approach

Frost deposition and its effect on the outdoor heat exchanger airflow and heat transfer of a heat pump is a transient process. In response to the frost buildup on the heat exchanger, the heat pump constantly changes the outdoor coil refrigerant inlet conditions, which include the refrigerant inlet temperature, pressure and flow rate. The variations of these conditions, together with the change of heat exchanger heat and mass transfer coefficients, frost layer properties, air flow rate, etc. simultaneously determine the transient performance of the outdoor coil. In other words, the transient behavior of the outdoor coil is a response to a combination of a variety of variables.

For heat pump applications, frost formation is usually a slow process. It typically takes from 30 to 90 minutes for frost to grow enough to require defrosting of the evaporator. Therefore, it would be reasonable to apply a quasi-steady state approach to modeling the frost growth and predicting the performance of heat exchanger under frosting conditions.

In a simulation model, the frost growth process needs to be divided into many small time steps. At each time interval, the heat exchanger is assumed to be working at steady state conditions. Both air and refrigerant inlet parameters and flow rates are fixed at each time step and provided by fitted equations of measured data. Also, the thermal and physical characteristics of the frosted coil are kept constant during each time step. This allows for the calculation of the heat and mass transfer and the frost properties at each time step. At the start of next time step, the amount of frost on the coil surface added is the product of the calculated frost growth rate and the time interval at the previous time step. The change in airflow rate, heat and mass transfer coefficients and thermal resistance of frost layer is evaluated of each time step. Thus, a new steady state simulation at each time step is run in accordance with the updated calculated variables. The transient performance of a frosted evaporator is thus analyzed at the successive time steps based on the variation of operating conditions and properties related to and affected by frost accumulation.

The magnitude of the time step, ΔTime, is crucial for the application of the quasi-steady state approach. Through comparing the preliminary calculation results running on several time steps (20, 40, 60, 90 and 120 seconds), it was found that the value of time interval doesn't affect the accuracy of the predictions significantly. Considering the total computation time and the effect of accumulated errors, a constant time step (one minute) was employed throughout the simulation process. Because the startup process of the system is highly time dependent, this constant and relatively large time interval may cause

some discrepancy between the simulation and experimental data at the beginning of frosting process. The quasi-steady state process is an idealization of the actual transient frosting process. The application of this approach implies that the thermal equilibrium can be established during each time step.

Calculation Procedure and Algorithm

The frosted evaporator model is used to evaluate the coil performance variables such as coil capacity, frosting rate, air flow pressure drop, outlet states of both air and refrigerant during frost buildup on the evaporator surface. An iteration procedure is required to perform this task. The flow chart of the frosted evaporator model is shown in Figure 5.1.

At first, the model prepares the initial input data: air and refrigerant state parameters at the inlet of evaporator, and air and refrigerant flow rates. Then it reads in the coil geometry data, frost layer initial values, total simulation time and time step increment. The details are described in a later section of this chapter.

The quasi-steady state simulation of a frosted evaporator starts at time zero. At the outset of each time step, refrigerant state parameters at the entrance of each circuit are calculated by the distributor model based upon equality of enthalpy during the throttling process.

The main part of the model is composed of three basic iteration loops: the tube loop, circuit loop and refrigerant distribution loop. Evaluation of heat/mass transfer and frost performance for a single tube is executed in the tube loop. The calculation starts with the refrigerant inlet tube of a given circuit and progresses to the following tubes along the refrigerant flow direction till the outlet is reached. Figures 5.2 and 5.3 present the tube calculation sequence for two and three row coils, respectively. Each vertical line in these figures represents a circuit. Numbers indicate locations of each tube that are shown in the coil circuit diagrams (Figures 3.5 and 3.6).

At the beginning of the calculation of each tube, the refrigerant properties are always known and fixed at the tube entrance. They are equal to either the circuit inlet properties or the outlet properties of the proceeding tube. Meanwhile, the temperature and humidity of the air upstream of the tube may be determined because of the parallel flow characteristic of the test coils. In the process of calculations, the refrigerant properties at tube exit and the frost layer properties are assumed first. These estimated properties are then updated with new calculated values until the calculated value of the refrigerant enthalpy at tube outlet converges.

In the tube loop, once basic performance calculations for a tube are completed, the frosting subprogram is called to estimate frost growth. Because the estimation of frost layer properties is based upon a section-by-section approach on the fin surfaces, the values of the frost layer for a tube have to be determined first at each section, and then section calculation results are averaged to obtain frost

information for the fins of a particular tube. If the temperature of outdoor coil surface is equal or above 0^oC (32^oF), the main program does not call the frost growth model.

When all the tube calculations in one circuit are completed, the upstream air properties of the tubes at the second or third row need to be updated. The calculation loop for each circuit is stopped when the refrigerant enthalpy at the circuit outlet converges. The process is repeated for each circuit.

Fin-and-tube heat exchangers generally have several refrigerant circuits. Although refrigerant superheats at different circuit outlets may be different based upon the heat and mass transfer as well as the mass flow in each circuit, the outlet pressures are the same because the circuits are combined at the outlet manifold. The state properties (temperature and pressure) at the inlet of each circuit are known and fixed, but the mass flow rates of the refrigerant are not. Therefore, an iterative calculation procedure is necessary to adjust the refrigerant distribution in each circuit to obtain the same pressure drop throughout each circuit. The refrigerant mass flow is first assumed to be same for each circuit and is maintained unchanged until the calculation of all circuit loops have been completed. The fraction of refrigerant total flow rate through each circuit is then iteratively adjusted so that same pressures at each circuit exit is obtained. The coil steady state calculation loop at a given time step is ultimately finished when the convergence of circuit exit pressure iteration is reached.

At the end of each time step, the increased airside pressure loss due to the frost layer is estimated. A new airflow rate is calculated by the pressure drop and airflow subprogram and updated for the next time step. When the main program determines that all the calculations at a time step have been finished, it stores the relevant calculation results and then starts the next time loop. Time starts at zero and increases gradually based on the size of the time step set at the beginning of simulation.

The program will stop when the specified total pre-set simulation time is reached or the spacing between fins of any row is totally blocked off by the frost.

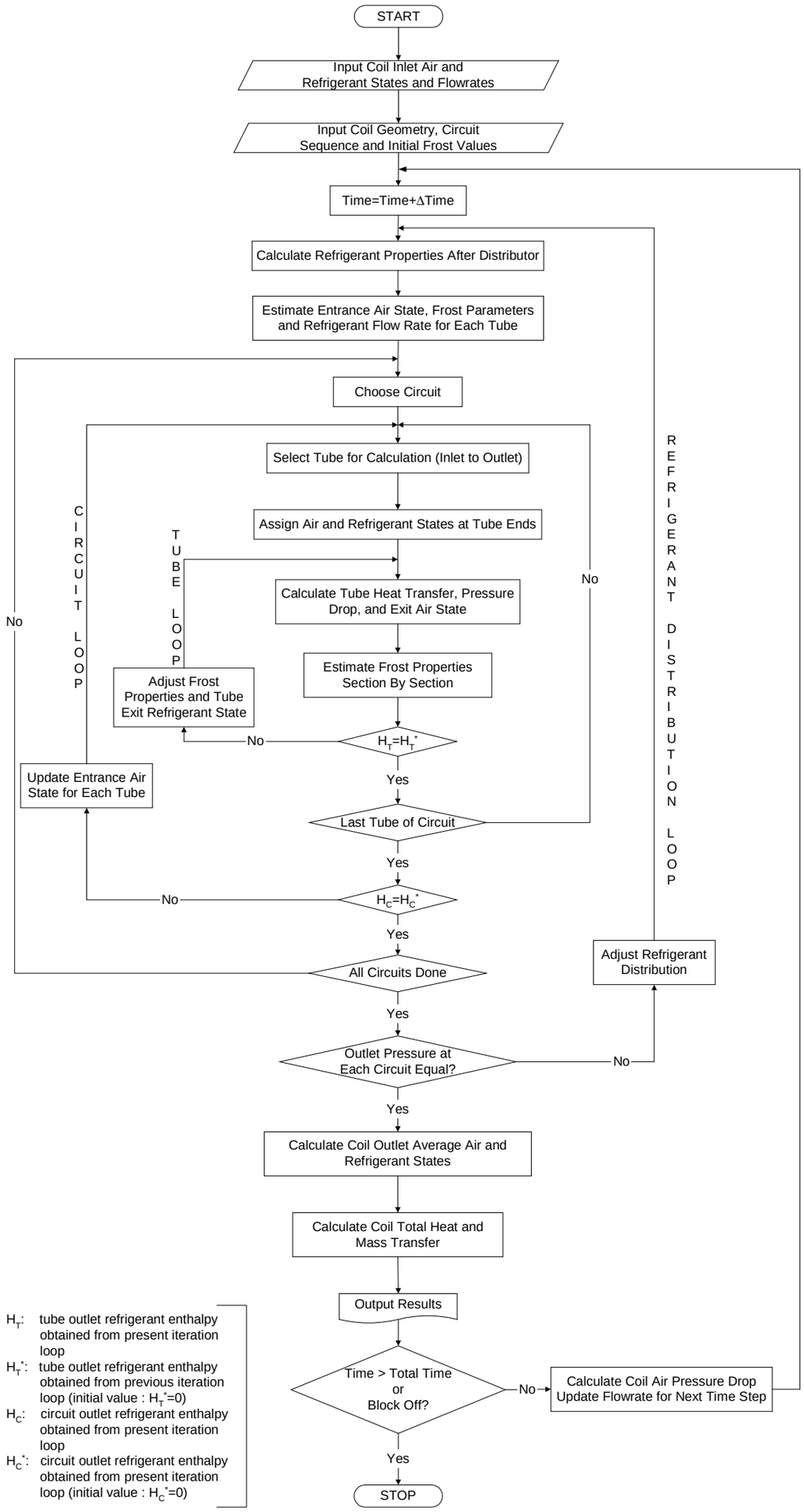

Figure 5.1 Flow chart of frosted evaporator model

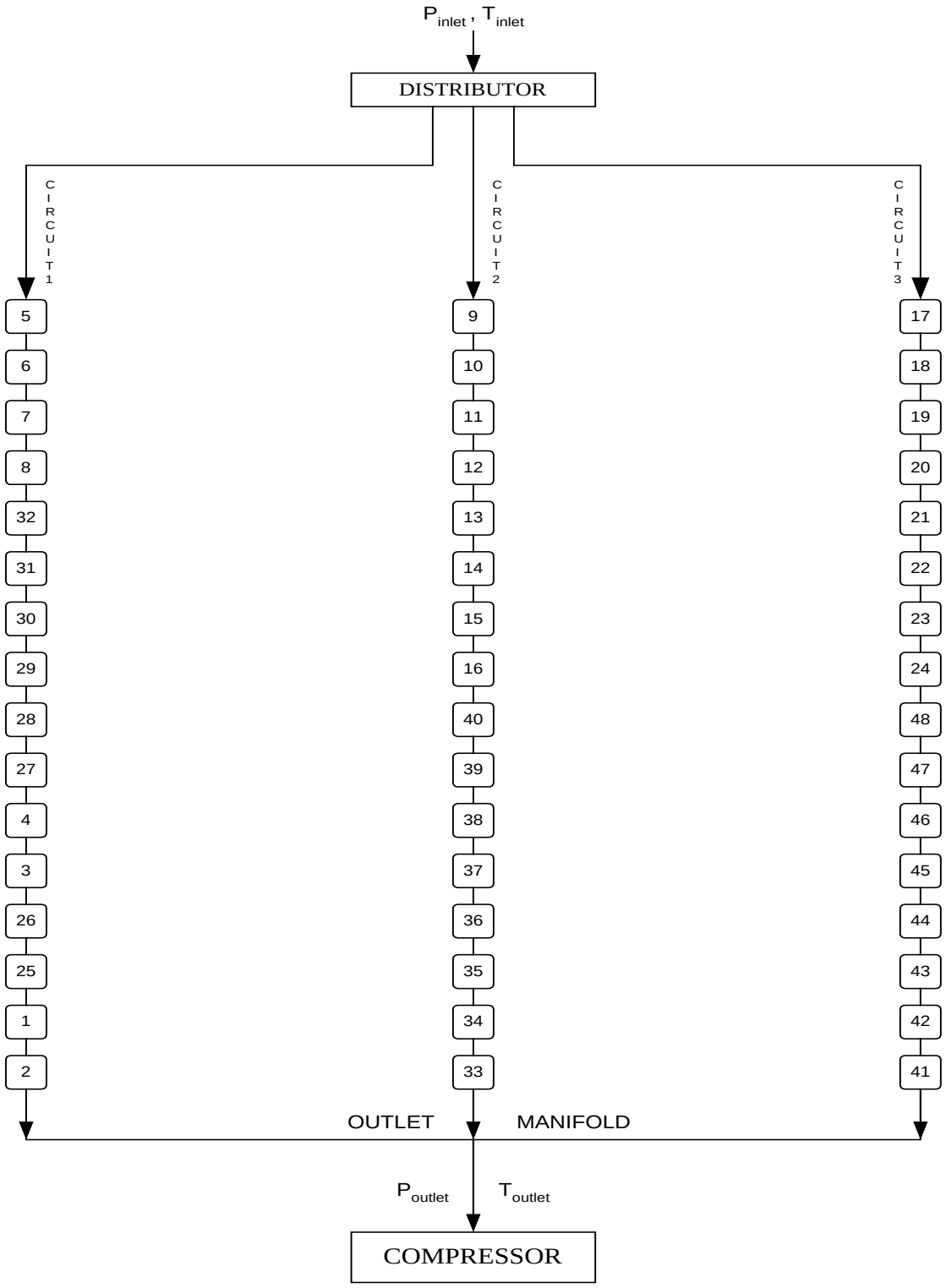

Figure 5.2 Tube calculation sequence for two-row coils

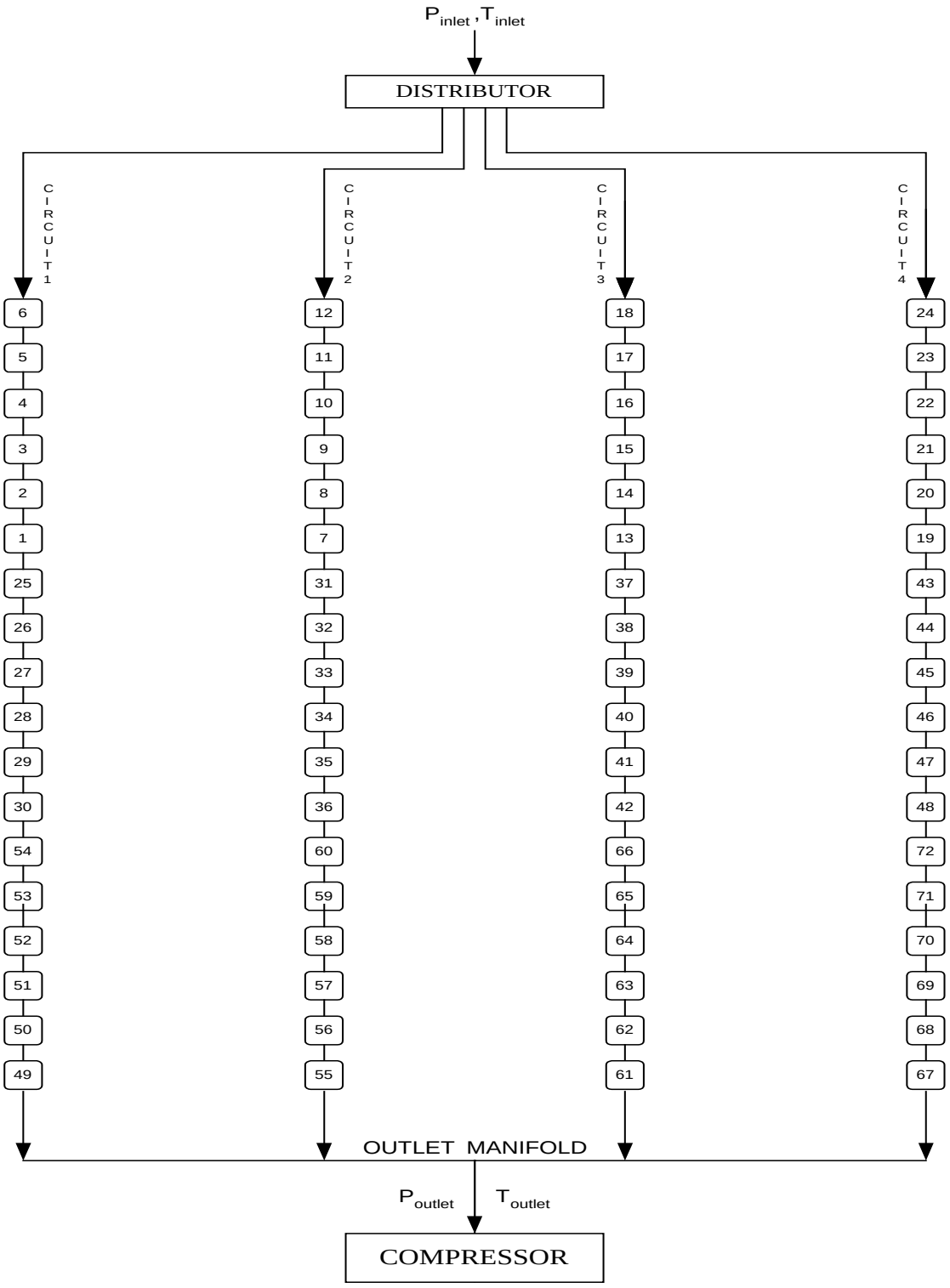

Figure 5.3 Tube calculation sequence for three-row coils

Model Structure and Organization

The current frosted evaporator model, PRJT1002, has been organized into a modular format and internally documented with extensive comments. The simulation program contains a main program and six subprograms, and each subprogram is composed of relevant subroutines. Data exchange among them is performed by common blocks. Figure 5.4 is the basic program structure of the model.

BASIC PROGRAM STRUCTURE

- Main Program:
  - FEModel (frosted evaporator model)
- Subprograms:
  - EVPHXF (conduct tube-by-tube simulation)
  - PCFROST (predict frost growth on fin surface)
  - PRCFM (update coil air flow rate)
  - RFRGRNT (calculate refrigerant properties)
  - PSYCHRO (calculate air psychrometric properties)
  - AUXLRY (prepare auxiliary data for program)
- Input File:
  - INPUT (input parameters of model)
- Output Files:
  - MOUTPUT (major calculation results for the whole coil)
  - DOUTPUT (detailed calculation results for each tube)
  - SECTFRST (frost calculation results for each section)
  - SECTAIR (air calculation results for each section)
  - AIRFLOW (air flow rate calculation information)
  - DIAGNOSE (iteration records and intermediate outputs)

Figure 5.4 Program structure of the frosted evaporator model

Each of the above subprograms contains a series of subroutines to be called by the main program or other subprograms. The structures and operations of four major subprograms (EVPHXF, PCFROST, PRCFM and RFRGRNT) are discussed below.

EVPHXF

Frost growth on the coil surface is a complex dynamic process. Based on the experimental observation, the growth of frost layer is not uniform over the coil. Generally, more frost accumulates on the fin surfaces of the first row than those of the back row. Similarly, frost growth is not uniform among different refrigerant circuits.

Both uneven distribution of frost and different coil geometry parameters such as fin pitch, require that the simulation model needs to estimate finned tube performance individually. Therefore, the NIST model, EVSIM, which uses a tube-by-tube approach, was chosen as the basis for the present frosted evaporator model.

EVSIM is a steady state model developed to predict heat exchanger performance under dry or wet working conditions. EVPHXF, the major subroutine of EVSIM, was retained and modified to allow it to work with other subprograms to construct the frosted evaporator model. Substantial modifications had to be made in the logic and structure of EVPHXF before it could serve as a subprogram for the quasi-steady state frosting model.

The model applies the tube-by-tube approach to compute the heat transfer rate and pressure drop from the inlet to the exit of coil. Performance of each tube is analyzed separately during each time step. At the outset of tube loop calculation, the model assumes uniform air distribution for each tube, and same air mass flow rate is specified.

Air properties at the entrance of the first row of finned tubes are the same as those at the coil entrance, which can be measured directly during tests. Air temperature and humidity at the exit of each row of finned tubes are calculated by assuming adiabatic mixing of the air stream from the exit of each tube. The tube downstream air properties are assumed at first, and then updated with new calculated values as the tube iteration loop is executed. In the tube iteration loop, the upstream air parameters are always fixed. The values are renewed in the circuit iteration loop. This procedure is considered reasonable for the circuitry with cross tube arrangement.

The refrigerant inlet properties of a tube, such as temperature, pressure, quality and mass flow rate, are specified based on the proceeding tube calculation results. Similar to the downstream air property calculations, the refrigerant parameters at the outlet of a tube are first assumed and then estimated through an iteration procedure.

Mean air and refrigerant properties for each finned tube are used to calculate the heat transfer and refrigerant-side pressure drop. Since only conditions at the tube inlet are known when the calculation starts, the outlet properties of both the air and refrigerant have to be assumed to execute the calculation. Downstream air and refrigerant properties may not be accurately known at first, so an iterative loop is used to update the outlet state of both the air and refrigerant using the calculated results of previous iteration step. The iterative calculation is continued until the successive values of refrigerant enthalpy at the tube

exit converge within the imposed tolerance. Under frosting conditions, the frost layer properties also have to be updated at each iteration loop.

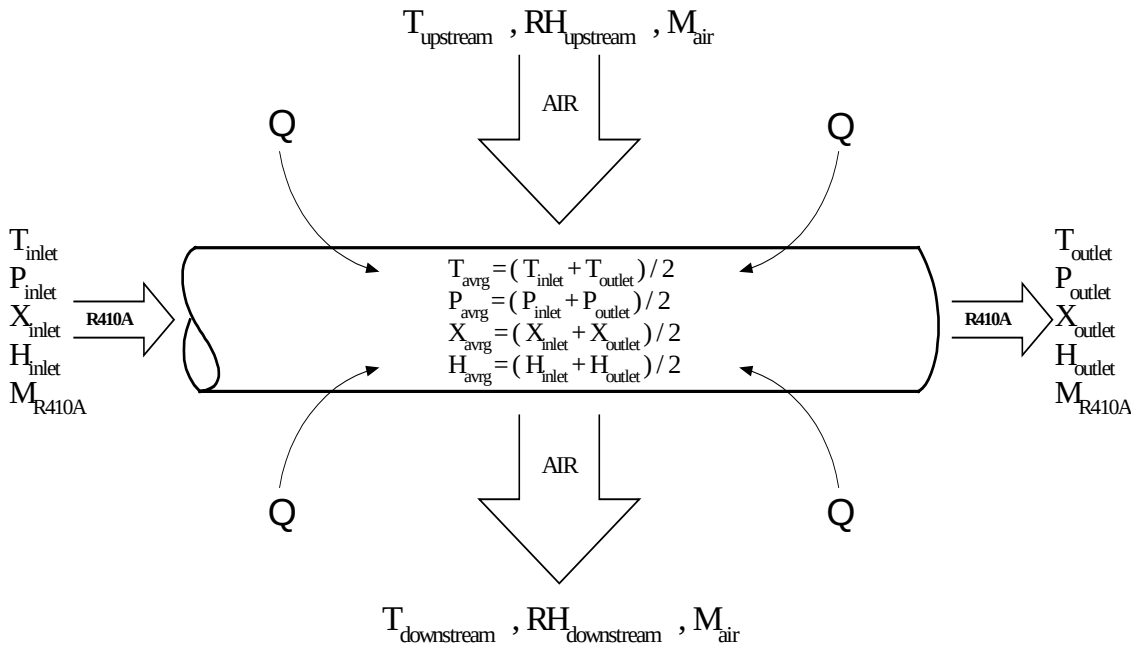

Figure 5.5 Parameters for tube calculation in EVPHXF

In the tube loop, after EVPHXF finishes the heat transfer and refrigerant pressure drop calculations for a tube, it calls PCFROST to estimate frost growth information for the next iteration step. Once properties of the frost layer are updated, the new thermal resistance of frost layer can be obtained and the next loop of the heat transfer calculation starts again. At the end of the subprogram, the calculation information for a time step is saved for the beginning of the next time step.

Because heat and mass transfer are usually different for each tube, the refrigerant pressure drop for each tube is not uniform. If the refrigerant circuitry is not symmetric, the refrigerant mass flow rates and the pressures at the outlet of each circuit may also be different. Therefore, the refrigerant distribution of each circuit has to be adjusted using the calculated total pressure drop of each circuit.

The selection of tubes for performance evaluation is same as the refrigerant flow direction, i.e. from the circuit inlet to circuit outlet. This forward calculation scheme assures the refrigerant state parameters at the entrance of each tube are always known.

PCFROST

Subprogram PCFROST is the frost growth model. It was developed to predict the frost layer growth as a function of time and position on the fin surface using a section-by-section method. The subprogram estimates the growth of the frost layer based upon the entering air temperature, humidity, air velocity and frost surface temperature. The growth of the frost layer is assumed to be uniform in each section.

A flow chart of the subprogram PCFROST is shown in Figure 5.5. This subprogram is called by EVPHXF for each tube calculation. Some of the necessary input data used in PCFROST are provided by EVPHXF at the beginning of each calculation. These include refrigerant and air inlet properties, airflow rate, coil dimensions and starting frost properties. Based on the initial conditions, variations of air enthalpy, temperature and humidity ratio, as well as frost thickness, density, conductivity and surface temperature, are calculated, respectively, section by section. The increases in frost density, conductivity and thickness are evaluated using energy balance equations and frost property equations. After the section loop is completed, the averaged properties of the frost layer are obtained for each tube at the given time step.

Because of the application of the section-by-section method, the frost properties at each section of an individual finned tube can be determined and stored in a series of dimensional arrays, and averaged once the section calculation loop is finished. The mean frost heights corresponding to each section in the airflow direction can be obtained based on all the values for the same depth sections for the different tubes in the same row. Major properties from the frost growth model, PCFROST, such as frost height, conductivity, density and frost surface temperature are carried back to EVPHXF and used to determine air pressure drop, heat and mass transfer in the heat exchanger section.

Typically, frost formation on the clean fin surface can be divided into two periods: 1) crystal growth period and 2) fully developed frost layer growth period (Hayashi, et al., 1977). At the start of frost growth period, water droplets are condensed and subcooled on the cold fin surface, then ice crystals form and grow in an ice-column form. Because the crystal growth period is short compared with the whole frosting test and some drainage remains on the coil surfaces after defrost cycle. This period is not modeled in PCFROST.

The section-by-section analysis depends on the knowledge of the variations of heat and mass transfer coefficients with both time and position. The average tube heat transfer coefficient based on Gray and Webb's correlation (1989) is obtained from the subprogram EVPHXF, which changes at each time step in the transient process. The Saboya and Sparrow's correlation (1974) is used to assign local distribution of heat transfer coefficients for each section. The local and average mass transfer coefficients for the finned tube can be obtained by the analogy between heat and mass transfer.

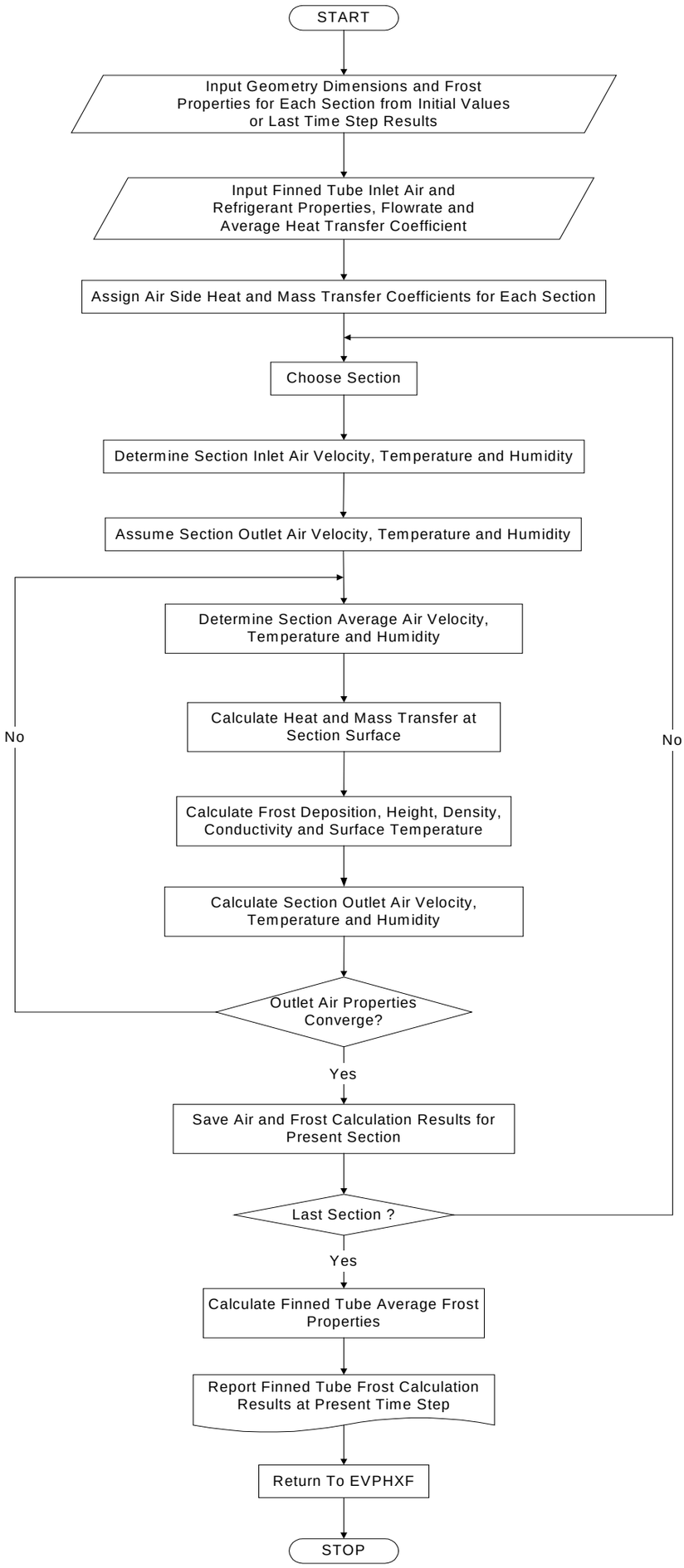

Figure 5.6 Flow chart of subprogram PCFROST

Because of the application of the section-by-section method, the frost properties at each section of an individual finned tube can be determined and stored in a series of dimensional arrays, and averaged once the section calculation loop is finished. The mean frost heights corresponding to each section in the airflow direction can be obtained based on all the values for the same depth sections for the different tubes in the same row. Major properties from the frost growth model, PCFROST, such as frost height, conductivity, density and frost surface temperature are carried back to EVPHXF and used to determine air pressure drop, heat and mass transfer in the heat exchanger section.

Typically, frost formation on the clean fin surface can be divided into two periods: 1) crystal growth period and 2) fully developed frost layer growth period (Hayashi, et al., 1977). At the start of frost growth period, water droplets are condensed and subcooled on the cold fin surface, then ice crystals form and grow in ice-columns. Because the crystal growth period is short compared with the whole frosting test and some drainage remains on the coil surfaces after defrost cycle, this period is not modeled in PCFROST.

The section-by-section analysis depends on the knowledge of the variations of heat and mass transfer coefficients with both time and position. The average tube heat transfer coefficient based on Gray and Webb's correlation (1989) is obtained from subprogram EVPHXF, which changes at each time step in the transient process. The Saboya and Sparrow's correlation (1974) is used to assign local distribution of heat transfer coefficients for each section. The local and average mass transfer coefficients for the finned tube can be obtained by the Reynolds/Colburn/Chilton-Colburn analogy between heat and mass transfer.

The fin plates on each tube are artificially divided into ten sections starting at the entrance edges and ending at the exit edges. These are illustrated in Figure 5.6. This allows estimating the spatial variation of air properties and frost layer growth in two dimensions: perpendicular to the central fin surface and along the air flow direction.

It should be noted that because the tube hole occupies about 12% of the product of fin nominal length and width, the cross sectional area of the tube hole is subtracted when determining the surface area for the heat and mass transfer of the fin plate. The increase in heat transfer surface area of the fin, caused by the presence of frost crystals, is neglected.

The mass transfer occurring at the frost surface is calculated using an energy and mass balance. The frost density is determined by the amount of mass diffusion into the frost layer with the height at the previous time step. The frost conductivity is related only to the frost density by a simple correlation.

The model includes an estimate of the one-dimensional variation of the frost layer properties in the nominal direction of the fin surface. Diffusion inside the frost layer can be considered by estimating different thermo-physical properties (density and thermal conductivity) of the frost layer. The densification of the frost leads to an increased thermal conductivity and thus retards the increase of frost layer thermal resistance. The average frost thickness for a given time and fixed surrounding air conditions

can be more accurately predicted than in the case of assuming uniform frost density or frost conductivity over the whole fin plate.

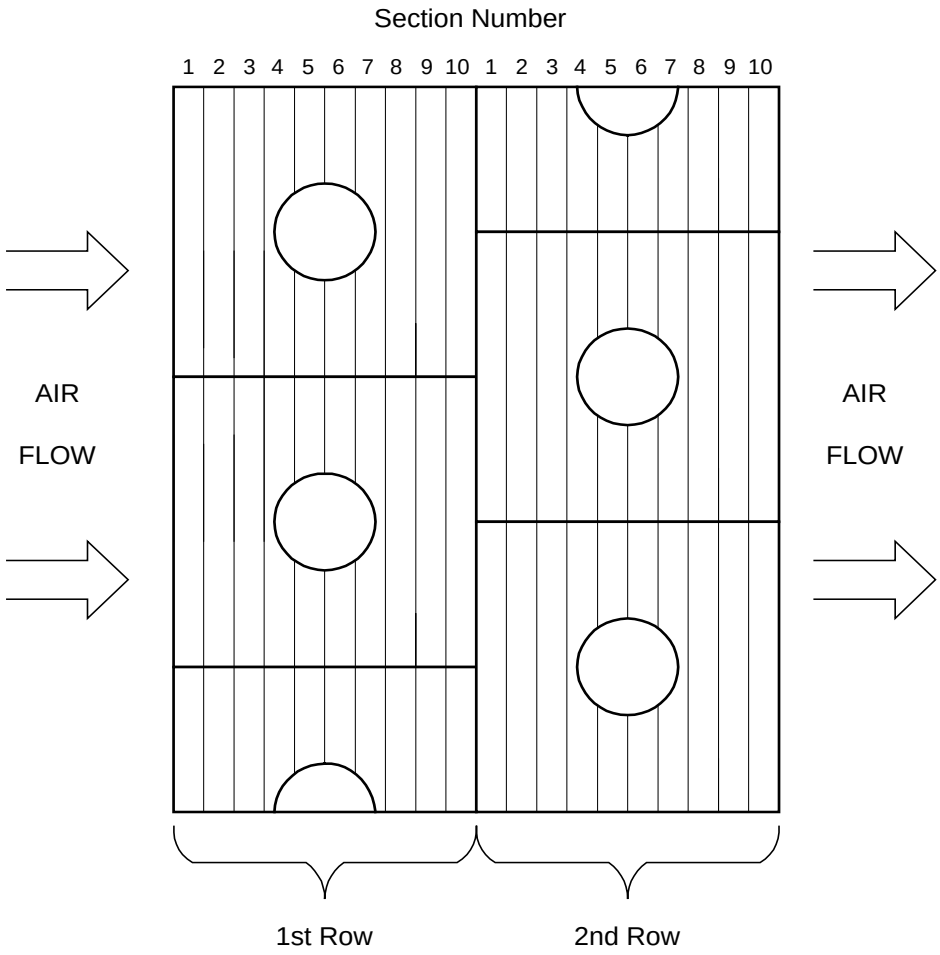

Figure 5.7 Schematic section-by-section diagram

In spite of the radial distribution characteristic of the fin surface temperature, the assumption of uniform fin surface temperature for individual section has been applied to simplify the calculation of frost surface temperature. In the section-by-section model, all the properties corresponding to each section are constant in one section iteration loop except the average and outlet air state parameters.

PRCFM

To consider the decrease in airflow rate as frost grows, the pressure and fan model, PRCFM, was developed to estimate the airflow resistance through the frosted coil, and use a fan characteristic curve to estimate the degradation in airflow. The prediction of airflow through frosted coil has a large effect on the accuracy of the entire frosted evaporator simulation. With frost accumulating on the heat exchanger, it blocks some of the free flow area of the channels between the fin surfaces. As a result, the airside pressure drop through the frosted coil increases gradually. PRCFM is called in the main program at the end of each time step to update the airflow rate across the frosted coil due to the blockage of increased frost accumulation.

The fan characteristic curves are used in PRCFM to determine the new airflow rate at each time step for the frosted evaporator. Experimental data for the two propeller fans used in this project were obtained from a series of fan tests conducted in an AMCA fan chamber. The data were curve-fit into proper mathematical expressions for use in the pressure drop subprogram. Because the fan curves are achieved together with the unit top cover, the pressure drop across the fan cover is not considered separately. The fan pressure-flowrate curves need to be used to find the airflow rate corresponding to the airside pressure drop estimated by the calculation subroutines. These routines mainly account for frictional drag created by the fins and tubes, as well as the contraction and expansion loss in the airflow passages between the fins created by frost forming on the fins.

Both static and total air pressure variations from the inlet to the outlet of outdoor coil unit are shown in Figure 5.7.

The difference between the static pressure at the exit of the outdoor unit and barometric pressure is taken as ΔP_{static}. This item is then subtracted from the fan static pressure rise to obtain the absolute static pressure upstream of fan. Here, the velocity head difference at heat exchanger leaving face and fan inlet is considered as well.

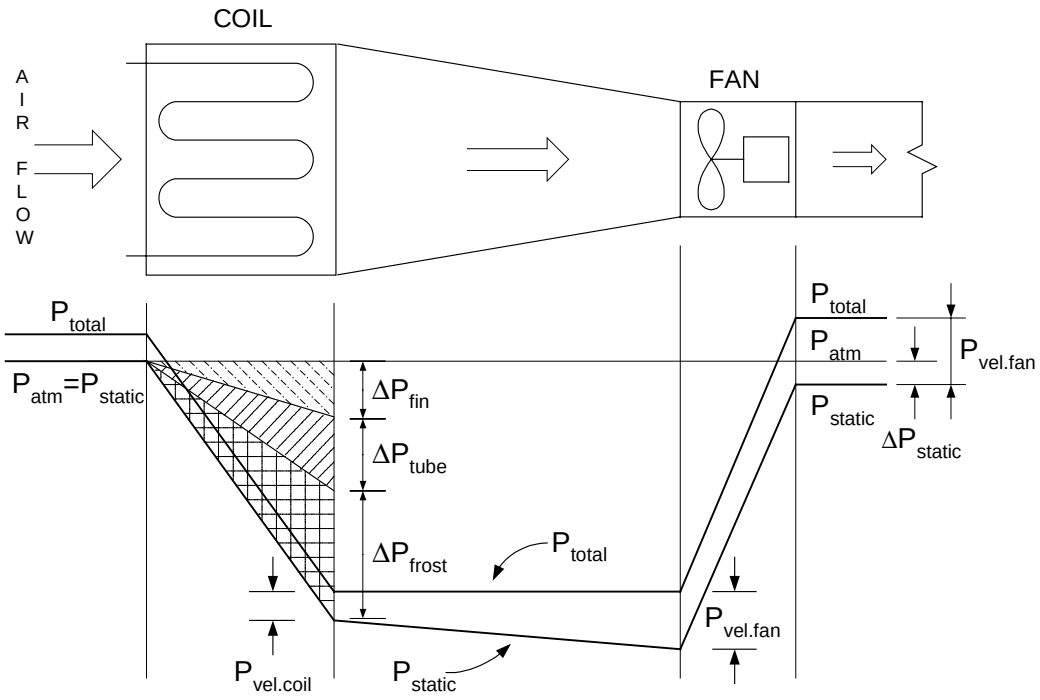

Figure 5.8 Pressure profile of outdoor coil-and-fan unit

The static air pressure drop through the frosted coil can be evaluated using fan static pressure, coil outlet static pressure and velocity head change inside the coil-and-fan unit:

$$\Delta P_{coil.static} = \left(\Delta P_{fan.static} - \Delta P_{static}\right) - \left(P_{vel.fan} - P_{vel.coil}\right) \tag{5.1}$$

Where:

$\Delta P_{coil.static}$:	coil static pressure drop
$\Delta P_{fan.static}$:	fan curve static pressure
ΔP_{static} :	gauge static pressure at fan exit
$P_{vel.fan}$:	velocity head of air through fan
$P_{vel.coil}$:	velocity head of air through coil

Thus, the aerodynamic pressure rise through fan and unit cover is:

$$\Delta P_{fan.static} = (\Delta P_{coil.static} + \Delta P_{static}) + (P_{vel.\,fan} - P_{vel.coil}) \tag{5.2}$$

If the static pressure at the unit outlet is kept at the barometric pressure and the variation of velocity head inside coil unit is neglected, the value of the static pressure drop through the coil ($\Delta P_{coil.static}$) should be equal to that of the pressure increase across the fan ($\Delta P_{fan.static}$). The operating performance of the outdoor fan directly depends on the air pressure drop through the frosted coil.

To balance the increased airflow resistance due to frost growth, the operating point of the outdoor fan should move up along the fan curve to the left to provide a higher pressure. The move to the left on the fan curve also produces a decrease in flow. Figure 5.8 shows the procedure of the operating point moving on the fan characteristic curve.

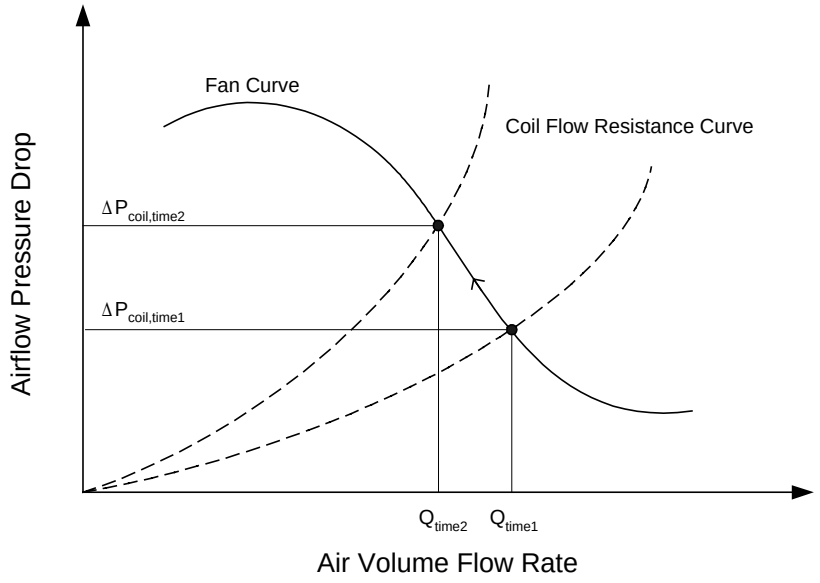

Figure 5.9 Correlation of fan curve and coil flow resistance

In the subprogram PRCFM, air psychrometric properties are calculated based upon the average air temperature across evaporator coil. The air pressure drop across the frosted coil is obtained with several subroutines in PRCFM, which mainly account for friction drags of fin surfaces and tube bank, as well as contraction and expansion losses across the frosted fin channels.

At the first time step, the initial air pressure drop is determined from the input airflow rate. Then, at the following time steps, calculation results for frost layer from PCFROST, together with the air flow rate obtained at the end of last time step by PRCFM, are used to determine the new coil pressure drop at the present time step. Finally, at the end of the calculation, a new airflow rate can be found by using a Newton-Rapson iteration technique applied to the fan characteristic curve and the airflow pressure drop through coil. Figure 5.9 shows the flow chart of subprogram PRCFM.

During the internal calculation of PRCFM at a time step, the Newton-Rapson iteration scheme is applied to determine the airflow rate at a given pressure drop. The possible dual-direction of the attempting calculation of Newton-Rapson iteration might estimate a value far away from the true value. To assure, under no circumstance, the variation of airflow rate could be positive.

RFRGRNT

RFRGRNT is a subprogram which provides thermophysical and transport properties of refrigerant for the frosted evaporator model. R-410A is used as the refrigerant for the heat pump systems tested in this project. It is a near azeotropic binary mixture of 50% R32 and 50% R125.

Only two refrigerants (R12 and R22) were available in EVSIM. Due to its inability to provide R-410A thermal and physical properties, a series of new subroutines and functions were developed for the frosted model. The present subprogram RFRGRNT is able to calculate not only R-410A but also many other new HFC replacements by inputting the appropriate coefficients. Four methods are currently used for R-410A thermodynamic property calculations: Martin-Hou EOS (AlliedSignal), Extended Martin-Hou EOS (DuPont), REFPROP (NIST) and EES (F-Chart Software). AlliedSignal Inc. provides thermodynamic properties based on the Martin-Hou equation of state. DuPont developed their extended Martin-Hou EOS to fit test data from their thermodynamic property chamber. NIST employed a more general model to predict the thermodynamic properties of mixtures in REFPROP, which applies mixing rules to the pure fluid Helmholtz energies of the mixture components.

After comparing the above four methods (Appendix A), AlliedSignal's Martin-Hou EOS was chosen for use in RFGRNT to calculate the R-410A thermodynamic properties. Because the liquid viscosity values calculated by AlliedSignal Martin-Hou EOS are found to be higher than the measurement by about 40%, DuPont's equations were used to develop subroutines for R-410A transport property calculation.

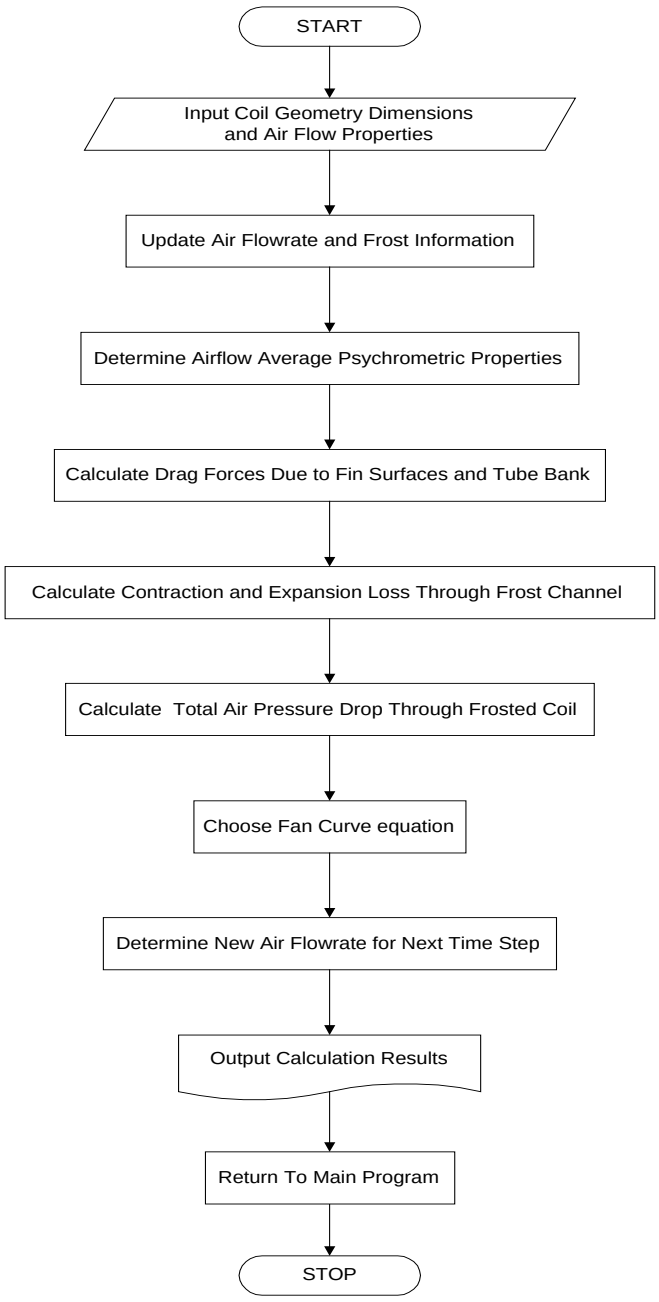

Figure 5.10 Flow chart of subprogram PRCFM

Model Input and Output

The frosted evaporator model is used to calculate heat exchanger performance under frosting conditions as a function of initial airflow rate and ambient conditions. The ambient entering temperature and relative humidity are always assumed constant during each simulation. Although the tube-by-tube evaporator model can evaluate uneven airflow distribution among the individual tubes, uniform air velocity profiles at the entrance of testing coil were assumed for all simulations. The velocity component in the vertical direction is considered to be zero.

The frosted evaporator model requires a series of input parameters and physical constants. They are obtained by either external input data file or curve-fitting equations of test data.

To reduce the amount of data that the user must specify for each run, some of the input data are read by the program from an input data file named INPUT.dat, which provides evaporator design data (Table 2.1), refrigerant flow distribution sequence (Figures 5.2 and 5.3), air inlet conditions, refrigerant name, running time and initial airflow rate. These parameters are unlikely to be changed frequently from one use of the program to another.

Apart from input data file, the model acquires other input variables from the curve-fitting equations of the test data. These data include refrigerant temperature, pressure and mass flow rate at the inlet of evaporator (before distributor), and air flow rate through frosted coil. Table 5.1 lists a set of the curve-fitting equations used by the model for the two-row standard coil with high airflow during 35°F frost test.

Use of curve-fitting equations has some advantages over reading data directly from an input file in that it could avoid influences caused by fluctuations of individual points in the test data. Especially, during the later periods of most frosting tests, the hunting of the TXV causes large unstability associated with the test data of refrigerant inlet parameters. The curve-fitting equations are able to keep the varying tendencies of these parameters.

The simulation of the transient freezing process is very sensitive to the variations of both air and refrigerant inlet conditions. A small discrepancy of any inlet condition could have significant effects on the results of simulation model. This requires the best curve-fitting equations be used to accurately describe the time-varying inlet parameters. Because the flexibility of the test data under different experimental conditions, no fixed format of curve-fitting equation was chosen. Therefore, no coefficient of curve-fitting equation is assigned by the input file. All the necessary equations are directly input at the start of main program. This feature allows the user to choose different mathematical equations to better fit the experimental data before running the new tests.

It should be emphasized that because of the fast transient behavior at the startup of the heat pump system, there exist large uncertainties associated with the measurements of inlet properties during the first few minutes. Because the curve-fitting equations are obtained based on the experimental data over the

whole freezing process, the deviation at the start of system can be large. Therefore, for the first three to four minutes, the input data are given individually based upon the moving average value in one minute.

Table 5.1 Curve-fitting equations of the test data for the two-row standard coil (20/20 fpi) with high airflow (2700 cfm) during 35°F frost test

Refrigerant Inlet Pressure (P_0)	P_0 = 119.305 @ TIME = 0 118.555 @ TIME = 1 124.125 @ TIME = 2 When TIME > 2 $P_0 = 123.6156 + 0.7706673*TIME - 0.1483136*TIME^2 + 0.00728707*TIME^3 - 0.00014446*TIME^4 + 9.6E\text{-}7*TIME^5$ (psia)
Refrigerant Inlet Temperature (T_0)	T_0 = 33.5 @ TIME = 0 33.2 @ TIME = 1 35.5 @ TIME = 2 When TIME > 2 $T_0 = 35.67364 + 0.3319693*TIME - 0.06986096*TIME^2 + 0.00344154*TIME^3 - 0.0000668*TIME^4 + 4.3E\text{-}7*TIME^5$ (^oF)
Refrigerant Mass Flow Rate (RMASS)	RMASS = 344.34 @ TIME = 0 270.30 @ TIME = 1 281.52 @ TIME = 2 When TIME > 2 $RMASS = 285.2007 + 2.35019*TIME - 0.38373*TIME^2 + 0.01972*TIME^3 - 4.188E\text{-}4*TIME^4 + 3E\text{-}6*TIME^5$ (lb_m/h)
Air Volume Flow Rate (CFM)	$CFM = 2662.859 + 20.54542*TIME - 3.482096*TIME^2 + 0.1644918*TIME^3 - 0.00428054*TIME^4 + 4.323E\text{-}5*TIME^5 - 8E\text{-}8*TIME^6$ (cfm)

The prediction of pressure drop or airflow across the frosted coil has the largest effect on the accuracy of model simulation. It affects the frost growth and the frost growth, in turn, changes the airflow. To avoid the influence of inaccurate estimation of the airflow and obtain better calculation results, at each time step, the airflow in the present simulation is provided from curve-fitting equation based upon the experimental data instead of the simulation results at the end of each time step.

A set of initial values of frost height, conductivity and density are assumed at the start of modeling. This initial frost layer is required because the frost growth model considers the frost layer to be a porous media. The equations for a porous media cannot be used when there is no frost on the fin surface. Therefore, at the start of the numerical calculations, the initialization of the frost layer properties is necessary. A very small thickness (0.01mm) was chosen as the initial frost height. The growth rate of frost layer shows little dependence on the assumed initial thickness so that the estimated results of frost growth are fairly insensitive to the initial values selected.

During the simulation process, six external data files are opened to keep information for the calculation process separately. A summary output and a detailed output are available for the frosted evaporator model. The main output file (MOUTPUT.dat) contains a summary of coil performance information (e.g. heat transfer capacity, air flow rate, pressure drop, frosting rate, frost layer height, air and refrigerant outlet conditions). It saves the continuous calculation results throughout the entire sequence of computations. The program has a more detailed output file (DOUTPUT.dat), which records the completed output for individual iteration loops. This output file provides an option for more specific calculation information.

Both spatial and temporal variations of the frost layer and air properties corresponding to each section are provided by the subprogram PCFROST and written in two output file SECTFRST.dat and SECTAIR.dat, respectively. While SI units are used in the internal calculations of subprogram, PCFROST, all the output results are in English units.

The calculation results of airflow model PRCFM are stored into a data file named AIRFLOW.dat. In addition, all the necessary iterative records and intermediate calculation results of the model are recorded for diagnostic purpose by the file DIAGNOSE.dat. Thus, the process of iterative calculation and the operation of program can be monitored and analyzed easily.

CHAPTER VI

MODEL CALCULATIONS

The literature review produced no studies involved in the evaluation of airside heat transfer coefficient and friction factor for fin staged coils. The main reason is that no heat pump manufacturers are currently applying front fin staging on their outdoor heat exchangers. New methods for calculating the airside heat transfer coefficient and friction factor must be developed and applied to the simulation model of fin staged coil. Physical principles and calculation correlations are discussed.

Refrigerant R-410A Property Calculation

In this project, R-410A is used as the refrigerant for heat pump unit. This refrigerant is a near azeotropic binary mixture of 50% R-32 (CF_2H_2) and 50% R-125 (CF_3-CF_2H). As one of the primary long-term HFC alternatives for HCFC-22, R-410A serves in a variety of residential and commercial air conditioning equipment. It has a significantly higher capacity and pressure than R-22 and an intrinsically low toxicity. Allied Signal names their R-410A product as Genetron AZ-20. The commercial designation by DuPont is SUVA410A.

Knowledge of the refrigerant properties is essential for the design and application of air-conditioning and refrigeration equipment. In the present simulation, a tube-by-tube method has been applied to calculate the heat transfer rate and pressure drop of the outdoor heat exchanger. Highly accurate thermodynamic and transport properties of the heat transfer fluid, such as enthalpy, pressure, temperature, density, viscosity, thermal conductivity and specific heat, are required. Local heat transfer coefficients and friction factors also needed for each individual tube.

There are five methods currently available for R-410A thermodynamic property calculations: Martin-Hou EOS (Allied Signal), Extended Martin-Hou EOS (DuPont), REFPROP (NIST), van der Waals EOS (Yokozeki, 1996) and EES (F-Chart Software). Allied Signal Inc. (1996) provides Genetron AZ-20 thermodynamic table based on the Martin-Hou equation of state. Using this equation of state and other thermodynamic relations, a complete set of refrigerant R-410A thermodynamic properties can be determined under any conditions.

DuPont developed the extended Martin-Hou EOS because the Clapeyron equation is less accurate for mixtures having different liquid and vapor compositions (Bivens and Yokozeki, 1996). The Martin-Hou method uses the Clapeyron equation to calculate latent heat of vaporization and to obtain saturated liquid enthalpies and entropies. However, the Clapeyron equation is not accurate for mixtures that have different liquid and vapor compositions. In the extended Martin-Hou equation of state and coefficients for

R-410A, the Martin-Hou procedure is still applied. An empirical fit of the saturated liquid enthalpy is used to replace the Clapeyron equation. Also an empirical fit of the dew point pressure curve is used. As reported by Bivens and Yokozeki (1996), the extended Martin-Hou equation of state has accuracy within 1-2% of the experimental data.

Different from Allied Signal and DuPont, NIST employs a more general model to calculate the thermodynamic properties of mixtures in REFPROP, which applies mixing rules to the pure fluid Helmholtz energies of the mixture components. REFPROP implements three models for the thermodynamic properties of pure fluids: the modified Benedict-Webb-Rubin (MBWR) and Helmholtz equations of state, and an extended corresponding states (ECS) model. Mixture calculations employ a model which applies mixing rules to the pure-fluid Helmholtz energies. By applying mixing rules to the Helmholtz energy of the mixture components, it allows the use of high-accuracy equations of state for the components, and the properties of the mixture will reduce exactly to the pure components as the composition approaches a mole fraction of 1. The flexibility of the adjustable parameters in this model allows an accurate representation of a wide variety of mixtures.

Yokozeki (1996) used the classical van der Waals EOS to develop the general binary mixture equations of state. With the pure-compound equations, the equations of state for general mixtures were constructed using the conventional mixing rules. The thermodynamic calculations are simpler than with any other many-term equations of state, and the parameters in the equations can be obtained in a relatively simple manner from rather limited experimental data. After few empirical modifications, this relatively simple method of thermodynamic calculations could be successfully applied to the binary mixture of R-32 and R-125 with the same level of accuracy as that in pure compounds.

EES uses a simplified version of the DuPont extended Martin-Hou correlation. No detailed description about this simplified correlation was found in the public domain. Appendix A shows the calculation equations and the comparisons of R-410A saturated and vapor property calculation for the different methods. Coefficients for R-410A property calculation by the methods are also included in Appendix A.

Only two refrigerants (R-12 and R-22) were available in EVSIM. Due to its inability to provide R-410A thermalphysical and transport properties, a series of new subroutines and functions for the property calculation of R-410A were developed in the frosted evaporator model. The Martin-Hou EOS (Martin and Hou, 1955) has been widely used in the air-conditioning and refrigerant industry. For R-410A, the binary mixture system forms azeotropes with high molar fraction of R-32. A composition of this mixture behaves like an azeotrope in the sense that the bubble and dew point pressures are nearly the same (<1%). So, the refrigerant R-410A can be treated as azeotropes and Martin's procedure (Martin 1959) can be applied after using the empirical fitting correlation (Bivens et al, 1995). The Mark V of the ORNL heat pump model and the present data acquisition system of the psychrometric rooms both use the

Allied Signal's standard Martin-Hou EOS. The calculation results from this correlation match the Allied Signal's property test data very well. Therefore, the standard Martin-Hou EOS has been chosen for use in the refrigerant property subprogram of the present frosted evaporator model to calculate the R-410A thermodynamic properties.

Chi's (1979) 5^{th} power polynomial equations for refrigerant viscosity and conductivity calculations in the original EVSIM were developed particularly for refrigerant R-12 and R-22. In the evaporation temperature range of an heat pump outdoor coil, the liquid and vapor thermal conductivity of R-410A is higher than that of R-22. The liquid viscosity of R-410A is much lower than that of R-22, while its vapor viscosity is slightly higher than that of R-22. To obtain better property calculations of refrigerant R-410A, the Chi's correlation needs to be replaced. Because the liquid viscosity values calculated by Allied Signal Martin-Hou EOS were found to be higher by about 40% (Dr. Rice) than the test data. DuPont's curve-fitting equations of R-410A transport property calculation were chosen to develop subroutines for the present frosted evaporator model, which are included in Appendix A as well.

Some of the refrigerant subroutines came directly from the ORNL heat pump model (Fischer and Rice, 1983). Others were developed to meet the needs of more detailed refrigerant properties for the tube-by-tube method. Both thermodynamic and transport properties at single- or two-phase states can be calculated by these subroutines at specific pressures, temperatures, qualities, etc. The present subprogram of refrigerant property calculation estimates properties not only for refrigerant R-410A, but also more than twenty refrigerants. The different refrigerants can be chosen at the beginning of the main program before the subprogram of the refrigerant property calculation is called. Constants of the selected refrigerant have been included in the refrigerant subprogram.

Refrigerant Side Heat Transfer and Pressure Drop

Because there is no general empirical correlation currently available to estimate the evaporation heat transfer coefficient and the pressure drop for refrigerant R-410A flowing inside enhanced copper tubes, the original R-22 calculation equations of EVSIM continue to be used. The appropriate corrections on the basis of the comparison of experimental results between R-22 and R-410A have been done.

Refrigerant Side Heat Transfer Coefficient

For analyzing the heat transfer within the evaporator involving phase change, refrigerant flow is subdivided into separate heat transfer zones (subcooling, two-phase and superheated). The two-phase heat transfer characteristics is strongly related to the flow pattern. In EVSIM, the two-phase heat transfer zone inside a horizontal tube included two flow patterns: annular flow and mist flow. The quality value of 0.85 was selected as the border point between these two flow patterns (Domanski, 1989). Refrigerant generally enters an evaporator from the expansion device at two-phase state and forms an annular flow instantly.

The quality increases with the proceeding flow and the annular flow pattern is maintained until the quality reaches about 0.85 to 0.90, at which refrigerant vapor has enough kinetic energy to gradually destroy the liquid layer and patches of dry wall appear. The annular flow pattern then transitions to mist flow. It's likely that the refrigerant leaves in a superheated state.

The refrigerant heat transfer coefficients for the different flowing regions in the evaporator are calculated by using different empirical equations. A correlation developed by Gungor and Winterton (1986) is used to calculate the evaporation heat transfer coefficient for the annular flow regime inside smooth tubes:

$$h_{an} = E \cdot h_{liq} + S \cdot h_{pool} \tag{6.1}$$

$$h_{liq} = 0.023 \cdot \mathrm{Re}^{0.8} \cdot \mathrm{Pr}_l^{0.4} \cdot K_l / D_i \tag{6.2}$$

$$h_{pool} = 55 \cdot P_{red}^{0.12} \cdot (-\log_{10} P_{red})^{-0.55} \cdot M^{-0.5} \cdot q^{0.67} \tag{6.3}$$

$$E = 1 + 24000 \cdot Bo^{1.16} + 1.37 \cdot X^{-0.86} \tag{6.4}$$

$$S = (1 + 1.15 \times 10^{-6} \cdot E^2 \cdot \mathrm{Re}^{1.17})^{-1} \tag{6.5}$$

where,

h_{liq}:	liquid convection heat transfer coefficient
h_{pool}:	pool boiling heat transfer coefficient
E, S:	weighting factors to average h_{liq} and h_{pool}
X:	flow vapor quality
q:	heat flux
K_l:	thermal conductivity of refrigerant liquid
M:	molecular weight of refrigerant
D_i:	tube inner diameter
P_{red}:	reduced pressure
Re:	Reynolds number
Pr_l:	liquid Prandtl number
Bo:	boiling number

The heat transfer coefficient for mist flow, h_m (flow quality range 0.85-1.00), was calculated in EVSIM by weighting the heat transfer coefficient values at the end of annular flow and the start of single-phase superheated flow:

$$h_m = (1.0 - X) \cdot h_{an} + (X - 0.85) \cdot h_{sp} \tag{6.6}$$

where,

X:	average fractional flow quality for the mist flow in a tube
h_{an}:	heat transfer coefficient at the end of annular flow (X=0.85)
h_{sp}:	heat transfer coefficient at the saturated vapor point (X=1.0)

The single-phase (subcooling liquid or superheated vapor) convective heat transfer coefficeint, h_{sp}, for refrigerant flowing through a smooth, heated horizontal tube can be calculated by the most frequently used empirical equation:

$$h_{sp} = 0.023 \cdot \mathrm{Re}_{sp}^{0.8} \cdot \mathrm{Pr}_{sp}^{0.4} \cdot K_{sp} / D_i \tag{6.7}$$

where

Re_{sp}:	Reynolds number of single-phase refrigerant
Pr_{sp}:	Prandtl number of single-phase refrigerant
K_{sp}:	thermal conductivity of single-phase refrigerant
D_i:	tube inner diameter

In the tube-by-tube simulation procedure, the individual tube of the heat exchanger is the calculation unit. To estimate the refrigerant-side heat transfer coefficient for each tube, the phase states of the refrigerant flowing inside the heat exchanger tubes need to be determined by the tube inlet and outlet states. In the two-phase region, the calculation relation of the refrigerant-side heat transfer coefficient corresponding to the specific flow patterns for each tube can be chosen based on the vapor quality values at both ends of the tube. A single flow state (i.e., subcooling, annular, mist or superheated flow) is normally found throughout the length of the tube. For the tube where the transition of the refrigerant flow pattern occurs, such as from the annular flow to the mist flow at x=0.85, the distribution fraction of the refrigerant flow pattern inside the tube needs to be determined first. Then, the refrigerant-side heat transfer coefficient of the whole tube can be obtained by averaging the values of heat transfer coefficient with respect to the two parts with different flow patterns.

A review of recent research on the heat transfer and pressure drop characteristics of refrigerant R-410A during evaporating inside coil tubes reveals that only a limited number of studies have been published (Wijaya and Spatz, 1995, Ebisu and Torikoshin, 1998 and Wang et al., 1998). Wijaya and Spatz (1995) conducted the heat transfer and pressure drop experiments for R-410A (w/o oil) on both

condensation and evaporation performance. The condenser/evaporator test sections consist of smooth, horizontal copper tubes of 3/8inch (9.53mm) outer diameter (OD) and 0.305inch (7.75mm) inner diameter (ID). The saturated condensing temperatures were 115°F (46.1°C) and 125°F (51.7°C), while the saturated evaporating temperature was 40°F (4.4°C). The average inlet and exit qualities for the condensation tests was 87% and 25%, respectively, and for the evaporation tests they were 20% and 90%, respectively. The mass flux was varied from 118 $Mlb_m/ft^2 \cdot h$ (160 $kg/m^2 \bullet s$) to 414 $Mlb_m/ft^2 \cdot h$ (561 $kg/m^2 \cdot s$). Their data indicated that the condensation heat transfer coefficients of R-410A were slightly higher (about 2% to 6%) than those of R-22. The pressure drops for R-410A were significantly lower (about 25% to 45%). However, the evaporation heat transfer coefficients of R-410A were much higher (about 23% to 63%) than those of R-22, and its pressure drops were significantly lower (about 20% to 38%) than those of R-22.

Ebisu and Torikoshi (1998) provided experimental data on the local heat transfer coefficient and pressure drop for R-410A flowing inside a horizontal smooth tube with an outside diameter (OD) of 7.0 mm (0.28 inch). The saturated temperatures of the refrigerant at the test section were maintained at 278°K (36.85°F) and 323°K (121.73°F), respectively. Measurements of the heat transfer coefficient and pressure drop were carried out for the refrigerant mass fluxes of 300 $kg/m^2 \cdot s$ (221 $Mlb_m/ft^2 \cdot h$) and 150 $kg/m^2 \cdot s$ (111 $Mlb_m/ft^2 \cdot h$) under a constant heat flux of 7.5 kW/m^2 (2.39 $MBtu/ft^2 \cdot hr$). They found that the evaporative heat transfer coefficients of R-410A were about 20% higher than those of R-22 up to a quality of 0.4, but both refrigerants showed similar heat transfer coefficients at the quality of 0.6. On the other hand, R-410A showed slightly lower condensing heat transfer coefficients than R-22 for all qualities. The pressure drops of R-410A were about 30% lower than those of R-22 during evaporation and condensation. The comparison of the experimental result to the existing correlation (Yoshida et al. 1991) showed good agreement for the evaporation heat transfer coefficients. Meanwhile, a new correlation of two-phase friction multipliers for evaporation and condensation pressure drops was developed.

Wang et al. (1998) studied the two-phase evaporation heat transfer and pressure drop characteristics for both R-410A and R-22 in a smooth tube with a 6.54 mm (0.257 inch) ID. The data were taken at an evaporation temperature of 2°C (35.6°F). The mass flux was between 100 $kg/m^2 \cdot s$ (73.75 $Mlb_m/ft^2 \cdot h$) and 400 $kg/m^2 \cdot s$ (295 $Mlb_m/ft^2 \cdot h$), and the heat flux was between 2.5 kw/m^2 (0.793 $MBtu/ft^2 \cdot h$) and 20 kw/m^2 (6.34 $MBtu/ft^2 \cdot h$). The effects of heat flux and mass flux on the heat transfer coefficients were examined. The heat transfer coefficients of R-410A were 10-20% higher than those of R-22 when the mass flux was 100 $kg/m^2 \cdot s$. For the mass flux 400 $kg/m^2 \cdot s$, the heat transfer coefficients of R-22, with the changing of heat flux, may be higher than those of R-410A at a certain vapor quality. The pressure drops of R-410A were about 30-40% lower than those of R-22.

Although the above investigations agree with their results qualitatively, they are quantitatively inconsistent with each other. The quantitative differences in the heat transfer coefficients and the pressure drops may be ascribed to the different experiment conditions.

The experimental comparisons indicate that both evaporation heat transfer and pressure drop characteristics of R-410A are equal to or better than those of R-22. The higher heat transfer and working pressure associated with R-410A can be very beneficial in improving the heat transfer efficiency and reducing the producing cost of the air-cooled heat exchanger. Due to the improved refrigerant-side heat transfer, the size and area of the heat exchanger can be reduced. In addition, smaller diameter tubes may be employed in the practical design to increase the refrigerant mass flux. As a result, the higher refrigerant mass flux enhances the heat transfer coefficient inside tube, thus the heat transfer efficiency can be increased. The converse implies that equivalent heat exchanger performance could be obtained with less material.

No empirical correlation of the evaporation heat transfer coefficient based upon the test data was provided except by Ebisu and Torikoshin (1998). They compared their data for heat transfer coefficient with the existing equations of Yoshida et al. (1991). Because the empirical correlation of Yoshida et al. (1991) was developed for a pure refrigerant, its calculated values showed significant underestimation of the experimental results (over 20%) at two different mass flow rates. At the present time, due to limited R-410A data available on the evaporation heat transfer, there exists no reliable correlation to describe the evaporation heat transfer and friction characteristics for R-410A in a wide operation range of heat pump evaporator.

All the experimental data showed that the evaporation heat transfer coefficient for R-410A was much higher than that of R-22, and the pressure drop of R-410A was significantly lower than that of R-22. Therefore, the appropriate modifications of the inside tube heat transfer and pressure drop calculations become necessary. Because there is no specific correlation available in the open literature to calculate the evaporation heat transfer coefficient and the pressure drop for R-410A in the primary operating range of a heat pump evaporator, the original R-22 calculation equations of EVSIM were used. The corrections on the basis of the experimental results of comparative studies between R-22 and R-410A were conducted.

The corrections of heat transfer and pressure drop calculation for R-410A should be based upon the test data with the same or similar evaporation conditions (that is the same mass flux, heat flux, evaporation temperature, tube geometric configuration, etc). The frost formation and growth on the outdoor coil of heat pump system is a transient process. Evaporation temperature, pressure, heat and mass flux all reduce with the deterioration of heat exchange performance. In this project, 35^{o}F (1.67^{o}C) and 28^{o}F (-2.22^{o}C) were set as the outdoor air dry-bulb temperatures for the frost tests, respectively. The tube outside diameters of all the fin staged coils were 0.375 inch (9.53 mm). The varying ranges of the primary operation parameters (including high, medium and low fan speed tests) that were observed to affect the local heat transfer coefficients are listed in Table 6.1. These parameters include heating flux, refrigerant mass flow and evaporation temperature.

Table 6.1 The ranges of outdoor coil operation parameters for the frost tests

TEST	MASS FLUX		HEAT FLUX		EVAPORATION TEMPERATURE*	
	$kg/m^2 \cdot s$	$Mlb_m/ft^2 \cdot h$	kW/m^2	$MBtu/ft^2 \cdot h$	^oC	^oF
35^oF	129 ~ 184	95 ~ 136	2.03 ~ 2.71	0.64 ~ 0.86	-17.8 ~ -8.3	0.0 ~ 17.1
28^oF	110 ~ 166	81 ~ 122	1.69 ~ 2.26	0.54 ~ 0.72	-20.5 ~ -10.0	-4.9 ~ 14.0

*The evaporation temperature is defined as the mean of the evaporator inlet temperature and the corresponding saturation temperature of evaporator outlet pressure

The test data used to correct the heat transfer and pressure drop calculation for R-410A were selected based upon the practical operation ranges of the frosted evaporator in Table 6.1. After a critical review on the available experimental results in the public domain, the data of Wang et al. (1998) were chosen because the experimental conditions in their study matched with the evaporation conditions of the fin staged coils in the present project.

Figures 6.1 and 6.2 illustrate the comparative results of the heat transfer coefficients and the pressure drop gradients between R-410A and R-22 by Wang et al. (1998). The evaporation heat transfer coefficient and pressure drop were taken at the saturated evaporation temperature $T_{sat}=2^oC$ ($35.6\ ^oF$) over a mass flux range from 100 $kg/m^2 \cdot s$ (74 $Mlb_m/ft^2 \cdot h$) to 400 $kg/m^2 \cdot s$ (295 $Mlb_m/ft^2 \cdot h$). For a lower mass flux, $G=100kg/m^2 \cdot s$ (74 $Mlb_m/ft^2 \cdot hr$), the effect of heat flux on the heat transfer coefficient is shown in Figure 6.1. The evaporation heat transfer coefficients of both refrigerants increased with the mass flux. The data curves were approximately linear with vapor quality. For the lowest heat flux, $q=2.5kw/m^2$ (0.793 $MBtu/ft^2 \cdot h$), the heat transfer coefficient of R-410A showed almost no change with vapor quality; whereas, the heat transfer coefficient of R-22 increased continuously with vapor quality. At the low vapor quality of 0.1, the value of the heat transfer coefficient for R-410A was about 30% higher than that for R-22. As the quality increased, the differences between R-410A and R-22 gradually decreased and finally disappeared at the high vapor quality 0.85. Meanwhile, the experimental data shown in Figure 6.2 indicated that the two-phase pressure drop gradient (expressed as dP/dZ) increased with both refrigerant mass flux and vapor quality. The data curves showing the pressure drops of refrigerant R-410A and R-22 displayed similar increasing trends as the amount of vapor quality increased. It is clear that R-410A has lower pressure drop compared to the baseline refrigerant R-22. At the low mass flux, $G=100kg/m^2 \cdot s$ (74 $Mlb_m/ft^2 \cdot h$), an approximately 25% reduction in the pressure gradient was observed for R-410A.

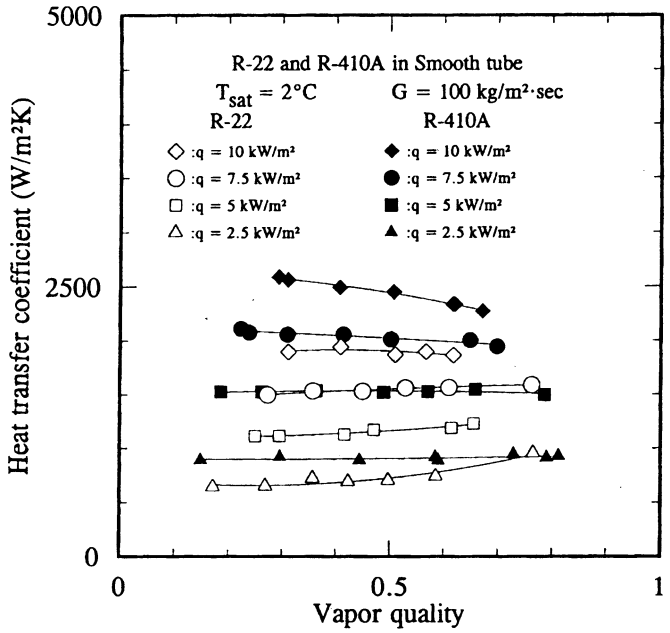

Figure 6.1 Effect of heat flux on the evaporation heat transfer coefficient at mass flux G=100kg/m^2·s (Wang et al. 1998)

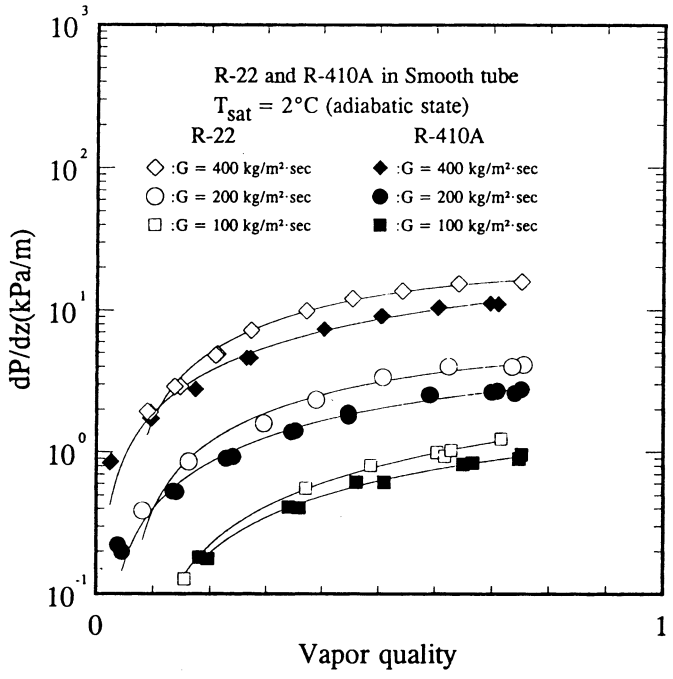

Figure 6.2 Pressure drop gradient vs. flow quality at various mass flows (Wang et al. 1998)

As described above, the frosted evaporator model can calculate the heat transfer and pressure drop of the refrigerant in the flow direction and determine the portions of specific flow regimes (i.e., subcooling, two-phase or superheated flow) for each tube. Therefore, the modifications on the calculations of both R-410A heat transfer coefficient and pressure drop were classified according to the different flow regimes.

Based on the experimental data of Wang et al. (1998), a linear multiplier function (Equation 6.8) was developed to describe the heat transfer coefficient difference between R-410A and R-22 quantitatively.

$$h_{R410A} = \frac{h_{R22}}{70\% + \frac{30\%}{0.70} \times (X - 0.1)} \tag{6.8}$$

Thus, the heat transfer coefficient of annular flow for R-410A was obtained by combining the Equation 6.1 and 6.8.

In addition, for the quality region 0<X<0.1 and 0.8<X<1.0, the constant multipliers 70% and 100%, respectively, have been chosen to correct the calculation of the two-phase heat transfer coefficient for R22. The correlation of single-phase convective heat transfer coefficeint, expressed in Equation (6.7) as a function of two nondimensional parameters (Reynolds and Prandtl numbers), refrigerant thermal conductivity and tube inner diameter, can be used directly to calculate the R-410A single-phase heat transfer coefficent. None modification was necessary.

For the quality region 0<X<0.1 and 0.8<X<1.0, the constant multipliers 70% and 100%, respectively, were chosen to correct the calculation of the two-phase heat transfer coefficient for R22. The correlation of single-phase convective heat transfer coefficeint, expressed in Equation (3.7) as a function of two nondimensional parameters (Reynolds and Prandtl numbers), refrigerant thermal conductivity and tube inner diameter, were used directly to calculate the R-410A single-phase heat transfer coefficent.

In the present test coils, the copper enhanced-surface tube with an outside diameter of 3/8 inch (9.52 mm) was employed. Boiling of the refrigerant mixture inside horizontal tube was highly dependent upon the surface structure. The enhanced surface, such as micro-fin surface, can efficiently improve the heat transfer characteristics of refrigerant flowing inside tubes. The effect of enhanced-surface tubing on the refrigerant-side heat transfer can be considered in two ways. One is that the enhanced-surface tube can be treated as a plain tube with an equivalent diameter. The approach to determine the equivalent diameter was suggested by Tandon et al. (1986) and Webb et al. (1971). Another method is that, while calculating the refrigerant-side heat transfer, the enhanced-surface tube is still treated as a plain tube with

the same diameter as the real values, then a multiplier constant or correlation needs to be applied to take into account the enhancement of evaporation heat transfer inside tube. The multiplier is strongly related to the refrigerant mass flux and vapor quality. A review of the literature reveals that few comparative data were found on the evaporation performance of R-410A inside both smooth and enhanced surface tubes. Furthermore, there was no detailed information available on the tube enhancement geometry from the manufacturer. So, an approximate correction factor of 1.5 was assumed in the present model to multiply the values of heat transfer coefficient for the smooth tube estimated from the equation 6.1 through 6.8.

Refrigerant Side Pressure Drop

In a heat pump evaporator, the total pressure drop experienced by the refrigerant flowing in a tube results from the pressure drop due to friction, momentum and gravity effects as well as the pressure drop due to flow losses in the tube return bends. The gravitational pressure drop was neglected in this model. Generally, the pressure drop in the two-phase flow region is much more than that in the pure vapor region on the basis of equal tube length. The refrigerant-side pressure drops were calculated separately for the single-phase or two-phase region of the evaporation coil by the distinct correlations. The frictional pressure drop for single-phase flow inside straight tubes with smooth surface was calculated by the Fanning equation:

$$\frac{dP}{dL} = \frac{2 \cdot f \cdot G^2}{D_i \cdot \rho} \tag{6.9}$$

$$f = 0.046 \cdot \mathrm{Re}^{-0.2} \tag{6.10}$$

The pressure drop due to momentum change was calculated by the following equation:

$$\frac{dP}{dL} = -G^2 \frac{dv}{dL} \tag{6.11}$$

where,

P:	pressure drop
L:	length of the evaporator tube
D_i:	tube inner diameter
G:	refrigerant mass flux
v:	refrigerant specific volume

The pressure drops due to friction and momentum effects in the single-phase region were computed using Equation 6.9 through 6.11 with the properties and parameters referring to the single-phase (either liquid or vapor) refrigerant region.

Equation 6.12 (Pierre 1964) shows the two-phase pressure drop correlation for a working fluid undergoing an evaporation process, which was used in the present frosted evaporator model:

$$\Delta P = \left(f_m \frac{L}{d_e} + \frac{x_2 - x_1}{x_m} + \frac{n}{2}\xi_{tm} \right)\left(\frac{M}{A} \right)^2 v_m \tag{6.12}$$

where

ΔP:	pressure drop of a tube
f_m:	mean friction factor
L:	length of the evaporator tube, not counting the bend
d_e:	tube hydraulic diameter
x_2-x_1:	quality change from tube inlet to outlet
x_m:	mean quality value of a tube
n:	number of return bends
ξ_{tm}:	resistance factor of the return bend
M:	mass flow rate
A:	cross section area of a tube
v_m:	mean specific volume of refrigerant

The pressure drop in the two-phase region of each tube was calculated as the sum of friction, momentum, and return bend components. The first and second terms of Equation 6.12 account for pressure drops due to friction and momentum change in the straight tube, respectively. The third term ($n/2*\xi_{\tau m}$) takes into account return bend pressure drop, which was not included in the pressure drop calculation of EVSIM. The pressure drop of the return bends in the single-phase region was computed by this term as well.

Pierre (1964) conducted the experimental study on the pressure drop of return bends and divided the resistance factor for the tube bends into two components:

$$\xi_{tm} = \xi_{om} + \xi_{fm} \tag{6.13}$$

ξ_{om} is due to the turning in the bends. For practical cases, it is set 0.8 to 1.0 for the oil-free medium, and 1.1 to 1.3 with oil present. ξ_{fm} is due to the friction in the bends. The value is selected from Table 6.2 (Pierre 1964).

The pressure drop ratio between straight tube and bend depends on the evaporator design. In case where the straight tube is short, the pressure drop in the return bend may be of the same order of magnitude of the pressure drop in the straight tube. With the effect of tube bend considered in the pressure drop calculation, the estimated pressure drop value through the evaporator is 10% to 30% higher

depending on the flow rate through the evaporator. This correlation has been verified to provide better agreement with experimental data by O'Neal and Gong (1996).

Table 6.2 ξ_{fm} values for oil-free or oil-present medium

D/d*	Oil-free Medium	Oil-present Medium
3	0.14	0.33
4	0.19	0.44
6	0.28	0.66
8	0.38	0.88
10	0.47	1.10

* D/d represents the ratio between the bend diameter D and the tube diameter d

The pressure drop of refrigerant flowing through the enhanced surface tube is higher than that through the smooth tube. Similarly, a constant multiplier, 1.5, has been assumed and applied in the calculation of refrigerant-side pressure drop. In addition, to adapt the pressure drop calculation from R-12 to R-410A, a simple multiplier, 75%, was assumed based upon the experimental comparison of Wang et al. (1998) in Figure 6.2.

For this study, a thermostatic expansion valve (TXV) was used as the expansion device to control the refrigerant mass flow for the evaporation coil. Meanwhile, another flow control device, the distributor, was installed after the TXV to help equalize the refrigerant mass flow and balance the pressure drop at each circuit outlet. A pressure transducer and the thermocouple were mounted just upstream of the distributor and were used to monitor the refrigerant state at coil inlet. The data obtained were the refrigerant state parameters before the distributor rather than the real values of the parameters at the inlet of the evaporator. The entrance temperature and pressure of an evaporator operating in a heat pump system is not constant under frosting conditions. These properties are essential for the simulation of the frosted evaporator model. To provide accurate entrance state parameters for each coil circuit, the distributor pressure drop model of the Oak Ridge heat pump model (Fischer and Rice, 1983) was modified and applied to estimate the pressure drops while refrigerant flowing through both the distributor nozzle and tubes. The pressure drops of the distributor components were first calculated using empirical correlations for one size of distributor nozzle and tube, and then corrected by additional empirical equations for non-standard inlet temperature, tube length, and distributor loading for different refrigerant. The description of the correlation can be found in the manual of Oak Ridge heat pump model (Fischer and Rice, 1983). Because there were no specific fitting coefficients available for refrigerant R-410A, the pressure drop calculations were approximated based on the equations for the refrigerant R-22. A multiplier is used to adjust the calculated parameters of the refrigerant state at evaporator outlet close to the test data.

Air Side Heat Transfer Coefficient

The evaporator consists of a staggered array of circular tubes and fins. The calculations of air-side heat transfer coefficient for individual fin-and-tube row, fin surface and tube surface, respectively, are described below.

Average Heat Transfer Coefficient of Each Row

For a typical fin-and-tube heat exchanger, the refrigerant side resistance is generally less than 20% of the overall resistance, the contact resistance between fin and tube is less than 15%, and the resistance of copper tube wall can be negligible. The dominant thermal resistance is on the airside. Therefore, accurate correlations for the airside heat transfer coefficient are essential to evaluate the total heat transfer between the air and refrigerant.

Many semi-empirical correlations have been developed to estimate the heat transfer coefficient of fin-and-tube heat exchangers. In general, however, most of them evaluate the multi-row coil as a whole and present the overall heat transfer coefficient of the coil rather than the local heat transfer coefficient corresponding to each individual row.

EVSIM was developed based on a tube-by-tube simulation method. It requires detail airside heat transfer coefficient for each fin-tube inside the coil. The flat fin surface correlation of Gray and Webb (1986) was selected by EVSIM developers to calculate the air-side heat transfer coefficient (Domanski, 1989). One advantage of this correlation is that it allows the user to evaluate the heat transfer coefficient of the coil, row-by-row.

The Gray and Webb correlation provides an average j-factor value for a heat exchanger with four or more tube rows. The number of tube rows has a small effect on the average heat transfer coefficient as the row number became greater than four. The correlation has the following form:

$$j_4 = 0.14 \cdot \mathrm{Re}^{-0.32} \left(\frac{S_t}{S_l} \right)^{-0.502} \left(\frac{S}{D_o} \right)^{0.0312} \tag{6.14}$$

where,

j_4: j-factor for four or greater number of rows
Re: Reynolds number
S_t: tube spacing normal to air flow
S_l: tube spacing in air flow direction
S: spacing between adjacent fins
D_o: outside diameter of tube

It can be seen that the heat transfer coefficient is dependent upon the air velocity and the geometry of fin-and-tube array. Under frosting conditions, both variables change continuously as frost accumulates on the coil. To describe the transient variation of the heat transfer coefficient during the freezing process, the calculation of the heat transfer coefficient is repeated at each time step based upon the updated inlet operating conditions and geometric parameters of freezing coil.

To calculate the average j-factor for a heat exchanger with less than four rows, j_N (where N<4), Gray and Webb (1986) provided the following equation:

$$j_N = j_4 \cdot 0.991\left[2.24 \cdot \mathrm{Re}^{-0.092}(N/4)^{-0.031}\right]^{0.607(4-N)} \tag{6.15}$$

Assuming that each row weights equally on the average airside heat transfer coefficient of the coil, the j-factor value for the depth row N of a R-row heat exchanger, $j_{N,R}$, can be obtained according to the average values of the whole coils with N and N-1 row numbers

$$j_{N,R} = N \cdot j_N - (N-1)\, j_{N-1} \tag{6.16}$$

j_N and j_{N-1} represent the average j-factors for heat exchangers with N and N-1 depth rows, respectively, obtained by equation 6.14 or 6.15.

The Gray and Webb correlation was developed based upon heat exchangers with multi-row, continuous plate fins, and a staggered tube row configuration. The fin pitch of each row was also the same. This differs from the geometry of fin staged coils, where the fin spacing decreases with each row. The condition that each row with same geometry parameters is never available. Each row weights differently on the average airside heat transfer coefficient of the whole coil. To the author's knowledge, no information has been previously published showing the row-to-row variation in heat transfer coefficient for fin-and-tube heat exchanger with a different fin pitch for each row. Because there is no correlation available for the heat transfer coefficient calculation of fin staged coils, the Gray and Webb correlation was used, but revision has to be made to account for the effect of fin staging on the heat transfer coefficient of each row.

In a fin-and-tube heat exchanger, the downstream rows have negligible effect upon the performance of the upstream rows. So, for a fin staged coil, the original Gray and Webb correlation can be used directly to calculate the value of the airside heat transfer coefficient for the first row. For all other rows of the fin staged coil, a weighting method was developed to account for the effect of the upstream rows on the downstream row heat transfer. For example, while calculating the second row j-factor value of fin staged coil with row1 having a fin density, F1, and row2 having a fin density, F2, both the second

row j factors of standard coils with (F1/F1) or (F2/F2) are calculated first by equation (6.14) and (6.15). Then two weighting factors, W1 and W2, are assigned to calculate the estimated j factor of a staged coil by equation:

$$j_{2,R}^{F1/F2} = W1 \cdot j_{2,R}^{F1/F1} + W2 \cdot j_{2,R}^{F2/F2} \tag{6.17}$$

The superscript, F1 and F2, indicate the fin pitch of the two-row fin staged coil.

For the third row of a fin staged coil, the j-factor can be calculated by applying three weighting factors which are correspond to the third-row j factors of three standard coils with F1, F2 and F3 fin pitches, respectively.

$$j_{3,R}^{F1/F2/F3} = W1 \cdot j_{3,R}^{F1/F1/F1} + W2 \cdot j_{3,R}^{F2/F2/F2} + W3 \cdot j_{3,R}^{F3/F3/F3} \tag{6.18}$$

The determination of weighting factors was based upon a series of fixed air velocity tests over a range from 70 to 310 fpm (0.3556 to 1.5748 m/s), in which the outdoor coils operated under dry working conditions. Through adjusting the calculated heat transfer capacities to match with the test data, the values of weighting factors could be chosen.

The correlation of Gray and Webb (1986) was developed by applying a multiple regression technique to laboratory data on 16 heat exchangers. The correlation can be used to predict the air-side heat transfer coefficient and friction factor as a function of the Reynolds number and the geometric variables of heat exchanger. However, for this correlation, the applicable range of Reynolds number was relatively high (2,400 to 24,700 on a tube diameter basis). Also the data bank correlated by their equations was generally for large tube diameters.

With frost accumulating on the surfaces of fins and tubes, the air flow rate decreases gradually due to the blockage of the air flow passages by the frost. In addition, during the frosting tests, three air flow rates (high: 2800 cfm; medium: 2200 cfm; low: 1400 cfm) were set as the outdoor coil initial values. So, for all the tests, the Reynolds numbers based on tube collar diameter range from 500 to 1600, which were out of the Reynolds number range of the Gray and Webb correlation. Both Colburn j factor ($St \cdot Pr^{2/3}$) and Fanning friction factor, f, of the fin-and-tube heat exchanger are inversely proportional to the Reynolds numbers.

The power law correlation of Gray and Webb was developed by a multiple regression techniques. Care must be exercised in extrapolating the correlation to conditions beyond the range of Reynolds numbers in the original data. Furthermore, at low Reynolds numbers, the influence of the row effect to the Colburn j factors increases at the same time, there are higher test uncertainties associated with the lower Reynolds numbers.

To assure the Gray and Webb correlation can be applied in this project, a literature survey was conducted. It is found that Chang and Wang (1995) provided the experimental validation of Gray and Webb correlation at relative low Reynolds numbers.

In Figure 6.3, the experimental data and the calculation results of Gray and Webb correlation were presented as plots of Colburn j factor and Fanning friction factor f against Reynolds number based on the tube collar diameter in the range of 400 to 8000. For flat fins, the experimental j factors were in good agreement (within 5%) with the predictions of the Gray and Webb correlation. Based on the comparison of Chang and Wang (1995), the Gray and Webb correlation was chosen to estimate the air-side heat transfer coefficient and friction characteristics for this study.

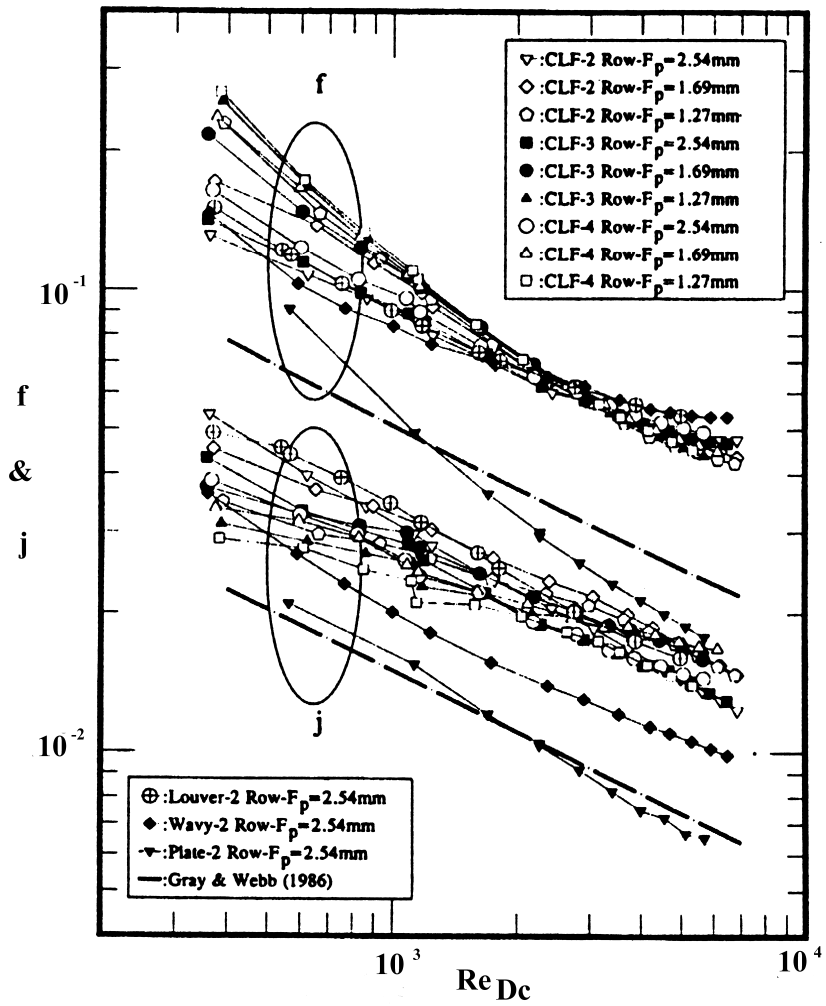

Figure 6.3 Comparison conducted by Chang and Wang (1995) on the experimental data and the calculation results of Gray and Webb correlation

The heat transfer performance of a finned surface is highly dependent on the pattern of the fins. Many high efficient fin surfaces have been applied in residential and commercial air conditioning applications, such as spine fin, wavy fin, lanced fin, louver fin and convex louver fin. By promoting shedding and restarting of boundary layer, all these enhanced fins give a lower heat transfer resistance than the flat fin. Therefore, the enhanced fins have been applied by the manufacturers of heat exchanger to improve the heat transfer performance and reduce the size and weight of heat exchanger.

In this study, the fin staged coils, provided by Carrier Corporation, use an enhanced fin surface: 7 element lanced sine-wave fin, which has arrays of small strips raised from the sine wavy plate. The geometry is similar to the popularly used convex louvered fin, which is a combination of the wavy and louvered fin geometry. In the open literature, no published data were found for this kind of lanced fin while Carrier Corporation conducted tests on these fins, their test data and the empirical correlations were proprietary. Thus, no heat transfer coefficient data were available for this kind of lanced fin.

All of the equations developed above were based on a flat fin geometry. To estimate the heat transfer coefficient for a lanced fin surface, EVSIM applies a multiplier function (Nakayama and Xu, 1983) in conjunction with the calculation equations for the heat transfer coefficient for a flat fin. The correction accounts for the heat transfer enhancement due to the raised strips of lanced fins. One feasible method for this project is that still using flat fin heat transfer coefficient correlation and lanced fin semi-empirical multiplier to estimate air-side heat transfer coefficient for the seven element lanced sine-wave fins. Meanwhile, the effect of airflow turbulence due to the frost layer blockage needs to be considered in the selection of this multiplier as well.

In addition, owing to the corrugated surface of the sine-wave fins, the heat transfer area of the fin surface is larger than that of the flat fin with the same dimensions. Because the exact specifications of the fin surface area were not available, no corrections for fin surface area were made.

Figure 6.4 and Table 6.3 illustrate the calculation results of heat transfer coefficient by the revised Gray and Webb correlation. The values of heat transfer coefficient have been calculated for the individual rows of each coil at a given face velocity.

The solid lines and the dotted lines in Figure 6.4 represent the variations of heat transfer coefficeint for each rows for three standard and two fin staged coils. The calculations show the continuous decrease in the heat trasnfer coefficient with each row. For the entrance row of coil, the heat transfer coefficeint is highest but declines rapidly with each row for the standard coils. From the first row to the third row, the heat transfer coefficient reduces by approximately 40% for the standard coils. The slope of the curve also decreases with the number of tube rows. This implies that the effect of each row tends to diminish with each successive row. This feature is a typical characteristic of heat transfer coefficient in the depth of coils at low Reynolds numbers. For a constant fin pitch, the heat transfer coefficient of each

row is independent of the total number of coil tube rows. This may be attributed to the negligible effect of downstream tube rows on the heat transfer coefficients of the upstream rows.

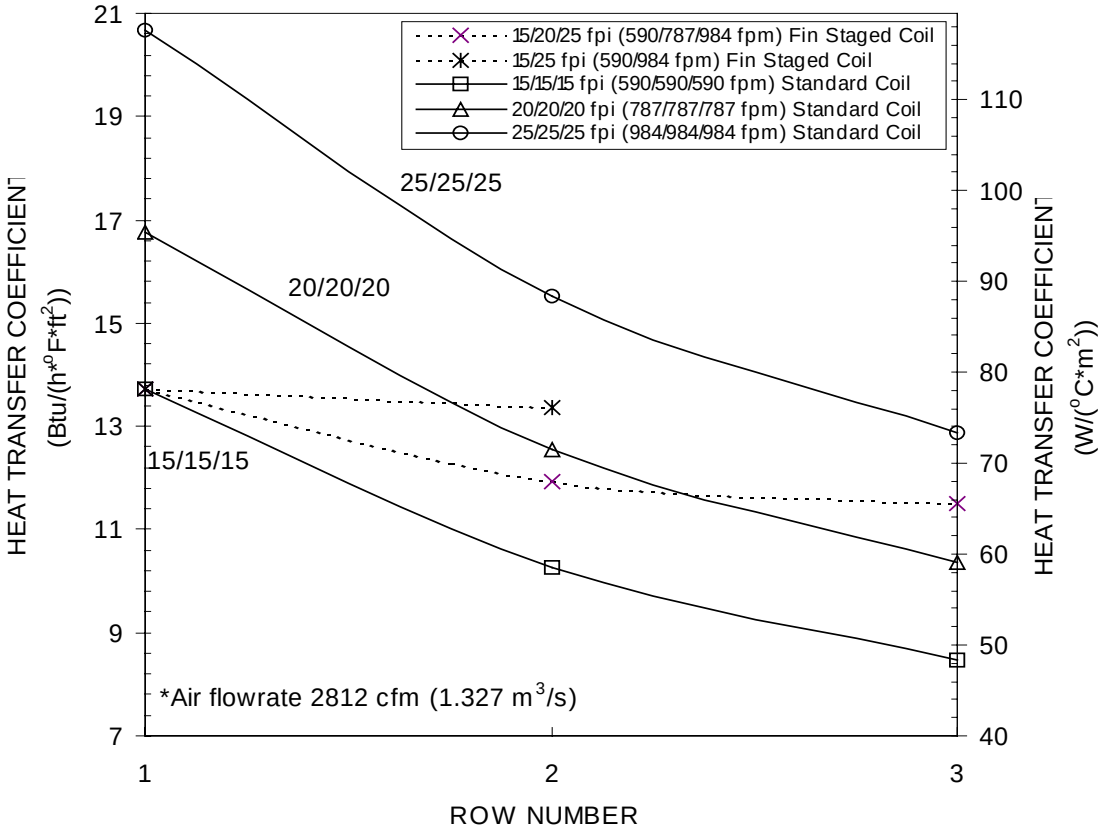

Figure 6.4 Heat transfer coefficient calculation for fin staged coils

Table 6.3 Heat transfer coefficients (Btu/(h·°F·ft²)) for standard and fin staged coils

Row Number	Fin Staged Coil			Standard Coil		
	15/20	15/25	15/20/25	15/15/15	20/20/20	25/25/25
1	13.7	13.7	13.7	13.7	16.8	20.7
2	11.9	13.4	11.9	10.3	12.6	15.5
3	N/A	N/A	11.5	8.5	10.4	12.9

* At 2812 cfm (1.327 m^3/s) air flowrate

The calculation results also depict the effect of fin pitch on the heat transfer coefficient of each row. It can be observed that increasing the fin spacing leads to a reduction in the heat transfer coefficient. For the smallest fin spacing, the heat transfer coefficient is largest. Fin spacing affects the heat transfer characteristics of each individual row of the coil. Although the illustrated calculation is for a specific air flow rate, similar trends also can be observed for coils with other airflow rates. All the trends presented above are consistent with the experimental results of other researchers (Richard 1973, McQuiston 1978).

For fin staged coils tested in this project, the fin pitch of the front row was always less than that of the back row. Compared to a standard coil, each tube row of a fin staged coil deteriorates the heat transfer of the subsequent row. The revised Gray and Webb correlation takes into account this negative effect and presents a value between the heat transfer coefficients corresponding to the rows of standard coils with different fin pitches.

It should be noted that some researchers (Rich 1973, Chang et al 1995 and Wang et al 1997) reported that fin pitch had either a slight or no effect on the Colburn j factors for plain, louvered and wavy fin geometries. Apparently, the additional turbulence generated by enhanced fin surfaces reduces the dependence of the factor on fin pitch compared with that of flat fins In Figure 6.4, it is seen that the calculated j factor values show a significant dependence on fin pitch. Because the Gray and Webb correlation was developed for that fins, it might overpredict the effect of fin pitch on the j factor for the 7-element lanced sine wave fin.

The analysis of airside heat transfer coefficient depends upon two factors. One is the effect of fin staging. Another is the effect of frosting. The first factor has been discussed through the revised Gray and Webb correlation. Techniques for the analysis of the coil with only sensible heat transfer have been well studied and documented (McQuiston 1978, Oskarsson 1990). However, when freezing occurs simultaneously with the heat transfer, the effect of frost layer growth on the flow field and the geometric configuration of the coil leads to the airside heat transfer coefficients that vary spatially and temporally.

The initial frost deposits on the coil surface increase the airside convective heat transfer coefficient because of the added roughness that is provided to the surface of the tubes and fins by the frost. Tao et al (1993) studied the characteristics of frost growth on a flat plate during the early growth period. The typical frost growth process consists of two stages. The first stage corresponds to the liquid phase when water droplets are subcooled. During the second stage, the ice crystals start growing in an ice-column form, which acts as a kind of spine fin at the surface of outdoor coil. From the heat transfer standpoint, the initial frost deposits are desirable because the rough frost surface behaves as additional fins to disturb the boundary layer. Thus, the convective heat transfer at the air frost interface is enhanced temporarily. However, as frost continues to accumulate, it starts to block the gaps between the fins. Frost also deposits at the concave and leeward areas of wavy fin surfaces. These two effects reduce the local

turbulence of enhanced fins and make it performs more like flat fins. Therefore, the heat transfer coefficient of a fin surface begins to decrease.

The initial frost deposition increases the surface roughness and also the heat transfer area of coil. Because the frost layer is a kind of porous media with lots of extended microscopic surfaces, additional heat transfer area may be added to the coil through the deposition of frost. This additional surface area would enhance the heat transfer capacity of the coil. However, it is clear that the qualitative estimation of the increase of surface area is difficult to conduct. Therefore, a simplification made in the model is that the area added by frost deposition is neglected and the outer heat transfer area of coil is constant throughout the frosting tests.

Besides surface roughness, air velocity and some geometric parameters of the coil affect the convective heat transfer coefficient as well. The variation of air velocity between adjacent fins due to partial blockage of the air passages is difficult to determine. The analysis presented in Chapter VII reveals that the average air velocity through coil tends to increase first and then decrease later, which is a result of the decrease of both the cross sectional area of air flow passages between the fins and the total airflow through the coil as frost grows. The effect of the variation of air velocity is accounted for in the calculation of the Reynolds number. The variation of air velocity with pressure up through the outdoor coil is highly dependent upon the characteristics of the fan.

As verified by visual observations, the frost accumulated on the fin and tube surfaces changes the coil geometry. Both tube outside diameter and fin thickness increase with the growth of the frost layer. For the purpose of simplifying the analysis, it is assumed that the average thickness of the frost layer is used to account for the increasing amount of fin thickness or tube diameter. In equation 6.14, with other conditions being constant, the j-factor value decreases with both the reduction of fin spacing and the growth of tube outside diameter. To account for the effects of fin thickness and tube diameter on the heat transfer coefficient due to the increasing frost layer, the corresponding variables in Equation 6.14 need to be updated at the calculation of each time step. Hence, the calculated heat transfer coefficient includes the combination effect of both variables.

During the frost test, the value of heat transfer coefficient initially increases as frost begins to form on the fin surface, then decreases as frost continues to grow. The initial increase is caused by the added surface roughness due to the initial frosting. As the frost layer continues to grow, its effect on the geometry of the coil becomes dominant and results in a decrease in the heat transfer coefficient. Hence, the value of heat transfer coefficient increases at the early of freezing process, and eventually decreases with time.

The frost roughness depends on variables such as air velocity, temperature, relative humidity, surface temperature and geometry, affect the frost surface roughness. This increases the difficulty to quantitatively study the typical effect of frost roughness on the heat transfer coefficient. Due to the

shortage of published data, the present model does not take into account the effect of the variation of surface roughness. Therefore, the calculated heat transfer coefficient shows a continuous reduction as time elapses.

Overall, in the calculation of average heat transfer coefficient of the freezing coil, the variation of value is thought to be the combined effect of air velocity, fin thickness and tube diameter.

Local Heat Transfer Coefficients of Individual Fin Surface

The revised Gray and Webb correlation provides an estimate of the average heat transfer coefficient for each row. These values are used to calculate the heat transfer capacity of coil. The heat and mass transfer between the air and the fin and tube surface is mainly determined by the flow structure. Saboya and Sparrow (1974, 1976a, and 1976b) presented experimental results for the spatial distributions of the local heat transfer rates in fin-tube heat exchanger. Their results are applied to each section to estimate the variation of heat transfer coefficient on the fin surfaces. The introduction of the variation of local heat transfer coefficient makes it possible to estimate the air-side pressure loss through the passage between the fins as a result of nonuniform frost growth inside the heat exchanger.

Saboya and Sparrow (1974, 1976a, and 1976b) used a naphthalene sublimation technique to study the local heat transfer variation on fin surfaces for fin-and-tube heat exchangers having a multiple number of rows. Local and average transfer rates were determined from measurements of the mass transfer in an analog system consisting of a pair of naphthalene plates and an array of spacer disks, which are arranged in the staggered configuration on equilateral triangular centers for the testing of a two-row heat exchanger. Their experimental results provided a better understanding of the complicated heat and mass transfer characteristics inside fin-and-tube heat exchanger.

The two dimensional distribution curves of local mass transfer rates are shown in Figures 6.5 and 6.6, which are associated with a one-row or two-row heat exchanger, respectively, with flat fins. The numerical value in the figures represents the ratio of local mass transfer rate at axial station x to the average of mass transfer rates at all axial stations. By applying a heat-mass transfer analogy, the mass transfer results presented in Figures 6.5 and 6.6 can be converted to heat transfer ratios.

The local measurements reveal that the transfer rates at axial stations on the forward part of the fin are substantially higher than the average value and those on the rear part of the fin are well below the average value. The transfer rates at the entrance region are large due to the developing boundary layer. In addition, a vortex which develops in front of the tube enhances the local transfer rate upstream of the tube. For the heat exchanger with a staggered tube array, because of the repeated blockage of the staggered tube bank, there is a small wake region behind each tube. As a result, the fin surface downstream of the tube is relatively ineffective and contributes less to the performance of heat and mass transfer. This wake region,

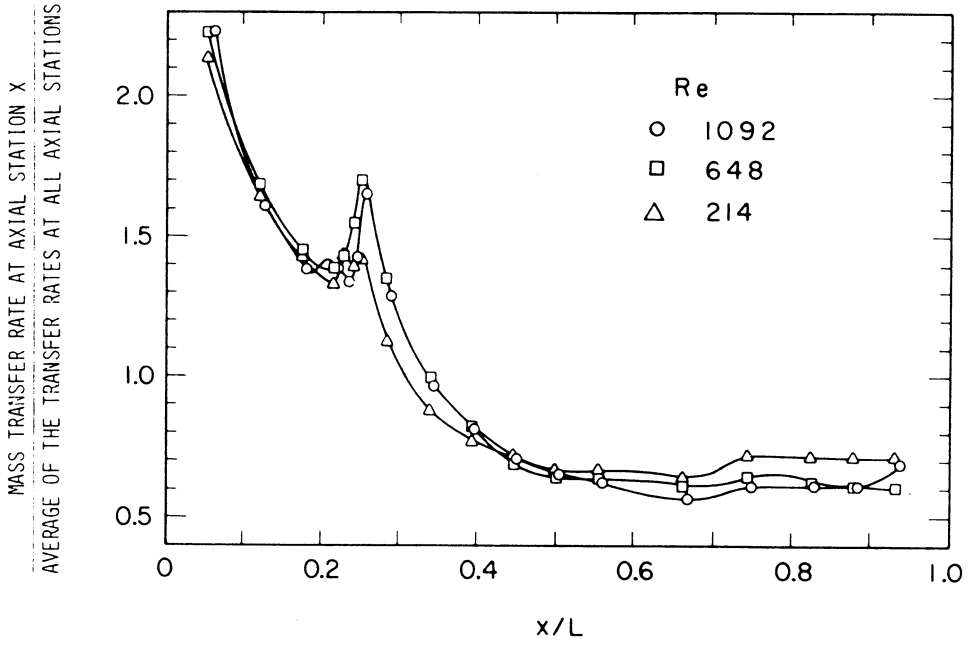

Figure 6.5 Variation of mass transfer rate for one-row heat exchanger (Source: Saboya and Sparrow 1974)

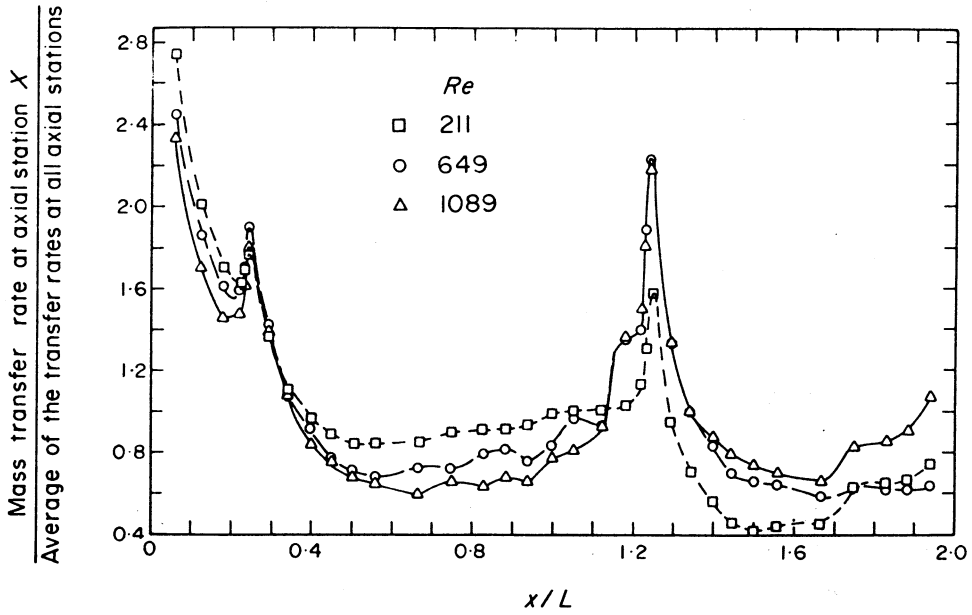

Figure 6.6 Variation of mass transfer rate for two-row heat exchanger (Source: Saboya and Sparrow 1976)

together with the growth of boundary layer with increasing x, explains the relatively low transfer rates downstream of the tube. For the two-row heat exchanger, the regime of low transfer rates from the first row continues into the front portion of the second-row fin surfaces. Because of another vortex system which develops in front of the tubes of the second row, peaks appear again in the mass transfer rates, as indicated in Figure 6.6.

As can be seen from Figures 6.5 and 6.6, although there are some differences in the magnitudes of local ratios at different Reynolds numbers, in general, the three curves are remarkably close together, which means that the axial distribution ratios are relatively insensitive to the Reynolds number. This demonstrates the possibility applying single simplification of unchanging distribution ratios to simplify the calculation of heat and mass transfer on the fin surface during the frosting process.

In the original model of frost formation, uniform heat transfer coefficients at all sections of fin surface were assumed. However, the experimental results presented by Saboya and Sparrow (1974 and 1976) revealed that large spatial variations existed for the local heat transfer on fin surfaces. To provide more reasonable predictions on frost layer growth, the Saboya and Sparrow (1974 and 1976) data were used to estimate the distribution of heat and mass transfer coefficient in the frost model.

Figure 6.7 illustrates the two dimensional distribution contour of heat transfer coefficient ratio for each section in the standard two-row coil (20/20 fpi). The corresponding ratio of local heat transfer coefficient to the average value overall the fin surface of the whole row is given at each section. Two peaks appear at the first and fourth section in each row. These peaks represent the effect of the boundary layer development at the leading edge of each fin and the vortex ahead of each tube. The heat transfer coefficient at the leading edge is substantially higher than that at the secondary peak. This implies that the enhancement of heat transfer by boundary layer development is larger than that by the vortex system upstream of the tube. Such a high coefficient value should enhance both the local heat and mass transfer, which affect the frost accumulation at the leading edge.

The standard or fin staged coils tested in this project were different from the two-row heat exchanger with continuous fin surfaces tested by Saboya and Sparrow. The coil for this project had two sets of single-row fin arrays with either the same or different fin pitches. The rows are arranged one behind the other with a small gap and there is no connection between the fins on any row. Therefore, at the second row of the coil, one might expect a developing boundary layer region. This should cause the heat transfer at the leading edge section of the second row to be comparable to a continuous fin. Therefore, as an individual one-row fin surface, a primary peak was assumed to exist at the leading edge of the second row. This peak was lower compared to the corresponding peak of the first row.

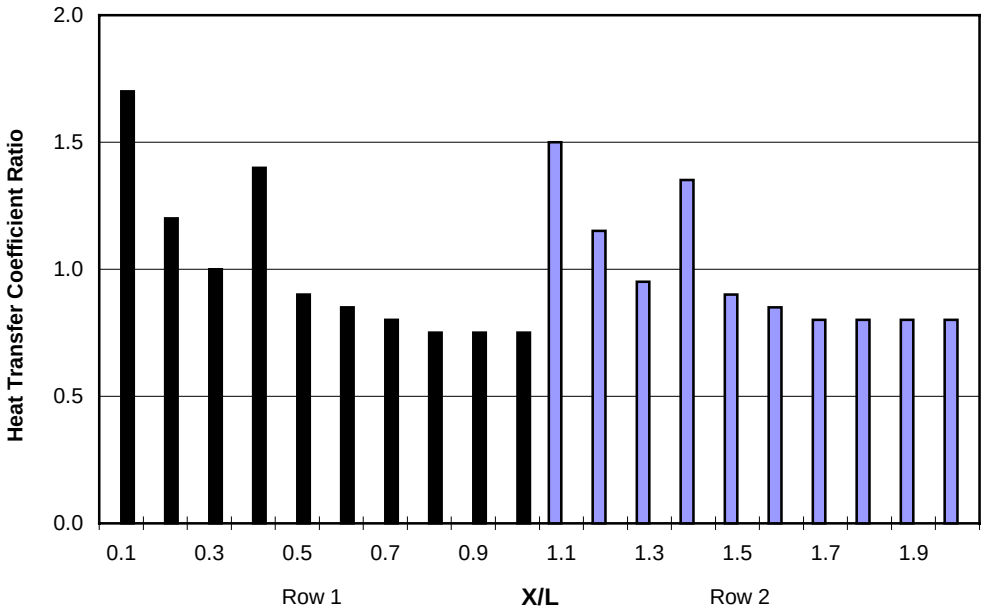

Figure 6.7 Local heat transfer coefficient distribution diagram for the two-row baseline coil

In the testing of the coils for this study, an alternate growth and disruption of the boundary layer as the air passed through the fin surface occurred due to the disturbance of the lanced fins. This reduced the negative effect of the boundary layer and improved the heat transfer at the rear portion of fin surface. This was reflected as the reduction of the difference between maximum and minimum values in the assumption curves compared to that of the experimental curves of Saboya and Sparrow, which were obtained based upon plate fin surfaces.

Because the distribution ratios are dimensionless, the areas under each of the two curves are the same and equal to one. At the range of low Reynolds numbers, the average heat transfer coefficient of the first row is relatively higher than that of the second row. Therefore, the absolute values of local heat transfer coefficients at the second-row sections should be lower.

The regions of high heat transfer is the beginning of the boundary layer development at the first section of the fin surface and the vortex-dominated zone adjacent to the upstream section of the tube. By comparison, in the area behind the tube, the heat transfer ratio is low. For each coil row, the heat transfer coefficients on the forward sections of fin surface are higher than those on the rear sections. The variation of local heat transfer coefficient for both rows are similar except the range of the second row was less than

that of the first row. The distribution ratio diagram shows both qualitative and quantitative characteristics of the local heat transfer coefficient for a two-row standard coil.

Frost formed on the fin surface blocks the flow channel between two adjacent fin plates and influences both the roughness of fin surface and the local air velocities. The heat transfer coefficient is not only a function of location but also depends on the geometric variation along the fin surface. For frosted coils, the geometry constantly varies due to the growth of the frost. The distribution trend of local heat transfer coefficients should change with time. However, to simplify the calculations, the presence of frost layer was assumed to have no effect on the distribution of local transfer coefficients, which was time-independent. The ratio curves were kept constant throughout the whole simulation process. The magnitude variation of local transfer coefficient was only determined by the change of average transfer coefficient value obtained from the revised Gray and Webb correlation.

The strategy aimed at estimating the local mass transfer was based on a section-by-section approach. The mean value of heat transfer coefficient over the fin area of each row of the coil was calculated by the revised Gray and Webb (1986) correlation in subprogram, EVPHXF, and transferred to the frost formation subprogram, PCFROST. Then, the local variation of the heat transfer coefficients on the fin surface was estimated based on the Saboya and Sparrow (1974 and 1976) experimental data results. Thus, by applying the distribution ratio assumed above, the average value of heat transfer coefficient could be subdivided into location-dependent heat transfer coefficient section by section along fin surface. Lastly, the local mass transfer coefficient for each section required by the frost formation calculation was obtained by means of the analogy between heat and mass transfer.

Heat Transfer Coefficient of the Tube Surface

Because frost forms both on fins and tube surfaces, the model needs to account for the frost formation that occurred on the evaporator tube surface. The variation of heat transfer for a tube inside coil is quite complicated and determined by many factors, such as tube position, tube bank arrangement, geometry of fin-and-tube assembly, flow pattern, air velocity, fin type, operation condition. For an individual tube, the local heat transfer varies in the longitudinal and circumferencial directions as well.

For low Reynolds numbers, generally, the heat transfer of a fin-tube in the first row is similar to that of a single tube and considerably lower than that of the inner row tubes. The intensity of flow turbulence in the depth of the coil leads to this increasing trend of heat transfer of the inner fin-tubes. In a staggered tube banks, the flow is comparable with flow on a curved channel of periodically converging and diverging cross section. Thus the velocity distributions around tubes in different rows have similar characters.

Available experimental information on the heat transfer distribution of tube banks inside heat exchangers and the effect of frost accumulation on the local heat transfer of tube surface is rather scarce. To simplify the calculation, the heat transfer coefficient of the tube surface was assumed to be constant on

the tube periphery and equal to the average value of the row where the tube is located. This makes the prediction of uniform thickness of frost layer in the tube radical direction.

Considering the existence of fin collars, the tube outside area exposed to the airflow accounts for only 3.1% of the overall area of coil outside surface for standard coil (20/20 fpi). Even for the row with widest fin spacing (15 fpi), the fin surface area is much greater than the tube surface area. The error of heat transfer calculation caused by this simplification should be negligible.

Due to the relatively low temperature, more frost accumulates on the tube surface. Thus, an inaccurate assumption of heat transfer coefficient could cause more error on the frost mass calculation.

The tube diameter increases with more frost accumulating on the surface. The Gray and Webb correlation (1986) in Equation 6.14 indicates that the mean heat transfer coefficient of coil almost has no variation with the tube diameter, whose effect is taken into account by the calculation of Reynolds number. This means that increasing the tube diameter does not significantly improve the overall heat transfer performance of coil. In addition, a high heat transfer area appears near the front stagnation of the tube, which is generated by the formation of vortex flow in front of the tube and has been discussed in the previous section. The high heat transfer area varies with the tube diameter. As the tube diameter is increased, the area becomes large and the value of second peak becomes higher.

Air Side Pressure Drop

To study the distribution of frost on the fins of the heat exchangers, the fins on each row were divided into ten sections along the airflow direction in PCFROST. Temporal and spatial dependent variations of the local frost and air variables, such as frost height, density, conductivity, weight, air temperature and humidity, etc. were estimated in the model. The pressure drop due to the contraction and expansion of air through the frosted fin passages was estimated in the subprogram PRCFM.

At the start of the frost growth process, the amount of frost was small, which had little effect on the calculated pressure drop. As the frost height increased, the effect of frost blockage on the pressure drop gradually increased and began to dominate the calculated pressure drop.

The frost model estimated a frost distribution on the fin surface along the airflow direction that looked like a "throat" in a nozzle. The airflow experienced an initial contraction at section 1 and then subsequent expansions from section 2 to section 10 as shown in Figure 6.8.

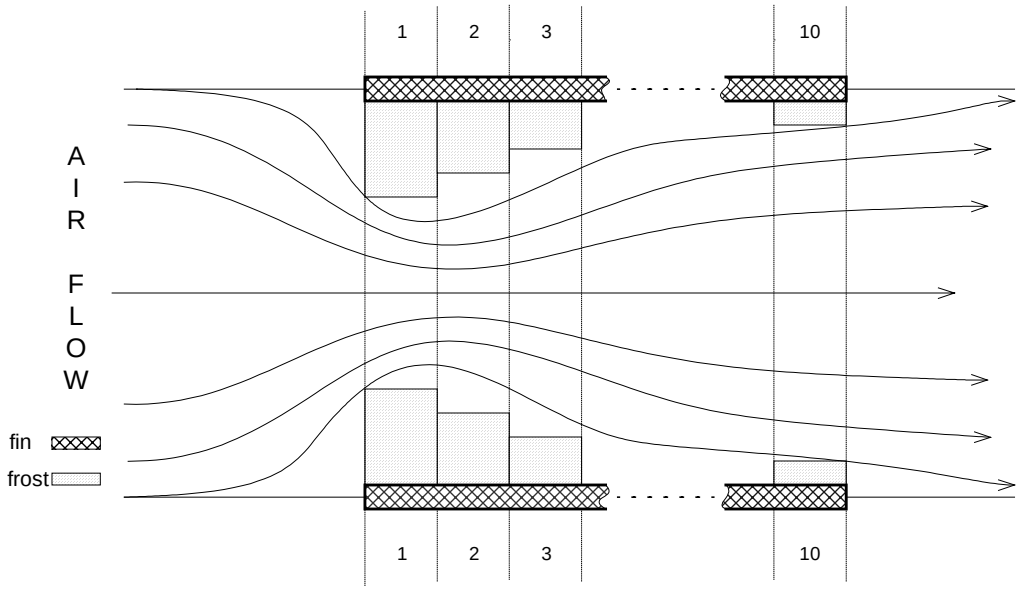

Figure 6.8. Sketch of the contraction and expansion of airflow between frosted fins

For the dry heat exchanger, the friction drag force is the sum of the drag from a bare tube bank (ΔP_{tube}) and the drag caused by the fins (ΔP_{fin})

$$\Delta P_{coil.dry} = \Delta P_{fin} + \Delta P_{tube} \tag{6.19}$$

The term ΔP_{tube} can be measured for a bare tube bank of the same geometry as the heat exchanger except without fins. And the tube drag accounts for a major portion of the total pressure drop compared with the losses due to fin surface friction for dry or wet coils. Meanwhile, the term ΔP_{fin} can be obtained based on a set of bare fins with same geometry as well.

Because the air-side heat transfer coefficient is typically much smaller than the tube-side value, some improvement are used to increase the air-side UA (the product of heat transfer coefficient and area) value such as staggered tubes and enhanced fin surfaces. Although the staggered tube arrangement gives more aerodynamic turbulence to airflow and provides higher performance than the inline tube arrangement, it causes more pressure drop to the airflow through the heat exchanger. The airflow pattern in fin-and-tube heat exchangers is complex. The use of enhanced fin geometry introduces further complications and makes it difficult to predict the airflow pressure drop analytically or numerically. Friction factor correlations for a variety of fin-and-tube heat exchangers are typically obtained using semi-empirical multiple regression techniques. Some researchers subtracted entrance and exit losses from total coil pressure drop and didn't include them in the friction factor correlation. Others considered them together.

In the pressure drop subprogram PRCFM, the subroutine PDAIR was used to predict the air pressure drop through a finned tube heat exchanger, which was originally developed by ORNL (1983). Gray and Webb's (1986) friction correlation was applied to calculate the dry coil air pressure loss. Hosoda's correlation was used to calculate the enhanced factor for wet coil pressure drop. The original ORNL code did not account for the friction drag and blockage due to the frost accumulating on the fin surface.

Gray and Webb's (1986) correlation assumes that the pressure drop is composed of two terms. The first term accounts for the drag forces on the fins, and the second term accounts for the drag force on the tubes. The friction factor of heat exchanger is given by:

$$f = f_{fin}\frac{A_{fin}}{A_{total}} + f_{tube}\left(1-\frac{A_{tube}}{A_{total}}\right)\left(1-\frac{t_{fin}}{p_{fin}}\right) \tag{6.20}$$

where,

f_{fin}:	friction factor associated with fin area
f_{tube}:	friction factor associated with bare tube area
A_{fin}:	surface area of fins
A_{tube}:	surface area of bare tubes
A_{total}:	airside surface area (fins and tubes)
t_{fin}:	fin thickness (change with time due to frost accumulation)
P_{fin}:	fin pitch (change with rows for fin staging coil)

This friction correlation doesn't include the pressure losses at the inlet or outlet of the heat exchanger due to contraction and expansion.

The friction factor (f_{fin}) associated with the fins was estimated by:

$$f_{fin} = 0.508\ \mathrm{Re}_{D_{tube}}^{-0.521}\left(\frac{S_{tube}}{D_{tube}}\right)^{1.318} \tag{6.21}$$

where,

Re_{Dtube}	the Reynolds number based on tube outside diameter
S_{tube}:	tube spacing normal to flow
D_{tube}:	tube outside diameter (increase with time due to frost accumulation)

The friction factor (f_{tube}) associated with the tubes is obtained from the Zukauskas (1972) correlation for flow normal to a staggered bank of bare tubes. The Zukauskas friction factor (f_{tz}) was defined differently than the definition of f_{tube} in Gray and Webb's equations. The relation between the two definitions is given by:

$$f_{tz}\,N\,X = f_{tube}\frac{A_{tube}}{A_{c.t}} = f_{tube}\left(\frac{\pi\,D_h}{S_{tube} - D_h}\right) \tag{6.22}$$

where,

X:	an empirical function of R_e and S_t/S_1
A_{tube}:	surface area of bare tube
$A_{c.t}$:	minimum flow area for bare tube bank
D_h:	tube hydraulic diameter

Finally, the air pressure loss of the dry coil based on the fanning friction factor is

$$\Delta P_{coildry} = f\left(\frac{G^2}{2\rho}\right)\left(\frac{4L}{D_h}\right) \tag{6.23}$$

where,

G:	mass velocity based on the minimum coil flow area
ρ:	humid air density
L:	coil length in the air flow direction

Carrier's seven-element sine wave fin is a combination of both wave and interrupted fins. Because no performance data were available for this type of fin, Gray and Webb's fanning f factor correlation for plain fins, together with a multiplier, was used to predict the air flow pressure drop due to tube and fins.

The difference between dry and freezing coils included one more drag force component (ΔP_{frost}) accounting for the frost blockage:

$$\Delta P_{coil.\,frost} = \Delta P_{fin} + \Delta P_{tube} + \Delta P_{frost} \tag{6.24}$$

The increase in pressure drop due to frost formation was the result of the blockage of frost to the free flow area, the rise in friction factor resulting from the increased Reynolds number, and the change of surface roughness.

The variation of air flow and coil geometric parameters due to frost growth was considered while evaluating the friction factor in Gray and Webb's correlation at each time step.

When the frost grows, it fills the small gap between the fin strips, which makes the fin surface looks "smooth", which reduces the friction pressure drop due to strip interruption. On the other hand, the roughness of the frost surface increases the friction pressure loss of the airflow through coil. Overall, the surface roughness of frost coil is apparently increased compared with that of clean coil working in dry

conditions. Therefore, a multiplier was applied to take into account the effect of the roughness to increase the calculation of ΔP_{fin} and $\Delta P_{tube.}$

Under frosting conditions, the pressure drop through the heat exchanger depends primarily on the flow velocity and free flow area. The correlation of pressure drop due to frost blockage with time is dependent on the effect of the geometric variation of frost channel on the pressure drop with time.

Because of the accuracy in measuring the quantities required for the friction factor as well as the variations of many parameters during the frosting process, no empirical friction factor correlations for frosted fin-and-tube heat exchangers have been developed. Therefore, a method needed to be developed to account for the contraction and expansion effects on air pressure drop with time.

The flow process involved following an abrupt expansion in the frost channel is illustrated by Figure 6.9. The energy loss related to an abrupt expansion mainly comes from the turbulence at the flow separation area.

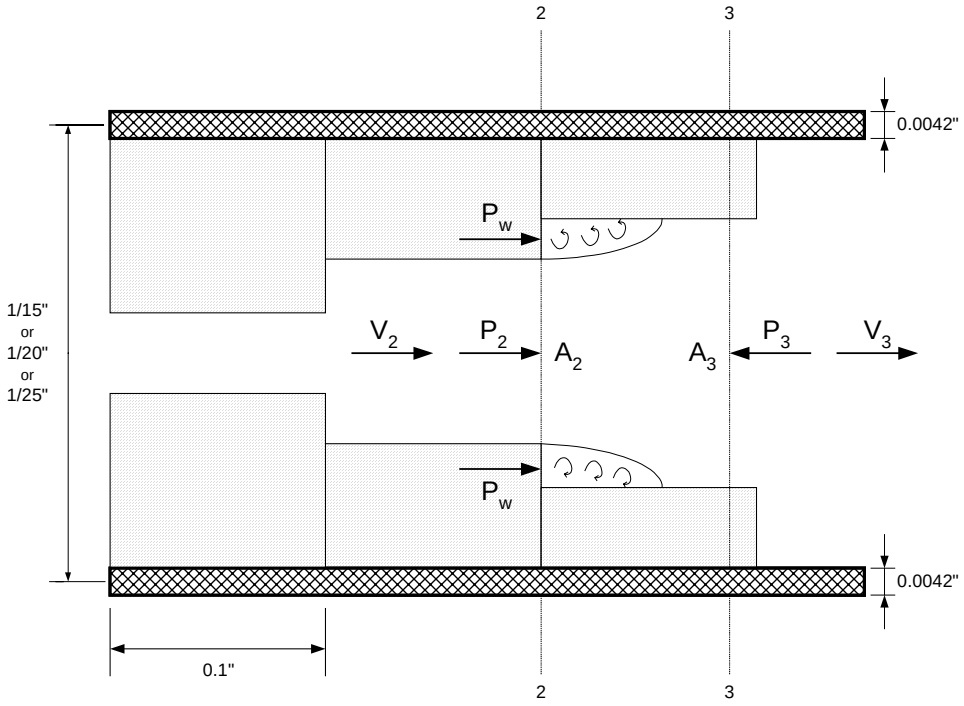

Figure 6.9 Sketch of the expansion of air flow between frosted fins

Using conservation of momentum analysis and neglecting wall friction, the summation of the forces in the direction of flow can be equated to the rate of change of momentum between cross section 2 and 3.

$$\rho\, Q(V_3 - V_2) = P_2 A_2 + P_w (A_3 - A_2) - P_3 A_3 \tag{6.25}$$

The static pressure P_2, P_3 and P_w were assumed to be constant over the flow cross section. Meanwhile, for subsonic flow, the pressure on the downstream face is equal to the static pressure in the air flow just prior to expansion (Nusselt, 1940).

$$P_2 = P_w \tag{6.26}$$

So, P_w in the above equation can be substituted by P_2.

Though the Re number is relative low for the air flow through air conditioner coils, due to the disturbance of frost and fin strips, the air flow is assumed to be turbulent inside the flow channels under all the test conditions of this project. Thus, the velocity distribution at the cross area of each section was assumed uniform. In addition, the variation of air humidity and temperature are not included in the psychrometric property calculation.

The continuity equation for incompressible fluid,

$$Q = A_2 V_2 = A_3 V_3 \tag{6.27}$$

can be substituted into the momentum equation and the result rearranged to solve for P_2-P_3:

$$\frac{P_2 - P_3}{\rho g} = \frac{V_3^2 - V_2 V_3}{g} = \frac{V_3^2}{g}\left(1 - \frac{A_3}{A_2}\right) \tag{6.28}$$

The Bernoulli Equation can be written with h_2, which represents the pressure head loss due to the expansion of section two:

$$\frac{P_2}{\rho g} + \frac{V_2^2}{2g} = \frac{P_3}{\rho g} + \frac{V_3^2}{2g} + h_2 \tag{6.29}$$

Equation (6.28) and (6.29) can be combined to solve for h_2

$$h_2 = \frac{(V_2 - V_3)^2}{2g} = \left(\frac{V_2}{V_3} - 1\right)^2 \frac{V_3^2}{2g} \tag{6.30}$$

If the continuity equation is applied again, the pressure head loss can be represented as:

$$h_2 = \left(\frac{A_3}{A_2} - 1\right)^2 \frac{V_3^2}{2g} \tag{6.31}$$

This expression is known as the Borda-Varnot relation, which has been verified experimentally for fully turbulent flow by Schutt, 1929.

The above equations of expansion are reduced based on the condition that the upstream free flow length is long enough to allow any interrupted flow to return to normal flow, which means upstream local flow distribution has no effect on the downstream local pressure loss. The geometric section parameters of this ASHRAE project coils are listed in Table 6.4 for reference.

Table 6.4. Fin channel geometric variables

Fin Pitch	15 fpi	20 fpi	25 fpi
Section Length	1/10"	1/10"	1/10"
Fin Thickness	0.0042"	0.0042"	0.0042"
Fin Space (initial)	[(1/15)-0.0042]" =0.0625"	[(1/20)-0.0042]" =0.0458"	[(1/25)-0.0042]" =0.0358"
Fin Space/Section Length	0.625	0.458	0.358

According to the previous experimental studies, the continuous sections might have an effect on the pressure loss. However, without further numerical analysis, it is difficult to verify how the two continuous sections affect each other. On one hand, the upstream expansion disturbs the flow profile and increases the loss of next expansion. On the other hand, if the section length is not sufficiently long to allow the airflow to contract or expand fully, the local swirl region is not completely developed on the section itself. The real loss generated could be less than the calculation value. Therefore, a summation coefficient, K_e, was used to account for the interaction of continuous sections. It could be greater or less than 1 (0.5-2.0), and becomes closer to 1 with the reducing of frost channel width.

The total expansion head loss through frost channel is

$$h_{\exp ansion} = K_e \times \left(\sum_{2}^{10} h_i + h_{exit} \right) \tag{6.32}$$

The expansion loss at the exit of frost channel is also included.

A series of expansions at the subsequent sections are preceded by an abrupt contraction at section 1. The air flow stream experiences an initial contraction to $A_{1'}$ and than a re-expansion to A_1, which is illustrated in Figure 6.10. Even though airflow is rapidly accelerated at the entrance of frost channel, pressure loss is minor because the process of converting static pressure to velocity pressure is stable. This means that the loss of mechanical energy is considered to take place mainly during the irreversible re-expansion after an initial contraction to a vena contracta. The theory for the contraction is an extension of the expansion analysis above.

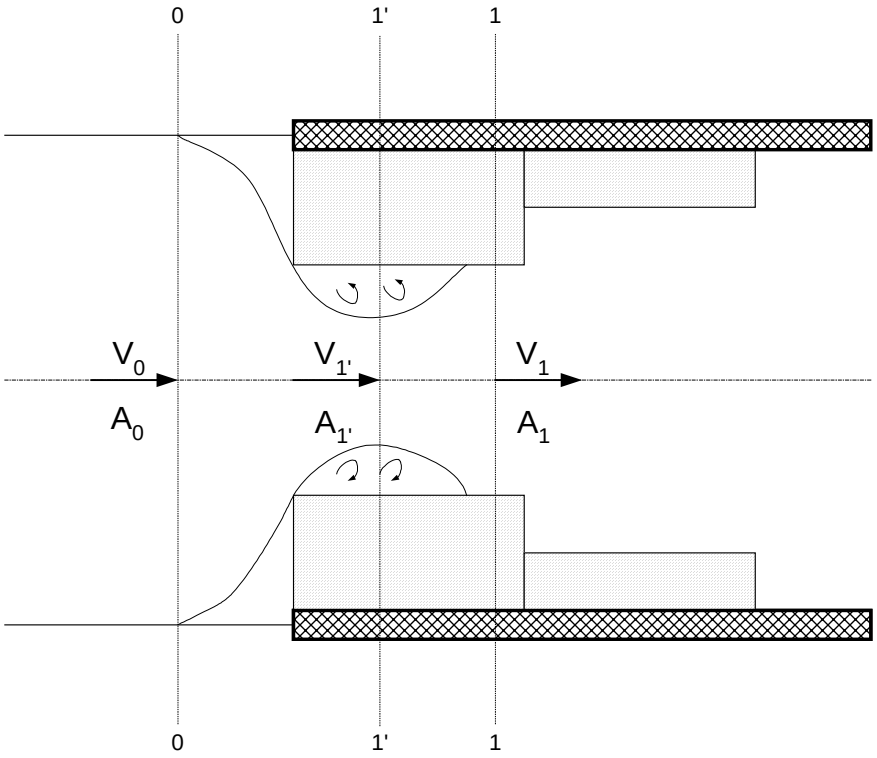

Figure 6.10 Sketch of contraction of air near the entrance to frosted fins

From the continuity equation:

$$\frac{A_{1'}}{A_1} = \frac{V_1}{V_{1'}} \tag{6.33}$$

The re-expansion pressure head loss at section 1 is given by:

$$h_1 = \frac{(V_{1'} - V_1)^2}{2g} \tag{6.34}$$

Combining Equations (6.33) and (6.34) to solve for h_1:

$$h_1 = \left(\frac{V_{1'}}{V_1} - 1\right)^2 \frac{V_1^2}{2g} = \left(\frac{A_1}{A_{1'}} - 1\right)^2 \frac{V_1^2}{2g} \tag{6.35}$$

Because it is impossible to get an accurate value of $A_{1'}$, an approximate semi-emperical equation is applied, which expresses the pressure head loss h_1 as a function of the contraction-area ratio and the air velocity through section 1:

$$h_1 = 0.5\left(1 - \frac{A_1}{A_0}\right)\frac{V_1^2}{2g} \tag{6.36}$$

Similar to the expansion, a contraction coefficient, K_c, is introduced to adjust the calculated value:

$$h_{contraction} = K_c \times h_1 \tag{6.37}$$

The overall head loss, $h_{overall}$, or pressure loss, ΔP_{frost} , for each row of coil is obtained by summing the head losses for each individual section due to the direct expansion or irreversible free expansion that follows the abrupt contraction

$$h_{overall} = h_{contraction} + h_{expansion} = K_c \times h_1 + K_e \times \left(\sum_2^{10} h_i + h_{exit}\right) \tag{6.38}$$

The pressure drop under frosting conditions is then:

$$\Delta P_{frost} = h_{overall} \tag{6.39}$$

The above equations are developed based on the assumption that air is flowing through a plain fin channel. For the coils in this project, a constant spacing between the fin plates of heat exchanger could be maintained for individual tube row. However, the fins are not straight and parallel to the macro airflow. In fact, they are waved in a sine curve. When viewed from above, a series of travelling waves are observed. This flow pattern could cause deviations from the above calculations. The effect of this geometric complexity of fin surface on fin friction factor has been considered by applying a multiplier in the Gray and Webb' correlation.

Because the ten sections were divided artificially, the frost height predicted for each section was not continuous. Abrupt (right-angle) contractions and expansions are assumed. For a real system, the frost height changes continuously in the airflow direction. This assumption might introduce an overestimate of the pressure loss.

All these uncertainties are considered while choosing the values of K_e and K_c. The applicability of this theoretical contraction and expansion model still needs to be verified by frosting test data. Therefore, the coefficients, K_c , and, K_e , also serve as the multipliers to adjust the simulation pressure drop to agree with the indirect pressure drop test data.

The above equations indicate that the significant parameters involved in the pressure drop due to frost blockage are the air velocity and the frost layer thickness. The specific application of this analysis requires inputting these two variables for each section from PCFROST.

The analysis is used to compute the dynamic pressure drop of frost heat exchanger at successive time steps. All the parameters related to the frost growing, such as air velocity, frost height, coil geometric parameters, etc. are the function of time, which should be updated at each time step.

The fin staging coils studied in this project are multiple-row heat exchangers (either 2 or 3 rows). Because of discontinues of fin plates and difference of fin pitch of each row, the frost channel contraction and expansion pressure losses should be computed for each row of the coil separately. The summation is the coil total pressure drop due to frost blockage.

CHAPTER VII

MODEL VALIDATION AND DISCUSSION

To verify the validity of the frosted evaporator model, the frosting performance of three two-row coils at the same test conditions were simulated and compared with experimental data. The three coils include one baseline coil, 20/20 fpi (787/787 fpm), and two fin staged coils, 15/20 fpi (590/787 fpm) and 15/25 fpi (590/984 fpm). Three tests were used in the comparisons. All of them were conducted at the same outdoor conditions with a dry bulb temperature of 35^{o}F (1.67^{o}C) and the wet bulb temperature of 33^{o}F (0.56^{o}C). The starting airflow rate was approximately 2800 cfm (1.322 m^{3}/s). The indoor air conditions and flow rate were held constantly at 70^{o}F (21.1^{o}C) DB, 60^{o}F (15.6^{o}C) WB, and 1100 cfm (0.519 m^{3}/s). This is the standard heavy frosting condition for heat pump tests (ARI 1989).

In this chapter, the comparisons of simulation results and experimental data have been organized into four sections: (1) outdoor coil cooling capacity, (2) frost growth along fin surface, (3) airflow pressure drop cross frosting coil, and (4) airflow rate drop with time. Detailed comparisons between the experimental results and the numerical analysis are provided in each section.

Outdoor Coil Cooling Capacity

Baseline Coil

Figure 7.1 shows both the simulated and measured air-side and refrigerant-side capacities. The experimental capacities were determined from energy balances on the air-side and of refrigerant-side of the evaporator. The dotted lines represent the coil air-side capacities. The instability of air-side experimental data was mainly caused by small fluctuation in the airflow rate (Figure 7.2) and hunting of the thermal expansion valve (TXV) which occurred in the later parts of the test (Figure 7.3).

Both air and refrigerant side capacities showed considerable drop during the test as frost formed on the coil. This decrease was caused by the reduction of airflow, the increase of thermal resistance of frost layer, and the change of heat transfer coefficient. Although the driving potential (temperature difference) between air and refrigerant increased with the drop of evaporation temperature, the total heat transfer rate still decreased.

The experimental air-side and refrigerant-side capacities were within 1 to 2 MBtu/h (0.293 to 0.586 kW). This difference can be attributed to a combination of experimental error, the transient response of the heat exchanger, and the thermal storage of frost layer.

Due to the relatively large time interval (one minute) and the inaccurate input data from curve-fitting equations of test data, the simulation results do not agree well with the experimental data during the first 5-minute startup of test. However, after that, good agreement was obtained between simulated and measured capacities. The difference were within ±10%.

It should be noted that at startup, the measured refrigerant-side capacity shows a high initial value caused primarily by the uncertainty of the refrigerant flow measurement that occurred due to the switch of the cycle from defrost to heating operations. As a consequence, the model did not show good agreement in Figure 7.1 with the experimental data until approximately five minutes into the test.

During the last 15 minutes of the test, the difference between the air and refrigerant side capacities increased gradually. This phenomenon may be attributed to the relatively slower coil response to the rapid decrease in evaporation temperature which occurs as frost accumulated on the coil with time. Another reason may be the inaccuracy of the airflow measurement. As the airflow decreased, the pressure drop across the multi-nozzle bank decreased as well. As the airflow rate dropped the proper measurement range of a specific nozzle combination, the uncertainty of the airflow measurement increased. The smaller the airflow rate, the more severe this problem became.

The evaporator of a heat pump transfers both sensible and latent heat energy from the air to the refrigerant as frost forms on it. Simulation results on the sensible and latent capacities are compared with experimental data in Figure 7.4.

The experimental sensible and latent capacities were determined from both air temperature and humidity measurements made across the outdoor heat exchanger. As the frost layer grew and blocked the airflow passages between the fins, the sensible heat transfer rate continued to drop from 19 MBtu/h (5.565 kW) to 13 MBtu/h (3.808 kW) during the 55-minute test.

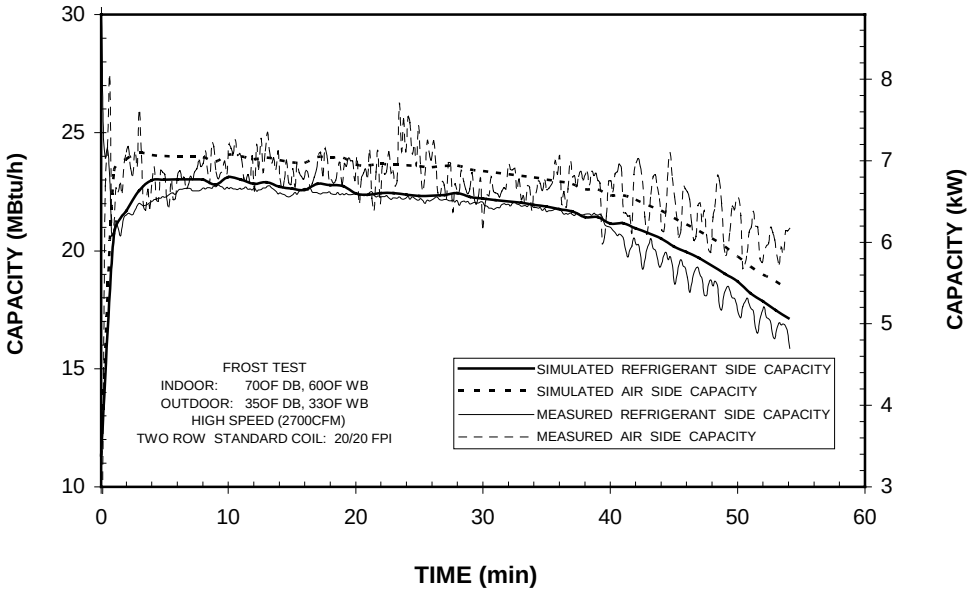

Figure 7.1 Air-side and refrigerant-side capacities of the two-row baseline coil (20/20 fpi) with high airflow (2800 cfm) during 35°F frost test

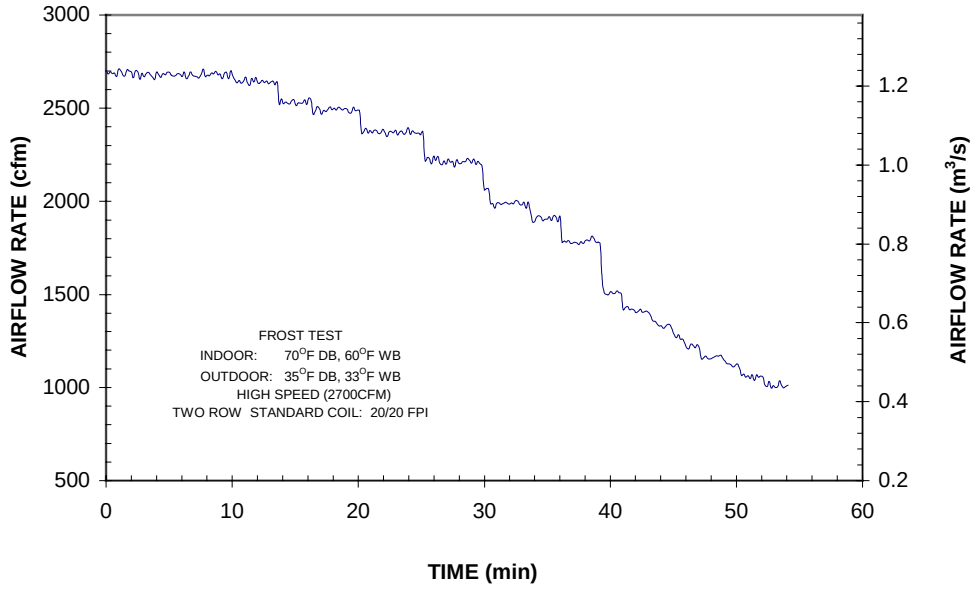

Figure 7.2 Airflow rate for the two-row baseline coil (20/20 fpi) with high starting airflow (2800 cfm) during 35°F frost test

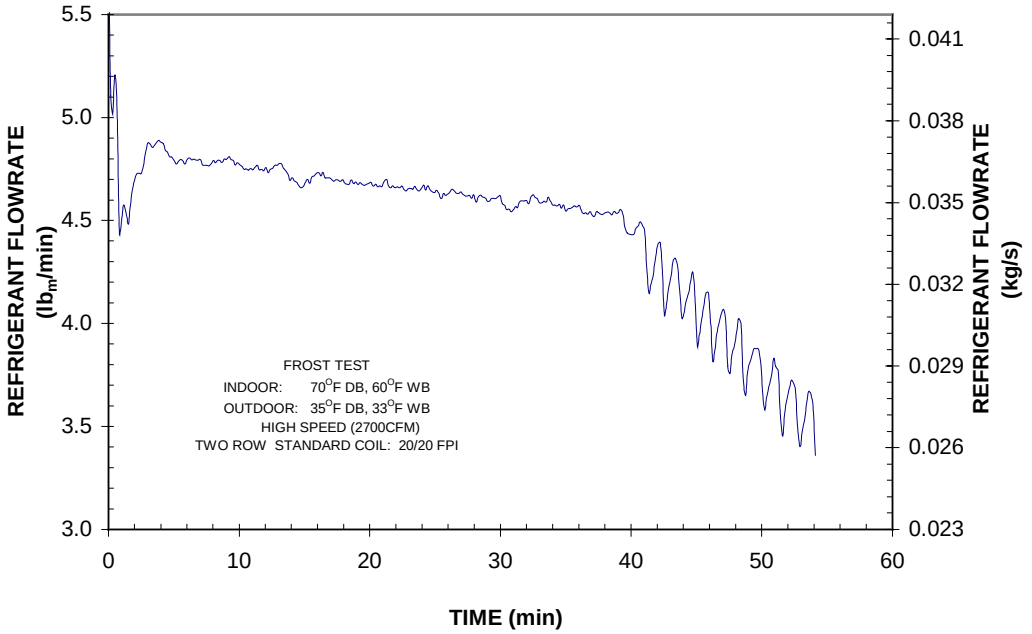

Figure 7.3 Refrigerant mass flow rate for the two-row baseline coil (20/20 fpi) with high airflow (2800 cfm) during 35°F frost test. Hunting of the TXV is evident after 40 minutes

The experimental latent heat transfer rate reached a maximum in the first 5 minutes, then declined, and after about 20 minutes began to slowly increase. The initial peak value of the test appears to be due to a combination of large airflow through the coil and the enhanced heat transfer by the surface roughness due to frost formation on the fin surface. Frost increased the surface roughness on the fins at the beginning of test, which increased the heat and mass transfer coefficients. The increase during the last 35 minutes may be attributed to the reduction of evaporation temperature (Figure 7.5). Although the simulation shows increasing amount of latent heat transfer rate at the later portion of the test, it was unable to predict the peak at the beginning of test because the model did not include any roughness effects of the frost surface on the heat transfer coefficient.

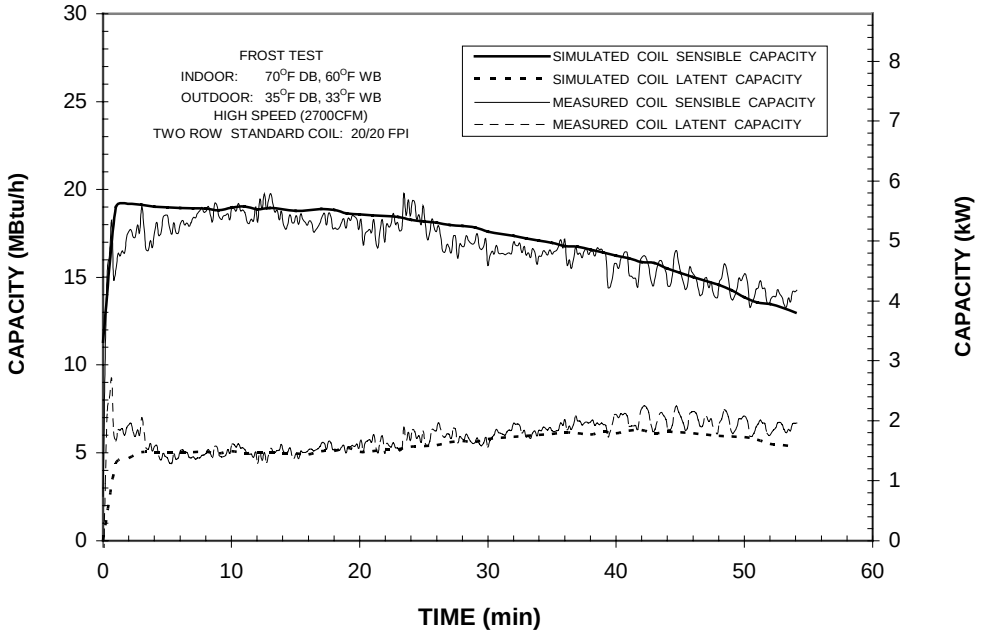

Figure 7.4 Air-side sensible and latent capacities for the two-row baseline coil (20/20 fpi) with high airflow (2800 cfm) during 35°F frost test

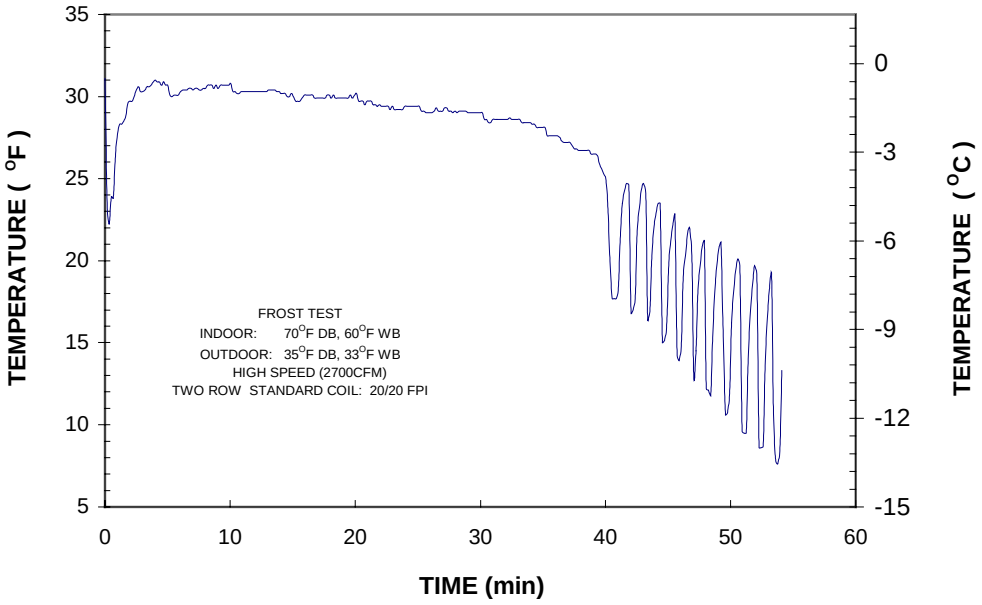

Figure 7.5 Refrigerant temperature at the coil outlet for the two-row baseline coil (20/20 fpi) with high airflow (2800 cfm) during 35°F frost test

As frost forms on the fin surface, the frost provides a small insulating layer between the air stream and the fin surface. The frost is composed of an ice matrix and pores filled with moist air. This increases the coil total thermal storage and heat conduction resistance between air and refrigerant.

The thermal storage of the frosted coil includes three components: tubes, fins and frost layer. The storage value of fins is dominant. Both tube and fin thermal storage decrease with the continuous reduction of evaporation temperature during the frosting tests. However, with more frost accumulating on the coil surface, the thermal storage of the frost layer may keep rising in spite of the average temperature of frost layer decreasing with the drop of evaporation temperature. The reduction of frosted coil thermal storage with the decreasing evaporation temperature may not compensate for the increase of frost thermal storage due to more frost accumulated on the coil. Thus, an energy imbalance between air and refrigerant side capacities occurs.

For the test conditions used for these tests, the calculations demonstrated that the increase of the coil total thermal storage could not be ignored. The overall variation of coil thermal storage was positive. The heat lost by the air to the coil was more than the heat gained by the refrigerant. Hence, in the simulation model, the variation of coil total thermal storage was considered in the energy balance calculations at each time step. As can be seen in Figure 7.1, the trends of air-side and refrigerant-side simulation values are similar except that they differ by a relatively constant gap, which represents the increase of coil total thermal storage.

For the transient behavior of the heat exchanger, one of the important parameters would be the time required for the whole coil to reach steady state when the inlet parameters changed. In a heat exchanger with transient heat transfer, the response of one outlet fluid parameters to a change of corresponding inlet fluid parameters may be not instantaneous. The lag is affected by the thermal capacitance of the heat exchanger and fluids, as well as the resistance to heat transfer. For a frosted coil, with more frost accumulating on the heat exchanger surface, the response time increases due to the rise of coil total capacitance and heat conduction resistance between air and fin surface. Meanwhile, the continuous variation of frost properties makes this phenomenon more complex.

In the present model, the quasi-steady state method is used to deal with the transient process of freezing coil by introducing step changes of coil inlet parameters. The basis of this method builds on steady state heat transfer calculations. At each time step, the coil is assumed to be in dynamic equilibrium and no transient heat transfer is considered. Hence, this implies an assumption that the response time of frosted coil to the variations of operation conditions is instantaneous.

If this idealization is violated, the transient heat transfer of the frosted coil has to be taken into account. The problem then becomes more complicated due to the transient heat transfer analysis, and the quasi-steady state method could not be used. Therefore, the value of response time determines the application of quasi-steady state approach. With the exception of the air inlet temperature and humidity, all other inlet parameters and some coil properties were time-dependent. Because multiple parameters varied while others were constant, it was very difficult to quantitatively analyze the transient response time of the frosted heat exchanger

In the simulation, the thermal resistance and the thermal storage of frost layer are considered to influence frost accumulation on the heat transfer calculations at each time step. Both variables increased with frost growth on the coil surface. However, because of the characteristics of the steady state heat transfer calculations associated with the quasi-steady state approach, it inherently could not provide the transient analysis of coil heat transfer due to thermal storage effects. Meanwhile, the heat conduction through the frost layer was transient in nature and is dependent upon the frost thermal conductivity, specific heat, density and height. Similarly, the influence of transient heat conduction between air and refrigerant was neglected as well.

Comparing Figures 7.1 and 7.4, it would appear that the present quasi-steady state technique provides satisfactory modeling of the transient affects of frost on a coil. However, more numerical analysis and experiment investigation still needs to be completed to verify the reasonability of this approach.

The comparisons of simulated and measured coil outlet parameters, which include refrigerant outlet temperature and pressure as well as air outlet temperature and humidity ratio, are shown in Figures 7.6 through 7.9. The simulation model tracks the varying trends of coil outlet parameters very well.

Figures 7.6 and 7.7 present the variation of refrigerant pressure and temperature at the coil outlet, respectively. The curves show that the evaporator outlet temperature and pressure were not constant during the frost test. At the beginning of the test, when the compressor first started, both temperature and pressure at the evaporator outlet first decreased, reached a minimum, then climbed back at about 3 minutes. Afterward, the pressure showed a steady decrease with relatively small fluctuations. Because the superheat temperature at the evaporator outlet continued increasing with time, the outlet temperature remained more constant than that of pressure at the evaporator outlet.

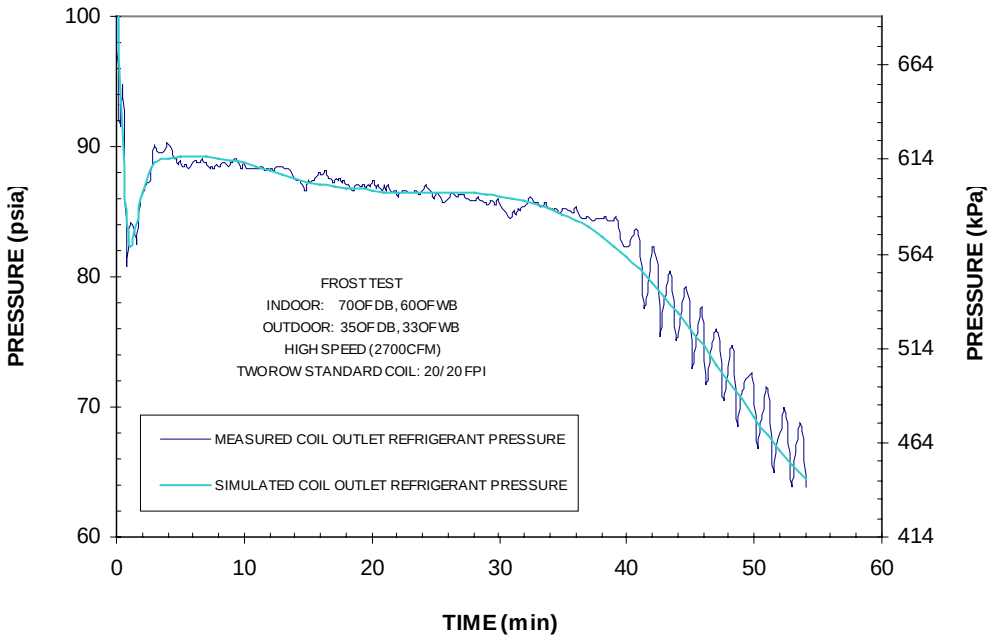

Figure 7.6 Simulated and measured coil outlet refrigerant pressures for the two-row baseline coil (20/20 fpi) with high airflow (2800 cfm) during 35°F frost test

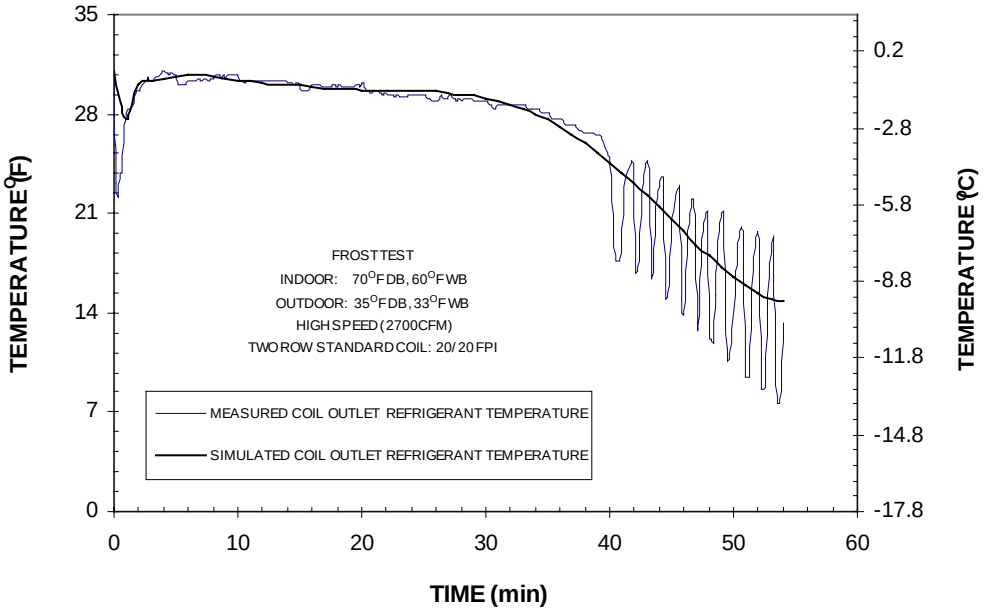

Figure 7.7 Simulated and measured coil outlet refrigerant temperatures for the two-row baseline coil (20/20 fpi) with high airflow (2800 cfm) during 35°F frost test

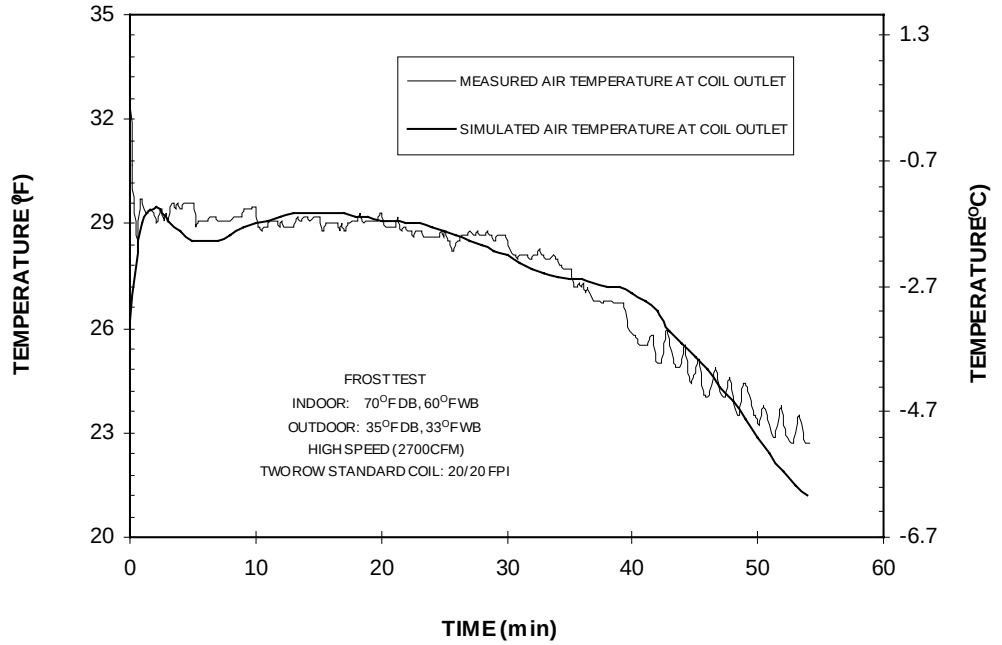

Figure 7.8 Simulated and measured coil outlet air temperatures for the two-row baseline coil (20/20 fpi) with high airflow (2800 cfm) during 35°F frost test

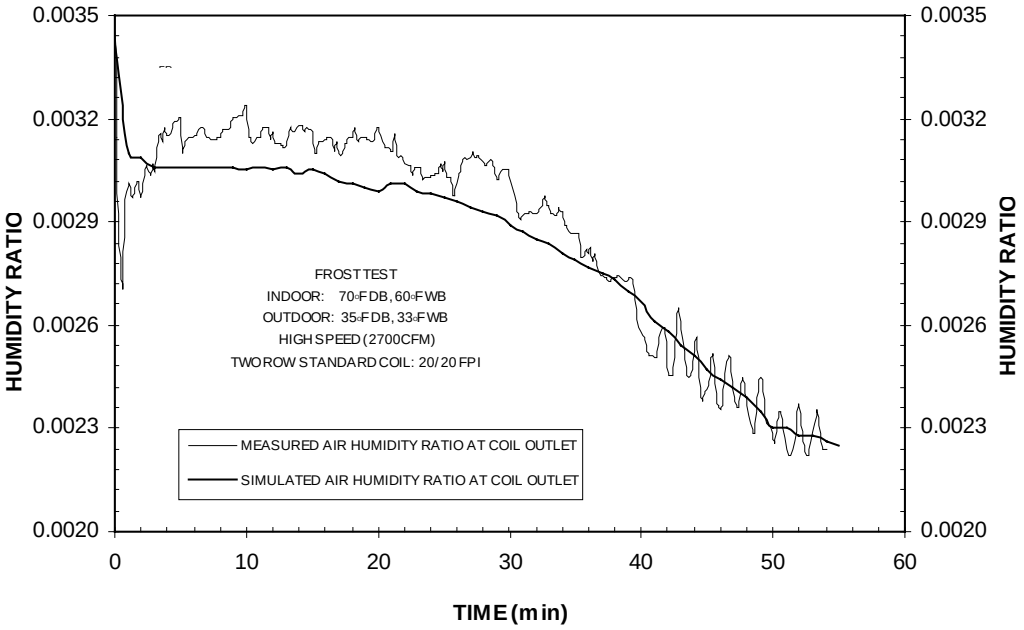

Figure 7.9 Simulated and measured coil outlet air humidity ratios for the two-row baseline coil (20/20 fpi) with high airflow (2800 cfm) during 35°F frost test

During the last part of test, the curves decreased more rapidly. This phenomenon can be explained by the accelerated degradation of the air-side heat transfer and airflow. With frost accumulation, the frost layer blocked the airflow passages between fins and gradually insulated the fin and tube surface from the surrounding air. All these deteriorated the coil air-side heat transfer significantly. Model predictions reveal that the temperature and the pressure of refrigerant at coil outlet show trends similar to the test data.

The air temperature and humidity ratio showed similar trends to the coil refrigerant pressure and temperature. Both gradually decreased during the first 30 minutes of the test, then they began to fall rapidly during the last 15 minutes. The decreasing evaporation temperature, together with the lower airflow rate, caused this rapid drop of airflow temperature and humidity ratio at coil exit.

Fin Staged Coil

Figures 7.10, 7.11, 7.12 and 7.13 show the variations of coil simulated and measured capacities with time. The air-side heat transfer surface is one of the major factors in determining coil heat transfer. At low Reynolds numbers, the average heat transfer coefficient for the coil first row is much higher than that of the second row. Thus, the reduction of effective heat transfer surface with the use of fin staging would degrade the heat transfer capacity of coil, which is shown in Figures 7.10 and 7.11.

Between the two fin staged coils, because the heat transfer coefficient for the second row of a two-row coil is substantially lower than for the first row at low Reynolds numbers (which has been illustrated in Chapter VI), a slight addition of heat transfer surface at the second row had a negligible effect on the total heat transfer capacity of the coil.

Both air-side capacity curves clearly showed the trends went higher in the last parts of tests. This differs from the trends on the refrigerant-side capacity. This might be caused by the measurement error generated when the air flow rate dropped below the proper measurement range of the open nozzle combination of the psychrometric chamber. The present simulation model did not predict this abnormal trend of increasing capacity. All the simulation results decrease at the end of tests.

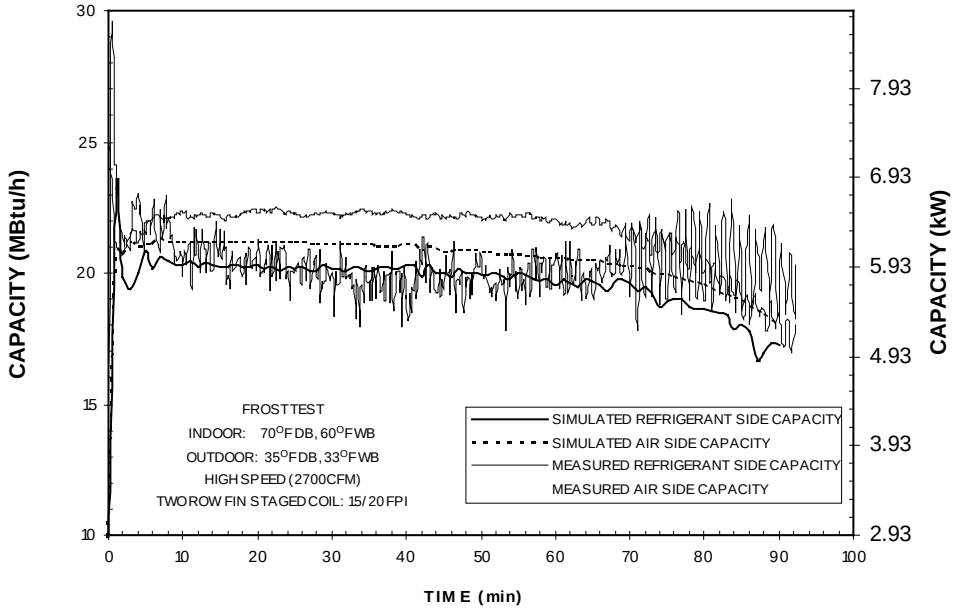

Figure 7.10 Air-side and refrigerant-side capacities for the two-row fin staging coil (15/20 fpi) with high airflow (2800 cfm) during 35°F frost test

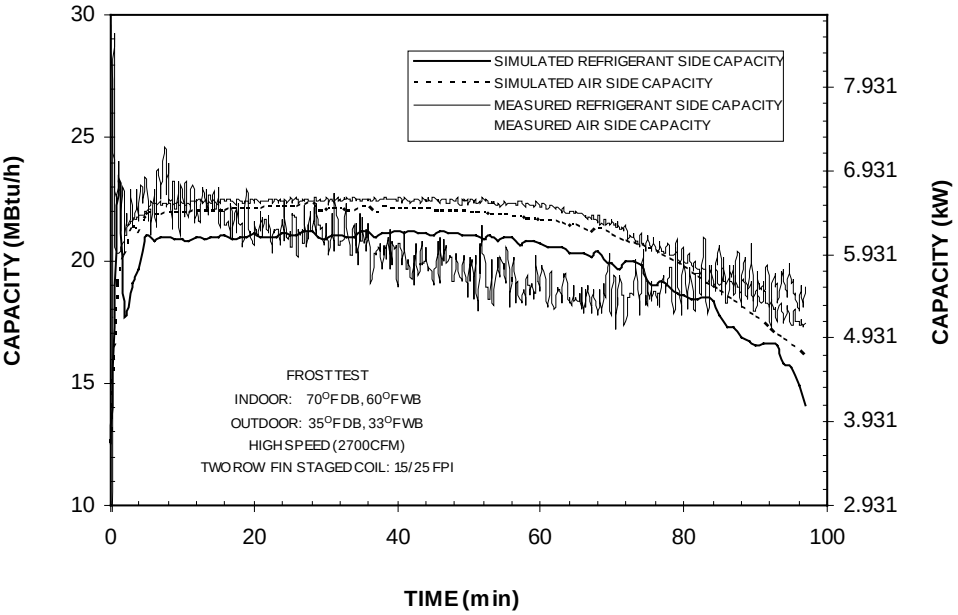

Figure 7.11 Air-side and refrigerant-side capacities for the two-row fin staging coil (15/25 fpi) with high airflow (2800 cfm) during 35°F frost test

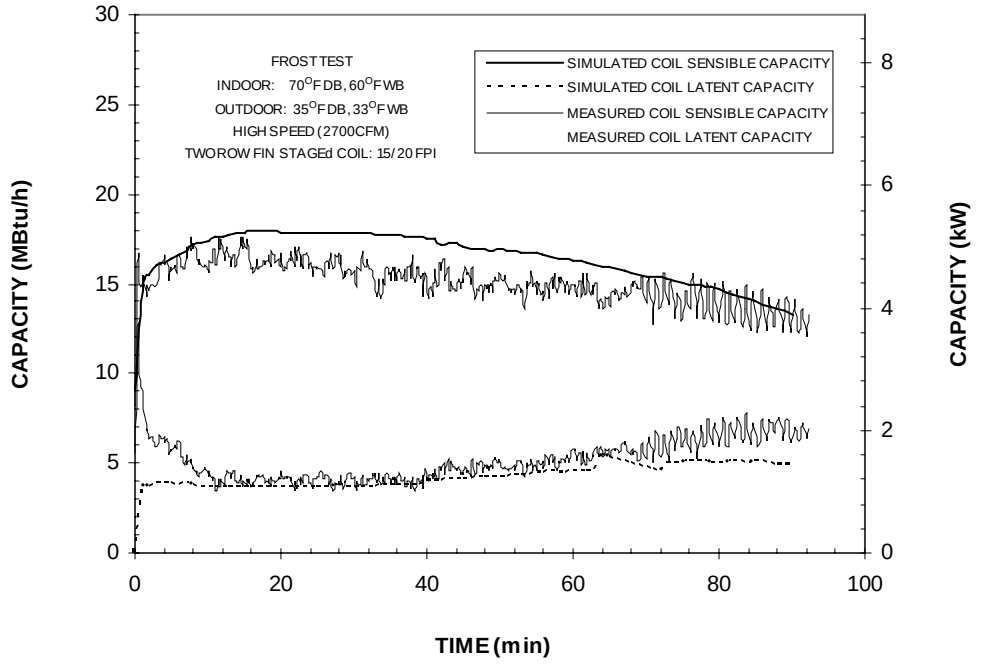

Figure 7.12 Air-side sensible and latent capacities for the two-row fin staging coil (15/20 fpi) with high airflow (2800 cfm) during 35°F frost test

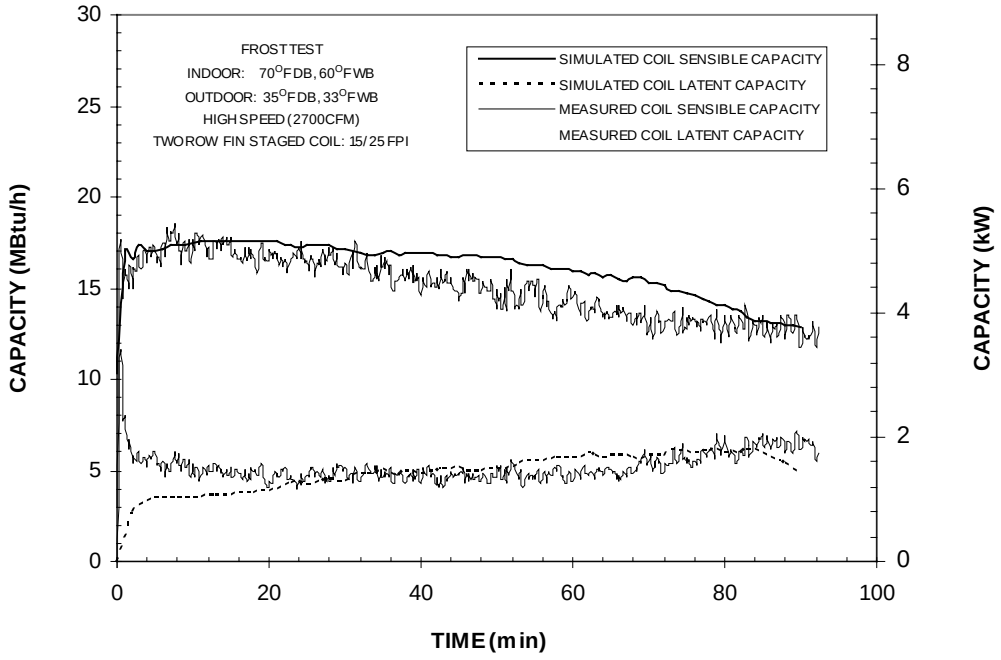

Figure 7.13 Air-side sensible and latent capacities for the two-row fin staging coil (15/25 fpi) with high airflow (2800 cfm) during 35°F frost test

Frost Growth along Fin Surface

For all tests, only the frost heights at the leading edge of the fins on the front row could be measured. Thus, all comparisons of frost height in this section are on the leading edge.

The simulation model was able to predict position and time dependent distribution of frost layer. Simulation results of frost growth on heat exchanger fin surface have shown that there exist large spatial and temporal variations in the frost growth that depends upon the structure of the heat exchanger (fin spacing and row number) and the operating conditions (temperature, humidity and airflow).

Baseline Coil

Figures 7.14 and 7.15 show the simulated growth of the frost layer with respect to time for the two different rows. The thin smooth curves show the calculated frost growth along a series of divided sections on the fin surface. The average frost height for the whole row is present as well. For the purpose of comparison, the simulated frost growths at the first section, together with the measured frost heights at the leading edge, are shown in Figure 7.16. Two bold broken lines indicate the experimental observation of leading edge frost growth at two points located on the different circuits, respectively.

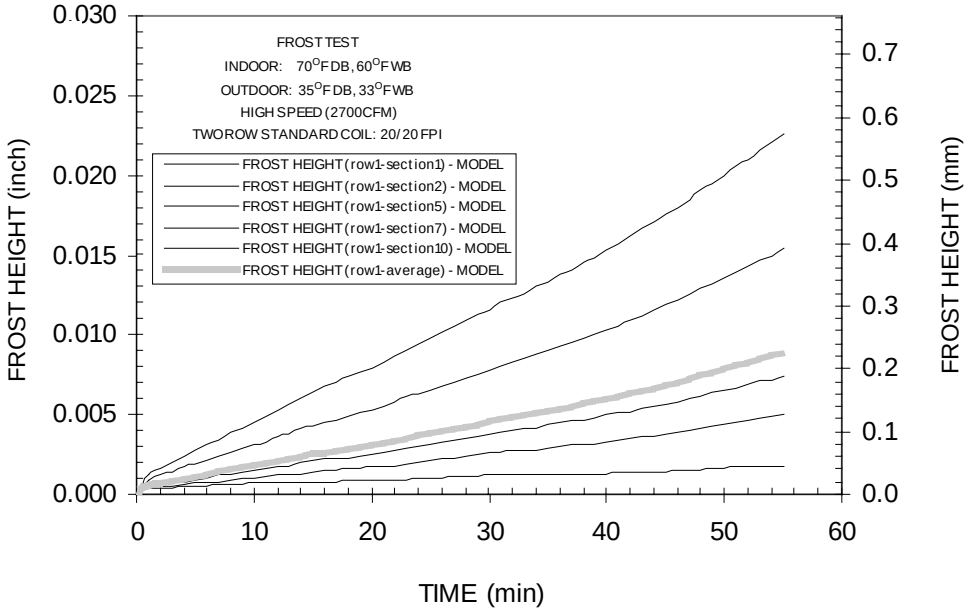

Figure 7.14 Simulated frost growth along first-row sections for the two-row baseline coil (20/20 fpi) with high airflow (2800 cfm) during 35°F frost test

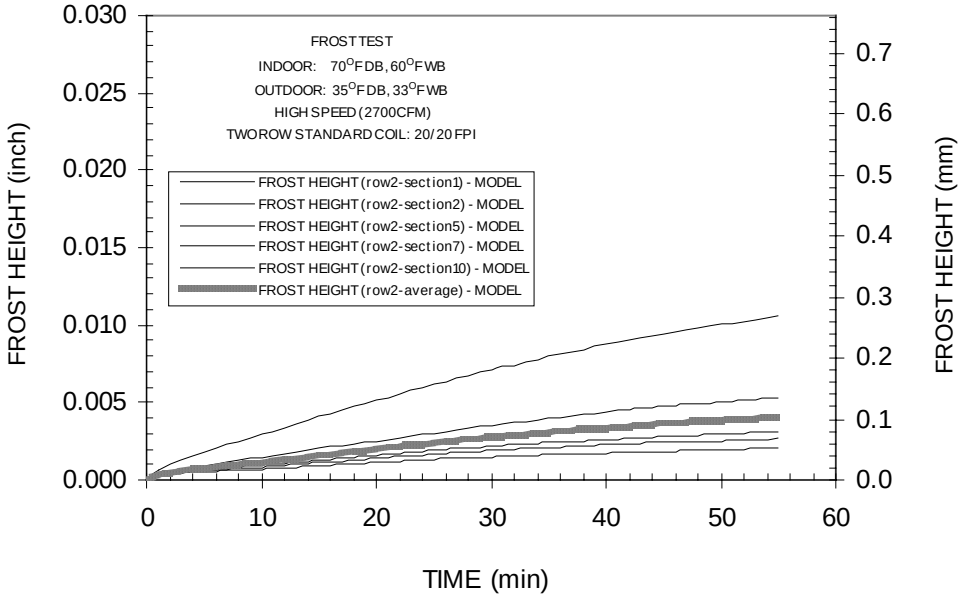

Figure 7.15 Simulated frost growth along second-row sections for the two-row baseline coil (20/20 fpi) with high airflow (2800 cfm) during 35°F frost test

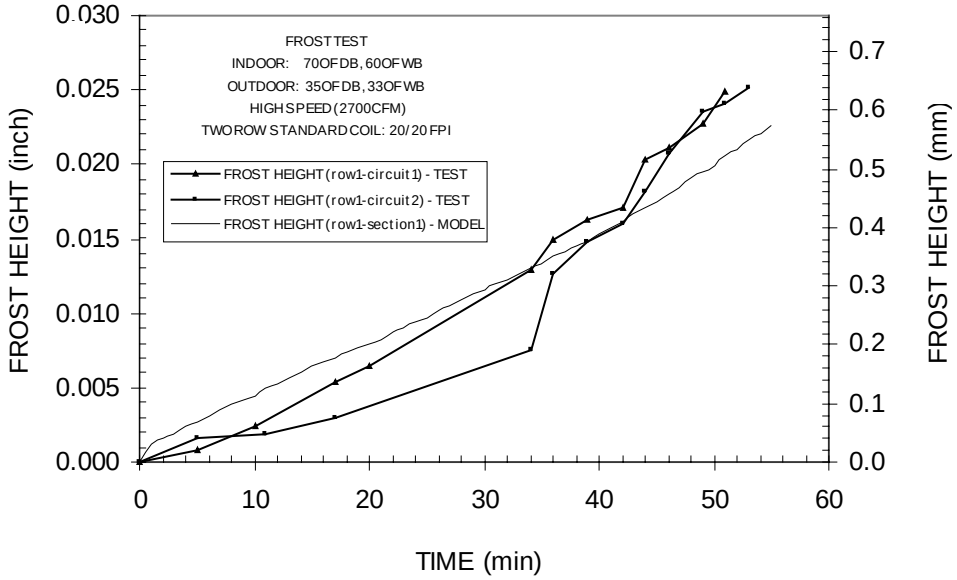

Figure 7.16 Comparison of simulated and experimental frost growth at the leading edge of the two-row baseline coil (20/20 fpi) with high airflow (2800 cfm) during 35°F frost test

With the model assumption of the variation of the local heat and mass transfer coefficients along the fins, the predictions of frost layer height varied in thickness with fin depth and time. The growth profiles of the frost layer at different sections were nearly linear with time (Figures 7.14 and 7.15). While the values were different, the trends were similar in the two figures. The frost layer didn't grow evenly over the entire fin surface. The upstream fin surface normally has the fastest growth rate. The frost at the leading section had the highest growth rate and the average frost height was only about half of the leading edge value. This phenomenon can be attributed to the fact that the maximum local heat and mass transfer coefficients were at the leading edge.

In Figure 7.16, the frost layer thickness increased with time. Based on the experimental observations, the frost heights at both measured points increased almost linearly with time up until approximately 35 minutes. The frost grew faster during the last 20 minutes of the test.

The frost height measurement during the early part of the test had a large uncertainty. At the early portion of the frost test, uneven frost deposition was often observed on different circuits due to unbalanced refrigerant distribution in the coil. As frost blockage increased, more airflow was diverted to the area with less frost. This ultimately caused the frost deposition to be more uniform. This phenomenon could be used to explain the disagreement of the two test curves in Figure 7.16. In addition, the video cameras, which were mounted close to the front of the coil face, may have partially blocked the airflow and disturbed the uniform airflow field going into the coil where the points were monitored. All these increased the uncertainty of measured frost growth at the leading edges.

During the first 30 minutes of the test, the model appeared to overpredict the frost growth at the leading edge. However, the model still estimates a total frost thickness of 0.022 inch (0.559 mm) at the end of 53 minutes.

Through raising the local heat transfer coefficient, the calculated frost height at section one could be increased furthermore to match the test measurement. However, because the pressure loss due to the contraction at section one mainly depended upon the local frost height, the increase of frost height would generate unreasonably high pressure drops at the end of the test. This would cause the airflow calculation subprogram PRCFM to not work properly, which is discussed later in Section 7.3 and 7.4. For the purpose of obtaining the overall agreement of the model analysis, the frost height of the leading edge section was not adjusted.

The preliminary calculations showed a decelerating tendency (concave curve) of frost growth at each section. Clearly, this didn't agree with the experimental observation. It could be explained by the effect of frost layer tortuosity on the calculation, which is one of the determining factors of water diffusion into the frost layer.

The tortuosity is a measurement of frost porosity. The greater the tortuosity, the more difficulty it's for the water vapor to diffuse into the frost layer to increase its density. In the frost calculation

subprogram PCFROST, the rate of frost deposition was broken up into two parts: one for density increase of frost layer and one for growth of frost layer height. Thus, the less water vapor would diffuse into the frost layer and more of them would go to increase the frost height.

Sanders' tortuosity correlation (1974) was used in PCFROST, which was based on the test data for some unconsolidated media, such as sand, powders, or steel wool (O'Neal, 1982), and might cause substantial errors in model calculations. Therefore, a multiplier more than one is applied to increase the portion of frost deposition for growth calculation. After adjustment, the present simulation result shows a better agreement in growing trend with the test data.

The simulation results for frost thickness versus time in the fin longitudinal direction are present for both rows in Figure 7.17, which shows the two-dimensional prediction of frost layer growth along fin surface for the baseline two-row coil (20/20 fpi). Inspection of the figure indicates that the frost at the leading edge and the frost close to the tube front surface had the highest heights and as a whole, the height of frost layer decreased rapidly with the depth of fin surface. At the rear part of fin surface, almost no frost growth was predicted. This simulation result mainly comes from the application of different local heat and mass transfer coefficients, which has been discussed in Chapter VI.

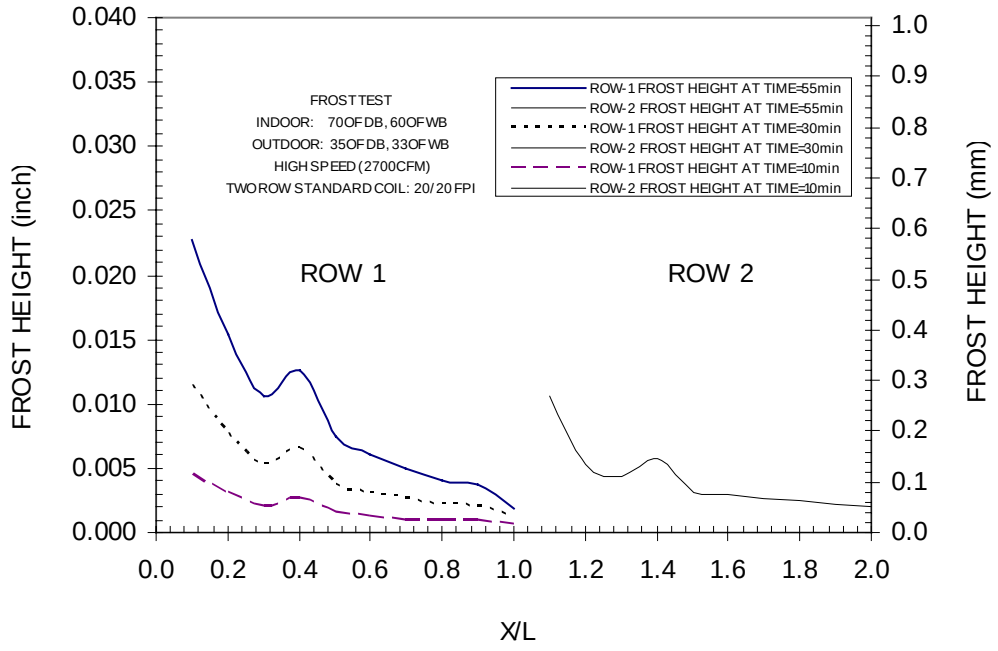

Figure 7.17 Simulated frost growth along fin surface for the two-row baseline coil (20/20 fpi) with high airflow (2800 cfm) during 35°F frost test

The simulation predicted two peaks, a primary one at the leading edge and smaller one at 40% of the way through the fin. The frost height at the leading edge peak was substantially higher than that at the

peak in front of the tube. Different mechanisms of enhanced heat and mass transfer are found to result in the generation of two peaks. For the peak at the leading edge section, the boundary-layer development was the determining factor. The relatively thin boundary layer allowed more thermal energy and moist transfer at section one. With the boundary-layer growth at the following sections, the local heat and mass transfer coefficients gradually decreased, which caused the corresponding reduction of the frosting rates.

From Figure 7.17, it is seen that the second peak was located at the vortex-dominated zone adjacent to the upstream face of tube. High values of the heat transfer coefficient at the vortex zone yielded relatively high frosting rates, which caused the second peak. This phenomenon agrees with the fact that higher frost accumulation at the fin base around the tube was due to the lower fin surface temperature and higher local heat and mass transfer coefficients. In addition, the difference of the two peaks implies that the effect of the initial boundary-layer development on the frost growth was more pronounced than that of vortex disturbance in front of tube.

The two-dimensional model cannot give a complete description of frost distribution on the entire fin surface. However, it should be noted that the spatial distributions of frost depositions in the crosswise direction of two peak section areas are different. For the section with the leading edge peak, the frost height should be even over the whole section area due to the same mass transfer conditions.

In contrast, the second peak in the figure represented the average height of the frost deposition over the entire section. The frost accumulated in the forward vortex zone of the tube was substantially higher than the average and those at the airflow channel area between two tubes, where the frost height should be much lower.

Clearly, the airside pressure loss through the frosted channel was mainly caused by the frost peak at section one. The second peak provided almost no blockage to the airflow due to the fact that most of the frost was accumulated in the front of the tube, whose effect has been considered in the calculation of drag force of tube banks. This agreed with the pressure drop calculation analysis where the pressure loss due to the contraction at the leading edge was the dominant component in the contraction and expansion pressure drop model.

The frost growth at the second row showed the same tendencies as that of the first row. Similarly, two peaks appeared at the sections of leading edge and in the front of the tube. This may be attributed to the assumption of similar distributions of local heat and mass transfer coefficients for both rows.

The only difference between the rows was that the absolute values of frost height at the second row were less than those at the first row. This simulation result demonstrated that the second-row fins of a two-row coil were less effective as heat and mass transfer surfaces than the first-row fins. The difference between the calculated average heat transfer coefficients of each row and the gradually reduction in

humidity difference between frost surface and airflow in the fin depth direction are probably the main reasons why the calculated frost growth at the second row was slower than that at the first row.

Almost no frost growth was predicted on the rear part of the second row fin surfaces. This was confirmed by the visual observation with a video camera setup inside the coil. The fin surface temperature should have been relatively higher at the rear part of the fins on the second row. Meanwhile, the airflow generally has the lowest humidity ratio at the end of fin surface. When the air humidity ratio is equal or less than the saturated humidity ratio at the frost surface temperature, no water vapor could condense out of the airflow and freeze on the fin surface. Therefore, this explains why no frost deposition could occur at the trailing edges of coil.

Although no detailed measurement of frost layer distribution inside the heat exchanger could be provided to validate the simulation result, this non-uniform distribution of frost deposition was consistent with the test results of Chen et al. (1999).

Because no local frost thickness distribution along fin surface was measured to validate the calculation of frost growth, the result of simulated frost mass accumulation is compared with the test data in Figure 7.18. The experimental value was calculated by multiplying the air mass flow rate with the humidity loss of airflow through coil, which was determined by measuring the coil entrance and exit relative humidity.

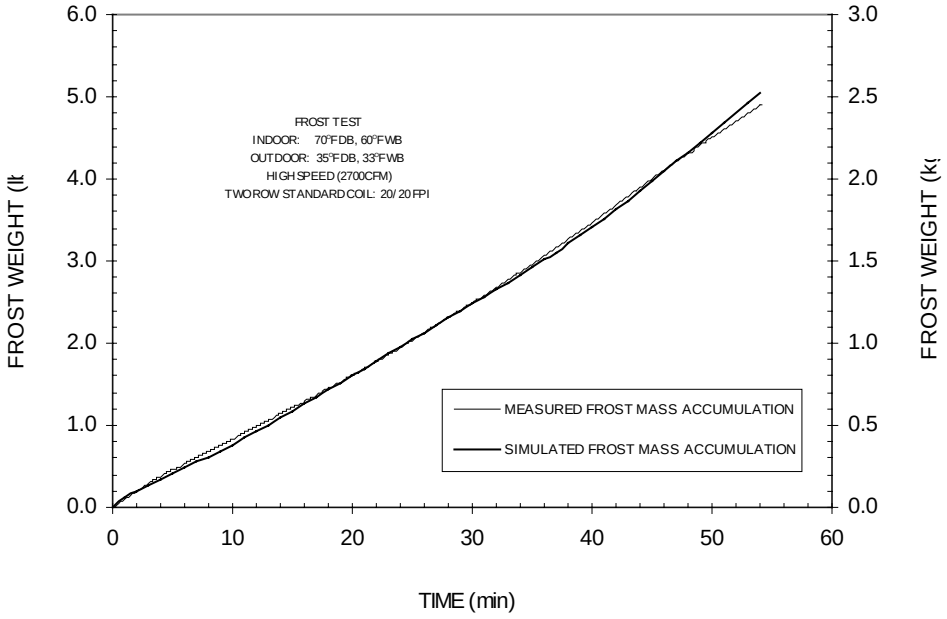

Figure 7.18 Simulated and experimental frost mass accumulation for the two-row baseline coil (20/20 fpi) with high airflow (2800 cfm) during 35°F frost test

The amount of frost on the coil was dependent on the surface geometry, the air flow rate, the evaporation temperature, the operating time, and the ambient air state, which was kept constant in the current experimental study. It was approximately linear with time in Figure 7.18. A satisfactory agreement can be obtained between experimental data and the model. This indicates, as a whole, the frost model can give a reasonable prediction of frost accumulation on the coil, which is the convincing basis for the predictions of frost formation model. As we know, due to the sensitivity of the frost height on the frost mass accumulation, any discrepancy in the predicted frosting rate can have significant effects on the calculation results of frost height.

Figure 7.18 shows the slope of the curve (frosting rate) approximately to be constant. As the air velocity decreased, the mass transfer coefficient gradually decreased along with the heat transfer coefficient. Thus, the frosting rate should decrease with time. On the other hand, the mean temperature of air passing through the coil (Figure 7.8) also decreased with the reduction of airflow. This trend would tend to increase the rate of moisture condensing out of the air stream. Furthermore, with the deterioration of heat transfer, the evaporation temperature reduced (Figure 7.23), which caused the surface temperature of the evaporator to drop with time. This trend would enhance the driving potential of mass transfer. The fin surface temperature and the air mean temperature had opposing effects on the frosting rate. The net result of the effects of these three variables on the mass transfer driving potential determined the growth of frost. These balanced each other in this test. Thus, the frosting rate was approximately constant during the whole frosting process. This will probably not always be the case. The quantitative effect of each of the parameters depends upon the particular test conditions and changes with respect to each other.

Fin Staged Coil

Figures 7.19 through 7.22 show the effect of fin staging on the frost growth of heat exchangers. Increasing the fin spacing of the first row of the coil could prolong the time to fully frost the evaporator. Based on the experimental data of the frost growth process, less frost was formed at the leading edge of the two fin-staged coils during most tests. Especially for the 15/25 FPI coil, at the first eighty minutes the fin leading edges were almost unfrosted. However, in the last twenty minutes, because of the rapid drop in the evaporation temperature, the frost started to form and grew extremely fast.

Despite the absence of frosting at the leading edge, frost could have formed inside the coil. From the increase of frost mass accumulation (Figures 7.23 and 7.24) and airflow pressure drop (Figure 7.26), it can be inferred that some frost formed and that it blocked the airflow inside the coil. Most probable areas are the tube outside surface and the fin root region due to their relatively lower surface temperatures and higher local heat and mass transfer coefficients. It is hypothesized that the frost first formed on the tube surface, then extended outward to the nearly fin surface. The fin leading edges were the last to frost.

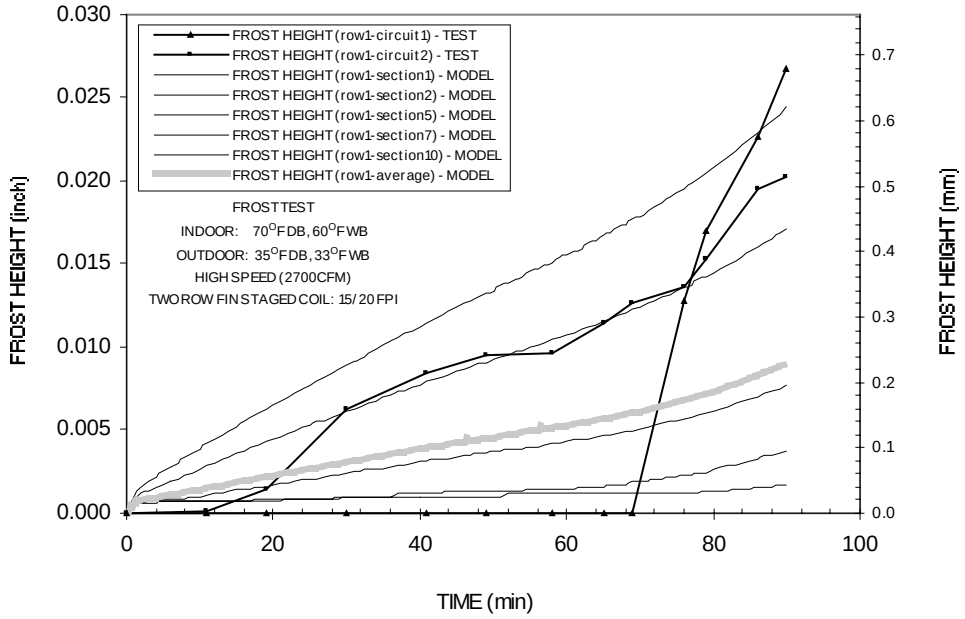

Figure 7.19 Simulated and experimental frost growth at the first row of the two-row fin staged coil (15/20 fpi) with high airflow (2800 cfm) during 35°F frost test

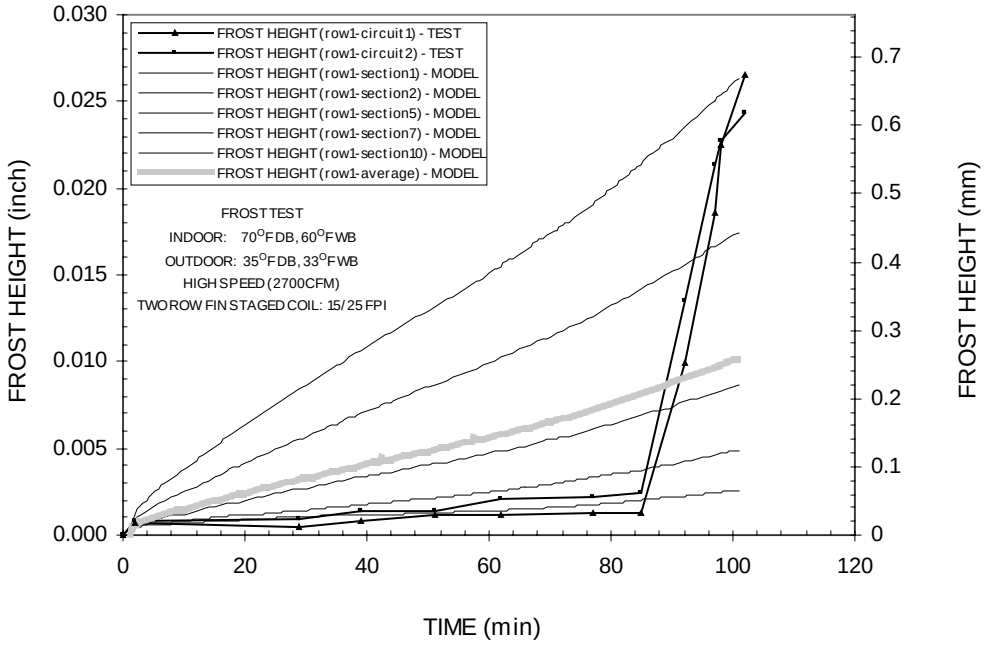

Figure 7.20 Simulated and experimental frost growth at the first row of the two-row fin staged coil (15/25 fpi) with high airflow (2800 cfm) during 35°F frost test

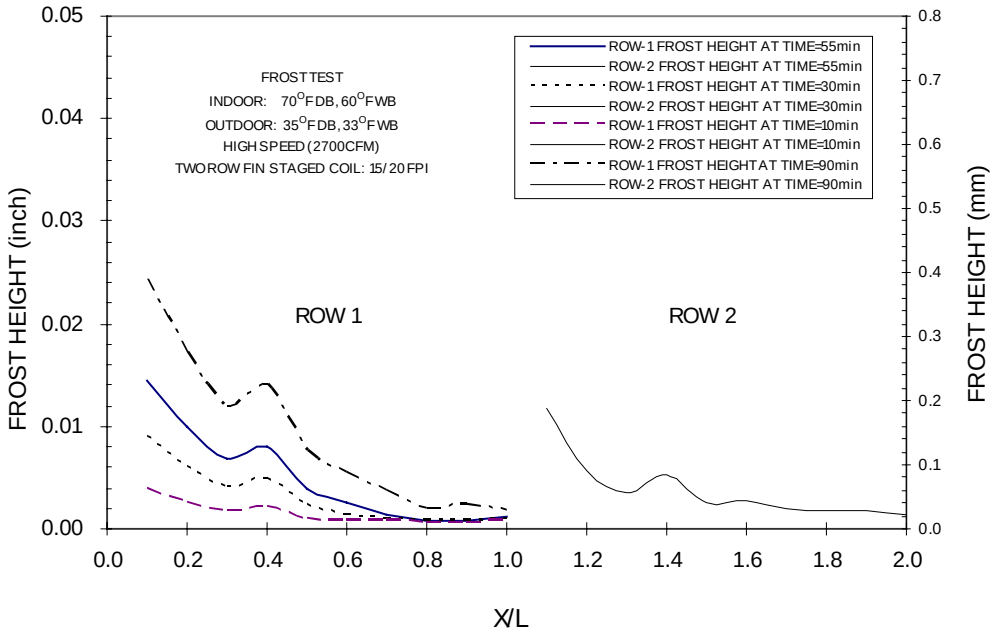

Figure 7.21 Simulated and experimental frost growth along fin surface for the two-row fin staged coil (15/20 fpi) with high airflow (2800 cfm) during 35°F frost test

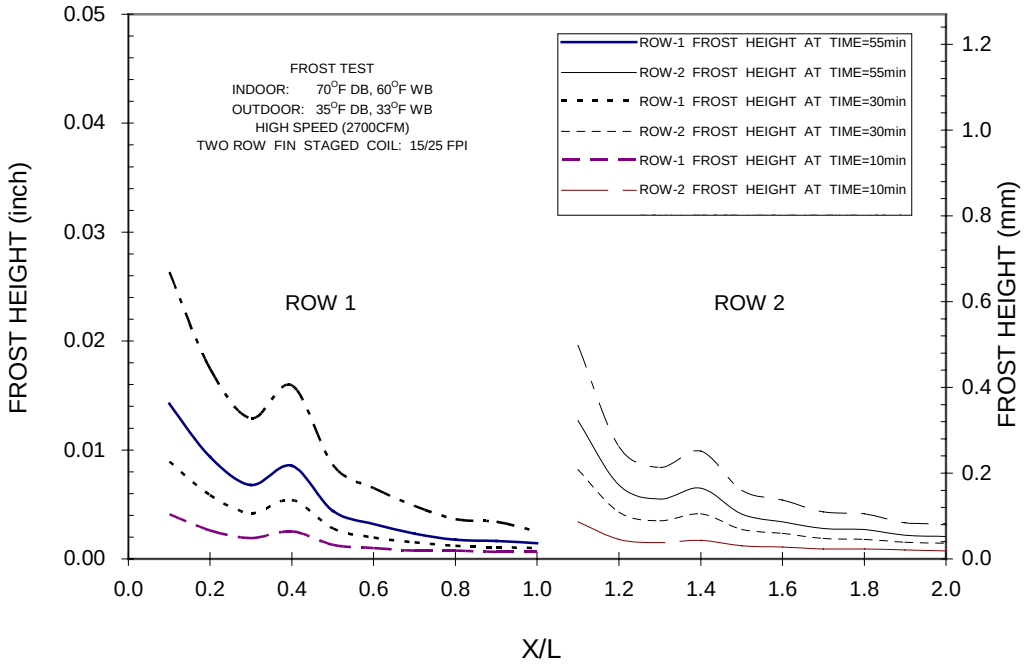

Figure 7.22 Simulated and experimental frost growth along fin surface for the two-row fin staged coil (15/25 fpi) with high airflow (2800 cfm) during 35°F frost test

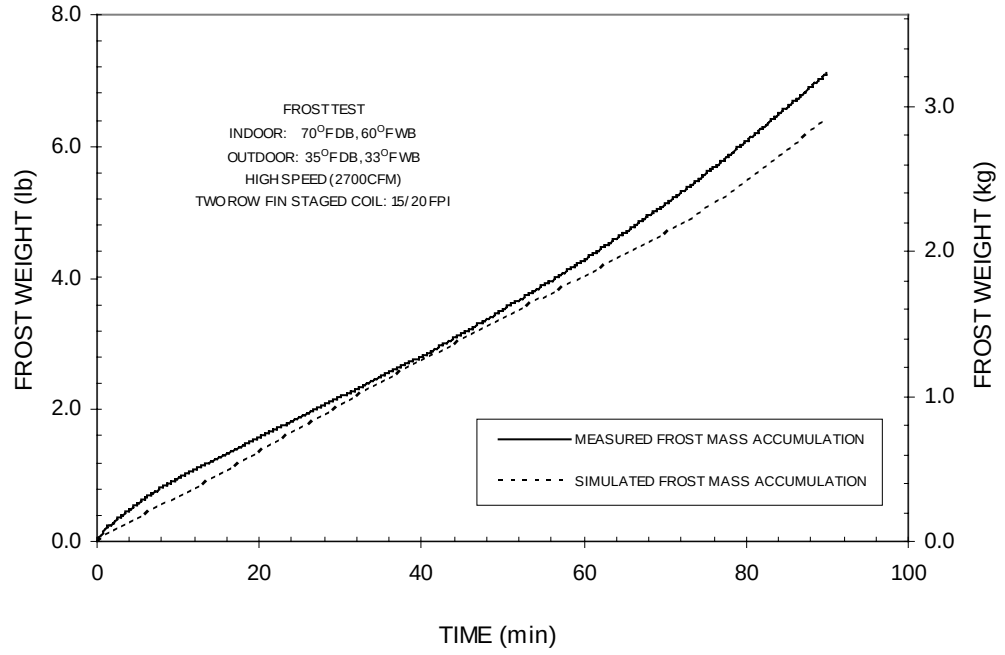

Figure 7.23 Simulated and experimental frost mass accumulation for the two-row fin staged coil (15/20 fpi) with high airflow (2800 cfm) during 35°F frost test

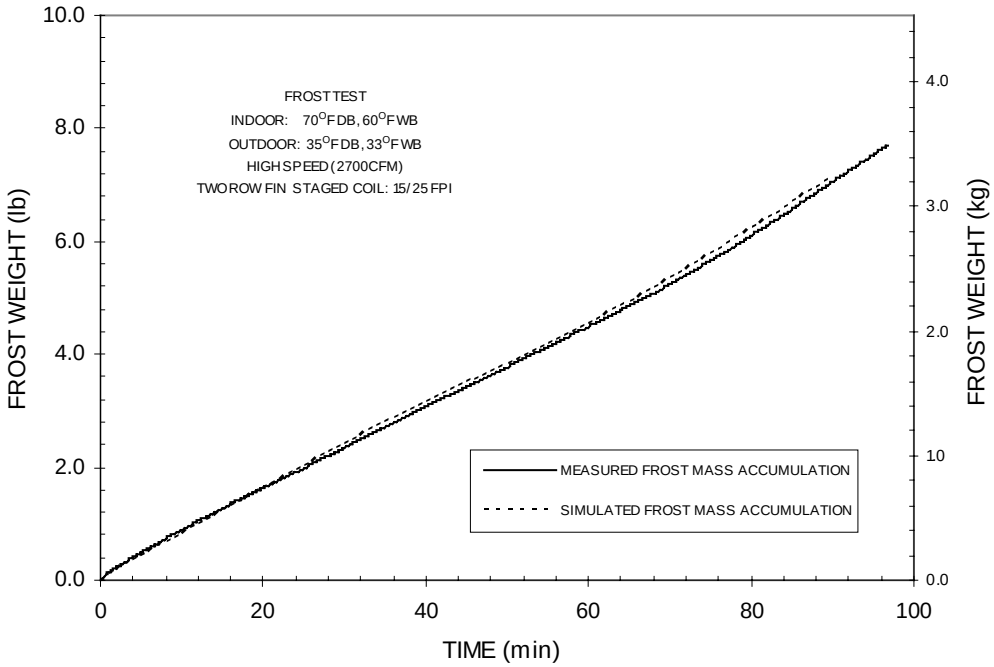

Figure 7.24 Simulated and experimental frost mass accumulation for the two-row fin staged coil (15/25 fpi) with high airflow (2800 cfm) during 35°F frost test

However, due to the higher heat and mass transfer coefficients and high humidity of airflow at the coil entrance, the frost grew very fast once freezing started.

In the frosting test of the 15/25 fpi coil, the dew point temperature of the inlet airflow was about 30.5^{o}F with a dry bulb temperature 34.7^{o}F. Thus, only when the surface temperature of the leading edge area was below the air dew point temperature of 30.5^{o}F, water could condense out of the moist air on to the fin surface. With the rapid decrease of evaporation temperature and airflow rate, the temperature gradient between the air blowing through the fin surface and the refrigerant, as well as the lower air velocity, drove more energy and moisture from the air to the fin surface. From the frost growing process, it is easy to infer that the fin surface temperature around the leading edge of the fin staged coil was relative higher compared to that of the baseline coil at the early portion of test, even if the evaporation temperatures for fin staged coils were a little bit lower than that of baseline coil.

This phenomenon may be attributed to the smaller heat transfer rate at the face area of fin staged coil. Due to the large fin spacing, a smaller heat transfer area was available for the first row of fin staged coil. Meanwhile, from the calculation we know that the average heat transfer coefficient for the first row also reduced with the increased fin pitch. Both of these cause a smaller heat transfer rate at the same airflow rate. Therefore, the fin surface temperature at the leading edge was higher and needed more time to cool to the airflow dew point temperature so that moist could condense out of the saturated moisture air.

Less fin density at the first row reduces the heat and mass transfer when air blows through the fin surfaces of first row, and relatively less frost accumulated at the front face of fin staged coils. This allows the airflow with higher temperature and humidity ratio to reach the rear part of heat exchanger, which promoted heat and mass transfer of the second row of the coil because the temperature and humidity difference remained large and the decrease of airflow volume rate was relatively slow. Therefore, more frost accumulated at the second row of the fin staged coil.

A decrease in the frost growth at the first row and a resulting increase at the second row presented in the simulation were consistent with the theoretical analysis. This demonstrated that fin staging can make the fin surfaces at the rear row of the coil work more efficiently and improve the performance of the heat exchanger under frosting conditions. Meanwhile, compared with a two fin staged coils, as the fin spacing of the second row decreased, the frost accumulation showed an increase because the calculated heat and mass transfer rates of the second row increased.

The simulation model did not track the growth trends of frost layers for staged coils at the leading edges very well. Especially for the test of 15/25 FPI coil, there existed a large deviation between the simulation and the experiment. Besides the local transfer coefficients, the spatial growth of frost layer also depended upon the fin surface temperature. The fin surface temperature was not uniform. In the fin staged coil tests, the distribution of fin surface temperature were the dominant factor for frost formation.

Airflow Pressure Drop across Frosting Coil

Frost formation on the heat exchanger can lead to an increase in pressure drop and decrease in airflow rate. This section compares the simulated and experimental results of air pressure drop as a factor of time.

Figure 7.25 shows the simulated and experimental pressure drop for the baseline coil (20/20 FPI). The original test data for pressure loss showed fluctuations. This was attributed primarily to the manual adjustment of coil outlet static pressure and the random nature of frost deposition. The curve of measured pressure drop present in Figure 7.25 is a multi-point moving average of the original data.

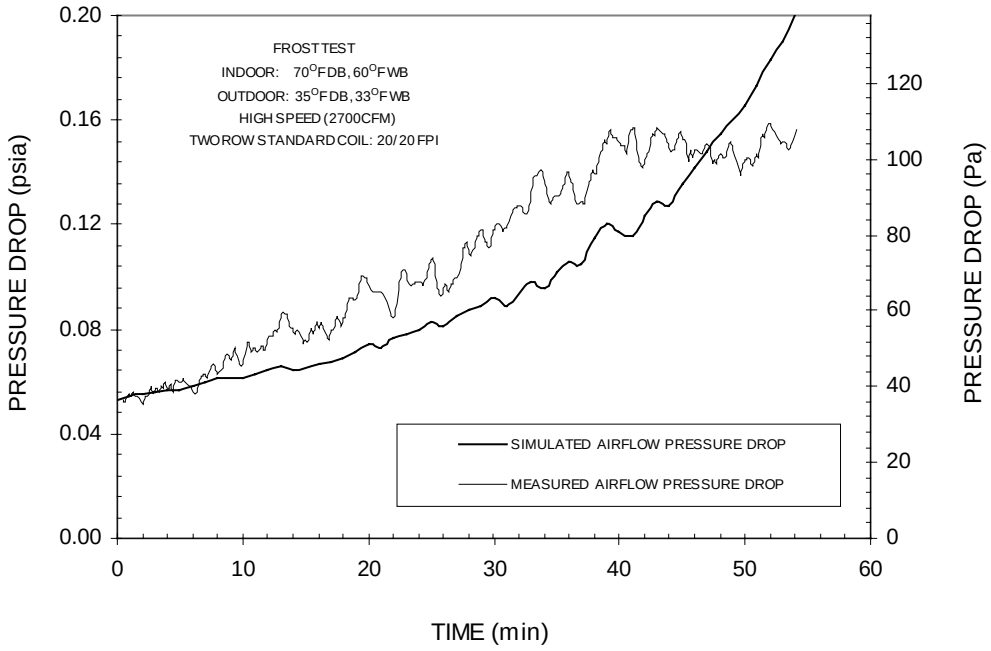

Figure 7.25 Simulated and measured air pressure drop for the two-row baseline coil (20/20 fpi) with high airflow (2800 cfm) during 35°F frost test

The experimental data indicated that the frost layer had a large effect on the airflow pressure drop. The pressure drop is seen to rise dramatically as the coil frosted up. The measured value at the end of test was almost 4 times of the initial value while coil was dry. The reduction of free flow area due to the blockage of frost accumulation was the main reason of the pressure drop increase.

From Figure 7.25, it should be noticed that the measured pressure drop didn't increase at the same rate throughout the test. During most of test, the pressure drop seemed to increase constantly. However, for the last part of the test, the slope was reduced and the curve was nearly flat. The same phenomenon also can be observed in other test results.

An axial propeller-type fan was used to move the airflow through the frosted coil during the tests. The fan curves relating the volumetric airflow rate and either pressure drop or fan power consumption were provided in Chapter III. A relatively flat curve of pressure curve verse flow was shown in Figure 3.36 for low air flows. Also there exists a dip on the curve to the left of peak pressure. This fan may have been chosen based on the normal dry or wet operating conditions. During the whole frost test, the airflow decreased from 2800 cfm to 900 cfm. Most of time, the fan work below the design point. As the airflow decreased, the pressure provided by the fan first increased, then reached a maximum value of approximately 1700 cfm, then the pressure remained relatively constant. Because the static pressure at the outlet of the coil was always kept near zero during the test, the air pressure drop through the frosted coil was approximately equal to the pressure head provided by the fan. Therefore, the air pressure loss followed the trend of the fan pressure curve and stopped increasing during the last part of test. This indicates that the performance of an evaporator under frosting conditions is affected by the characteristics of the fan. It is clear that to satisfy the frost working conditions, a fan with a steeper pressure curve should be chosen. Thus, with the frost gradually blocks the coil, an increasing pressure head provided by the fan can slow down the reduction of airflow. This would improve the overall heat transfer performance of frosted coil.

Another reason for the flatness of the measured pressure drop may be attributed to the penetration resistance of the frost. The frost is a porous and crystalline material, which is permeable and allows the air to blow through the coil even after the entrance face of coil is entirely blocked by frost. During the tests, before the frost blocked the airflow passages, most of air flowed through the channel between two adjacent frost layers and the pressure loss due to contraction and expansion was dominant. However, once the frost channel was completely blocked, the pressure loss due to contraction and expansion disappeared, and was replaced by the penetration resistance of the frost gradually increased as more frost formed to thicken the frost.

Comparing the curves in Figure 7.25, it can be seen that the model can give a consistent initial pressure drop with the measured data. As the frost layer grew, the difference between the simulated and measured pressure drops gradually increased. The model underestimated the pressure drop. However, the simulated pressure drop keeps increasing at last part of test. This caused the model to overpredict the pressure drop.

At the beginning of the test, the agreement between the simulated and measured pressure drop indicated that the Gray and Webb's friction correlation worked well at dry working conditions, which accounted for the friction drag and blockage of fin surfaces and tubes. The differences later may be explained by the calculation of pressure drop due to contraction and expansion. The air pressure drop is mainly dependent upon the spatial distribution of frost deposition and the growth history of the frost layer. As described before, the complicated variation of air pressure drop due to frost blockage was simplified by

using the contraction and expansion model to estimate the pressure loss while air flowing through the frost channel.

As more frost accumulates on the coil surface, especially when the frost growth causes a large fraction of blockage, the pressure drop due to contraction and expansion gradually becomes dominant. The total pressure drop is mainly dependent upon the calculated pressure drop due to contraction and expansion. In the contraction and expansion model, the pressure drop calculation is sensitive to the frost height and the square of the local airflow velocity.

As can be seen in Figures 7.26 and 7.27, a tendency of reduction is noted for all the section velocities except that at section one of first row. The variation of velocity corresponding to a given section is a combination of the growth of frost height and the decrease of airflow rate due to the blockage of frost. The continuous decrease of average section velocity indicates that the reduction of free flow area of frost channel was slower than the decrease of coil airflow rate. The trend of velocity at the top section is different from those of the others. Because of the fast growth of frost height at section one, even if the airflow decreases with the frost blockage, the ultimate result is that the local velocity keeps rising. Especially during the last part of the test, owing to the "windproof" assumption of frost blockage, the local velocity of section one became unreasonably high. Although the velocity could be adjusted by reductions the frost height at the top section, this would cause more deviation between the simulated and measured frost heights at the leading edge. This increasing velocity of section one is thought to be the direct reason for the calculated pressure drop rapidly increasing the end of test.

Because the calculation of tube and fin drag forces was based on the whole heat exchanger by Gray and Webb's correlation, even the pressure loss due to contraction and expansion in the frosted channel could be obtained for each section, the detail pressure drop profiles inside coil were impossible to obtain.

As a method to account for the frost blockage to the airflow, the contraction and expansion model is highly dependent upon the frost deposition on the fin surface, which should be applied based on either the model prediction or the experimental observation of frost layer distribution. From the simulation results of frost layer growth at the leading edges of fin staged coils, it is evident that the present model tends to overestimate the frost height early in the tests, but agrees better later. This causes that the contraction and expansion model calculates pressure drop for fin staged coil on the basis of incorrect frost layer distribution. Although the simulated pressure drop could match the experimental result through adjusting the correlated multipliers or coefficients, and there perhaps exists the similar mechanism of contraction and expansion inside the frosted fin staged coils, it is farfetched to apply the present contraction and expansion model to estimate the air pressure drop. Therefore, no comparison between simulated and measured pressure drop or airflow rate will be discussed for the fin staged coils.

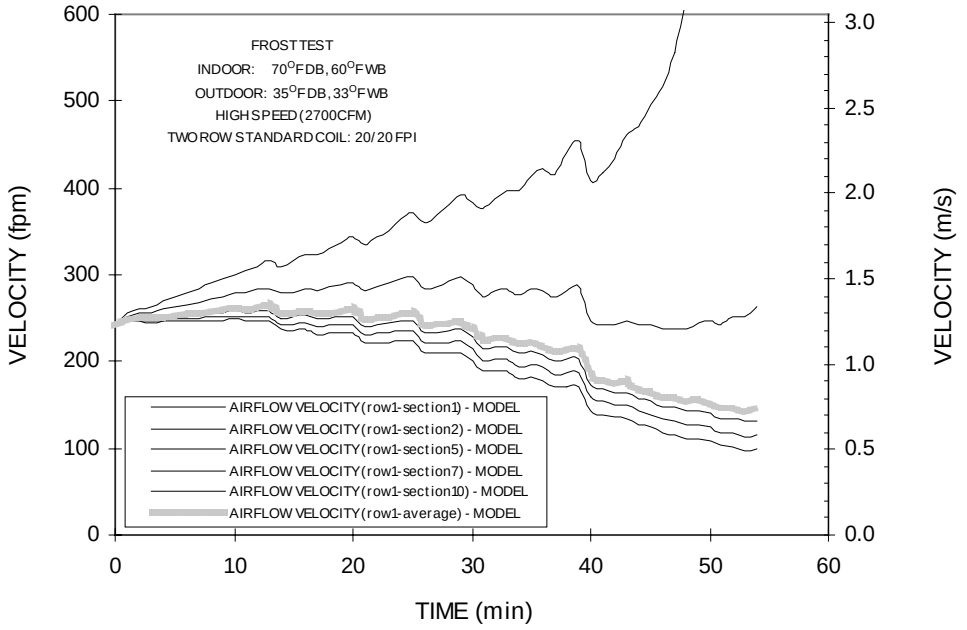

Figure 7.26 Variations of local air velocity at the first row sections for the two-row baseline coil (20/20 fpi) with high airflow (2800 cfm) during 35°F frost test

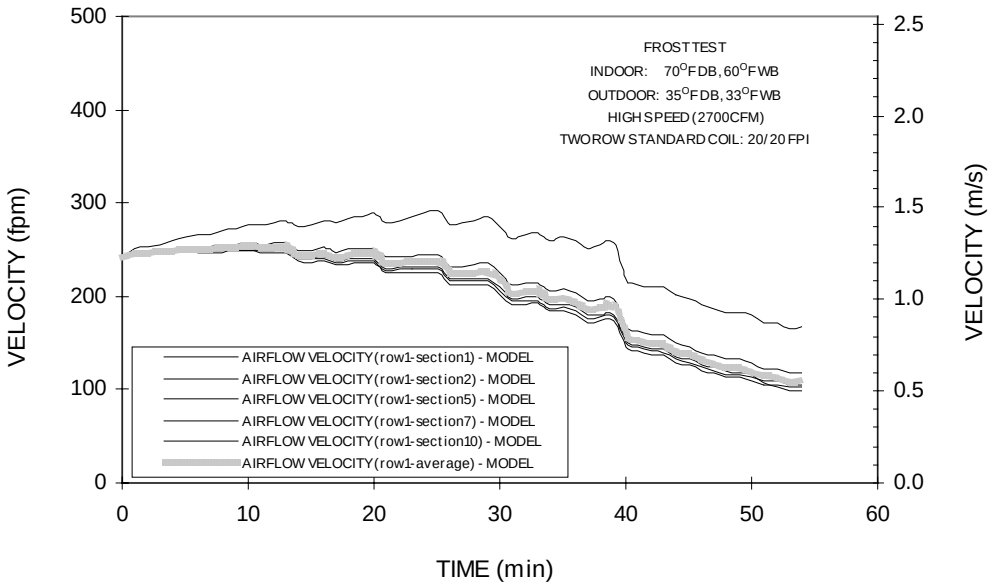

Figure 7.27 Variations of local air velocity at the second row sections for the two-row baseline coil (20/20 fpi) with high airflow (2800 cfm) during 35°F frost test

Airflow Rate Drop with Time

The drop in airflow due to the blockage of frost deposition is shown in Figure 7.28. In the high-speed test, the airflow decreased from initial 2800 cfm when coil was clean to approximately 900 cfm at the end of test when the heating capacity of indoor coil had a 20% drop. It is evident that frost accumulation not only increased the air pressure drop but also blocked the airflow.

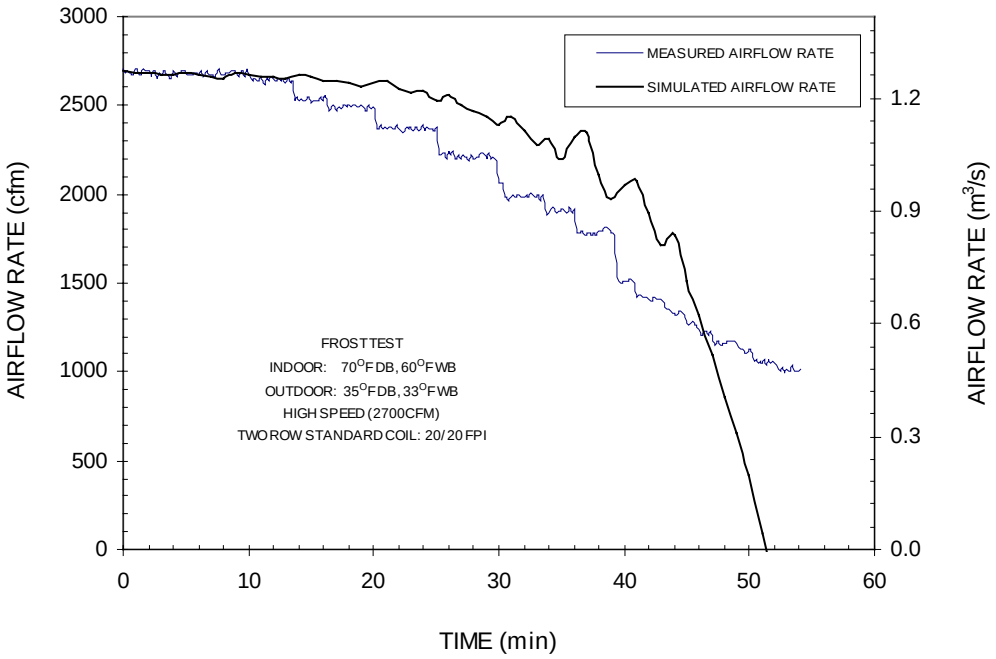

Figure 7.28 Simulated and measured airflow rate for the two-row baseline coil (20/20 fpi) with high airflow (2800 cfm) during 35°F frost test

To keep the static pressure at the coil exit close to zero, the speed of chamber booster fan was adjusted manually during the test. This caused the stair-type decrease in measured airflow rate. In addition, the airflow shows a relatively constant value over a fairly long initial period (almost fifteen minutes in this 35°F DB test). This may have been caused by the condensate on the coil requiring sufficient time to grow and then freeze. The effect of frost layer blockage was minor at the early part of the test. Work by Gong (1996) in his dissertation demonstrated that the condensate droplets need time to coalesce and freeze

Frost formation leads to the decrease of free flow area of the gap between the fins as well as an increase of roughness of heat exchanger surface. As a result of these effects, the volume flow rate through coil reduces rapidly, which is a major indicator of the impact of frost on the coil performance.

As can be seen, the airflow rate obtained by simulation agrees well with the test data at the first ten minutes. After that, the model begins to underestimate the reducing rate of airflow. However, during the last part of test, the calculated value drops rapidly and caused the simulation to be less than the test data. This difference can be understood by the comparison of simulated and experimental air pressure drop. The larger simulated pressure drop shown in Figure 7.25 created the rapid drop in estimated airflow.

In the numerical model, for a specified pressure drop during the frosting process, the air volume flow rate is determined based on the fan curve equation. The variations of volume flow rate and pressure drop due to the blockage of frost are coupled. Based on the coil system and fan curves, due to the air-side resistance of coil increasing with frost formation, both coil system curve and its intersection point with fan curve move up. Thus, the pressure drop increases and the airflow rate decreases. It is the continuous increase of air pressure drop that results in the rapid reduction of airflow rate at the end of test.

In the airflow model PRCFM, due to the two-way feature of Newton-Rapson iteration and the over high pressure prediction at the end of test, the fan curve equation had to be adjusted at the range of low air flow rate to avoid the occurrence of unreasonable solutions.

CHAPTER VIII

CONCLUSIONS AND RECOMMENDATIONS

The effects of fin staging on the frosting performance of heat pump evaporators and the whole heat pump system have been studied experimentally and theoretically. The conclusions from this study are presented and discussed in this chapter. The limitations and drawbacks of the research work as well as the recommendations for the future study are also discussed.

Conclusions

Frost degrades the performance of fin-and-tube outdoor coil as well as the whole heat pump system. The objective of the experimental part of this study was to quantify how staging fins could improve the frost defrost performance of the heat pump evaporation system. A series of frosting tests were conducted on the heat pump with different evaporators at several frosting conditions. Performances of the heat pump unit with baseline or staged fins were compared and analyzed.

In the second step of this work, a frosted evaporator model was developed as an analytical tool for the frosting performance of both the baseline and fin staged heat exchangers. The model provided reasonable heat and mass performance predictions for the fin-and-tube heat exchanger under frosting conditions. The model provided estimates of variables such as: frost growth, airflow, pressure drop, energy transfer and refrigerant outlet state. The model was verified by comparing the simulation results with the experimental data.

Experimental Test

The objective of the experimental study was to quantify the effect of fin staging on the frost/defrost performance of heat pump evaporators. To accomplish this objective, an off-the-shelf heat pump was tested with five (three two-row and two three-row) evaporators over a range of outdoor temperatures and humidities and a range of airflow rates typical of those found in residential sized heat pumps. These tests showed that for a given two-row heat pump operating at the standard ANSI/ASHRAE 35 ^{o}F (1.7 ^{o}C) frosting conditions, fin staging increased cycle time and COP. There was a small decrease in peak capacity at lower initial airflow rates. At a lower temperature of 28 ^{o}F (2.2 ^{o}C), cycle time continued to be enhanced with fin staging, and cyclic COP was within 5% of the base case when fin staging was used.

Outdoor conditions affected the degree to which heat pump performance was improved by fin staging. As the conditions were changed from 35 ^{o}F (1.7 ^{o}C) and 82% RH to 28 ^{o}F (-2.2 ^{o}C) and 90% RH, the improvement in cycle time and COP was reduced by half. At 35 ^{o}F (1.7 ^{o}C), for both relative humidities of 82% and 95%, fin staging effects were similar. The 15/25 fpi fin staged coil, for example, had a 4% increase in the cyclic COP over the 20/20 fpi baseline coil at 82% RH, but at 95% RH, the cyclic COP of the staged coil was 9% higher than the base coil. Outdoor conditions affected the thickness and mass of frost that formed on the evaporator fins.

In addition to outdoor conditions, the amount of airflow through the evaporator was found to have a substantial impact on the improvement from fin staging. In general, as airflow dropped, cycle time and COP dropped due to a decrease in the evaporating temperature, which promoted faster frost growth. Fin staging provided a higher and more stable evaporating temperature, which led to delayed frost growth. As a consequence, cycle time at all flow rates was increased, and, in most cases, the cyclic COP was increased. These differences between the particular staged coil and the baseline coil varied with airflow. At 35 ^{o}F (1.7 ^{o}C), decreased airflow through the 15/20 fpi coil tended to reduce the benefit of fin staging on frost/defrost cycle time (from 30 to 70%), while decreased airflow through the 15/25 fpi coil slightly increased this benefit. At 28 ^{o}F (-2.2 ^{o}C), reduced airflow from high to medium had a positive affect on the benefit of fin staging on cycle time. In general, though, the COP improvement with the fin staged coils increased as the initial airflow through the evaporator decreased.

Fin geometry was an important variable in determining the potential advantages of fin staging on two-row heat pump performance. The 15/20 fpi coil had wider fin spacing on the front row of the evaporator and generally improved cycle time above the 20/20 fpi baseline coil. Cyclic COP for this coil generally increased from 5 to 10%, except at 28 ^{o}F (-2.2 ^{o}C) and high airflow when the cyclic COP dropped 4.5%. The 15/25 fpi coil increased cycle time from 50 to 100% above the base case and cyclic COP rose above that of the baseline coil by 4 to 10%, depending on outdoor conditions and airflow. This was not true, however, at the 28 ^{o}F (-2.2 ^{o}C) dry bulb temperature and high airflow test conditions. The cyclic COP of the 15/25 fpi coil was 9% below that of the base case. Overall, this coil accomplished what it was designed to do by delaying frost growth and prolonging the time needed before defrost.

Testing of the three-row coils indicated that circuiting might need to be optimized. This coil was not a standard design, and the benefits from fin staging on heat pump performance were marginal. These improvements showed greater improvement at lower temperatures, which showed the dependence of performance on outdoor conditions. An established circuiting design should be tested to verify a performance improvement due to fin staging.

These tests showed dependence between airflow, outdoor conditions, fin geometry, refrigerant circuiting, and heat pump performance. Widening of the space between the fins of the front row increased cycle time and cyclic COP, but narrowing of the back row seemed to reduce the benefit in COP compared

to the base case while increasing the benefit in frost/defrost time. Reduced airflow increased the benefit in COP, but decreased the benefit in cycle time. Further research should investigate other fin densities and configurations and other airflow rates to help localize the optimum staging for the heat pump.

Numerical Simulation

An analytical model to simulate the performance of fin staging on heat pump coils under frosting conditions was developed based on the fundamental heat and mass transfer principles. A comprehensive literature search was done and the best correlations available were selected for the numerical model. With the specified entering refrigerant state, flow rate and initial airflow, the frosted evaporator model was able to reasonably predict the performance of fin-and-tube heat exchangers under frosting conditions.

The frosted evaporator model appeared to provide satisfactory simulation of the heat exchanger during the frost buildup process. Comparisons with the test data indicated that the model could capture the trends of the coil capacity, pressure drop and airflow. The predicted frost growth at the leading edges of the front row appeared not to agree well with the measurements of the fin staged coils. The model also provided a variety of other simulation results including frost mass accumulation, air velocity inside coil, air and refrigerant outlet state, and so on. Overall, the numerical results were in reasonable agreement with the test data under various frosting operation conditions.

The transient performance of the frosted evaporator was analyzed with the quasi-steady state approach. During each time step, the heat and mass transfer processes of the heat exchanger were regarded as the steady state. The calculation results at one time step were stored and used for analysis at the next time step.

Five major subprograms were included in the frosted evaporator model: heat transfer, frost formation, airflow drop, refrigerant property and air psychrometric property calculation. In the heat transfer calculation subprogram, the application of the tube-by-tube calculation strategy had a profound effect on the success of the simulation model. After the frosted evaporator model had been developed, the air-side heat transfer coefficient was modified furthermore to simulate the fin staged coils by adjusting the j-factors of the coil rows with different fin spacing.

The section-by-section evaluation scheme was combined with the tube-by-tube approach to model the mass transfer process in the frost formation subprogram. The two-dimensional fin surface was divided into a number of parallel non-overlapping sections. Each of the sections was the calculation unit for the mass transfer. The local heat and mass transfer coefficients of individual section were determined following the work of Saboya and Sparrow (1974, 1976a and 1976b). The heat and mass transfer, as well as air and frost properties over the fin surface, were assumed consistent for each fin section during each time step. By incorporating the section-by-section frost growth simulation scheme in the frost formation subprogram, the model could provide more detailed and accurate numerical analysis of the frost growth

process on the fin surface. Thus, the frosted evaporator model was very useful as an analysis and prediction tool to complement the experimental study.

The frost growth subprogram was developed based on the molecular diffusion of water vapor, energy and mass balances, as well as equations of state. The subprogram treated the frost layer as a porous media with transient and one-dimensional heat and mass transfer. This allowed the subprogram to adjust the frost density and thermal conductivity to account for the changes in the frost layer structure as a result of the occurrence of vapor diffusion. The variation of frost height in the airflow direction and frost properties, such as surface temperature, density and thermal conductivity, could be provided by the subprogram. The frost growth predicted by the model had a monotonically decreasing trend along the fin surface. For the baseline coil, the simulated frost heights at the leading edges compared well with the measured values. However, the model overestimated the frost growth at the leading edges for the fin staged coils.

The present airflow subprogram could account for the contraction and expansion effects on the air pressure drop through the frosting coil. Verification of results of the subprogram was compared against experimental measurements. The trends for the calculated pressure drops across the frosted coils were similar to those found in the test. The differences between the test data and model prediction were in the reasonable range. This allowed the subprogram to provide better prediction of the airflow drop with frost growth.

The refrigerant property subprogram was expanded to include any non-azerotropic refrigerant mixture as the working media. Performance of a heat exchanger filled with different refrigerants can be analyzed by the model with the aid of this subprogram.

The numerical results presented in this work clearly showed the capability of the model to analyze the frosting performance of the heat exchanger. The validated simulation model provided a better means to understand and analyze the physical nature of the frost growth. The model also can be use to predict the effects of the variations of hat exchanger geometry, airflow rate, air temperature and humidity, etc on the overall performance of the frosted heat exchanger.

Additionally, this dissertation contains adequate information about the algorithm, organization and procedure of the numerical model so that further improvement could be made with a minimum of difficulty.

Recommendations

Some limitations and drawbacks of the work performed in the present study are provided. Also, a few suggestions are recommended for the further study.

Experimental Test

Two-row fin staged coils should be considered as an alternative to conventionally designed two-row coils. The test results of this study indicate a measurable benefit from fin staging in the two row designs. The "sandwich" design used in two-row heat pump coils allows for the first and second rows to be manufactured separately and joined together during the final assembly of the coil. Thus, it would be possible to readily manufacture a 15/25, 15/20, etc. coil for use in a heat pump. The exact combination of fins on the two rows that would provide optimal performance at a minimum price in heating and cooling modes would have to be determined via testing and cost analysis.

Increasing airflow should be considered for heat pumps in heating operations. The effect of airflow on performance was included in this study because of the desire to test fin staging over a range of conditions. The effect on frosting performance between the low and the high airflow tests even on the baseline coil indicated that higher velocities (more airflow) through the evaporator should be considered. The frost grew slower and the cycle times were much longer as the airflow was increased. A manufacturer would need to consider at what point the increased power requirements and costs in the outdoor fan outweighed the benefit in higher COPs with the higher airflow.

Other fin staging techniques should be investigated. Ogawa et al (1993) looked at other fin staging geometries, such as side staging. Some of the techniques would require special manufacturing of the fins and heat exchangers, but may also show some benefits to the cycle time and COP.

Fin staging provided a direct benefit for the outdoor heat exchanger by delaying frost growth on the leading edge and prolonging cycle time. This also provided a higher peak capacity in most cases and a resulting increase in the measured COP during the frosting cycle. However, longer frosting times resulted in more frost accumulation on the evaporator fins, which took more time and larger energy expenditure to melt. This trade-off resulted in marginal improvements in cyclic COP and overall system performance. Perhaps more frequent defrosts would solve this problem. Other defrost initiation schemes could be used, such as calling for a defrost after the COP dropped below the peak value. The testing showed that the COP typically peaked, then began to degrade as the frosting cycle progressed. It may be advantageous to call for a defrost earlier in the cycle rather than waiting for a 20% degradation in heating capacity.

In this experimental study, only two video cameras were set to monitor the frost growth at two leading edge positions of the front row of the test coils. The uneven frost growth on different locations of the leading edges could be observed during the tests. The growing tendencies of two individual points described had uncertainty. The averaged frost height might not represent the overall frost growth on the

coil leading edges. More video cameras should be installed in front of the test coil. That would provide more measurement points and provide better average frost height measurement on the leading edges.

One difficulty with the IMAQ system was that it only showed the frost growth at the leading edges of the front row of the evaporator. The configuration of fin-and-tube heat exchanger limited the view beyond the leading edge of the front row. So the IMAQ system was not able to monitor the frost growth along the fin surface except on the leading edge of the front row. For multiple row evaporators, there is a significant difference in the distribution of frost accumulation along the fin length. For the fin staged coil, it is expected that frost would more form on the rear row because of the wider fin spacing of the front row compared to the rear rows. However, the IMAQ system could not provide any information on the frost growth in the back row. Additionally, due to the use of the closeup lens, the depth of the image field of the lens was relatively small. The capturing equipment providing greater depth of the image field is expected in the future tests.

During some frost tests, the distribution of frost growth varied vertically on the test coil. While some fins were almost blocked, others were still open. One reason might be the distributor. The test coils had either three or four parallel circuits. The R410A flow rates for each circuit may not have been same. The circuit with higher refrigerant flow had faster frost growth. In addition, there may have been different airflow through each circuit. The heat pump unit used a propeller fan to draw air through the “horseshoe” shaped outdoor test coil. The airflow distribution through the coil front face was typically not uniform. The top circuit probably had more airflow than the bottom circuit. As the top circuit became blocked, more air flowed through the bottom circuit which had less frost. Eventually, all the coil circuits became blocked with frost.

Numerical Simulation

In the heat transfer calculation, each coil tube was treated as the calculation unit using the tube-by-tube method. Consistent heat transfer conditions were assumed based on each tube for both the air and refrigerant sides. The tube-by-tube method usually provides a detailed and accurate calculation. However, the length of a single tube is long and the heat transfer on both air and refrigerant sides can have significant variations along the tube length. This problem might need to be considered for the heat pump outdoor coil under some frost operating conditions. To improve the calculation procedure, a tube could be further divided into several sections. In each section, the variations would be small so that consistent air and refrigerant properties, as well as other heat/mass transfer variables, could be regarded as reasonable assumptions. Thus, the tube-by-tube method could be extended to a section-by-section method.

Although the frosted evaporator model could account for the uneven air distribution along the face surface of the coil, uniform velocity of entering air stream was simply assumed because the air distribution was not measured. The propeller fan of the outdoor coil was installed at the top of the coil. For the clean coil, there should be more air flowing through the top circuit of coil than the bottom circuit. In addition, the observed frost growth among the coil circuits was not same. Some circuits had faster frost growth than the other circuit. This was another reason to cause uneven air distribution along the coil face. With the consideration of uneven air distribution, the model could be more likely to provided better performance predictions.

The model is able to simulate the frosting performance of a heat exchanger with flat or various enhanced fin surfaces, and tubes having smooth or enhanced inner surfaces. Performance estimations for the flat fin and smooth tube coils are expected to be most reliable because these basic, plain surfaces were well studied and their respective heat transfer correlations have been used in the model as the fundamental calculation equations. Performance estimation for the evaporator air side with enhanced fin surfaces may not be as accurate as the flat fins because each enhanced surface is different with its own heat transfer characteristics. General correlations may not represent their performance very well. In this study, the seven-element sine-wave lanced fin was used in the test coils, for which no general correlations were available and simple enhancement multiplies were used to account for the performance improvement with respect to the flat fins.

The tests were conducted based on the actual heat pump outdoor coils with a kind of enhanced fin: seven-element sine-wave lanced fin. The composition of many strips and slits on the fin surface might affect the accuracy of mass transfer calculation by the section-by-section method, which fits flat fin surface very well. Complicated variations in the geometry with lanced fins also affect the prediction of airflow by calculating the air contraction and expansion pressure drop through passages between adjacent seven-element sine-wave lanced fins.

The growth of a frost layer is normally divided into two stages: initially an ice-column frost structure followed by a fully developed porous frost layer or full growth stage. In the research of Tao and Mao (19994), an ice-column numerical model on the cold plate was used to predict the frost behavior during the early growth stage with convective heat and mass transfer over the ice columns, rather than diffusion within the frost. After the ice-column grew to a certain height, or after a transition time, a homogeneous porous medium model was applied to the frost layer full growth stage. The ice-column growth process during the initial period of the frosting test was not considered in the frosted evaporator model. Instead, a frost layer with a small height was assumed to have already existed at the beginning of frost growth calculation. The model directly started at the frost full growth stage. In the experimental study, the method of hot gas defrost was applied. For faster defrosting, no air was blown through the

outdoor coil. During defrost, the frost was melted and transported from coil surface by means of gravity. After switching to heating mode, the water droplets remaining on the outdoor coil surface immediately froze again. This was different from the initial frost growth process on the clear and dry fin surface.

With frost layer grows furthermore, the frost surface temperature may come to the ice point of 32 ^{o}F (0 ^{o}C) due to an increase in frost thermal resistance. Then, the frost surface begins to melt and frost thermal resistance decreases abruptly with melting. This causes the melted water on the upper frost layer to refreeze again. The process occurs cyclically. Because the relatively low air and evaporating temperature, the frost surface temperature kept below 32 ^{o}F (0 ^{o}C) during all frost tests. The melting-and-refreezing phenomenon was not observed. The frost was always in crystalline structure. However, during the test if the temperature of frost layer surface approached or above ice point temperature, the model just could stop calling the subprogram of frost formation, but no ability to calculate the melting-and-refreezing process in case with the rise of air or evaporating temperature.

In the simulation, at the leading edges of the fin staged coils, the frost started to form at the beginning of the frosting test and kept growing with time. This trend was not consistent with what was observed in then tests. The frost growth was dependent on the heat/mass transfer coefficients, fin surface temperature, frost layer properties, airflow rate and conditions. For the fin staged coils, the frosted evaporator model predicted a different trend of frost growth at the leading edges when compared to the measurements. The reason for the above difference was the lack of the detailed and accurate knowledge on the variations and distributions of the air-side heat transfer coefficient and fin surface temperature for the fin staged coils during the frosting process. The present model estimated the two parameters based on the empirical correlations for the dry unfrosted fin surfaces. If possible, the fin staged heat exchanger should be tested to obtain the variation and distribution information of the air-side heat transfer coefficient and fin surface temperature under both dry and frost working conditions. Then, these experimental results could be used in the model to produce more reasonable simulation results.

The frost deposited on the coil surface has a porous, crystalline structure. As a porous material, it allows the air to blow through in some situations. In the simulation model, the penetrable characteristic of frost layer was not considered. In contrast, it's assumed that the frost layer would not let air pass through the frost. However, in the tests, when the coil was observed to be totally blocked at the end of test, there was still approximately 900 cfm airflow across the frosted coil. This "windproof" assumption of frost blockage actually conflicted with the porous characteristics of frost. It became extremely obvious when the coil was wholly blocked. Also, this gave a reason why the predictions of frost growth at the first section were slower than the experimental observations in most cases. The drop of airflow was primarily a function of the reduction in free flow area of the air passage between adjacent fin surfaces. Without consider the amount of air blew through the frost blockage, it was reasonable for the air stream to need more free flow area in the air passages.

For the transient behavior study of the heat exchanger, one of the important parameters would be the time required for the whole coil to reach steady state when an inlet parameter changed. In a heat exchanger with transient heat transfer process, the response of one outlet fluid parameter to a change of the corresponding inlet fluid parameter is not instantaneous. The lag is determined by the thermal capacitances of the heat exchanger and fluids, as well as the resistances of heat and mass transfer. For a frosted coil, with more frost accumulating on the heat exchanger surface, the response time also increases with the rise of coil total capacitance and heat conduction resistance between air and fin surface. The continuous variations of the frost properties makes this phenomenon more complex.

In the frosted evaporator model, a quasi-steady state method was used to simulate the transient frosting process by introducing step changes of coil inlet parameters. This method is built on steady state heat and mass transfer calculations. At each time step, the coil was assumed to be in equilibrium. No dynamic heat or mass transfer was considered. This implied an assumption that the response time of the frosted coil to the variations of operation conditions was much less than the step time interval (one minute) chosen in the quasi-steady state model. This avoids having to model the process with the differential equations, effects of a series of variables as well as complicated initial and boundary conditions.

If this idealization is violated, the transient heat/mass transfer of the frosted coil has to be taken into account. The problem then becomes more complicated due to the transient heat and mass transfer analysis. The value of the response time determines whether the quasi-steady state approach can be used. During the frost tests, except the air inlet temperature and humidity kept relatively constant in the psychrometric rooms, all other inlet parameters and some coil properties were time-dependent. Because it was not only one parameter varied while the others kept constant, this made it very difficult to quantitatively analyze the transient response time of the frosted heat exchanger.

In the simulation process, the thermal resistance and the thermal storage of the frost layer were considered as the factors to affect the frost accumulation on the heat/mass transfer calculations at each time step. Both of them increased with frost growth on the coil surface. However, because of the characteristics of steady state heat/mass transfer calculations of quasi-steady state approach, it inherently could not provide the transient analysis of coil heat transfer due to the effects of frost capacitance. Meanwhile, the heat conduction through the frost layer was transient in nature and was dependent upon the frost thermal conductivity, specific heat, density and height. Similarly, the influence of transient heat conduction between air and refrigerant was neglected as well.

From the comparisons of Figures 5.1 and 5.4, it would appear that the present quasi-steady state technique provides satisfactory modeling of the transient behavior of frost on a coil. However, more numerical analysis and experiment investigation still needs to be completed to verify the reasonability of this approach.

The evaporator coils with different staged fin geometries were tested based on an actual heat pump unit. The completed simulation work focused on the fin staged evaporator. The entire performance of the heat pump system, such as the unit heating capacity, the coefficient of performance (COP), and the refrigerant flow rate, were monitored during the frost tests. To predict the system performance, the frosted evaporator model could be incorporated into a heat pump system model, in which the frosted evaporator model serves as a component module.

REFERENCES

AlliedSignal Inc., 1995. Generation AZ-20 Product Brochure, Cary, NC

ARI, 1989, *ARI Standard 210/240-1989*, Unitary Air Conditioning and Air-Source Heat Pump Equipment, Arlington, VA: Air-Conditioning & Refrigeration Institute

ASHRAE, 1983, *ASHRAE Standard 116-1983R*, Methods of Testing for Seasonal Efficiency of Unitary Air Conditioners and Heat Pumps, Atlanta, GA: American Society of Heating, Refrigeration and Air-Conditioning Engineers, Inc.

ASHRAE, 1989, *Laboratory Methods of Testing Fans for Aerodynamic Performance Rating*, Atlanta, GA: American Society of Heating, Refrigeration and Air-Conditioning Engineers, Inc.

Baxter, V. D., Moyers, J. G., 1984. Air-Source Heat Pump: Field Measurement of Cycling, Frosting and Defrosting Losses, *ORNL/CON-150,* Oak Ridge National Laboratory, Oak Ridge, TN

Beatty, K. O., 1951. Heat Transfer from Humid Air to Metal under Frosting Conditions, *ASRE Journal*, 59:1203-1207

Bechkey, T. J., 1986. Modeling and Verification of a Vapor Compression Heat Pump, *Proc. IIR Commissions*, Purdue University, 175-183

Bittle, B. B., Goldschmidt, V. W., 1983. Effect of Cycling and Frost Formation on Heat Pump Performance, *ASHRAE Transactions*, 89(2): 743-754

Bonne, U., Patani, A., Jacobsen, R. D., Mueller, A. A., 1980. Electric Driven Heat Pump Systems: Simulations and Controls II, *ASHRAE Transactions*, 86(1): 687-705

Bryant, J. A., 1995. Effects of Hydrophobic Surface Treatments on Dropwise Condensation and Freezing of Water, Ph.D. Dissertation, Texas A&M University, College Station

Chang, W. R., Wang, C. C., Tsi, W. C. and Shyu, R. J., 1995. Air Side Performance of Louver Fin Heat Exchanger, *Proceedings of Fourth ASME/JSME Thermal Engineering Joint Conference*, 4:367-372

Chen, H., Thomas, L., Besant, R. W., 1999. Measurement of Frost Characteristics on Heat Exchanger Fins. Part II: Data and Analysis, *ASHRAE Transactions*, 105(2): 294-302

Chi, J., 1979. A Computer Model HTPUMP for Simulation of Heat Pump Steady-State Performance, National Bureau of Standards, Internal Report, Washington, DC.

Chitti, M. S., Anand, N. K., 1996. Condensation Heat Transfer Inside Smooth Horizontal Tubes for R-22 and R-32/125 Mixtures, *International Journal of HVAC&R Research*, 2(1): 79-101

Chung, P. M., Algren, A. B., 1958. Frost Formation and Heat Transfer on a Cylinder Surface in Humid Air Cross Flow, Heating, Piping and Air Conditioning, 30:21-31

Crawford, R. R., Shirey, D. B., 1987. Dynamic Modeling of a Residential Heat Pump from Actual System Performance Data, *ASHRAE Transactions*, 93(2): 1179-1190

Didion, D. A., Kelly, G. E., 1979. New Testing and Rating Procedures for Seasonal Performance of Heat Pumps, *ASHRAE Journal*, 21(9): 40-44

Domanski, P. A., 1989. EVSIM-An Evaporator Simulation Model Accounting for Refrigerant and One Dimension Air Distribution, *NISTIR 89-4133,* National Institute of Standards and Technology, Gaithersburg, MD

Downing, R. L., 1974. Refrigerant Equations, *ASHRAE Transactions*, 80(2): 158-169

Ebisu, T., Torikoshi, K., 1998. Heat Transfer Characteristics and Correlation for R410A Flowing Inside a Horizontal Smooth Tube, *ASHRAE Transactions*, 104(2): 556-561

Ellison, R. D., Creswick, F. A., 1978. A Computer Simulation of Steady State Performance of Air-to-Air Heat Pumps, *ORNL/CON-16*, Oak Ridge National Laboratory, Oak Ridge, TN

Emery, A. F., Siegel, B. L., 1990. Experimental Measurement of the Effects of Frost Formation on Heat Exchanger Performance, *Transactions of ASME*, 139:1-7

Fischer, S. K., Rice, C. K., 1983. The Oak Ridge Heat Pump Models: A Steady State Computer Design Model for Air-to-Air Heat Pumps, *ORNL/CON-801R1*, Oak Ridge National Laboratory, Oak Ridge, TN

Flower, J. E., 1978. Analytical Modeling of Heat Pump Units as a Design Aid and for Performance Prediction, *Lawrence Livermore Laboratory Report*, *UCRL-52618*, Livermore, CA

Gungor, K. E., Winterton, R. H. S., 1986. A General Correlation for Flow Boiling in Tubes and Annuli, *International Journal of Heat and Mass Transfer*, 29(3): 351-358

Hayashi, Y., Aoki, A., Adachi, S., Hori, K., 1977. Study of Frost Properties Correlation with Frost Formation Types, *Journal of Heat Transfer*, 99: 239-245

Kondepudi, S. N., 1988. The Effects of Frost Growth on Finned Tube Heat Exchangers under Laminar Flow, Ph.D. Dissertation, Texas A&M University, College Station

Kondepudi, S. N., O'Neal, D. L., 1990. The Effects of Different Fin Configurations on the Performance of Finned-Tube Heat Exchangers under Frosting Conditions, *ASHRAE Transactions*, 96(2): 439-444

Kondepudi, S. N., O'Neal, D. L., 1993. Performance of Finned-Tube Heat Exchangers Under Frosting Conditions: I. Simulation Model, *International Journal of Refrigeration*, 16(3): 442-460

Kondepudi, S. N., O'Neal, D. L., 1993. Performance of Finned-Tube Heat Exchangers under Frosting Conditions: II. Comparison of Experimental Data with Model, *International Journal of Refrigeration*, 16(3): 461-472

Martin, J. J., Hou, Y. C., 1955. Development of an Equation of State for Gases, *AIChE Journal*, 1:142

McLinden, M. O., Klein, S. A., Lemmon, E. W., Peskin, A. P., 1998. NIST Thermodynamic and Transport Properties of Refrigerants and Refrigerant Mixtures-REFPROP, Version 6.01, Users' Guide, Physical and Chemical Properties Division, NIST, Boulder, CO

McQuiston, F. C., 1975. Fin Efficiency with Combined Heat and Mass Transfer, *ASHRAE Transactions*, 81(1): 350-355

McQuiston, F. C., 1978. Heat, Mass and Momentum Transfer Data for Five Plate-Fin-Tube Heat Transfer Surfaces, *ASHRAE Transactions*, 84(1): 266-293

Miller, W. A., 1984. Frosting Experiments for a Heat Pump Having a One-Row Spine-Fin Outdoor Coil, *ASHRAE Transactions*, 90(1): 1009-1025

Ogawa, K., Tanaka, N., Takeshita, M., 1993. Performance Improvement of Plate Fin-and-Tube Heat Exchangers under Frosting Conditions, *ASHRAE Transactions*: 99(1): 762-771

O'Neal, D. L., 1982. The Effect of Frost Formation on the Performance of a Parallel Plate Heat Exchanger, Ph.D. Dissertation, Purdue University, West Lafayette, IN

O'Neal D. L., Tree D. R., 1985. A Review of Frost Formation in Simple Geometries, *ASHRAE Transactions*, 91(2): 267-281

O'Neal, D. L., Peterson, K., Anand, N. K., Schliesing, S., 1989. Refrigeration System Dynamics during the Reverse Cycle Defrost, *ASHRAE Transactions*, 95(2): 123-144

O'Neal, D. L., Gu, Yian, Davis, Michael, 1995. A Study of Heat Exchanger Performance under Frosting Conditions, *ESL-TR-95/01-LG*, Energy Systems Lab, Texas A&M University, College Station, TX

O'Neal, D. L., Gong, Y., 1996. A Study of Heat Exchanger Performance under Frosting Conditions, *ESL-TR-96/01-LG,* Energy Systems Lab, Texas A&M University, College Station, TX

O'Neal, D. L., 1997. Evaluation of Fin Staging Methods for Minimizing Coil Frost Accumulation, ASHRAE Project 1002-TRP Proposal

Oskarsson, S. P., Kraknow, K. I., Lin, S., 1990. Evaporator Models for Operation with Dry, Wet, and Frosted Finned Surfaces, *ASHRAE Transactions*, 96(1):373-379

Payne, W V., O'Neal, D. L., 1992. Examination of Alternate Defrost Strategies for an Air-Source Heat Pump Multi-Stage Defrost, *Recent Research in Heat Pump Design, Analysis and Application*, AES, Vol. 28, ASME Winter Annual Meeting, Anaheim, CA

Payne, W V., O'Neal, D. L., 1993. The Effects of Outdoor Fan Airflow on the Frost/Defrost Performance of an Air-Source Heat Pump, *Heat Pump and Refrigeration Systems Design, Analysis and Applications*, AES, Vol.29, ASME Winter Annual Meeting, New Orleans, LA, 189-196

Rice, C. K., Jackson, W. L., 1994. PUREZ-The Mark V ORNL Heat Pump Design Model for Chlorine-Free, Pure and Near-Azeotropic Refrigerant Alternatives, Preliminary Documentation Package, Oak Ridge National Laboratory, Oak Rideg, TN

Rice, C. K., 1997. DOE/ORNL Heat Pump Design Model, Overview and Application to R-22 Alternatives, *3rd International Conference on Heat Pumps in Cold Climates*, Walfuidle, Nova Scotia, Canada, 123-134

Rice, C. K., 1998, Personal Communication, Oak Ridge National Laboratory, Oak Ridge, TN.

Rich, D. R., 1973. The Effect of Fin Spacing on the Heat Transfer and Friction Performance of Multi-Row, Smooth Plate Fin and Tube Heat Exchangers, *ASHRAE Transactions*, 79(2): 137-145

Rich, D. R., 1975. The Effect of The Number of Tube Rows on Heat Transfer Performance of Smooth Plate Fin and Tube Heat Exchangers, *ASHRAE Transactions*, 81(1): 307-319

Saboya, F.E.M., Sparrow, E.M., 1974. Local and Average Transfer Coefficients for One-Row Plate Fin and Tube Heat Exchanger Configurations, *J. Heat Transfer*, 96: 256-272

Saboya, F.E.M., Sparrow, E.M., 1976. Transfer Characteristics of Two-Row Plate Fin and Tube Heat Exchanger Configurations, *International Journal of Heat and Mass Transfer*, 19: 41-49

Sami, S. M., Comeau, M. A., 1992. Development of Simulation of Heat Pump with Non-Azeotropic Refrigerant Mixtures, *Int. J. of Energy Research*, 16: 431-444

Senshu, T., Yasuda H., Oguni K., Ishibane K., 1990. Heat Pump Performance under Frosting Conditions: Part I – Heat and Mass Transfer on Cross-finned Tube Heat Exchangers under Frosting Conditions, *ASHRAE Transactions*, 96(1): 324-329

Senshu, T., Yasuda, H., Kurodu, S., Atsumi, A., Oguni, K., 1990. Heat Pump Performance under Frosting Conditions: Part II – Simulation of Heat Pump Cycle Characteristics under Frosting Conditions, *ASHRAE Transactions*, 96: 330-336

Stoecher, W. F., 1957. How Frost Formation on Coils Affects Refrigeration Systems, *Refrigeration Engineering*, 12: 42-46

Tandon, T. N., H. K. Varma, C. P. Gupta, 1986. Generalized Correlation for Condensing of Binary Mixtures Inside a Horizontal Tube, *International Journal of Refrigeration*, 9: 156-166

Tao, Y. X., Besant, R. W., Mao, Y., 1986. Characteristics of Frost Growth on A Flat Plate during The Early Period, *ASHRAE Transactions*, 99(1): 739-745

Tuve, G. L., 1936. Performance of Fin-Tube Units for Air Heating, Cooling, and Dehumidifying, *ASHRAE Transactions*, 42(1029): 99-105

Wang, C. C., Fu, W. L., Chang, C. T., 1995. Heat Transfer and Friction Characteristics of Typical Wavy Fin-and-Tube Heat Exchangers, *J. Expl Thermal and Fluid Sci.*, 14(2): 174-186

Wang, C. C., Goang, J., Lin, S. P., Lu, D. C., 1998. An Experimental Study of Convective Boiling of Refrigerants R22 and R410A, *ASHRAE Transactions*, 104(2): 1144-1150

Webb, R. L., Eckert, E. R. G., Goldstein, R. J., 1971. Heat Transfer and Friction in Tubes with Repeated-Ribs, *International Journal of Heat and Mass Transfer* 14: 601

Welsby, P., Devottoa, S., Diggory, P. T., 1988. Steady and Dynamic State Simulation of Heat Pumps, *Applied Energy*, 31: 189-203

Wijaya, H., Spatz, M. W., 1995. Two-Phase Flow Heat Transfer and Pressure Drop Characteristics of R-22 and R-32/125, *ASHRAE Transactions*, 101(1): 1020-1026

Yasuda, H., Senshu, T., Kurodu, S., Atsumi, A., Oguni, K., 1990. Heat Pump Performance under Frosting Conditions: Part II-Simulation of Heat Pump Cycle Characteristics under Frosting Conditions, *ASHRAE Transactions*, 96: 330-335

Yokozeki, A., 1996. Thermodynamic Properties of Mixtures Based on Van Der Waals Equation of State-R-32/125 Binary System, *International Journal of HVAC&R Research*, 2(4): 284-311

Yonko, J. D., Sepsy C.F., 1967. An Investigation of the Thermal Conductivity of Frost While Forming on a Flat Horizontal Plate, *ASHRAE Transactions*, 73(2): 567-579

Young, D. J., 1980. Development of a Northern Climate Residential Air-Source Heat Pump, *ASHRAE Transactions*, 86(1): 671-686

APPENDIX A

R-410A PROPERTY

CALCULATION METHODS

The successful simulation and prediction of the frosted evaporator performance requires reliable thermodynamic and transport properties of the refrigerant in both the single- and two-phase regions. There are five methods currently available for R-410A thermodynamic property calculations: Martin-Hou EOS (AlliedSignal, 1996), Extended Martin-Hou EOS (DuPont, 1996), REFPROP (NIST), van der Waals EOS (Yokozeki, 1996) and EES (F-Chart Software). Both REFPROP and EES are commercial software packages. Neither provides published documentation that describes the detailed equations and coefficients used to estimate R-410A properties. Therefore, this appendix lists only three of the five calculation methods for R-410A properties. They are AlliedSignal standard Martin-Hou EOS, DuPont extended Martin-Hou EOS and empirical equations for transport properties, and Yokozeki's van der Waals EOS.

AlliedSignal Standard Martin-Hou Equations (USCS Units)

T_b=-62.878 ^oF	MWt.=72.558
T_c=162.500 ^oF	P_c=717.886 psia
ρ_c=31.2139 lb./cu.ft.	v_c=0.0320ft^3/lb

Martin-Hou coefficients used:

$$P = \frac{RT}{(V-b)} + \sum_{i=2}^{5} \frac{A_i + B_i T + C_i \exp(-KT_r)}{(V-b)^i} \qquad \text{(A.1)}$$

where P (psia), v (cu.ft./ib.), T (R), T_r=T/T_c

R=0.147903 b=0.5201834013E-02 k=0.5474999905E+01

i	A_i	B_i	C_i
2	-0.6291824867E+01	0.3614923532E-02	-0.164251901E+03
3	0.2758515284E+00	-0.2820548871E-03	0.516303638E+01
4	-0.1578745342E-02	0.0000000000E+00	0.000000000E+00
5	-0.2470426041E-04	0.5655830560E-07	-0.543923986E-03

Vapor pressure correlated as:

$$\ln(P_{vap}) = A + \frac{B}{T} + CT + DT^2 + \frac{E(F-T)}{T}\ln(F-T) \qquad \text{(A.2)}$$

where P_{vap} is in psia and T is in R

A = 0.1303495663E+02	B = -0.416576160E+04	C = 0.3807471667E-03
D = 0.0000000000E+00	E = 0.0000000000E+00	F = 0.0000000000E+00

Liquid density correlated as:

$$\rho = \rho_c + \sum_{i=1}^{4} D_i (1-T_r)^{i/3} \qquad \text{(A.3)}$$

where ρ is in lb./cu.ft.

D_1 = 0.3512693796E+02	D_2 = 0.1214476898E+03	D_3 = -0.1620426211E+03
D_4 = 0.9829573272E+02	ρ_c = 0.3121390984E+02	

Ideal gas heat capacity correlated as:

$$C_{\rho}^{o} = C_1 + C_2 T + C_3 T^2 + C_4 T^3 + C_5 / T \qquad \text{(A.4)}$$

where $C_\rho{}^o$ is in Btu/lb·R and T is in R

C_1 = 0.8363938559E-01 C_2 = 0.2339311077E-03 C_3 = -0.4207713700E-07
C_4 = 0.0000000000E+00 C_5 = 0.0000000000E+00

DuPont Extended Martin-Hou Equations (SI Units)

(1) Equation of state (Martin-Hou EOS)

$$P = \frac{RT}{V-b} + \sum_{i=2}^{5} \frac{A_i + B_i T + C_i \exp(-\kappa T / T_c)}{(V-b)^i} \qquad \text{(A.5)}$$

A_2 = -0.172178E+00	B_2 = 1.646288E-04	C_2 = -6.293665E+00
A_3 = 2.381558E-04	B_3 = -1.462803E-08	C_3 = 1.532461E-02
A_4 = -4.329207E-07	B_4 = 0.0	C_4 = 0.0
A_5 = -6.241072E-10	B_5 = 1.380469E-12	C_5 = 1.6041250E-07
R = 1.145502E-01	b_3 = 4.355134E-04	κ = 5.75

(P in kPa, T in K, V in m^3/kg, P_c = 4926.06 kPa; T_c = 345.28 K, d_c = 488.90 kg/m^3, Mol. Wt. = 72.584, and Boiling Point at Atmospheric Pressure = 221.654 K)

(2a) Saturated liquid pressure (bubble point)

$$\log_e(P/P_c) = \frac{1}{T_r}(A + BX + CX^2 + DX^3 + EX^4 + FX^5) \qquad \text{(A.6)}$$

$$X = (1 - T_r) - X_o; \qquad T_r = T/T_c \qquad \text{(A.7)}$$

A = -1.437600E+00	B = -6.871500E+00	C = -0.5362300E+00
D = -3.826420E+00	E = -4.068750E+00	F = -1.233300E+00

(P in psia, T in R, P_c = 714.4658903 psia; T_c = 621.50 R, and X_0 = 0.2086902)

(2b) Saturated vapor pressure (dew point)

$$\log_e(P/P_c) = \frac{1}{T_r}(A + BX + CX^2 + DX^3 + EX^4 + FX^5) \qquad \text{(A.8)}$$

$$X = (1 - T_r) - X_o; \qquad T_r = T/T_c \qquad \text{(A.9)}$$

A = -1.440004E+00	B = -6.865265E+00	C = -0.5354309E+00
D = -3.749023E+00	E = -3.521484E+00	F = -7.750E+00

(P in kPa, T in K, P_c = 4926.06 kPa; T_c = 345.28 K, and X_0 = 0.2086902)

(3) Saturated liquid density

$$d/d_c = A + Bx + Cx^2 + Dx^3 + Ex^4 \qquad \text{(A.10)}$$

A = 1.000000E+00	B = 1.9847340E+00	C = -1.767593E-01
D = 1.819972E+00	E = -7.1716840E-01	

(d in kg/m^3, T in K, d_c = 488.902 kg/m^3; and T_c = 345.28 K)

(4) Ideal heat gas capacity

$$C_p^o = A + BT + CT^2 + DT^3 \qquad \text{(A.11)}$$

A = 2.6760843E-01 B = 2.1153533E-03 C = -9.848184E-07
D = 6.4937810E-11 (C_p^o in kJ/kg·K, T in K, and $C_v^o = C_p^o - 0.1145502$)

(5a) Saturated liquid enthalpy

$$H_l = A + BX + CX^2 + DX^3 + EX^4 + FX^5 \qquad \text{(A.12)}$$

$$X = (1 - T_r)^{1/3} - X_o; \qquad T_r = T / T_c \qquad \text{(A.13)}$$

A = 221.1749 B = -514.9668 C = -631.6250
D = -262.4063 E = 1052.0 F = 1596.0
(H_l in kJ/kg, T in K, T_c = 345.28 K, and X_0 = 0.2086902)

(5b) Vapor enthalpy

$$H_g = AT + \frac{BT^2}{2} + \frac{CT^3}{3} + \frac{DT^4}{4} + PV + \left[\frac{A_2}{V-b} + \frac{A_3}{2(V-b)^2} + \frac{A_4}{3(V-b)^3} + \frac{A_5}{4(V-b)^4}\right] + e^{-\aleph T/T_c}\left(1 + \frac{\aleph T}{T_c}\right)\left[\frac{C_2}{V-b} + \frac{C_3}{2(V-b)^2} + \frac{C_4}{3(V-b)^3} + \frac{C_5}{4(V-b)^4}\right] + X \qquad \text{(A.14)}$$

A = 0.15305823E+00 B = 2.1153533E-03 C = -9.848184E-07
D = 6.4937810E-11 All other constants are same as in Equation (1)
(H_g in kJ/kg, T in K, P in kPa, V in m^3/kg, T_c = 345.28 K, and X = 298.7192)

(6a) Vapor Entropy

$$S_g = A\log_e(T) + BT + \frac{CT^2}{2} + \frac{DT^3}{3} + R\log_e(V-b) - \left[\frac{B_2}{V-b} + \frac{B_3}{2(V-b)^2} + \frac{B_4}{3(V-b)^3} + \frac{B_5}{4(V-b)^4}\right] + \frac{\aleph e^{-\aleph T/T_c}}{T_c}\left[\frac{C_2}{V-b} + \frac{C_3}{2(V-b)^2} + \frac{C_4}{3(V-b)^3} + \frac{C_5}{4(V-b)^4}\right] + Y \qquad \text{(A.15)}$$

A = 0.15305823E+00 B = 2.1153533E-03 C = -9.848184E-07
D = 6.4937810E-11 All other constants are same as in Equation (1)
(S_g in kJ/kg·K, T in K, V in m^3/kg, T_c = 345.28 K, and Y = 0.846399)

(6b) Saturated Liquid Entropy

$$S_l = S_g - \frac{H_g - H_l}{T} \tag{A.16}$$

(H_l, H_g in kJ/kg, S_l, S_g in kJ/kg·K, and T in K)

(7a) Saturated Liquid Viscosity in μPa·s (-50°C to 70°C)

$$\mu = 166 - 2.25 \cdot T + 1.81E-2 \cdot T^2 - 9.20E-5 \cdot T^3 \tag{A.17}$$

(T in **°C**)

(7b) Saturated Liquid Kinematic Viscosity in mm²/s (-50°C to 70°C)

$$\upsilon = 0.139 - 1.43E-3 \cdot T + 1.43E-5 \cdot T^2 - 1.04E-7 \cdot T^3 \tag{A.18}$$

(T in **°C**)

(7c) Saturated Vapor Viscosity in μPa·s (-20°C to 70°C)

$$\mu = 12.10 + 8.33E-2 \cdot T + 1.47E-4 \cdot T^2 - 4.67E-5 \cdot T^3 + 1.08E-6 \cdot T^4 \tag{A.19}$$

(T in **°C**)

(7d) Vapor Viscosity at One Atmosphere in μPa·s (-30°C to 120°C)

$$\mu = 11.70 + 3.98E-2 \cdot T \tag{A.20}$$

(T in **°C**)

(8a) Saturated Liquid Thermal Conductivity in mW/m °C (-50°C to 70°C)

$$k = 100.1 - 0.471 \cdot T + 6.86E-4 \cdot T^2 - 1.29E-5 \cdot T^3 \tag{A.21}$$

(T in **°C**)

(8b) Saturated Vapor Thermal Conductivity in mW/m °C (-20°C to 70°C)

$$k = 12.94 + 8.85E-2 \cdot T - 8.14E-4 \cdot T^2 + 5.29E-5 \cdot T^3 \tag{A.22}$$

(T in **°C**)

(8c) Vapor Thermal Conductivity at One atmosphere in mW/m °C (-30°C to 120°C)

$$k = 11.54 + 7.41E - 2 \cdot T \qquad \text{(A.23)}$$

(T in **°C**)

(9) Liquid Heat Capacity in J/g °C (-40°C to 50°C)

$$C_p = 1.603 + 5.727E - 3 \cdot T + 9.903E - 5 \cdot T^2 + 1.855E - 6 \cdot T^3 \qquad \text{(A.24)}$$

(T in **°C**)

Van der Waals Equations (SI Units)

(1) van der Waals equation

$$P = \frac{RT}{v + c - b} - \frac{a}{(v + c)^2} \tag{A.25}$$

$$a = \sum_{i,j=1}^{N} \sqrt{a_i a_j}(1 - k_{ij}) x_i x_j \tag{A.26}$$

$$a_i = a_{ci} a_i(T), \qquad a_{ci} = \frac{27}{64} \frac{(RT_{ci})^2}{P_{ci}} \tag{A.27}$$

$$a_i(T) = \sum_{k=0}^{4} \beta_{ik} \left(\frac{1}{T_r} - T_r\right)^k \tag{A.28}$$

$$k_{ij} = A_{ij} + B_{ij} T + C_{ij} T^2, \qquad k_{ij} = k_{ji}, \qquad k_{ii} = 0 \tag{A.29}$$

$$b = \sum_{i,j=1}^{N} \frac{b_i + b_j}{2}(1 - m_{ij}) x_i x_j, \qquad m_{ij} = m_{ji}, \qquad m_{ii} = 0 \tag{A.30}$$

$$b_i = \frac{1}{8} \frac{RT_{ci}}{P_{ci}} \tag{A.31}$$

$$c = \sum_{i=1}^{N} c_i x_i \tag{A.32}$$

Table A.1 Pure compound critical properties

	M_w, g/mol	T_c, K	P_c, kPa	D_c, kg/m^3	Z_c
R-32	52.02	351.36	5797	422.7	0.2446
R-125	120.02	339.4	3631	571.9	0.2676

Table A.2 EOS constants for pure compounds in Equation (A.28) and (A.32)

	R-32		R-125	
	Vapor-EOS	VLE-EOS	Vapor-EOS	VLE-EOS
β_0	1.000032	1.002449	1.005017	1.001717
β_1	0.6161940	0.5010681	0.5275089	0.5039978
β_2	0.4250635	-8.445462E-02	0.4930612	-6.298828E-02
β_3	0.2965353	8.148193E-03	-0.4133451	1.043701E-02
β_4	-0.3582382	0	0.1664058	0
c, m^3/kg	9.082531E-04	0	3.095998E-04	0

Table A.3 Binary parameters in Equations (A.29), (A.30) and (A.31) for-32/125 mixture

	Vapor-EOS	VLE-EOS
A_{ij}	0.7442428	-1.408335E-02
$B_{ij}(K^{-1})$	-5.057141E-03	8.609193E-05
$C_{ij}(K^{-2})$	8.412452E-06	0
m_{ij}	-6.434811E-02	1.047614E-02

(2) Ideal gas heat capacity

$$C_p^o = C_0 + C_1 T + C_2 T^2 + C_3 T^3 \tag{A.33}$$

Table A.4 Constant C_i (J/mol·K) corresponding to R-32 and R-125, respectively

	R-32		R-125	
	Vapor-EOS	VLE-EOS	Vapor-EOS	VLE-EOS
C_0	2.033775E+01	1.416518E+01	1.731620E+01	8.202527E+00
C_1	7.534468E-02	3.995665E-01	3.339437E-01	1.069961E+00
C_2	1.871870E-05	-2.155075E-01	-2.795803E-04	-5.582657E-03
C_3	-3.115527E-05	3.422978E-06	8.746460E-08	9.735151E-06

(3) Isochoric heat capacity

$$C_V = -T\int_{\infty}^{V}\left(\frac{\partial^2 P}{\partial T^2}\right)_V dV + C_p^0 - R \tag{A.34}$$

(4) Isobaric heat capacity

$$C_p = C_v - T\left(\frac{\partial P}{\partial T}\right)_v^2\left(\frac{\partial P}{\partial V}\right)_T^{-1} = C_v - T\left(\frac{R}{V-b} - \frac{a'}{V^2}\right)^2\left(\frac{2a}{V^3} - \frac{RT}{(V-b)^2}\right)^{-1} \tag{A.35}$$

(5) Saturated liquid volume

$$V_{sat} = \frac{RT_c}{P_c} Z^{\theta}, \qquad \theta = 1 + (1 - T_r)^{2/7} \tag{A.36, A.37}$$

$$Z = \left(\frac{P_c V_x}{RT_c}\right)^{\eta}, \qquad \eta = \frac{1}{1 + (1 - T_x / T_c)^{2/7}} \tag{A.38, A.39}$$

(6) Enthalpy

$$H = RT(Z-1) + RT^2 \int_{\infty}^{V} \left(\frac{\partial Z}{\partial T}\right)_V \frac{dV}{V} + H^0 = RT(Z-1-\frac{cZ}{V}) + \frac{Ta'-a}{V} + H^0 \qquad \text{(A.40)}$$

$$Z = \frac{V}{V-b} - \frac{a}{VRT} \qquad \text{(A.41)}$$

(7) Entropy

$$S = RT \int_{\infty}^{V} \left(\frac{\partial Z}{\partial T}\right)_V \frac{dV}{V} + R \int_{\infty}^{V} (Z-1)\frac{dV}{V} R\ln Z + S^0 = R\ln\frac{P(V-b)}{RT} + \frac{a'}{V} + S^0 \qquad \text{(A.42)}$$

The systematic comparisons of the thermodynamic property values obtained from different methods in both the saturated lines and the vapor region are presented as well. At the superheated region, note that all the state points could not be evaluated with REFPROP6.01 past about 150 ^{o}F while the rest of the methods would run through 160 ^{o}F. The compared results show that there exists difference on the property predictions of each method. Because neither the AlliedSignal standard nor DuPont extended Martin-Hou correlation has a specific subcooling representation, the plotted comparisons on the subcooling liquid properties calculated by different methods are not provided.

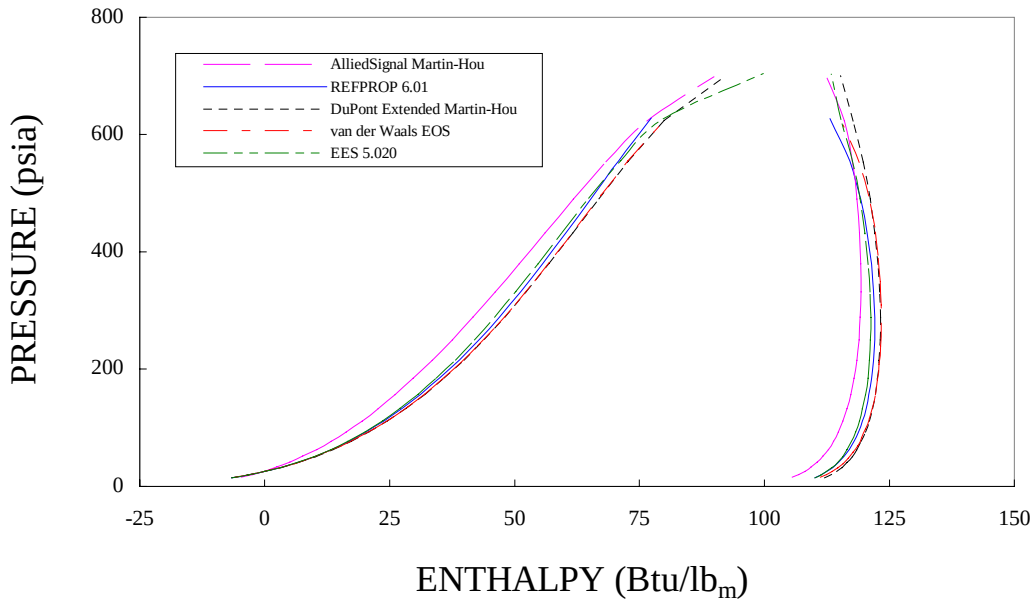

Figure A.1 R-410A saturated pressure-enthalpy (P-H) diagram obtained from the different calculation methods

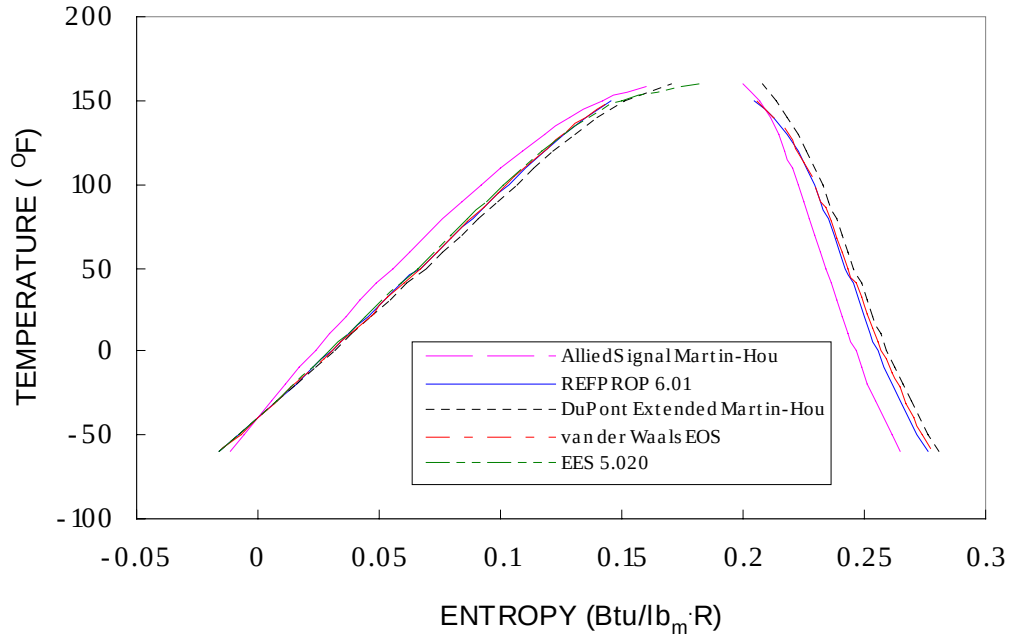

Figure A.2 R-410A saturated temperature-entropy (T-S) diagram obtained from the different calculation methods

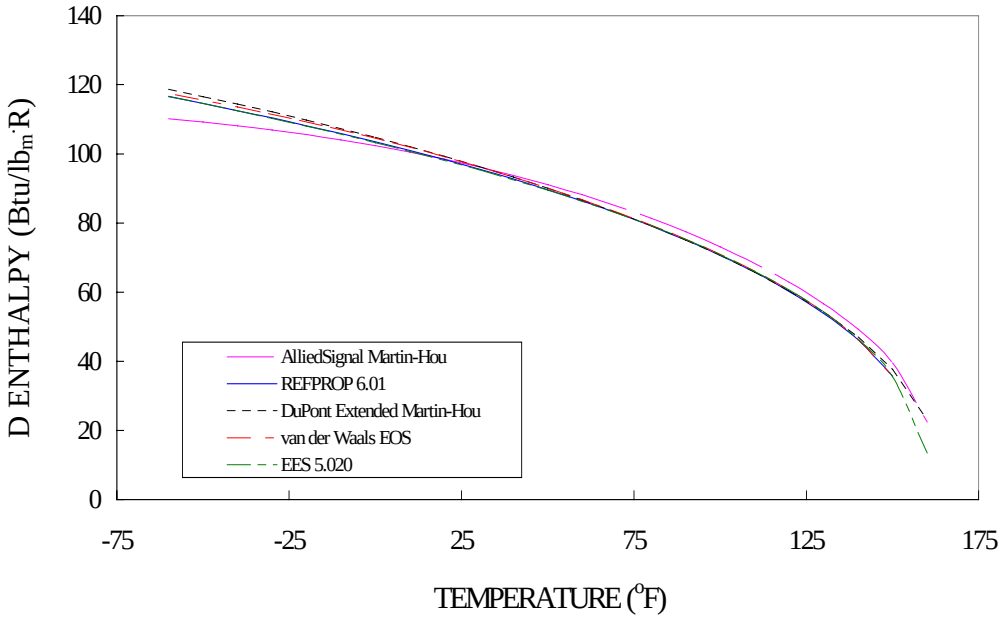

Figure A.3 R-410A latent heat diagram obtained from the different calculation methods

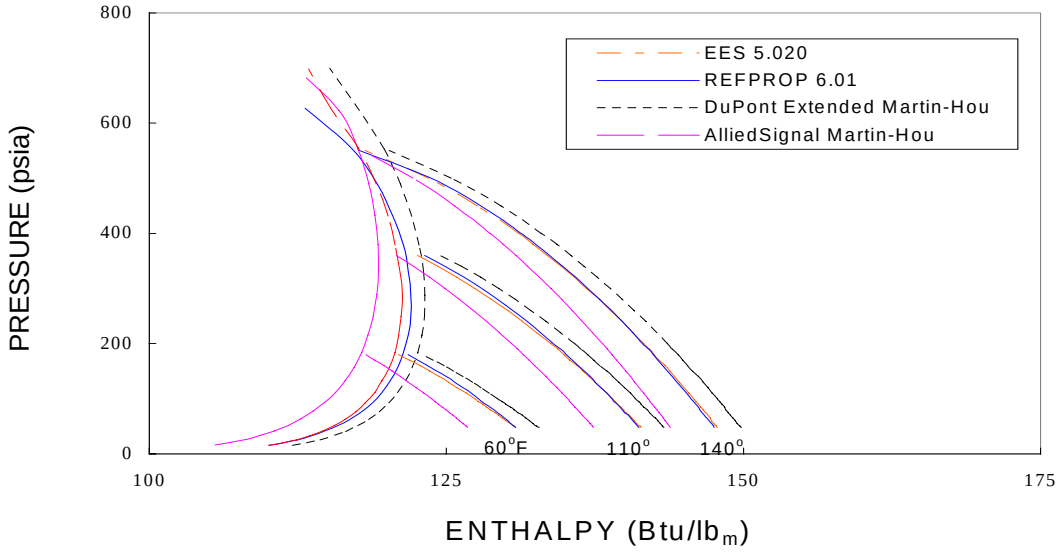

Figure A.4 R-410A pressure-enthalpy (P-H) diagram at superheated vapor zone for the different calculation methods

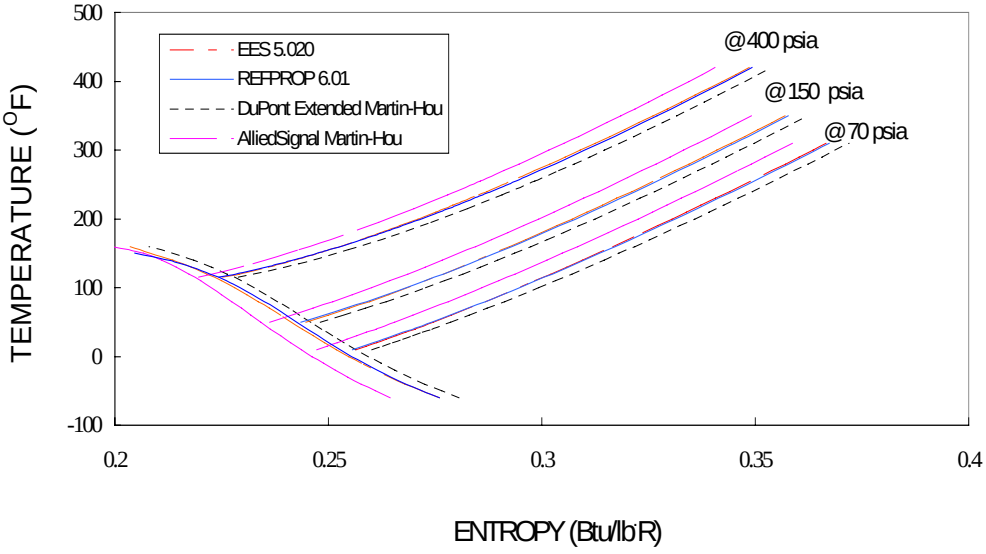

Figure A.5 R-410A temperature-entropy (T-S) diagram at superheated vapor zone for the different calculation methods

VITA

Jianxin Yang was born in Beijing, China. He graduated from Beijing 5th High School in July of 1987 and enrolled in Jiaotong University, Xi'an, China in the fall of that year. He received both his Bachelor of Science and Master of Science degrees in mechanical engineering from Jiaotong University in Xi'an, China in 1991 and 1994, respectively. While in graduate school, he worked as a graduate research assistant in the Air Conditioning and Refrigeration Lab, Jiaotong University. After graduation in 1994, Mr. Yang joined the China National Petroleum Chemical & General Machinery Engineering Corp., Beijing, China. He worked in the 2nd division of this corporation as a HVAC mechanical engineer for two years before entering the Ph.D. program at Texas A&M University in 1996. Mr. Yang worked as a research associate with the Energy Systems Laboratory at Texas A&M University. His permanent mailing address is No.275 DI AN MEN West Street, Beijing, China.